# Special Issue

# Diagnostic Timescale Methods for the Aquatic Environment: Current Challenges, Recent Improvements, and Applications

## Message from the Guest Editors

Timescale diagnoses (e.g., age, residence/exposure time, inverse of reaction rate) are powerful tools helping to analyze and understand passive and reactive transport processes taking place in the aquatic environment. This Special Issue aims at presenting recent advances in tracer and timescale methods. All types of contributions will be welcome, in particular those focusing on novel methodological developments (even if they are still being formulated) and applications aimed at addressing ecological problems. Numerical methods using Eulerian or Lagrangian approaches will be considered, as well as techniques based on remotely sensed or in situ data. We will seek a balance between contributions from natural sciences and engineering, as well as between numerical, observational and theoretical approaches.This Special Issue is intended to be a follow-up to a recently completed Water Special Issue entitled “Tracer and Timescale Methods for Passive and Reactive Transport in Fluid Flows” (mdpi.com/si/22716).

## Guest Editors

Prof. Dr. Eric Deleersnijder

Dr. Edward S. Gross

Prof. Dr. Zhe Liu

Dr. Lisa V. Lucas

Prof. Dr. Jian Shen

## Deadline for manuscript submissions

closed (28 February 2025)

**Water**

an Open Access Journal by MDPI

Impact Factor 3.0
CiteScore 5.8

mdpi.com/si/140682

*Water*
MDPI, Grosspeteranlage 5
4052 Basel, Switzerland
Tel: +41 61 683 77 34
water@mdpi.com

mdpi.com/journal/water

# Water

an Open Access Journal by MDPI

Impact Factor 3.0
CiteScore 5.8

mdpi.com/journal/water

# About the Journal

## Message from the Editor-in-Chief

In the context of global changes, the sustainable management of water cycles, going from global and regional water cycles to urban, industrial and agricultural water cycles, plays a very important role on the water resources and on their relationships with food, energy, biodiversity, ecosystem functioning and human health. *Water* invites authors to provide innovative original full articles, critical reviews and timely short communications and to propose special issues devoted to new technological and scientific domains and to interdisciplinary approaches of the water cycles. We ensure a critical review process and a quick turnaround between submission and final decision.

## Editor-in-Chief

Dr. Jean-Luc PROBST
Centre de Recherche sur la Biodiversité l'Environnement (CRBE) UMR CNRS/UPS/INPT/IRD, Centre National de la Recherche Scientifique (CNRS), University of Toulouse, Campus ENSAT, Auzeville Tolosane, Toulouse, France

## Author Benefits

**Open Access:**

free for readers, with article processing charges (APC) paid by authors or their institutions.

**High Visibility:**

indexed within Scopus, SCIE (Web of Science), Ei Compendex, GEOBASE, GeoRef, PubAg, AGRIS, CAPlus / SciFinder, Inspec, and other databases.

**Journal Rank:**

JCR - Q2 (Water Resources) / CiteScore - Q1 (Water Science and Technology)

MDPI

water

MDPI

*Article*

# Using Age Tracers to Estimate Ecological Rates in a Phytoplankton Model

**Edward Gross [1,2,*], Rusty Holleman [3], Wim Kimmerer [4], Sophie Munger [3], Scott Burdick [1] and John Durand [3,5]**

[1] Resource Management Associates, 1756 Picasso Avenue, Suite G, Davis, CA 95618, USA; scott@rmanet.com
[2] Department of Civil and Environmental Engineering, University of California, Davis, One Shields Avenue, Davis, CA 95616, USA
[3] Center for Watershed Sciences, University of California, Davis, One Shields Avenue, Davis, CA 95616, USA; cdholleman@ucdavis.edu (R.H.); smunger@ucdavis.edu (S.M.); jrdurand@ucdavis.edu (J.D.)
[4] Estuary & Ocean Science Center, San Francisco State University, Tiburon, CA 94920, USA; kimmerer@sfsu.edu
[5] Department of Wildlife, Fish and Conservation Biology, University of California, Davis, One Shields Avenue, Davis, CA 95616, USA
* Correspondence: ed@rmanet.com; Tel.: +1-530-564-7043

**Abstract:** The phytoplankton distribution in estuaries is influenced by multiple spatially variable growth and loss processes. As phytoplankton are transported by tidal and net flows, they are exposed to changing conditions of turbidity, depth, temperature, stratification, and grazing. Understanding the factors influencing the observed phytoplankton distribution patterns will allow better-informed restoration and water management efforts. We developed a Lagrangian approach driven by three-dimensional hydrodynamic model results and a simple representation of the production and losses of phytoplankton, allowing a highly efficient closed-form solution for phytoplankton biomass. Our analysis used continuous observations of chlorophyll concentration at four stations and a near-synoptic chlorophyll dataset collected underway from a boat in the channels of Suisun Marsh in the San Francisco Estuary. We divided the study region into four compartments defined by the water depth and location. For each observation location, hydrodynamic model simulations calculated the time that water parcels spent in each of these compartments and the mean depth encountered by water parcels in those compartments. Then, using that information and continuous monitoring data, we inferred compartment-specific grazing rates and two additional ecological parameters. The underway chlorophyll dataset was used for model validation. The model predicted patterns of observed spatial and tidal variability in chlorophyll in Suisun Marsh. The modeling indicated that the chlorophyll concentration at a point in space in time depends largely on the relative exposure to shallow areas, with positive net productivity and deep areas having negative net productivity.

**Keywords:** San Francisco Estuary; phytoplankton; chlorophyll; grazing; water age; time scales



**Citation:** Gross, E.; Holleman, R.; Kimmerer, W.; Munger, S.; Burdick, S.; Durand, J. Using Age Tracers to Estimate Ecological Rates in a Phytoplankton Model. *Water* **2023**, *15*, 2097. https://doi.org/10.3390/w15112097

Academic Editor: Bommanna Krishnappan

Received: 27 April 2023
Revised: 23 May 2023
Accepted: 27 May 2023
Published: 1 June 2023



## 1. Introduction

Phytoplankton abundance in estuaries is influenced by spatially and temporally variable physical and ecological processes that induce differences in growth and loss rates. Conditions that influence these rates include sunlight, nutrient availability, turbidity, water depth, temperature, stratification, and the density of benthic and pelagic grazers. Physical processes can both advect phytoplankton in the direction of net flows and mix water volumes with different properties. As water masses move with tidal and net flows, they carry with them phytoplankton, zooplankton, and physical and ecological properties, all of which can undergo transformations in their moving reference frame.

The problem of representing ecological processes occurring in moving water parcels is often solved by a two- or three-dimensional hydrodynamic model coupled with an ecological model on the same spatial grid. These coupled hydrodynamic–ecological models are often used to represent spatial variability in ecological and transport processes [1].

When applied to phytoplankton, ecological models typically compute variables such as nutrient concentrations, phytoplankton biomass, and zooplankton biomass on an Eulerian grid, simultaneously capturing local transformations and non-local transport processes (i.e., advection and dispersion). Phytoplankton models vary greatly in the complexity of processes and in spatial resolution (Ganju et al. 2015). The resolution of ecological parameters is often much coarser than the computational grid. For example, grazing rates that vary in time and space [2] are generally specified at far coarser scales than the hydrodynamic model grid. When applied to estuaries, these models are computationally intensive because they require the calculation of all these state variables at a short time interval (typically minutes) at many depth-averaged (two-dimensional) or three-dimensional computational elements. However, the rate constants for ecological processes in such models are typically much slower than for hydrodynamic processes, implying a mismatch in time scales that results in an inefficient method.

In contrast to ecological models that are tightly coupled with a hydrodynamic model and share its spatial and temporal resolution, an alternative approach is to simulate ecological processes and phytoplankton biomass at a coarser spatial or temporal resolution. The spatial resolution may be coarsened to a region, for example, the low-salinity zone of the San Francisco Estuary [3]. This mass-balance approach requires minimal computation but typically does not predict the spatial distribution of phytoplankton within the region. Large-scale spatial variability can also be represented using grid aggregation to compute ecological properties on a coarser spatial and temporal scale than hydrodynamics [4]. Correlative analyses can also provide insight into phytoplankton dynamics [5] but provide a limited scope to predict ecological conditions beyond those for which correlations were developed, or where covariate data are lacking.

Lagrangian approaches represent ecological processes in a water parcel as it moves through space. Information is incorporated into the Lagrangian frame by calculating the conditions (e.g., depth, clam abundance, and light intensity) encountered by a tracer that represents water parcels from a particular source. This approach is conceptually similar to the application of the widely used Streeter–Phelps equation to estimate dissolved oxygen concentrations in rivers. In both cases, the concentration is estimated from the concentration at a known starting location, the travel time to a downstream location of interest, and specified biogeochemical transformation rates. While even the simplest Eulerian modeling approach requires substantial computation to advect and disperse phytoplankton, ecological predictions in a Lagrangian frame become simple computations [6]. Such approaches are of particular interest for ecological models, as the formulations and ecological rate parameters are often uncertain.

One such Lagrangian mechanistic model [6] used water age with the net phytoplankton growth rate to estimate the time course of chlorophyll concentration as a water parcel is advected by tidal and net flows. By using a simple formulation, with no explicit state variables for nutrients or zooplankton, this approach allowed for a closed-form solution for chlorophyll concentration. Furthermore, Ref. [6] included a nonlinear parameter that can roughly represent a feedback mechanism, such as a nonlinear increase in zooplankton grazing with increased phytoplankton abundance.

We built upon the approach in [6] by including additional tracer-based calculations. Tracer-based estimates included the mean water age [7], mean partial age [8], and mean depth exposure [9]. Water age (hereafter "age") is a transport time scale quantifying the time elapsed since a water parcel entered a study area, which can be estimated using a tracer-based modeling approach [10]. A specific application of this flexible approach provides the algebraic mean age of all water parcels from a specific source as they are transported away from the source. Partial age [8] quantifies the time that the tracer has spent in a specific geographical region. This partial age, which we will refer to as "exposure time," can be calculated for distinct regions that could represent different compartments [8]. We use the term "compartment" instead of region because the compartments are not spatially contiguous. Property exposure tracking [9] is a tracer-based approach to estimate

a tracer's mean exposure to different properties. For example, mean depth exposure at a specific time and station is the mean depth encountered by water parcels in transit from a source to the station.

Using these tracer-based approaches to estimate the mean exposure time and mean depth encountered in different compartments, we developed a simplified and highly computationally efficient phytoplankton model. The model includes terms for processes known to be important for phytoplankton in the San Francisco Estuary, including light-limited growth [11] and grazing by clams [12] and zooplankton [13]. Additional terms of uncertain importance include phytoplankton mortality [14] and a nonlinear feedback term, as in [6]. Notably, the model did not include nutrient information since nutrient limitation is uncommon in the San Francisco Estuary [11]. In addition, the model does not explicitly predict zooplankton biomass in estimating grazing losses to zooplankton.

This parsimonious approach was applied to predict chlorophyll concentrations in Suisun Marsh, a large brackish-to-freshwater marsh in the northern San Francisco Estuary. Numerical optimization was used to determine the clam grazing rate, phytoplankton mortality rate, and a nonlinear feedback parameter. These parameters were fit to minimize the root-mean-squared deviation between the predicted chlorophyll and the chlorophyll observed at four in situ monitoring stations. Clam grazing rates were assumed to vary with compartment, as clams are more abundant in the main channel of Suisun Marsh than in shallower side channels [15] and absent from intertidal areas.

The model reproduced some patterns in the data and estimated clam grazing rates that were credible. The major advantage of this modeling approach is that it can efficiently estimate biogeochemical rate coefficients that produce predictions consistent with observations. Only one hydrodynamic and tracer simulation was required, and then chlorophyll concentrations were predicted in an offline model, and clam grazing rates were selected to minimize the error in chlorophyll predictions. This specific application is one example of how age tracer approaches can be used to infer ecological rates, which can then be corroborated by incorporation into a multi-dimensional biogeochemical model.

## 2. Materials and Methods

### *2.1. Study Area*

Suisun Marsh (Figure 1) is the largest tidal marsh system in the San Francisco Estuary [16]. It lies north of Suisun Bay, with hydraulic connections to Grizzly Bay (an arm of Suisun Bay) and to the Sacramento River at the seaward boundary of the California Delta. Suisun Bay is connected to the ocean through the Carquinez Strait, San Pablo Bay, and San Francisco Bay. Suisun Marsh has mixed semidiurnal tides propagating east from the Pacific Ocean and highly variable freshwater flow from the Delta. Formerly a dendritic tidal marsh, in the last century, Suisun Marsh was largely converted to managed wetlands, and the principal current use of the area is duck hunting and other recreation. Of a total area of ~405 $km^2$, ~210 $km^2$ is managed wetland, 31 $km^2$ is remnant tidal marsh, 104 $km^2$ is tidal sloughs, and the remainder is upland [16]. Suisun Marsh is a focal point for habitat restoration and scientific studies [17]. Fish populations have been monitored there since 1979 [18], and plans for the conversion of managed wetlands to open tidal wetlands are proceeding, with the expectation of a benefit for threatened and endangered species, including the delta smelt *Hypomesus transpacificus* [19] and the longfin smelt *Spirinchus thaleichthys* [20].

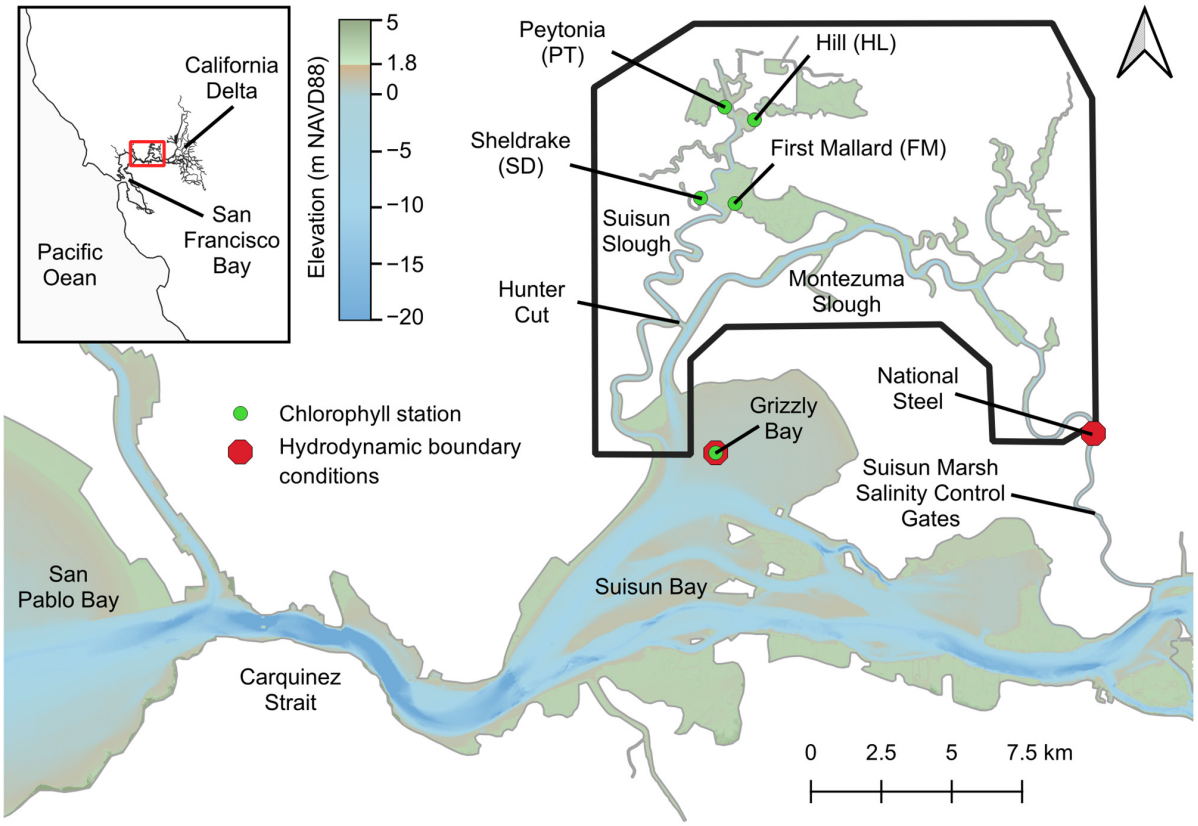


**Figure 1.** Study area, Suisun Marsh model domain (heavy black outline), bathymetry, stations providing chlorophyll data (the four northernmost stations), and data for model boundary conditions. The red box in the inset indicates the location of the region in the figure.

The recovery of these species is likely limited by food availability [21] as well as temperature [22,23] in rearing habitats throughout the upper estuary [21]. Phytoplankton biomass in the main channels of the northern San Francisco Estuary declined sharply in 1987, largely as a result of grazing by the introduced clam *Potamocorbula amurensis* [12]. Phytoplankton biomass and productivity have remained low [24], with similar declines in zooplankton, attributed to declines in food and consumption by clams [25], and declines in fish attributed to food limitation [19].

The continuing declines in fishes of special concern, including listed species, have stimulated efforts to increase shallow habitats in the hopes of stimulating planktonic production. Several restoration projects are proposed or ongoing within Suisun Marsh [26]. These projects are based on the assumption that the phytoplankton growth rate is light-limited and therefore high in shallow waters, allowing for the accumulation of biomass if clams are not abundant [2,27]. Phytoplankton biomass can be higher in small, dead-end sloughs in the marsh than in larger channels [28], and clams are abundant mainly in larger sloughs [15].

The Suisun Marsh Salinity Control Gates (SMSCG; Figure 1) at the east end of Montezuma Slough were designed to decrease salinity for the managed waterfowl habitat by opening on ebb tides and closing on flood tides. This leads to tidal pulses of freshwater moving westward through the main distributary channel of the marsh, Montezuma Slough. The gates are typically operated in spring but were operated on an experimental basis during August 2018 in an attempt to improve habitats for endangered fish species by reducing salinity in the marsh [17].

### 2.2. Overview of Approach

The analysis proceeded in three distinct steps. First, we developed the three-dimensional hydrodynamic model of Suisun Marsh and calibrated it by comparing model predictions to observed water level, flow, and salinity data.

Next, we applied the calibrated model to simulate the three-dimensional and time-varying distributions of a set of properties using numerical tracers. The computational domain was divided into four compartments: the main channel, side channel, low intertidal, and marsh plain (Figure 2). The numerical model calculated the time for water to travel from the seaward boundary in Grizzly Bay (Figure 1) to each element in the model for each time step in the simulation. In addition, the duration of exposure to these compartments and mean depth encountered in each were predicted.

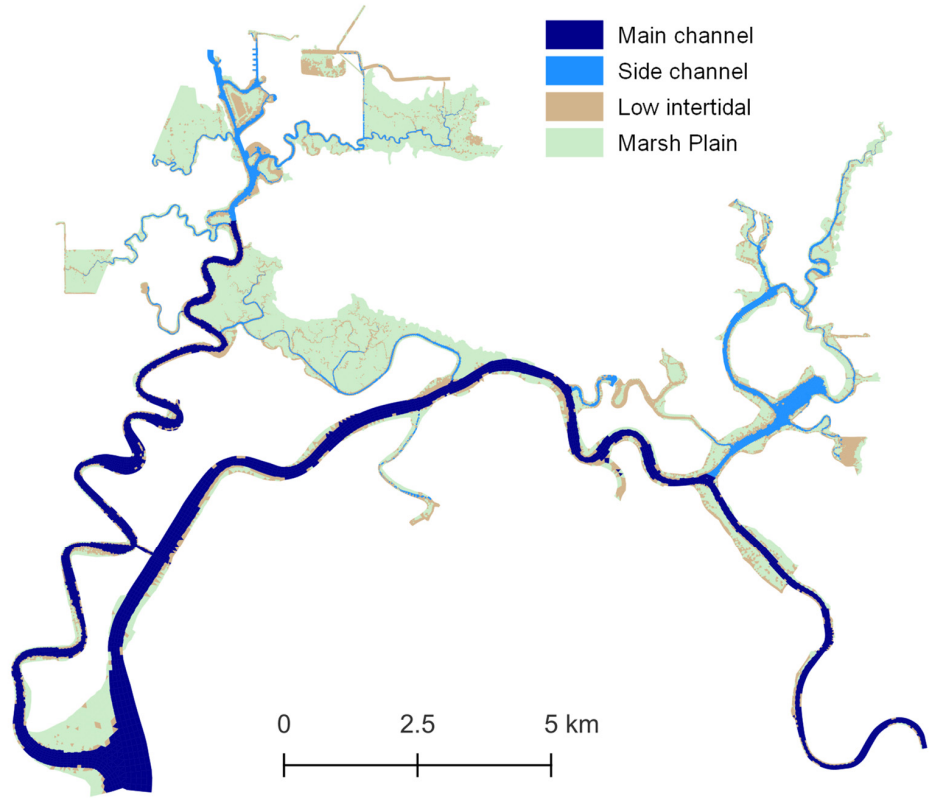


**Figure 2.** Compartment classifications of each cell in the model domain.

Third, we developed and applied a phytoplankton model to predict the chlorophyll concentration. Two datasets were used. To calibrate the model, we used continuous monitoring data collected at 15 min intervals at four stations (Figure 1). To validate the model, we used a near-synoptic dataset collected underway from a high-speed boat during a single day. Our approach estimated time-varying light-limited growth rates for each compartment and loss rates from clam grazing, zooplankton grazing, and phytoplankton mortality over the mean tracer age from the entry of the tracer from the seaward boundary. While the growth rate used an existing formulation without the adjustment of any parameters, four loss rate parameters were determined by optimizing the fit of the model to continuous monitoring chlorophyll observations. The four parameters were clam grazing in the main channel, clam grazing in the side channel, phytoplankton mortality, and a nonlinear parameter representing density-dependent feedback mechanisms [6]. Using estimates of these parameters determined by fitting, predicted chlorophyll was compared to the underway data. Finally, the contributions of individual processes in each compartment to chlorophyll predictions were analyzed.

### 2.3. Hydrodynamic Model

The hydrodynamic model domain extends through Suisun Marsh (Figure 1). The eastern boundary is located at the National Steel station north of the SMSCG (Figure 1), and the western boundary is at the junction of Montezuma and Suisun Sloughs with Grizzly Bay (Figure 1). This model domain extent was guided by the availability of data for boundary conditions.

The three-dimensional UnTRIM model [29] was applied in this domain with an unstructured computational mesh with edge lengths in the range of 2 m to 10 m in slough channels and up to 100 m near the Grizzly Bay boundary. This model simulates physical processes resulting in the transport of salt and other tracers and allows for the wetting and drying of computational cells [30] and a sub-grid-scale representation of bathymetry [31]. Bottom roughness and other model parameters were specified to be consistent with previous applications extending throughout the San Francisco Estuary [9]. Wind forcing was not included in the simulation and is expected to have a limited influence on transport in this region of strong tidal flows.

The model simulated hydrodynamics and tracer distributions (see Section 2.3) for 1 March 2018 to 1 September 2018 so that the tracer distributions were appropriately "spun up" from the initial condition of zero age for chlorophyll simulations from 23 June 2018 to 6 August 2018. The hydrodynamic model time step was 30 s. Boundary conditions were specified using continuous-flow and salinity data from the National Steel station operated by the California Department of Water Resources (DWR), salinity data from the USGS Grizzly Bay station (380631122032201), and stage data from the DWR Hunter Cut station (Figure 1). An initial salinity field throughout the model domain was derived by interpolating observed salinity.

Hydrodynamic model predictions were compared with observed stage and salinity data collected at continuous monitoring stations in the model domain (Figure 3). Performance metrics were computed at each calibration location, as in previous calibration efforts in the San Francisco Estuary [9]. Performance metrics included the coefficient of determination ($R^2$) and a commonly used model skill metric [32],

$$Skill = 1 - \frac{\sum_{i=1}^{n} |P_i - O_i|^2}{\sum_{i=1}^{n} \left( |P_i - \overline{O}| + |O_i - \overline{O}| \right)^2} \quad (1)$$

where $n$ is the number observations, $O_i$ and $P_i$ are the $i$th pair of observed and predicted values, and overbar denotes an average over $i$. Skill ranges from 0 to 1, with 1 indicating a perfect model.

### 2.4. Water Age and Property Tracking

An essential component of the Lagrangian tracer-based approach was the mean age of water, quantifying the time since it entered the model domain from the boundary in Grizzly Bay. Flows that enter the domain from the eastern end of Montezuma Slough have little influence on the study sites during the chlorophyll simulation period and were not tracked. To estimate age, we applied the widely used Constituent-oriented Age and Residence Time theory (CART) [33]. The equations for this approach are provided in Appendix A. A "partial age" approach, as defined in [8], quantified the exposure time of tracers to four spatial compartments (Figure 2). These habitats were defined based on bed elevation and location. Channel habitat was less than 0 m NAVD (North American Vertical Datum), corresponding approximately to mean lower low water in Suisun Marsh. The two compartments of the subtidal channel were the "main channel" and "side channel" (Figure 2), with the main channel corresponding to regions where clams were found to be abundant in field studies [15]. The low intertidal compartment extends from 0 to 1.8 m NAVD, approximately corresponding to bed elevation from mean lower low water to mean higher high water. The marsh plain compartment is located above mean higher high water, defined as above 1.8 m NAVD.

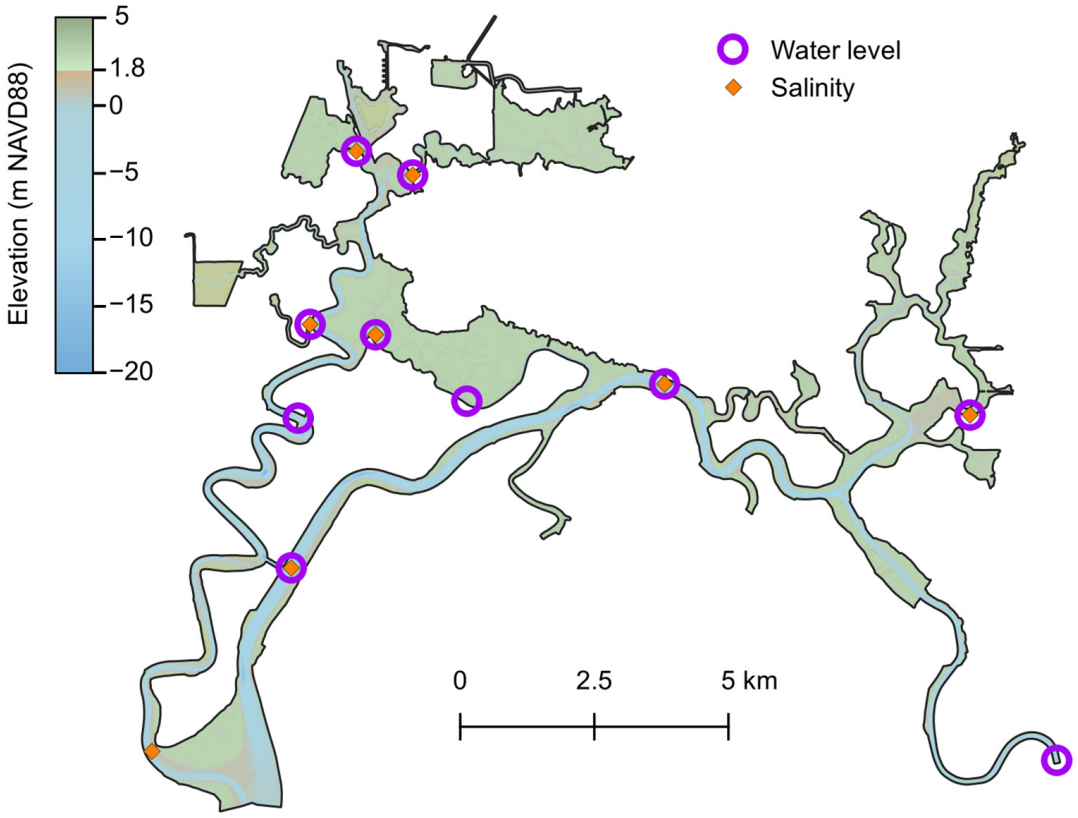


**Figure 3.** Hydrodynamic model bathymetry and stations with salinity and water level calibration data.

Property exposure tracking estimated depths encountered by tracers since entering from Grizzly Bay using the method described and applied in [9]. This method was generalized to estimate depth exposure in different compartments, as described in Appendix A.

### *2.5. Predicting Chlorophyll*

Chlorophyll concentration can be modeled in an Eulerian frame with a depth-averaged advection–reaction equation [6] (i.e., neglecting diffusion),

$$\frac{\partial P}{\partial t} + \nabla \cdot (\boldsymbol{u}P) = \left(\mu_{growth} - \mu_{loss}\right)P = \mu_{net}P \tag{2}$$

where $P = P(\boldsymbol{x}, t)$ is the chlorophyll concentration at an arbitrary position $\boldsymbol{x}$ (bold fonts denote vectors) and time $t$, $\mu_{growth} = \mu_{growth}(t)$ is the growth rate of phytoplankton and $\mu_{loss} = \mu_{loss}(t)$ is loss rate, and $\nabla \cdot (\boldsymbol{u}P)$ is the horizontal advection of chlorophyll by the hydrodynamic velocity vector $\boldsymbol{u}$.

Equation (2) can be rewritten in a Lagrangian frame for a specific water parcel following a horizontal trajectory $\boldsymbol{x} = \boldsymbol{x}(a)$ such that the left-hand side simplifies to an ordinary derivative with respect to age:

$$\frac{dP}{da} = \mu_{net}P \tag{3}$$

where $a$ is the total water age defined in Appendix A.

This approach was extended [6] to include a nonlinear term to represent food web interactions, such as increased zooplankton grazing at higher chlorophyll concentrations.

$$\frac{dP}{da} = \mu_{net}(1 + k_P P)P \tag{4}$$

where $k_P$ is a term for density dependence.

Equation (4), when integrated from $t - a$ to $t$, permits an analytical solution:

$$P(a) = \frac{P_{in}(t-a)e^{\overline{\mu_{net}}\ a}}{1 + k_p P_{in}(t-a)(1 - e^{\overline{\mu_{net}}\ a})} \tag{5}$$

where $P_{in}$ is the incoming chlorophyll concentration, and $a$ is the total water age at the time ($t$) and location ($\boldsymbol{x}$) of a chlorophyll prediction. The incoming chlorophyll concentration ($P_{in}$) is the measured chlorophyll at the Grizzly Bay station, low-pass filtered to remove tidal variability (Figure 4). The rate $\overline{\mu_{net}}$ is the mean net production rate from time $t - a$ to time $t$ as a water parcel travels from the source of the tracer (Grizzly Bay in our application) to $\boldsymbol{x}$. Note that while $\mu_{net}$ in Equation (4) may vary in time, the solution in Equation (5) depends only on the time-averaged rate $\overline{\mu_{net}}$.

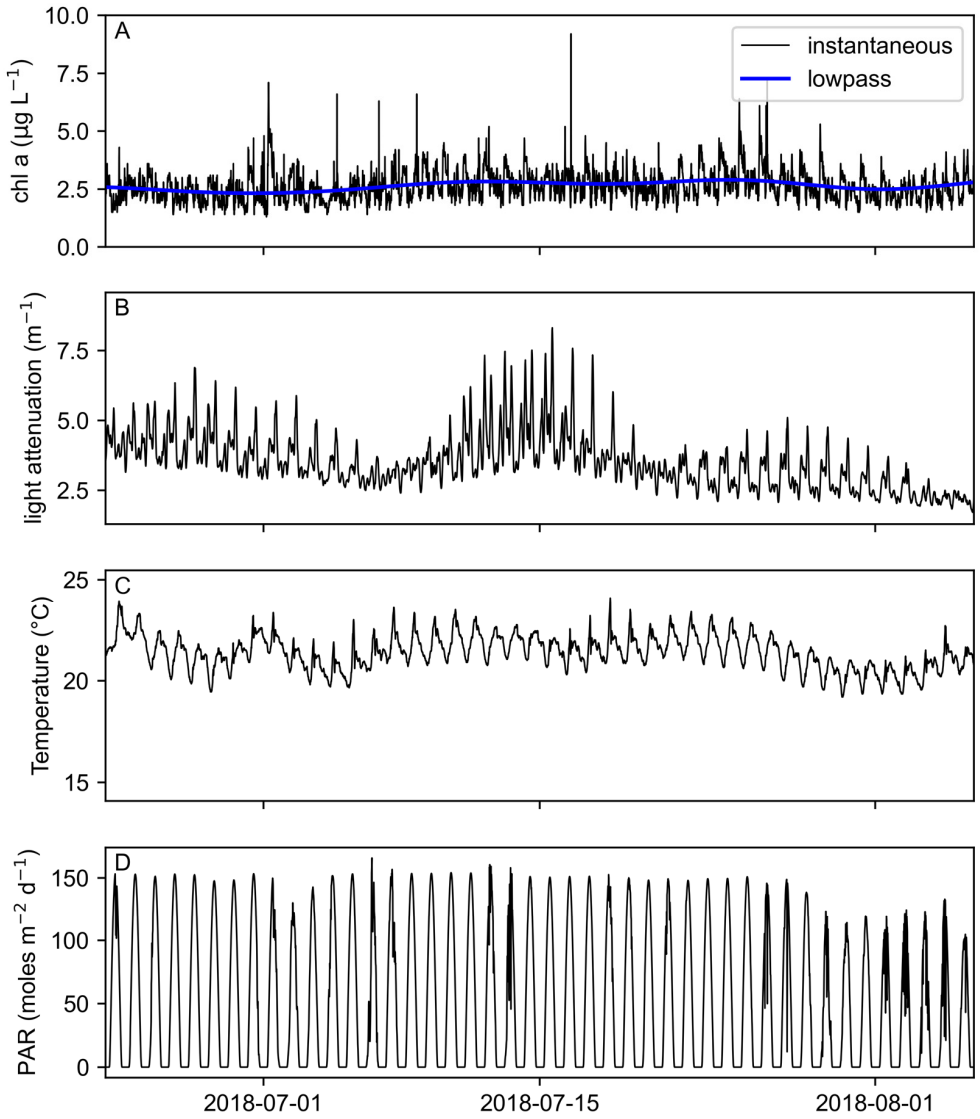


**Figure 4.** Model input data for chlorophyll simulation. (**A**) Measured and low-pass-filtered chlorophyll at the model boundary in Grizzly Bay, (**B**) light attenuation calculated from continuous turbidity values in Suisun Marsh, (**C**) temperature from continuous values in Suisun Marsh, (**D**) measured photosynthetically available radiation (PAR) at First Mallard station. The light attenuation and temperature data in panels B and C were calculated as the median value across the four continuous monitoring stations in Suisun Marsh (Figure 1).

This approach was generalized to multiple compartments with unique rates by averaging the compartment-specific rates according to the exposure time (partial age) for each compartment:

$$\overline{\mu_{net}} = \frac{1}{a}\int_{t-a}^{t} \sum_j \mu_{net,j}(t')\delta_j(t')dt\prime \approx \frac{1}{a}\sum_j \overline{\mu_{net,\ j}}a_j \quad (6)$$

where $\delta_j(t') \in [0,\ 1]$ reflects the exposure of water to compartment j at time $t'$, $\overline{\mu_{net,j}}$ is the mean rate ($d^{-1}$) in compartment $j$, and the exposure times to the individual compartments ($a_j$) sum to the total age ($a$) in days. The rates are time-averaged at each chlorophyll monitoring station over the period corresponding to the total age ($a$) to account for time-varying PAR, light attenuation, and temperature. Since $\mu_{net}$ appears in Equation (5) only as a time average, the solution is independent of the order in which compartments are encountered and depends only on the mean rate aggregated across compartments.

The chlorophyll simulation period was limited to the period when the tracer representing the fraction of water from Grizzly Bay that entered during the simulation period was continuously greater than 0.5 at each chlorophyll monitoring station. The fraction is less than one primarily because water initially in the domain, with a tracer concentration of zero, has not been fully exchanged with Grizzly Bay water. The resulting period was 23 June 2018 to 6 August 2018.

### *2.6. Estimating Phytoplankton Growth and Loss*

Several assumptions were implicit in the phytoplankton model formulation, including the lack of nutrient limitation. Clam grazing varied by compartment but was represented as constant in time. We specified time-varying but spatially uniform turbidity and temperature from observations at the four chlorophyll stations (Figure 1). Each spatially uniform value was estimated as the median of the data at the individual stations at a given time (Figure 4). We used equations from [14] to estimate the depth-averaged light-limited growth rate as follows:

$$\mu_{growth} = G_{max} f_I \quad (7)$$

where $G_{max}$ is the maximum potential growth rate ($d^{-1}$) at a given temperature, and $f_I$ characterizes the light limitation (see Table 1 for definitions of all variables).

$$G_{max} = 1.25\left(2^{(T-15)/10}\right) \quad (8)$$

$$f_I = min\left[\frac{I}{I_{max}},\ 1\right] \quad (9)$$

where $T$ is temperature in degrees Celsius, $I$ is water column mean photosynthetically active radiation (PAR), and $I_{max}$ is the irradiance supporting maximum water column growth, both in moles of photons $m^{-2}\ d^{-1}$.

$$I = \frac{E}{Hk}(1 - e^{-Hk}) \quad (10)$$

where $E$ is the surface PAR in moles of photons $m^{-2}\ d^{-1}$, measured at the First Mallard station (Figure 1) [34]. $H$ is water column depth (m), and $k$ is the light attenuation coefficient ($m^{-1}$).

$$I_{max} = 15.3\left(2^{(T-15)/10}\right) \quad (11)$$

**Table 1.** Definitions of variables in phytoplankton model and tracer simulations.

| Term | Definition |
|---|---|
| $P$ | Chlorophyll concentration (μg $L^{-1}$) |
| $\boldsymbol{u}$ | Hydrodynamic velocity vector (m $s^{-1}$) |
| $\mu_{growth}$ | Phytoplankton growth rate ($d^{-1}$) |
| $\mu_{loss}$ | Phytoplankton loss rate ($d^{-1}$) |
| $\mu_{net}$ | Net phytoplankton growth rate ($d^{-1}$) |
| $a$ | Mean age (d) |
| $k_P$ | Phytoplankton density-dependent gain/loss term (-) |
| $\boldsymbol{x}$ | Horizontal position vector (m) |
| $P_{in}$ | Boundary concentration of chlorophyll (μg $L^{-1}$) |
| $\overline{\mu_{net}}$ | Time-averaged net phytoplankton growth rate ($d^{-1}$) |
| $a_j$ | Mean exposure time to compartment j (d) |
| $j$ | Compartment index (-) |
| $G_{max}$ | Maximum growth rate at a given temperature ($d^{-1}$) |
| $T$ | Temperature (degrees C) |
| $f_I$ | Light limitation factor (-) |
| $H$ | Water column depth (m) |
| $I$ | Water column mean photosynthetically active radiation (moles $m^{-2}$ $d^{-1}$) |
| $I_{max}$ | Irradiance supporting maximum water column growth (moles $m^{-2}$ $d^{-1}$) |
| $k$ | Light attenuation coefficient ($m^{-1}$) |
| $S$ | Turbidity (FNU) |
| $M$ | Phytoplankton mortality rate ($d^{-1}$) |
| $Z$ | Microzooplankton grazing rate ($d^{-1}$) |
| $C$ | Clam grazing rate (m $d^{-1}$) |
| $C_{main}$ | Clam grazing rate in main channel (m $d^{-1}$) |
| $C_{side}$ | Clam grazing rate in side channel (m $d^{-1}$) |

The light attenuation coefficient, $k$ ($m^{-1}$), was estimated from turbidity using a relationship developed from data for the northern San Francisco Estuary [35]:

$$k = 0.069Turb + 0.90 \tag{12}$$

where 0.90 $m^{-1}$ is the background light attenuation, and $Turb$ is turbidity in FNU.

Growth rates were calculated from Equations (7)–(12). Temperature ($T$), irradiance ($E$), and turbidity ($S$) varied only in time, but $H$ varied in time, by station, and by compartment, necessitating a distinct growth rate calculation for each combination of station, compartment, and 15 min time interval. This growth rate therefore varied in time and by compartment and varied slightly among stations because of variation in the mean depth encountered by water as it traveled from the boundary through each compartment to each station. The parameters of these equations were taken from the literature, as described above, leaving no parameters in the growth formulation to be fit in the optimization.

In contrast, several loss rates were fit in our optimization because these rates are uncertain and likely both to be site-specific and to vary seasonally [15,36]. The loss terms in [14] are

$$\mu_{loss} = M + Z + C/H \tag{13}$$

where $M$ is the specified constant phytoplankton mortality ($d^{-1}$), $C$ is the clam grazing rate (m $d^{-1}$), which is constant in time, $H$ is water depth (m), and $Z$ is the time-varying microzooplankton grazing rate ($d^{-1}$), specified in our model as a function of the phytoplankton growth rate [3]:

$$Z = \max\left(0, -0.3 + 0.93\mu_{growth}\right) \tag{14}$$

where $\mu_{growth}$ was calculated for each compartment at each time interval in Equation (7). Mesozooplankton grazing was not specified with a distinct term but is considered to have a constant component, lumped in with the term $M$, and a component that varies with

chlorophyll levels, represented by the nonlinear coefficient $k_C$. Ecological processes that could contribute to $k_C$ include a density-dependent component of mortality.

The depth used in Equations (10) and (13) was estimated using property (depth) exposure modeling, described in Appendix A. The resulting depth represents the mean depth that water currently at a station has encountered in each compartment. For each observed chlorophyll value, the production term (Equation (5)) was calculated for each compartment over the time corresponding to the total age (i.e., from $t - a$ to $t$, where $t$ is the time of the observation). The loss rates were applied, resulting in net rates in each individual compartment, which were then weighted by fractional exposure ($a_j/a$) to each compartment (Equation (6)) to estimate chlorophyll at one specific time and location. The procedure was repeated for each individual chlorophyll observation independently of other chlorophyll observations. Changes in predictions were driven primarily by the spatially and tidally varying mean exposure time and mean depth in each compartment from the tracer simulations.

The unknown rates in the formulation above were phytoplankton mortality ($M$), the nonlinear coefficient ($k_P$), and clam grazing in the main channel ($C_{main}$) and side channels ($C_{side}$). Each of these variables is assumed to be constant in time and space (or constant within a compartment in the case of clam grazing), leaving a total of four unconstrained degrees of freedom in the model. The closed-form phytoplankton model (Equation (5)) using exposure times and property tracking, given a set of model parameters, predicts chlorophyll at the time and location of each observation. Differential evolution [37], a robust stochastic optimization approach from the Python *scipy* [38] library, was then used to find parameter values that minimize root-mean-squared error (RMSE) in predicted chlorophyll compared to the observed chlorophyll, described in Section 2.7, at the four stations (Figure 1) at 15 min intervals during the simulation period. The evaluation of RMSE for a single set of parameters entails 4224 distinct chlorophyll predictions and requires approximately 0.3 s on a laptop computer. Similar results were obtained from faster, deterministic optimization methods, but the possibility of local minima motivated the use of the more robust differential evolution.

In order to quantify the role of each individual growth or loss term, the right-hand side of Equation (4) was decomposed into contributions from these terms, and each was integrated separately. The numerical integration was performed by the *odeint* ODE solver in Python's *scipy* library [38].

### 2.7. Chlorophyll Observations

The UC Davis continuous monitoring data used in calibrating the model were collected from April to September 2018 at four stations (Figure 1; Sheldrake, First Mallard, Peytonia, and Hill Sloughs) located in channels of Suisun Marsh. At each station, a YSI EXO II sonde measured pressure, temperature, conductivity, chlorophyll fluorescence, turbidity, fluorescent dissolved organic matter (fDOM), pH, and dissolved oxygen. Sondes recorded data every 15 min and were serviced and calibrated approximately monthly. Calibrations for chlorophyll and turbidity were performed using standard solutions. Continuous chlorophyll data were corrected using simple multiple regression against values for chlorophyll concentration and turbidity obtained from whole-water grabs. Water grabs were analyzed in the UC Davis Geochemistry Lab using standard techniques [39]. Strong tidal variability was typically apparent in these data, with higher chlorophyll at low water suggesting higher phytoplankton biomass in low intertidal and marsh plain compartments than in channels.

A separate set of near-synoptic chlorophyll data [40] was collected underway from a high-speed boat on 27 July 2018 from 7:57 to 15:16 PST. The boat was fitted with a flow-through system equipped with an EXO v2 sonde (YSI, Yellow Springs, OH, USA) that was calibrated immediately prior to use [25]. These observations were collected at intervals of 1 s throughout the main channels of Suisun and Montezuma Sloughs while underway at speeds of up to 13 m $s^{-1}$, providing a map of chlorophyll concentrations at spatial intervals

of meters. In places where observations were dense, they were averaged within each hydrodynamic model grid cell (~10 m length) for comparison with predicted chlorophyll. These underway data were collected during the period of continuous data availability and were useful in examining spatial patterns in model accuracy due to large spatial extent.

Continuous monitoring data at each station were compared to the underway observations to assess biases between the two sets of observations. Continuous monitoring stations were located in smaller slough channels adjacent to Suisun Slough, while the underway data were collected in the main channels (Figure 1). To mitigate the effect of horizontal separation between a station and underway observations, station data at the time of high tide were compared to the underway data nearest to the station location, under the assumption that water in the channel (sampled by underway observations) would have advected to the station location during the flood tide. In these comparisons, continuous monitoring data were consistently lower than the underway data (Table 2). Possible reasons for the differences are different sensors deployed or differences in the calibration approach. The underway sensor data were calibrated to laboratory measurements on the day of the survey, while the continuous monitoring data were calibrated once per multiple-week deployment, so we assumed that the underway data gave more accurate estimates of chlorophyll concentrations. We used the calculated fixed offsets from the underway data to reduce chlorophyll in the continuous monitoring data (Table 2). Chlorophyll measured in underway surveys conducted outside our simulation period was also persistently higher than contemporaneous data from the continuous monitoring stations.

**Table 2.** Comparison of continuous monitoring station chlorophyll observations at high water to adjacent underway observations in the Suisun Slough channel, used to specify continuous data offsets.

| Station | Continuous (mg $L^{-1}$) | Underway (mg $L^{-1}$) |
|---|---|---|
| First Mallard | 2.08 | 6.49 |
| Sheldrake | 4.54 | 5.39 |
| Peytonia | 7.60 | 10.01 |
| Hill | 5.86 | 9.43 |

## 3. Results

### 3.1. Hydrodynamic Model Calibration

The hydrodynamic model predicted salinity and water level accurately during the portion of the hydrodynamic simulation period when the chlorophyll simulations were performed (Table 1). The model predicted water level particularly well, with a computed skill of 1.00, partially due to the limited spatial variability in water level in the small model domain. The model skill for salinity was 0.84, and predicted salinity was 0.35 lower than the observed salinity on average (Table 3). The range of observed salinity at the calibration stations during this period was 0.9 to 16.4 with a mean of 5.8.

**Table 3.** Model performance metrics averaged across continuous monitoring stations.

| Parameter | $R^2$ | Bias | RMSE | Skill |
|---|---|---|---|---|
| Water level | 0.99 | 0.00 | 0.06 | 1.00 |
| Salinity | 0.81 | −0.35 | 0.72 | 0.84 |

Hydrodynamic conditions were generally vertically well mixed throughout the model domain during the simulation period. A small degree of stratification formed intermittently at some locations during ebb tides.

### 3.2. Age and Property Exposure Predictions

The tracer concentration and mean age corresponding to the transport of water from the Grizzly Bay boundary to the marsh were calculated on the three-dimensional model grid at 30 min time intervals. An example snapshot of the tracer fields shows that the

Grizzly Bay tracer had filled most of the model domain (Figure 5) at the time of underway data collection. The mean exposure time was calculated for each of the four compartments (Figure 2) throughout the model grid and simulation. The calculated mean exposure times at each station varied tidally, as water with more exposure to low intertidal and marsh plain compartments and less exposure to the main channel passes by each station during the ebb tide. Exposure to the main channel was larger than exposure to other compartments at all stations (Figure 6A) because the tracer must pass through the main channel to arrive at the stations. At any location and point in time, the mean exposure times summed exactly to the mean age.

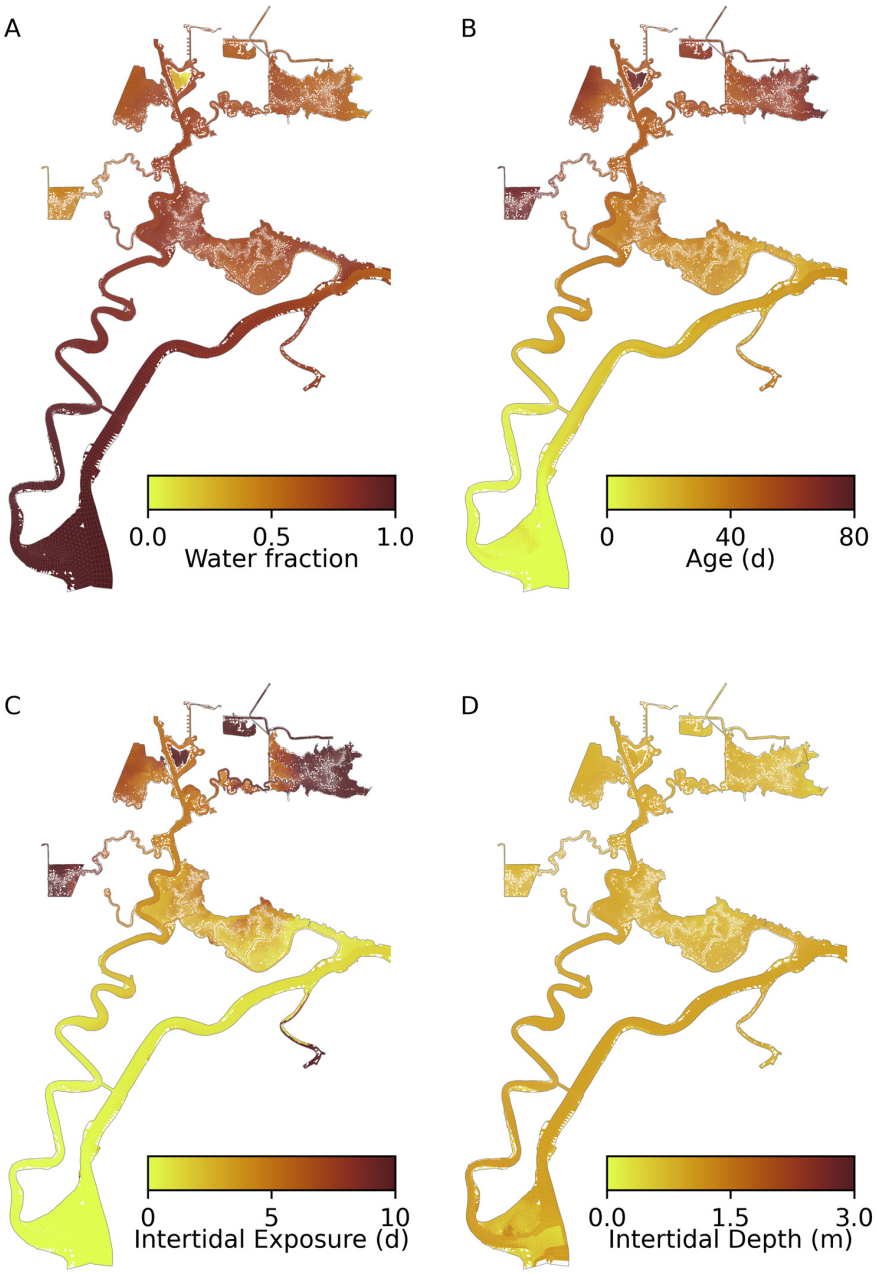


**Figure 5.** Example depth-averaged predicted age tracer fields on 27 July 2018 at noon corresponding to the time of underway data collection. (**A**) Depth-averaged fraction of water that has entered the domain from the Grizzly Bay boundary during the model run. (**B**) Mean age of the tracer. (**C**) Mean exposure time to low intertidal compartment. (**D**) Mean depth encountered by the tracer in low intertidal compartment.

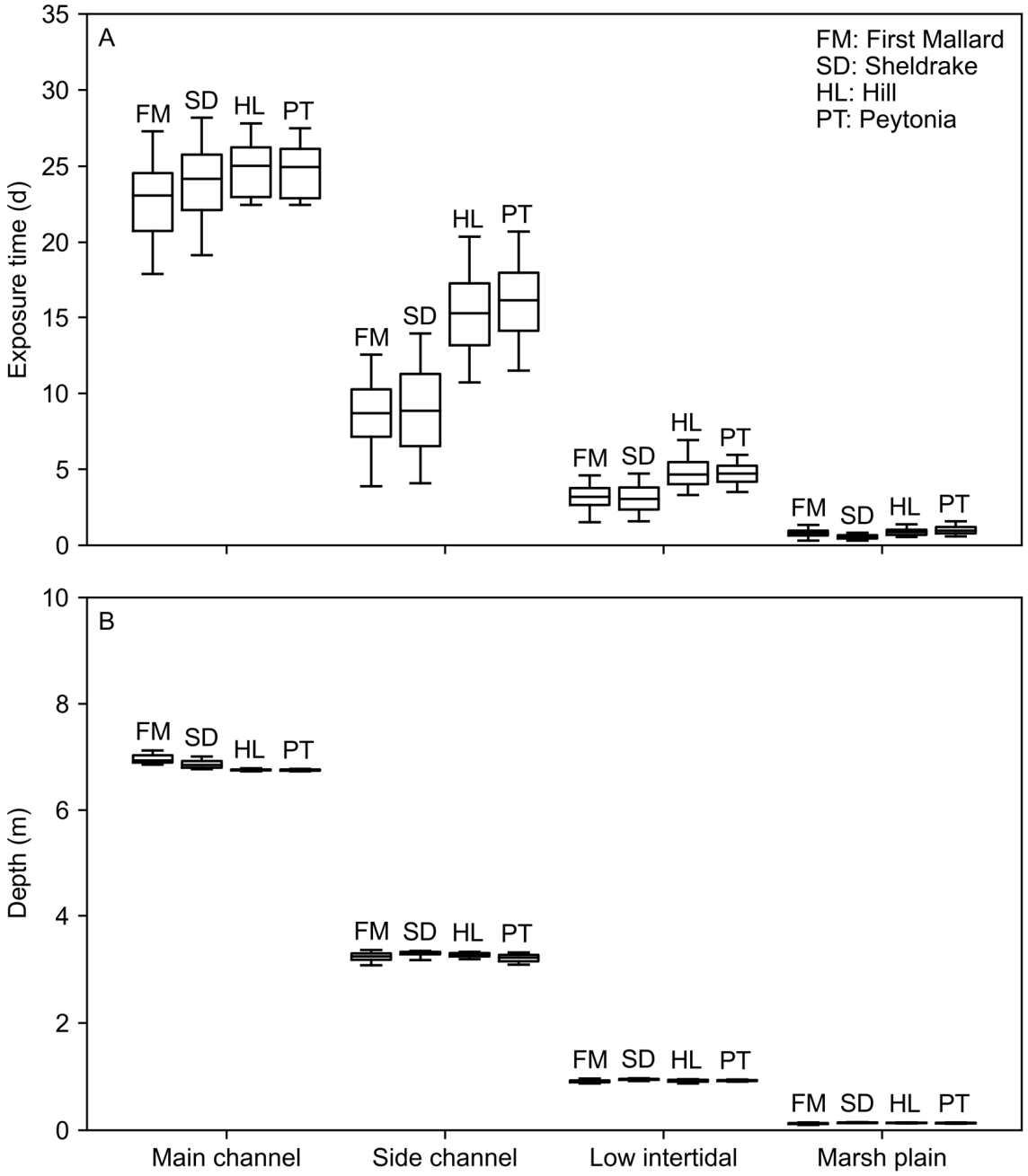


**Figure 6.** Predictions for tracer traveling from the Grizzly Bay boundary to each station during the simulation period. (**A**) Mean exposure times to each compartment. (**B**) Mean depth encountered while in each compartment. Boxes indicate interquartile ranges, horizontal lines indicate medians, and whiskers indicate the range of 95% of predictions.

The chlorophyll simulation period of 23 June 2018 to 6 August 2018 was chosen as the period when the tracer concentration representing the fraction of water from Grizzly Bay that entered during the simulation period was continuously greater than 0.5 at each chlorophyll monitoring station. The end time of the simulation corresponds to the timing of a significant fraction of water reaching the stations from the eastern entrance of Montezuma Slough when SMSCG gates were opened during flood tides starting in early August [17].

The mean depth encountered by the tracer was extracted from the simulation for each combination of station, time, and compartment. The mean depths encountered by the tracer between the Grizzly Bay boundary and each station varied little among stations but greatly among compartments (Figure 6B). The mean depths encountered were typically less

than 0.2 m in the marsh plain compartment, about 1 m in the low intertidal compartment, roughly 3 m in the side channel compartment, and approximately 7 m in the main channel compartment. Since more of the water column in shallow compartments was in the photic zone, these compartments had higher estimated phytoplankton growth rates.

### *3.3. Chlorophyll-a Predictions at Stations*

The parameters for both grazing in the side channel and phytoplankton mortality derived in the optimization were estimated to be zero, and the other two parameters were non-zero. The chlorophyll simulation using the estimated parameters (Table 4) allowed the accurate prediction of chlorophyll, which generally increased with the predicted water age (Figure 7). Median chlorophyll was predicted well at all four stations (Figure 8), with both observed and predicted chlorophyll increasing with the distance from Grizzly Bay, where tidally averaged measured chlorophyll was roughly 2.5 mg $L^{-1}$ (Figure 4) during the simulation period. The range of chlorophyll at each station was also predicted well by the model (Figure 8), except at Sheldrake Slough, where some observed values at high water were much higher than those predicted by the model. The tidal phase of variability in observed chlorophyll was predicted well by the model (Figure 9). The model predictions were largely unbiased, though the range of variability was underpredicted at the Sheldrake Slough station (Figure 8).

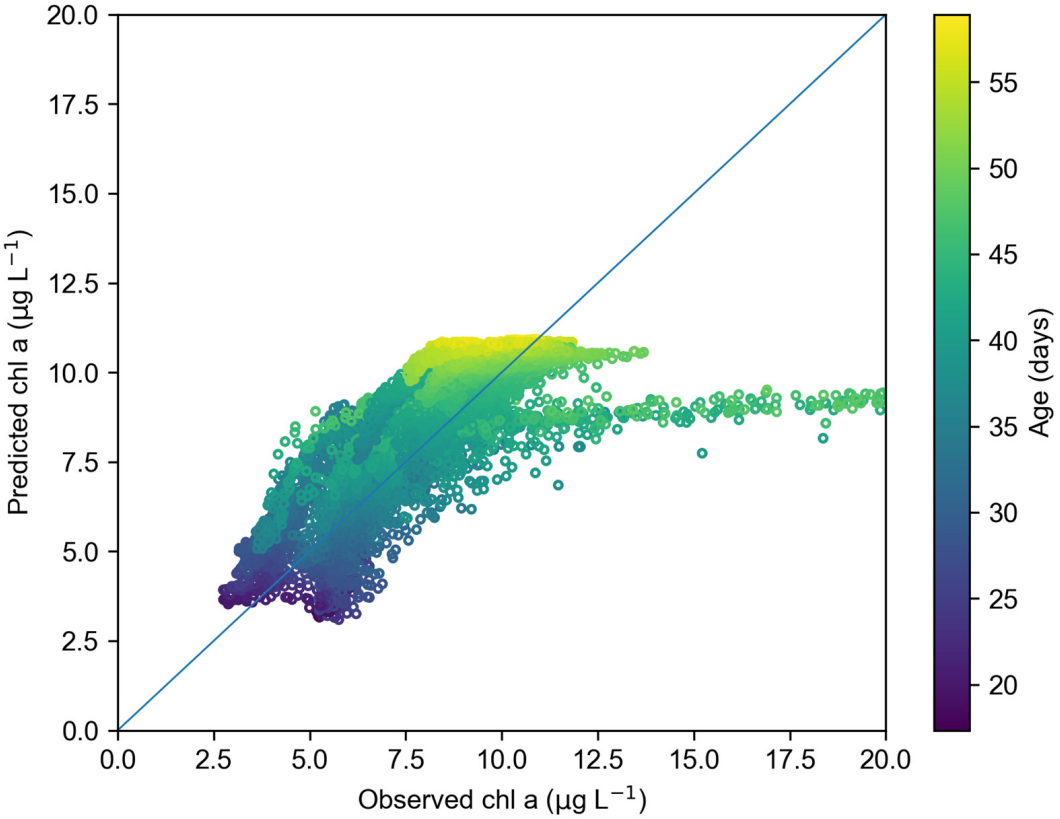


**Figure 7.** Predicted vs. observed chlorophyll at the continuous monitoring stations. Each circle is colored by the predicted total age. A 1:1 line is shown in blue. Approximately five percent of the chlorophyll measurements at Sheldrake Slough were greater than 20 mg $L^{-1}$ (not shown).

**Table 4.** Parameter values for clam grazing, density-dependent feedback parameter, and phytoplankton mortality estimated in optimization.

| Parameter | Location | Value | Units |
|---|---|---|---|
| $C_{main}$ | Main channel | 1.13 | m $d^{-1}$ |
| $C_{side}$ | Side channel | 0.0 | m $d^{-1}$ |
| $k_c$ | Global | −0.091 | L $\mu g^{-1}$ |
| $M$ | Global | 0.0 | $d^{-1}$ |

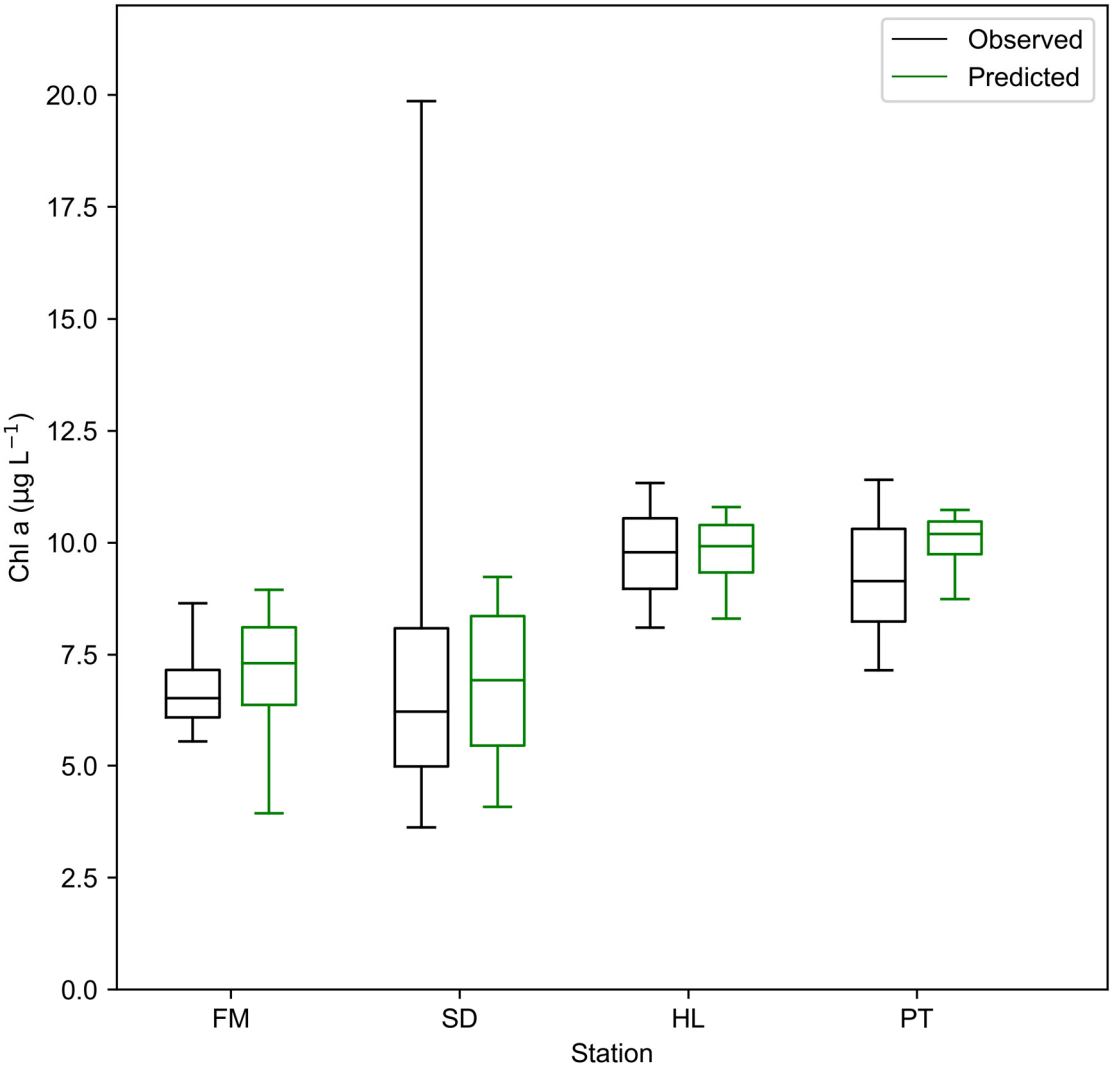


**Figure 8.** Quantiles of observed and predicted chlorophyll. The box is the interquartile range, the horizontal line is the median value, and the whiskers give the 0.05 and 0.95 quantiles.

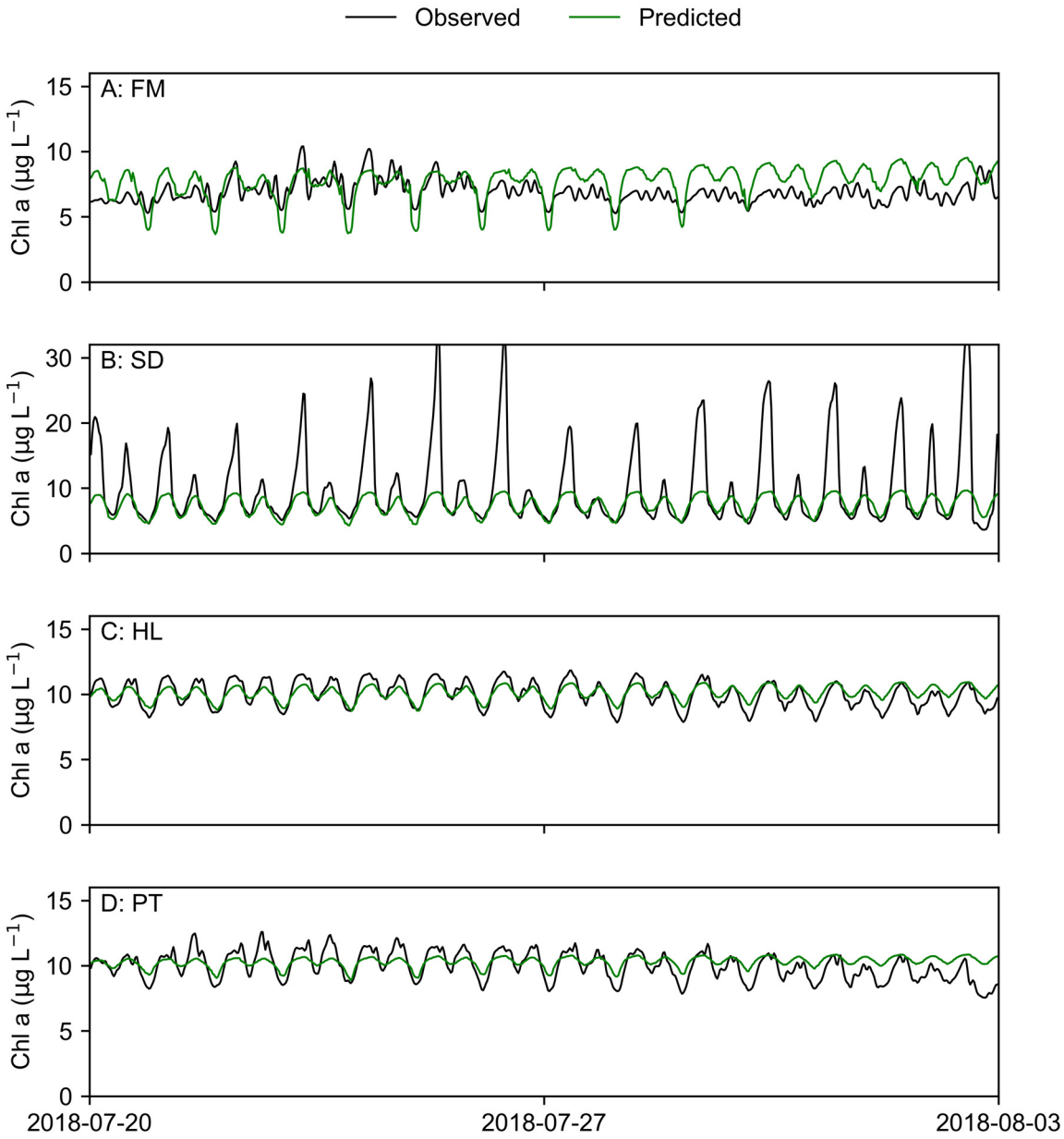


**Figure 9.** Observed and predicted chlorophyll at each station during a two-week period centered on the time of underway data collection. (**A**) First Mallard Slough station. (**B**) Sheldrake Slough station. (**C**) Hill Slough station. (**D**) Peytonia Slough station.

### *3.4. Chlorophyll Growth and Loss Terms*

We calculated the relative rates of various processes that result in the estimated changes in chlorophyll between the Grizzly Bay boundary and sampling stations (Figure 10). As evident in Equation (6), the contribution to chlorophyll predictions from the time spent in each compartment depends both on the compartment-specific rate (Figure 10) and on the compartment exposure time (Figure 6). The calculated growth and loss rates varied across compartments and, to a lesser degree, sampling stations. The net rates were negative (loss) in the channel regardless of the sampling station, while all net rates were positive (growth) for the other compartments.

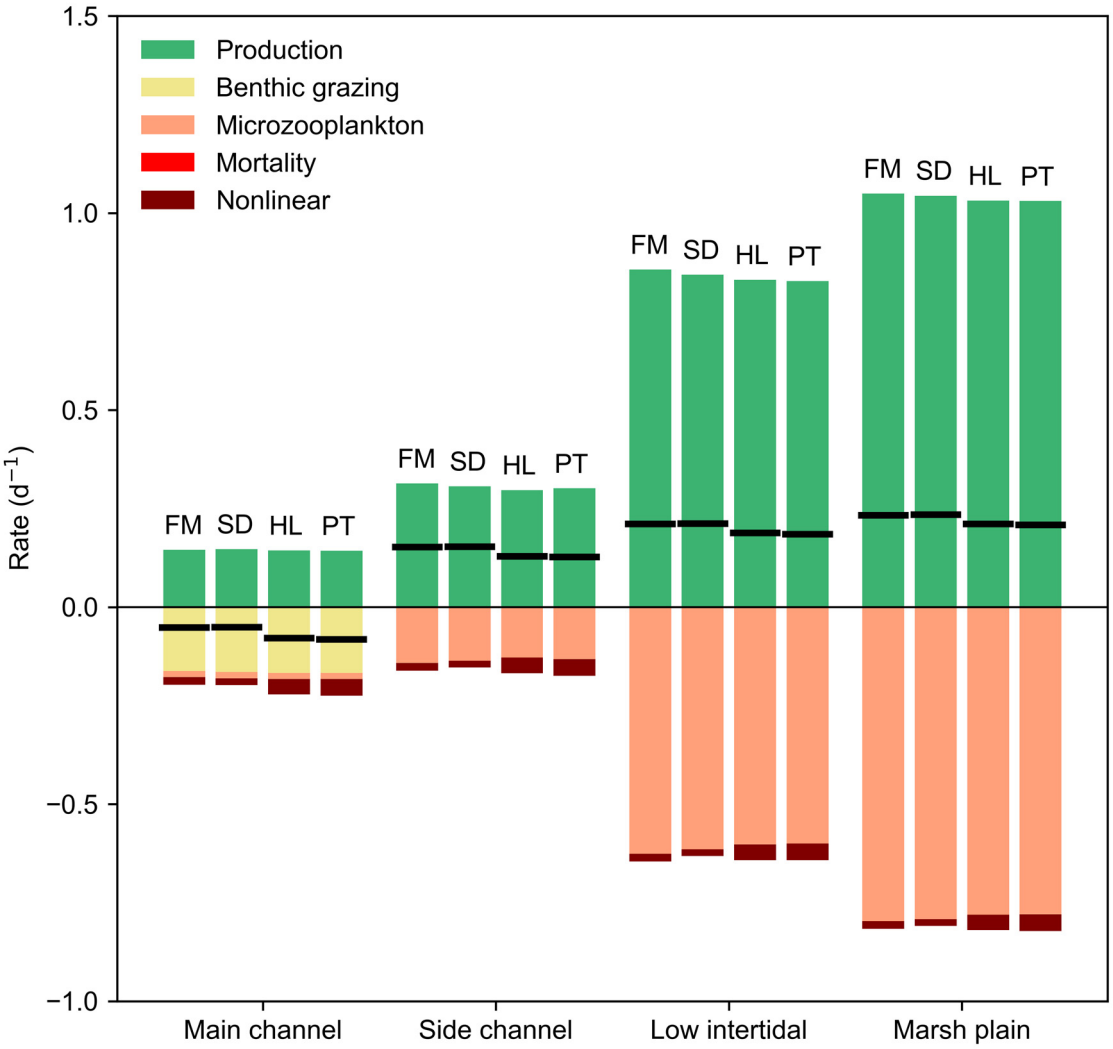


**Figure 10.** Calculated phytoplankton growth and loss rates averaged over the simulation period for each compartment (x-axis) and station (letters above individual bars; see Figure 1). The black horizontal line across each bar indicates the net growth rate. Net growth rates were negative in the main channel and positive elsewhere.

### *3.5. Phytoplankton Model Validation*

The underway chlorophyll data were not used for optimization but were saved for model validation. Chlorophyll was predicted by the model at the time and location of each of the 2369 thinned underway data points, and the two sets of data were compared (Figure 11A,B). Because the net production of chlorophyll was positive in the side channel, low intertidal, and marsh plain compartments (Figure 10), we explored the relationship of observed and predicted chlorophyll with the modeled mean exposure to these compartments (Figure 11C). Both observed and predicted chlorophyll show a clear increase with mean exposure to these "margin" compartments (Figure 11D).

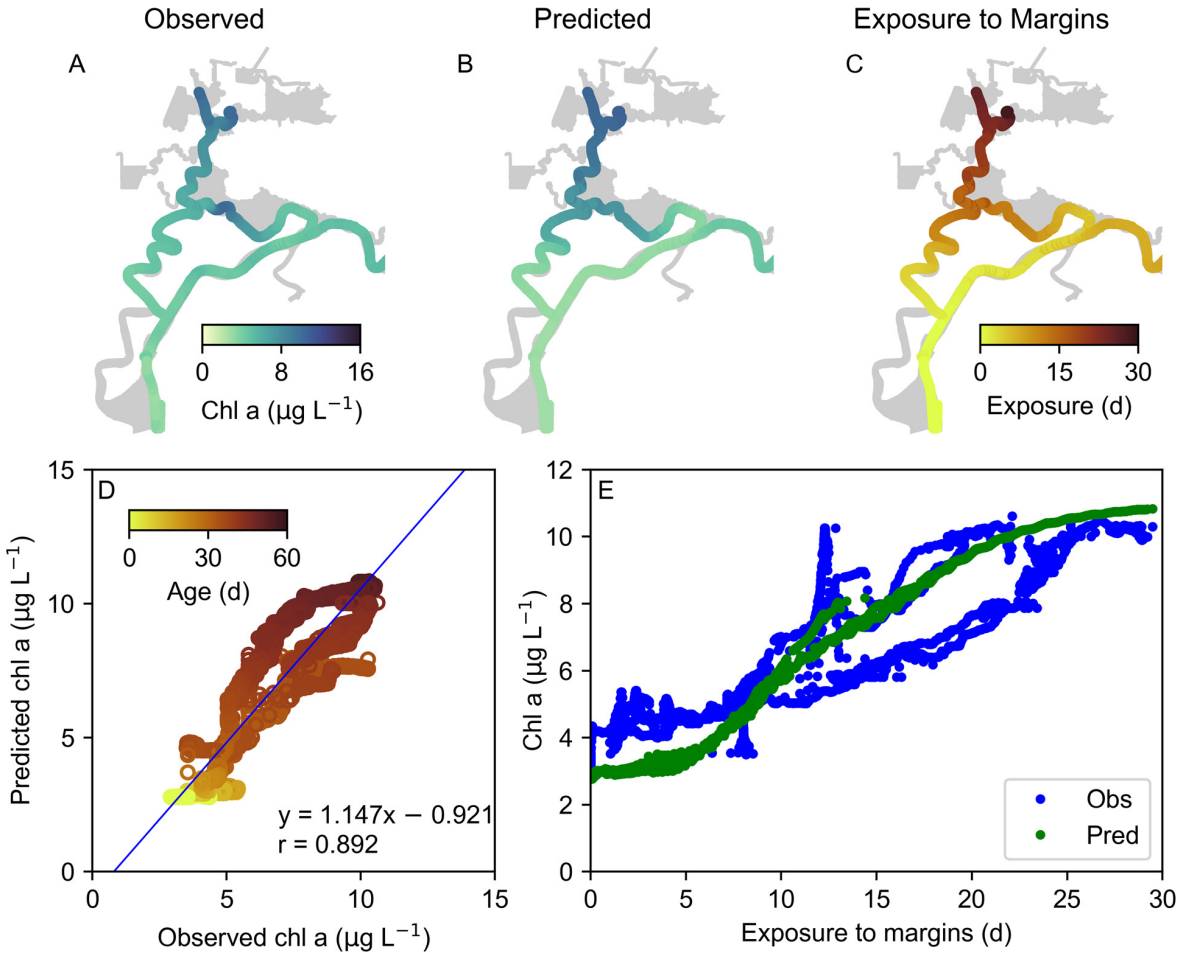


**Figure 11.** (**A**) Observed underway chlorophyll. (**B**) Predicted chlorophyll. (**C**) Mean exposure time to margin (side channel, low intertidal, and marsh plain) compartments. (**D**) Observed vs. predicted chlorophyll with a best-fit line. (**E**) Relationship of predicted and observed chlorophyll with mean exposure time to margin compartments.

## 4. Discussion

We developed a Lagrangian phytoplankton model, extending the methods of [6] to account for time spent in distinct spatial compartments with varying growth and loss rates. A property-tracking approach [9] provided estimates of the average depth encountered by the tracer in each spatial compartment. Growth and loss terms were parameterized using this depth information. We estimated growth rates over the travel time from the boundary by a light-limited growth formulation [14] and fit unknown loss rates to optimize the prediction of chlorophyll at fixed stations. Net flows during the study period were negligible, and hydrodynamic transport was dominated by tidal dispersion processes. Despite significant additional complexity relative to previous tracer-based Lagrangian models, such as [6], our approach maintained extremely high computational efficiency.

The Lagrangian model accurately predicted spatial and tidal chlorophyll variability across the four fixed stations by choosing optimal phytoplankton loss parameters representing clam grazing rates, general mortality, and a nonlinearity parameter representing increased losses with increased phytoplankton concentration. It underpredicted the observed peak chlorophyll at Sheldrake Slough, which occurred at low water and is possibly associated with unquantified discharges from managed wetlands. The predicted concentrations were all substantially larger than boundary concentrations, with predicted chlorophyll generally increasing with the distance from the boundary. The model accu-

rately predicted an independent underway chlorophyll dataset, and both the observed and predicted chlorophyll increased with exposure to shallow "margin" compartments.

The calculated growth and loss rates (Figure 10) varied among compartments, primarily because the water depth varied among compartments, and clam grazing was specified to occur only in the main channel. The average rates also varied slightly by station because water in transit from the Grizzly Bay boundary encountered depth profiles that differed among stations. As evident in Equation (6), the contribution to chlorophyll predictions from time spent in each compartment depends both on the compartment-specific rate (Figure 10) and on the compartment exposure time (Figure 6). For example, the high rates predicted for the marsh plain compartment have a small net effect on predicted chlorophyll due to the relatively short exposure time of the tracer to the marsh plain compartment (Figure 6). Predicted net losses in the main channel were exceeded by net gains across the other compartments at all stations (Figure 10). For that reason, chlorophyll at the stations was roughly 0.5 to 7.5 mg $L^{-1}$ higher than chlorophyll at the boundary (Figure 4D).

The robust optimization approach required 4100 biological simulations and 47.2 min on a laptop computer, corresponding to 0.69 s of computation for an individual chlorophyll model run. Most of this computational time is required for calculating the average growth rate for individual spatial compartments ($\overline{\mu_{net,j}}$) comprising time-averaged growth rates calculated using Equations (7)–(12) [14] and constant in time loss rates.

### *4.1. Suisun Marsh Phytoplankton Dynamics*

Several aspects of our approach and conclusions are consistent with previous studies in Suisun Bay and Suisun Marsh. Consistent with [15], the parameter-fitting approach estimated non-zero clam grazing only in the main channel. Consistent with [36], we assumed no nutrient limitations and used their microzooplankton grazing approach. While [36] estimated net phytoplankton loss in channels and net gains in shoals in the low-salinity zone (salinity from 0.5 to 5), which often overlaps with Suisun Bay, we similarly estimated the net loss of chlorophyll in the main channels and net growth in the other spatial compartments of Suisun Marsh. Though the tracers spent most of the time in the main channel (Figure 6A), the strong positive production in margin compartments offsets the losses in the main channel, giving increased chlorophyll predictions at fixed stations (Figure 8) relative to the model boundary in Grizzly Bay (Figure 4). The attributes of the shallow compartments that enhance phytoplankton production in our model are shallow depth and a lack of clam grazing, conceptually consistent with [27]. For this reason, the exposure time to the other spatial compartments ("margins") was predictive of observed and predicted chlorophyll (Figure 11). Though clam grazing occurred only in the main channel, it was the most important loss term due to the much larger main channel exposure compared to exposure times to other compartments (Figure 6). The predicted contribution of clam grazing to overall losses between the boundary and the four stations ranged from 51% at PT in Peytonia Slough (Figure 1) to 71% at SD in Sheldrake Slough (Figure 1).

We did not address several aspects of phytoplankton dynamics in Suisun Marsh, including seasonal variability in grazing and other loss parameters, but could do so with adequate data availability in other periods. Representing transport processes and phytoplankton dynamics in the wetter winter and spring conditions would also require consideration of incoming chlorophyll with freshwater inflows. These inflows may also cause some degree of salinity stratification, which would make our depth-averaged phytoplankton model less appropriate. We also did not account for phytoplankton biomass from managed wetland discharges. This could be challenging because chlorophyll concentrations in wetland discharges are generally not monitored.

### *4.2. General Applicability*

Our model can readily be extended to solve the coupled equations of an NPZ model by utilizing an ordinary differential equation integration approach while maintaining the Lagrangian approach, which obviates the need to solve the equations on a computational

grid. These ordinary differential equations could be integrated at orders of magnitude larger time steps than used in multi-dimensional hydrodynamic and tracer transport models. Multiple sources of water and chlorophyll can be added to our model by adding tracers to track these sources, including exposure to different compartments and the depth encountered in each. The model can also be applied to scenarios such as sea level rise using process rates determined from historical conditions. A Monte Carlo approach can be applied to account for uncertainty in rates and other model inputs.

The Lagrangian nature of the approach allows for high computational efficiency but also limits the applicability of the approach. To understand the strengths and limitations of the approach more generally, consider the examples of nutrient-limited phytoplankton production and light-limited phytoplankton production. The former is better suited to our approach than the latter. In a nutrient-limited phytoplankton model, the predicted phytoplankton biomass would evolve and interact with the nitrate and any additional nutrients in a coupled Lagrangian biogeochemical model using nutrient equations accounting for uptake by phytoplankton and other processes.

In contrast, light-limited phytoplankton modeling would be challenging. In many systems, including the SFE, turbidity is strongly variable in space and time and often covaries with depth. If the turbidity distribution is predicted by a sediment transport model or interpolated from observations, the tracer simulations can readily yield the average turbidity experienced but would not account for the covariability of turbidity, water depth, and incoming solar irradiation. This limitation can be partially addressed by tracking the exposure of a tracer to photosynthetically active radiation (PAR), resulting in the predicted average light exposure. However, typical light-limited growth equations are strongly nonlinear with light exposure and vary with temperature [14], such that aggregate light exposure may still be insufficient. To remedy that, one could instead calculate a light limitation factor in the transport model along with property-tracking tracers to track the average light limitation. Taking this approach a step further, the phytoplankton growth rate could be calculated in the hydrodynamic model, and a tracer could track the average growth rate experienced. At each step along this progression, more assumptions, formulations, and parameters are pushed into the hydrodynamic model tracer simulations, enabling complex dynamics but hindering subsequent exploration and optimization.

Given the limitations of age-tracer-based phytoplankton modeling, it should be considered a useful tool in conjunction with the Eulerian modeling of phytoplankton. For example, an age tracer approach could be utilized to estimate the values of several model parameters, which could then be incorporated into an Eulerian model that represents additional processes or more complex spatial variability in rates. The Lagrangian biogeochemical model is applicable to many waterbodies, provided that the simulations identify the provenance of nearly all water at the times and locations of biogeochemical predictions. For this reason, it would typically be more challenging to apply this approach in many oceanic and lake settings with high water ages. It is critical that transport processes are represented accurately by the hydrodynamic model used for tracer predictions. Biological rates can be estimated most reliably when the incoming constituent concentrations are known from observations or can reasonably be assumed to be constant and fit in the parameter optimization.

### *4.3. Management Implications*

Several restoration projects have been planned or implemented for the San Francisco Estuary. Part of the motivation of these projects is to provide food for aquatic organisms [41]. Endangered and threatened fish populations have declined simultaneously with their food species [42]. Because our analysis supports the understanding that shallow regions of Suisun Marsh are more productive than deep regions, an increased area of the low intertidal area and marsh plain can be expected to increase primary productivity. Some of this primary production in shallow regions will subsidize adjacent deep regions. The currently abundant managed wetlands are also highly productive and likely contribute

to the productivity of Suisun Marsh [43]. Our work suggests that productivity will be influenced by aspects of restoration design, including bed elevation and exchange between shallow habitats with channels, which can be influenced by breach and channel dimensions, among other factors.

Therefore, the benefits of restoration to open tidal habitats can be expected to vary among existing land uses. While the conversion of managed wetlands to open tidal habitats may not increase overall productivity, the restoration of currently dry areas is expected to benefit productivity. The benefits may decrease due to colonization by clams or aquatic vegetation, which may reduce productivity by shading out light to the water column [44]. In addition, note that the high predicted mean water age during summer conditions indicates the slow exchange with Suisun Bay and the low export of productivity from Suisun Marsh. Therefore, restoration in Suisun Marsh may have little influence on food resources in Suisun Bay during summer conditions. Subsidies of food resources might be increased by the management of tidal or freshwater flows to induce net transport through Suisun Marsh [17].

Due to the increased production predicted in shallower regions, Suisun Marsh phytoplankton dynamics may vary as the marsh depth evolves. With the sea level rise predicted to be as large as 2.7 m in the next 75 years [45] and low-sediment conditions in the San Francisco Estuary [46], which limit accretion, the drowning of marshes and a shift toward deeper water is likely. This is likely to lower the productivity of Suisun Marsh.

## 5. Conclusions

Our phytoplankton modeling approach generalizes the approach of [6] to allow distinct phytoplankton growth and loss rates to differ among spatial compartments. The net production in the main channel is negative (net loss), while the net production in other compartments is positive, showing the importance of distinguishing exposure to different compartments. The approach also allows for the rapid (~1 min) fitting of clam grazing rates and other parameters that produce chlorophyll predictions that are consistent with the observed chlorophyll. These predictions produced credible grazing rates. The Lagrangian approach described can be applied and extended substantially in future work to provide additional insight into the relative importance of different water sources and seasonal variability in loss rates.

**Author Contributions:** Conceptualization, E.G., R.H. and W.K.; Methodology, E.G. and R.H.; Software, E.G. and R.H.; Validation, E.G.; Investigation, E.G., R.H. and S.B.; Resources, J.D.; Data Curation, S.M. and J.D.; Writing—Original Draft Preparation, E.G.; Writing—Review and Editing, E.G., R.H., W.K., S.M. and J.D.; Visualization, E.G., S.B. and R.H.; Supervision, W.K. and R.H.; Project administration, W.K., R.H. and J.D.; Funding acquisition, W.K., R.H., J.D. and E.G. All authors have read and agreed to the published version of the manuscript.

**Funding:** This research was funded by the California Department of Fish and Wildlife (CDFW) and the Delta Stewardship Council (DSP) under Proposition 1—Delta Water Quality and Ecosystem Restoration Grant Program. Agreements that contributed to the work include DSP agreement number 18212 to San Francisco State University and CDFW agreement numbers Q1996064 and P1696010 to UC Davis.

**Data Availability Statement:** The datasets used during the current study are available from the corresponding author on reasonable request.

**Acknowledgments:** The authors thank Richard Rachiele for guidance and advice on model calibration and Stephen Andrews for leading the development of the RMA UnTRIM model interface, Eric Deleersnijder for useful advice on the use of constituent-based age and residence time theory, Lisa Lucas for suggesting an age-based phytoplankton modeling approach, and Brian Bergamaschi for discussing underway observations. Vincenzo Casulli developed the UnTRIM hydrodynamic model. The UC Davis Geochemistry Laboratory, under the direction of Randy Dahlgren, supported the water quality analysis. Matt Ferner at the San Francisco Bay National Estuarine Reserve supported sonde

maintenance and data collection. Data collection was supported by Denise Colombano, Alex Wick, and Natasha Ekasumara.

**Conflicts of Interest:** The authors declare no conflict of interest.

## Appendix A

An essential input to the Lagrangian tracer-based approach is the mean age of water since it was tagged at the model boundary (Grizzly Bay in our application). To estimate the mean age of a source of water, we simulated the transport of two conservative tracers in the hydrodynamic model [7]. The first tracer, representing the fraction of water that entered from the boundary, follows a three-dimensional advection–diffusion equation:

$$\frac{\partial C}{\partial t} + \nabla \cdot (\boldsymbol{u}C) = \frac{\partial}{\partial z}\left(K_T \frac{\partial C}{\partial z}\right) \tag{A1}$$

where $C$ is the tracer concentration with dimensions of mass per volume, $\boldsymbol{u}$ is a three-dimensional velocity vector with the dimensions of length per time, and $K_T$ is the vertical eddy diffusivity with dimensions of length squared per time. Horizontal eddy diffusion was neglected. The scalar advection–diffusion equation was integrated at a time step equal to or less than the hydrodynamic time step of 30 s. When necessary, the scalar time step was reduced from 30 s by using multiple "substeps" of the advection–diffusion integration to meet a stability condition [47].

This equation was discretized with a conservative finite volume approach. The discretized equation can be represented as

$$C^{n+1} = \mathcal{A}(C^n) \tag{A2}$$

where $\mathcal{A}$ is the discrete advection–diffusion operator [8] representing a hydrodynamic model's tracer transport solver, and superscripts denote the discrete-time level (i.e., $C^n$ is the spatial concentration distribution at time $n\Delta t$, and $\mathcal{A}$ represents the evolution of that distribution by advection and diffusion from time $n\Delta t$ to $(n+1)\Delta t$ for a computational time step $\Delta t$).

A second equation is used to represent age–concentration, which characterizes the age content of a water parcel [7,8]. Age–concentration is conceptually equivalent to the product of age and concentration and is more practical to compute than the age itself. The governing equation of age–concentration is similar to Equation (3),

$$\frac{\partial \alpha}{\partial t} + \nabla \cdot (\boldsymbol{u}\alpha) = \frac{\partial}{\partial z}\left(K_T \frac{\partial \alpha}{\partial z}\right) + C \tag{A3}$$

where $\alpha$ is the age–concentration with dimensions of time-mass per volume. Using the notation in Equation (A2), its discretized form is written as

$$\alpha^{n+1} = \mathcal{A}(\alpha^n) + \Delta t C^n \tag{A4}$$

where $\Delta t$ is the computational time step. The mean age was calculated as the ratio of the age–concentration and the tracer concentration.

$$a^n = \frac{\alpha^n}{C^n} \tag{A5}$$

where $a^n$ has dimensions of time. The initial conditions of the scalar transport equations were 0 concentration and 0 age–concentration throughout the domain. The boundary conditions of $C$ were 1 at the Grizzly Bay boundary and 0 at other boundaries. The boundary conditions of age–concentration were 0 at all boundaries.

An analogous approach was applied for partial age [8], which we will refer to as exposure time. The exposure time quantified the time that the tracer spent in each non-

contiguous spatial compartment. A unique tracer assigned to each compartment was incremented to accumulate partial age–concentration only within the assigned compartment. The partial age–concentration for compartment $j$ in computational cell $i$ was calculated as

$$\alpha_{i,j}^{n+1} = \mathcal{A}\left(\alpha_{i,j}^{n}\right) + \delta_{i,j}\Delta t C^{n} \tag{A6}$$

where $\delta_{i,j}$ is 1 if cell $i$ was in compartment $j$ and 0 otherwise. Then, the exposure time (partial age) to compartment $j$ was calculated as

$$a_j = \frac{\alpha_j}{C} \tag{A7}$$

To quantify the mean exposure of a tracer to a water property (depth in our application), we estimated the property–age–concentration $\beta$ with the equation

$$\frac{\partial \beta}{\partial t} + \nabla \cdot (\boldsymbol{u}\beta) = \frac{\partial}{\partial z}\left(K_T \frac{\partial \beta}{\partial z}\right) + \psi C \tag{A8}$$

where $\psi$ is the instantaneous value of the property. Its discretized form can be written as

$$\beta^{n+1} = \mathcal{A}(\beta^{n}) + \Delta t \psi^{n} C^{n}. \tag{A9}$$

Then, the mean property encountered by the tracer can be estimated as the ratio of the property–age–concentration and age–concentration.

$$b^{n} = \frac{\beta^{n}}{\alpha^{n}} \tag{A10}$$

where $b$ is the mean property encountered by the tracer. The initial condition and boundary conditions of $\beta$ were zero in the domain and at all boundaries.

By analogy to partial age–concentration, we estimated the partial property–age–concentration encountered in cell $i$ for each compartment $j$ as

$$\beta_{i,j}^{n+1} = \mathcal{A}\left(\beta_{i,j}^{n}\right) + \delta_{i,j}\Delta t \psi_{i}^{n} C^{n}. \tag{A11}$$

where $\psi_i$ represents the property value in cell $i$. The partial property value for cell $i$ indicating the mean property value encountered by the tracer in compartment $j$ is then

$${b_{i,j}}^{n} = \frac{{\beta_{i,j}}^{n}}{{\alpha_{i,j}}^{n}} \tag{A12}$$

We used this approach to estimate the depth encountered by the tracer in each compartment. In this case, $\psi_i$ in Equation (A12), the depth in cell $i$ at the time, was updated at each time step and cell in the simulation. In our application, $\beta$ in Equation (A9) was the water-depth–age–concentration associated with the tracer $C$, and $b_{i,j}$ was an estimate of the mean depth that the tracer in cell $i$ at time step $n$ has encountered in compartment $j$ since entering the domain.

## References


1. Liu, Q.; Chai, F.; Dugdale, R.; Chao, Y.; Xue, H.; Rao, S.; Wilkerson, F.; Farrara, J.; Zhang, H.; Wang, Z.; et al. San Francisco Bay Nutrients and Plankton Dynamics as Simulated by a Coupled Hydrodynamic-Ecosystem Model. *Cont. Shelf Res.* **2018**, *161*, 29–48. [CrossRef]
2. Thompson, J.K.; Koseff, J.R.; Monismith, S.G.; Lucas, L.V. Shallow Water Processes Govern System-Wide Phytoplankton Bloom Dynamics: A Field Study. *J. Mar. Syst.* **2008**, *74*, 153–166. [CrossRef]
3. Kimmerer, W.J.; Thompson, J.K. Phytoplankton Growth Balanced by Clam and Zooplankton Grazing and Net Transport into the Low-Salinity Zone of the San Francisco Estuary. *Estuaries Coasts* **2014**, *37*, 1202–1218. [CrossRef]
4. Blauw, A.N.; Los, H.F.J.; Bokhorst, M.; Erftemeijer, P.L.A. GEM: A Generic Ecological Model for Estuaries and Coastal Waters. *Hydrobiologia* **2009**, *618*, 175. [CrossRef]

5. Jassby, A.D. Phytoplankton in the Upper San Francisco Estuary: Recent Biomass Trends, Their Causes, and Their Trophic Significance. *SFEWS* **2008**, *6*, 2. [CrossRef]
6. Wang, Z.; Wang, H.; Shen, J.; Ye, F.; Zhang, Y.; Chai, F.; Liu, Z.; Du, J. An Analytical Phytoplankton Model and Its Application in the Tidal Freshwater James River. *Estuar. Coast. Shelf Sci.* **2019**, *224*, 228–244. [CrossRef]
7. Deleersnijder, E.; Campin, J.-M.; Delhez, E.J.M. The Concept of Age in Marine Modelling: I. Theory and Preliminary Model Results. *J. Mar. Syst.* **2001**, *28*, 229–267. [CrossRef]
8. Mouchet, A.; Cornaton, F.; Deleersnijder, É.M.; Delhez, É.J. Partial Ages: Diagnosing Transport Processes by Means of Multiple Clocks. *Ocean Dyn.* **2016**, *66*, 367–386. [CrossRef]
9. Gross, E.; Andrews, S.; Bergamaschi, B.; Downing, B.; Holleman, R.; Burdick, S.; Durand, J. The Use of Stable Isotope-Based Water Age to Evaluate a Hydrodynamic Model. *Water* **2019**, *11*, 2207. [CrossRef]
10. Lucas, L.V.; Deleersnijder, E. Timescale Methods for Simplifying, Understanding and Modeling Biophysical and Water Quality Processes in Coastal Aquatic Ecosystems: A Review. *Water* **2020**, *12*, 2717. [CrossRef]
11. Lopez, C.B.; Cloern, J.E.; Schraga, T.S.; Little, A.J.; Lucas, L.V.; Thompson, J.K.; Burau, J.R. Ecological Values of Shallow-Water Habitats: Implications for the Restoration of Disturbed Ecosystems. *Ecosystems* **2006**, *9*, 422–440. [CrossRef]
12. Alpine, A.E.; Cloern, J.E. Trophic Interactions and Direct Physical Effects Control Phytoplankton Biomass and Production in an Estuary. *Limnol. Oceanogr.* **1992**, *37*, 946–955. [CrossRef]
13. York, J.K.; McManus, G.B.; Kimmerer, W.J.; Slaughter, A.M.; Ignoffo, T.R. Trophic Links in the Plankton in the Low Salinity Zone of a Large Temperate Estuary: Top-down Effects of Introduced Copepods. *Estuaries Coasts* **2014**, *37*, 576–588. [CrossRef]
14. Cloern, J.E. Habitat Connectivity and Ecosystem Productivity: Implications from a Simple Model. *Am. Nat.* **2007**, *169*, E21–E33. [CrossRef] [PubMed]
15. Baumsteiger, J.; Schroeter, R.E.; O'Rear, T.; Cook, J.D.; Moyle, P.B. Long-Term Surveys Show Invasive Overbite Clams (Potamocorbula Amurensis) Are Spatially Limited in Suisun Marsh, California. *SFEWS* **2017**, *15*, 6. [CrossRef]
16. Moyle, P.; Manfree, A.; Fiedler, P. The Future of Suisun Marsh: Balancing Policy with Change. *SFEWS* **2013**, *11*, 10. [CrossRef]
17. Sommer, T.; Hartman, R.; Koller, M.; Koohafkan, M.; Conrad, J.L.; MacWilliams, M.; Bever, A.; Burdi, C.; Hennessy, A.; Beakes, M. Evaluation of a Large-Scale Flow Manipulation to the Upper San Francisco Estuary: Response of Habitat Conditions for an Endangered Native Fish. *PLoS ONE* **2020**, *15*, e0234673. [CrossRef]
18. Moyle, P.B.; Baltz, D.M. Patterns in Distribution and Abundance of a Noncoevolved Assemblage of Estuarine Fishes in California. *Fish. Bull.* **1987**, *84*, 13.
19. Sommer, T.; Mejia, F. A Place to Call Home: A Synthesis of Delta Smelt Habitat in the Upper San Francisco Estuary. *SFEWS* **2013**, *11*, 4. [CrossRef]
20. Grimaldo, L.; Feyrer, F.; Burns, J.; Maniscalco, D. Sampling Uncharted Waters: Examining Rearing Habitat of Larval Longfin Smelt (Spirinchus Thaleichthys) in the Upper San Francisco Estuary. *Estuaries Coasts* **2017**, *40*, 1771–1784. [CrossRef]
21. Feyrer, F.; Nobriga, M.L.; Sommer, T.R. Multidecadal Trends for Three Declining Fish Species: Habitat Patterns and Mechanisms in the San Francisco Estuary, California, USA. *Can. J. Fish. Aquat. Sci.* **2007**, *64*, 723–734. [CrossRef]
22. Halverson, G.H.; Lee, C.M.; Hestir, E.L.; Hulley, G.C.; Cawse-Nicholson, K.; Hook, S.J.; Bergamaschi, B.A.; Acuña, S.; Tufillaro, N.B.; Radocinski, R.G.; et al. Decline in Thermal Habitat Conditions for the Endangered Delta Smelt as Seen from Landsat Satellites (1985–2019). *Environ. Sci. Technol.* **2022**, *56*, 185–193. [CrossRef] [PubMed]
23. Davis, B.E.; Cocherell, D.E.; Sommer, T.; Baxter, R.D.; Hung, T.-C.; Todgham, A.E.; Fangue, N.A. Sensitivities of an Endemic, Endangered California Smelt and Two Non-Native Fishes to Serial Increases in Temperature and Salinity: Implications for Shifting Community Structure with Climate Change. *Conserv. Physiol.* **2019**, *7*, coy076. [CrossRef]
24. Cloern, J.E. Patterns, Pace, and Processes of Water-quality Variability in a Long-studied Estuary. *Limnol Ocean.* **2019**, *64*. [CrossRef]
25. Kimmerer, W.J.; Gartside, E.; Orsi, J.J. Predation by an Introduced Clam as the Likely Cause of Substantial Declines in Zooplankton of San Francisco Bay. *Mar. Ecol. Prog. Ser.* **1994**, *113*, 81–93. [CrossRef]
26. Bork, K.; Moyle, P.; Durand, J.; Hung, T.-C.; Rypel, A.L. Small Populations in Jeopardy: A Delta Smelt Case Study. *Envtl. L. Rep.* **2020**, *50*, 10714.
27. Lucas, L.V.; Thompson, J.K. Changing Restoration Rules: Exotic Bivalves Interact with Residence Time and Depth to Control Phytoplankton Productivity. *Ecosphere* **2012**, *3*, art117. [CrossRef]
28. Montgomery, J. *Foodweb Dynamics in Shallow Tidal Sloughs of the San Francisco Estuary*; University Of California, Davis: Davis, CA, USA, 2017.
29. Casulli, V.; Walters, R.A. An Unstructured Grid, Three-Dimensional Model Based on the Shallow Water Equations. *Int. J. Numer. Methods Fluids* **2000**, *32*, 331–348. [CrossRef]
30. Casulli, V. A High-Resolution Wetting and Drying Algorithm for Free-Surface Hydrodynamics. *Int. J. Numer. Meth. Fluids* **2009**, *60*, 391–408. [CrossRef]
31. Casulli, V.; Stelling, G.S. Semi-Implicit Subgrid Modelling of Three-Dimensional Free-Surface Flows. *Int. J. Numer. Meth. Fluids* **2011**, *67*, 441–449. [CrossRef]
32. Willmott, C.J. On the Validation of Models. *Phys. Geogr.* **1981**, *2*, 184–194. [CrossRef]
33. Delhez, E.J.M.; Deleersnijder, E. The Concept of Age in Marine Modelling: II. Concentration Distribution Function in the English Channel and the North Sea. *J. Mar. Syst.* **2001**, *31*, 279–297. [CrossRef]

34. NOAA National Estuarine Research Reserve System (NERRS). *System-Wide Monitoring Program*; NOAA: Washington, DC, USA. Available online: https://coast.noaa.gov/digitalcoast/data/nerr.html (accessed on 12 April 2022).
35. Stumpner, E.B.; Bergamaschi, B.A.; Kraus, T.E.C.; Parker, A.E.; Wilkerson, F.P.; Downing, B.D.; Dugdale, R.C.; Murrell, M.C.; Carpenter, K.D.; Orlando, J.L.; et al. Spatial Variability of Phytoplankton in a Shallow Tidal Freshwater System Reveals Complex Controls on Abundance and Community Structure. *Sci. Total Environ.* **2020**, *700*, 134392. [CrossRef] [PubMed]
36. Kimmerer, W.; Wilkerson, F.; Downing, B.; Dugdale, R.; Gross, E.; Kayfetz, K.; Khanna, S.; Parker, A.; Thompson, J. Effects of Drought and the Emergency Drought Barrier on the Ecosystem of the California Delta. *SFEWS* **2019**, *17*, 2. [CrossRef]
37. Storn, R.; Price, K. Differential Evolution—A Simple and Efficient Heuristic for Global Optimization over Continuous Spaces. *J. Glob. Optim.* **1997**, *11*, 341–359. [CrossRef]
38. Virtanen, P.; Gommers, R.; Oliphant, T.E.; Haberland, M.; Reddy, T.; Cournapeau, D.; Burovski, E.; Peterson, P.; Weckesser, W.; Bright, J.; et al. SciPy 1.0: Fundamental Algorithms for Scientific Computing in Python. *Nature Methods* **2020**, *17*, 261–272. [CrossRef] [PubMed]
39. Eaton, A.D.; Clescrei, L.S.; Greenberg, A.E. *Standard Method for the Examination of Water and Wastewater*; United Book Press, Inc.: Baltimore, MD, USA, 1995.
40. Bergamaschi, B.; Stumpner, E.; O'Donnell, K.; Hansen, A.; Gelber, A.; Richardson, E.; Kraus, T.; Downing, B.; Senn, D. Spatial Assessment of Nutrients and Water-Quality Constituents in Suisun Marsh with the Salinity Control Gate Reoperation Experiment; a Delta Smelt Resiliency Strategy Experiment 2018. 2021. Available online: https://www.usgs.gov/data/spatial-assessment-nutrients-and-water-quality-constituents-suisun-marsh-salinity-control-gate (accessed on 9 April 2023).
41. Durand, J. A Conceptual Model of the Aquatic Food Web of the Upper San Francisco Estuary. *SFEWS* **2015**, *13*, 5. [CrossRef]
42. Mac Nally, R.; Thomson, J.R.; Kimmerer, W.J.; Feyrer, F.; Newman, K.B.; Sih, A.; Bennett, W.A.; Brown, L.; Fleishman, E.; Culberson, S.D.; et al. Analysis of Pelagic Species Decline in the Upper San Francisco Estuary Using Multivariate Autoregressive Modeling (MAR). *Ecol. Appl.* **2010**, *20*, 1417–1430. [CrossRef]
43. Aha, N.M.; Moyle, P.B.; Fangue, N.A.; Rypel, A.L.; Durand, J.R. Managed Wetlands Can Benefit Juvenile Chinook Salmon in a Tidal Marsh. *Estuaries Coasts* **2021**, *44*, 1440–1453. [CrossRef]
44. Christman, M.; Khanna, S.; Drexler, J.; Young, M. Ecology and Ecosystem Impacts of Submerged and Floating Aquatic Vegetation in the Sacramento–San Joaquin Delta. *SFEWS* **2023**, *20*, 3. [CrossRef]
45. Dettinger, M.; Anderson, J.; Anderson, M.; Brown, L.; Cayan, D.; Maurer, E. Climate Change and the Delta. *SFEWS* **2016**, *14*, 5. [CrossRef]
46. Schoellhamer, D.H. Sudden Clearing of Estuarine Waters upon Crossing the Threshold from Transport to Supply Regulation of Sediment Transport as an Erodible Sediment Pool Is Depleted: San Francisco Bay, 1999. *Estuaries Coasts* **2011**, *34*, 885–899. [CrossRef]
47. Casulli, V.; Zanolli, P. High resolution methods for multidimensional advection–diffusion problems in free-surface hydrodynamics. *Ocean Model.* **2005**, *10*, 137–151. [CrossRef]

water

MDPI

*Article*

# Longitudinal Mixing in Flows with Submerged Rigid Aquatic Canopies

**Merenchi Galappaththige Nipuni Odara * and Jonathan Pearson**

School of Engineering, University of Warwick, Coventry CV4 7AL, UK; j.m.pearson@warwick.ac.uk
* Correspondence: nipuniodara@ymail.com

**Abstract:** The presence of dense submerged vegetation alters mixing characteristics in open channel flows as they cause differential velocities inside and above canopies. The prediction models for longitudinal mixing in the presence of submerged canopies often use the drag coefficient to represent the canopy, which limits the usability of the models when the canopy properties are not fully understood. Here, attempts were made to present a methodology which can be used for deriving the coefficient of longitudinal dispersion in the presence of submerged vegetation based on velocity measurements, using a mixing length approach to model turbulence. An experimental study was conducted in a large-scale laboratory facility to investigate the longitudinal dispersion characteristics in open channel flow with submerged aquatic vegetation canopies. Detailed velocity and solute tracer measurements were undertaken for a representative range of flow velocities. The velocity measurements were used for deriving turbulent shear stress, mixing length, and diffusivity using established theoretical and empirical relationships to derive the longitudinal dispersion. The longitudinal dispersion measured in two locations in the water column for the two canopy submergences was discussed based on the amount of vertical mixing and differential advection. The canopy with a smaller stem length (i.e., higher submergence ratio) has a higher vertical diffusivity, resulting in increased vertical mixing in the water column. The canopy with the higher stem length (i.e., lower submergence ratio) consists of minimal vertical diffusivity, causing the longitudinal dispersion measured above the canopy to be significantly high, even though the longitudinal dispersion measured inside the canopy is much lower. The mathematical model which was adapted for calculating the coefficient of longitudinal dispersion and the tracer results show good agreement, indicating that the N-zone model can accurately predict the longitudinal dispersion in submerged aquatic canopies when used with the presented methodology.

**Keywords:** water pollution; submerged vegetation; turbulent diffusion; shear dispersion; open channel flow; physical modelling



**Citation:** Nipuni Odara, M.G.; Pearson, J. Longitudinal Mixing in Flows with Submerged Rigid Aquatic Canopies. *Water* **2023**, *15*, 3021. https://doi.org/10.3390/w15173021

Academic Editors: Eric Deleersnijder and Giuseppe Pezzinga

Received: 4 July 2023
Revised: 3 August 2023
Accepted: 16 August 2023
Published: 22 August 2023



## 1. Introduction

Concerns about surface water pollution generate an increased demand for predicting pollution levels in both inland and coastal waters. Understanding how different hydrodynamic conditions affect the fate and pathways of pollutants once they enter a waterbody is crucial for preventing devastating environmental hazards related to water pollution. Often, aquatic vegetation is kept unremoved from the waterways due to the ecosystem services they provide [1], such as improving the water quality [2–5], reducing turbidity [6], resuspension of nutrients [3,7,8], providing food and shelter for aquatic fauna [3,9–12], and reducing erosion [3,9,13–15]. However, the presence of submerged vegetation in a conveyance channel will alter the mixing of soluble pollutants by introducing a velocity shear at the top of the canopy [16–18]. Therefore, studying pollution transport processes in the presence of submerged aquatic vegetation helps with maximising its ecosystem services while reducing the adversity of pollution transport, making it a widely studied topic. Most of these studies on aquatic vegetation parameterize the effects of vegetation

using a drag coefficient that depends on the canopy density, flow velocity, and the diameter and morphology of the individual canopy elements [19], thus requiring a comprehensive survey of the channel to determine a representative value for the drag coefficient because aquatic canopies exhibit a wide range of geometries [20].

This paper presents the findings of an experimental study comprising two canopy heights of submerged vegetation, where the velocity measurements are correlated with longitudinal dispersion properties of vegetated open channel flow using established numerical relationships to calculate the coefficient of longitudinal dispersion. A mixing length approach is used for modelling the turbulent shear stress, and the effect of canopy submergence on longitudinal mixing is also discussed based on corresponding velocity profiles.

## 2. Previous Work

### *2.1. Flow Velocity in the Presence of Submerged Vegetation*

In a wide channel with a bare bed (no effect due to side walls or vegetation), the streamwise velocity profile has a logarithmic shape [21]. If an open channel comprises a submerged sparse canopy where the canopy drag is smaller than the bed drag, the hydrodynamics will not deviate significantly from the open channel conditions, while the canopy contributes to increased bed roughness [19]. Dense aquatic canopies are a source of drag, and the presence of a dense submerged canopy results in a decrease in the flow velocity with distance into the canopy from the top, while increasing the flow velocity above the canopy [14,18,22]. A typical velocity profile in the presence of a dense submerged canopy is shown in Figure 1a. The presence of submerged vegetation also results in a vertical discontinuity of drag [23], resulting in an increase in velocity shear and turbulence intensity at the top of the canopy [11,18]. These processes create instability at the top of the canopy, developing discrete Kelvin-Helmoltz vortices [16] of elliptical shape, as shown in Figure 1b. These vortices are predominantly expressed when the canopy becomes flexible, resulting in a wavy motion in the upper part of the flexible canopies [24].

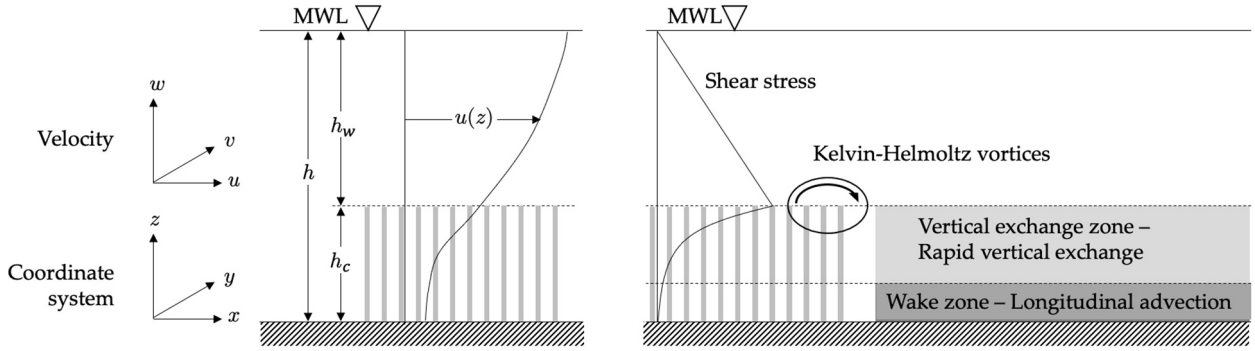


**Figure 1.** Flow hydrodynamics around submerged rigid aquatic canopies: (**a**) basic nomenclature of a vegetated open channel flow and the expected shape of the velocity profile; and (**b**) the shear stress profile and associated mixing processes in a vegetated channel (based on previous work, references provided in the body).

### *2.2. Longitudinal Dispersion in the Presence of Submerged Vegetation*

The rate of mass transport ($\dot{M}$) per unit width in the streamwise direction of a channel is given by Equation (1) [25] in the context of a depth averaged model,

$$\dot{M} = -hD\frac{\partial \overline{C}}{\partial x} \quad (1)$$

where $h$ is the depth, and the area per unit width of flow, $D$ is called the longitudinal dispersion coefficient which is a bulk transport coefficient representing the diffusive property of the velocity distribution of the flow and $\overline{C}$ is the depth average of the mean concentration.

$D$ is a property of the flow. For example, the velocity profile is logarithmic in wide channels without vegetation, and hence, the coefficient of longitudinal dispersion ($D$) can be expressed by Equation (2) [26],

$$D = 5.93\, hu_* \tag{2}$$

where $u_*$ is the friction velocity. The friction velocity is defined in Equation (3),

$$u_* = \sqrt{\frac{\tau_0}{\rho}} \tag{3}$$

where $\tau_0$ is the shear stress at the channel bed and $\rho$ is the density of the fluid.

Equation (2) can also be used for quantifying longitudinal dispersion in open channels with sparse vegetation if the canopy is sparse enough to maintain the logarithmic shape of the velocity profile. However, $u_*$ should be re-evaluated to include the roughness component of the canopy. When the canopy becomes dense, it modifies the velocity profile and the fate and transport of solutes, due to its considerable impact on flow dynamics [18,27]. In such situations, the mixing in the region above the canopy is dominated by large-scale shear dispersion [28]. The flow inside the submerged aquatic canopy can be divided into two regions: (1) a 'vertical exchange zone' consisting of Kelvin-Helmoltz vortices [16] in the upper part of the canopy where the rapid vertical turbulent exchange takes place [18], and (2) a 'longitudinal exchange zone' in the lower section of the canopy where mixing is dominated by longitudinal advection [17]. The vertical exchange zone created by the vortices penetrates only to a limited distance into the canopy [29] as the shear, which feeds energy to the vortices, is balanced by canopy dissipation [30]. The extent to which the vertical mixing layer grows increases with the depth of submergence and (generally) decreases when the canopy becomes dense or flexible [17]. These complex flow conditions in the presence of submerged canopies can make it challenging to measure longitudinal dispersion. For example, the routing method [31] was unsuccessful when evaluating the coefficient of longitudinal dispersion due to the delay in solute transport inside the canopy and the lack of cross-sectional mixing [32]. On the other hand, the moment area method [26,33] has been adopted for evaluating the coefficient of longitudinal dispersion in vegetated open channel flows [28,34,35].

When a drop of solute is added to a moving water body, it keeps mixing as it moves downstream with the water flow. The concentration time series created by the drop of solute can be measured experimentally using several monitoring stations along the flow. The temporal variance in the measured concentration time series increases along the flow. According to the moment area method, the rate of change in the temporal variance along the flow is used for calculating the longitudinal dispersion coefficient as shown in Equation (4),

$$D = \frac{1}{2}\frac{d}{dt}\left[u^2\sigma_t^2\right] = \frac{u^2}{2}\frac{\sigma^2_{t(x_2)} - \sigma^2_{t(x_1)}}{t_2 - t_1} \tag{4}$$

where $\sigma_t^2$ is the temporal variance of the concentration time series measured at different streamwise locations ($x_1$ and $x_2$), and $u$ is the flow velocity. $t_1$ and $t_2$ are the times when the centroid of the solute cloud passed the stations at $x_1$ and $x_2$.

Even though the moment area method can be applied in vegetated open channel flow conditions, there is a paucity of dispersion measurements inside the canopies. There may be limitations in measuring solute concentrations inside dense canopies, which is justified because turbulent diffusion inside dense canopies makes a negligible contribution to the longitudinal dispersion of the cross-section [28]. However, since the vertical exchange zone penetrates the canopy when the depth of submergence of the canopy is high, and the density of the canopy is low [17], it can be expected that some canopy configurations

will result in a considerable increase in longitudinal dispersion inside the canopies. The availability of experimental measurements in different canopy geometries will benefit the statistical modelling approaches which are developed for predicting longitudinal dispersion coefficients [36,37].

## 3. Methodology

The experiments were conducted in a 20 m long, 0.34 m wide, and 1.5 m deep flume in which the flow was created using a centrifugal pump. The vegetation was replicated as a 10 m long homogeneous canopy using plastic straws. Representing rigid vegetation with cylindrical dowels is a widely used approach [38–43] due to the ease of implementation and its authentic recreation of the salient features of the hydrodynamics of vegetated flows [42]. Two vegetation heights of 0.1 m $(h/h_c = 2.5)$ and 0.2 m $(h/h_c = 1.25)$ were tested, which resemble shallow submerged conditions $(1 < h/h_c < 5)$, as most submerged macrophytes exist in this range due to limitations caused by light penetration [19]. The water depth was kept constant at 0.25 m throughout the study, and the outlet was designed to facilitate altering the flow rate while keeping a constant water depth. The experimental setup, the arrangement, and the geometry of canopy elements and the placement of fluorometers with respect to canopies are shown in Figure 2.

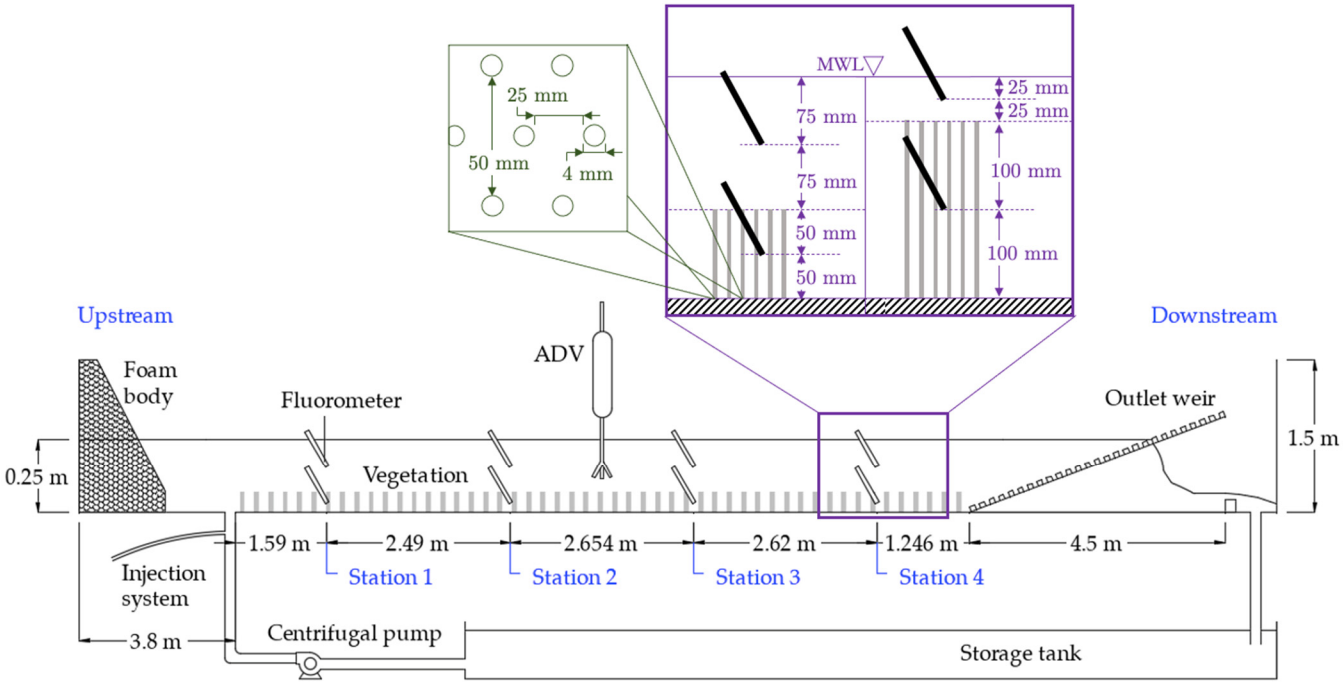


**Figure 2.** Experimental setup (not to scale): the side view of the testing flume, the placement of fluorometers for the two tested vegetation configurations, and the staggered grid layout of vegetation in the plan. In all the diagrams, the flow is from left to right.

### *3.1. Velocity Measurements*

To measure velocities, an acoustic Doppler velocimeter (ADV), which is commercially known as a Nortek Vectrino Profiler (manufactured by Nortek, Rud, Norway), was used. The ADV was mounted approximately in the middle (longitudinally) of the canopy (Figure 2), to facilitate the full development of the velocity profile and reduce the outlet's effect. The ADV was configured to measure the longitudinal $(x)$, transverse $(y)$, and vertical $(z)$ velocity components in a cylindrical sampling volume with a dimeter of 6 mm, at points with a spacing of 4 mm. The velocity measurements were collected at 100 Hz for 2 min for each vertical position of the probe. A seeding material (Timiron Supersilk from Merck, Darmstadt, Germany) was added to the flow to maintain a signal-to-noise ratio (SNR) of the instrument above 20 throughout the cylindrical volume for the duration

of the velocity data collection. The seeding material was first diluted in water to a concentration of ca. 2500 ppm (by volume) and a drop of liquid soap was added to the solution to keep the particles suspended in water for an increased duration. This seeding solution was continuously injected into the inlet pipe of the flume using a peristaltic pump with a flow rate of 40 mL/min until the velocity data collection was completed. The velocity measurements were conducted before the longitudinal dispersion measurements were commenced to prevent the two procedures from interfering with each other.

To measure velocities inside the canopy, a clear area with a diameter of 8 cm was created by removing the plastic straws. This is a common limitation when the velocities inside the canopies are measured using the ADV, due to the need to prevent the model vegetation from interfering with the velocity measurements by entering the cylindrical sampling volume. It was assumed that the effect from clearing the vegetation did not make a significant difference in the measured velocities based on a previous study [44], which compared the velocity measurements collected with the ADV inside a model vegetation (consisting of flexible blades attached to wooden dowels) when the vegetation was fully cleared in a circular area of a diameter of 10 cm versus when wooden dowels were retained (with no blades attached). Their findings denote that the presence or absence of wooden dowels within the clearing did not significantly affect the velocity measurements of the mean current.

The velocity measurements collected from the region between 40 mm and 60 mm from the transceiver were chosen for the analysis as they are the most reliable [45]. From those data, only the measurements with correlation coefficients higher than 80% were used for calculating the velocity profiles and turbulent shear stress profiles. The velocimeter is susceptible to pulse interference when measuring velocities near boundaries, which is called a "weak spot". The "weak spot" of the velocity data occurs at approximately 80 mm and 90 mm above the channel bed depending on a few parameters (such as the speed of sound, boundary surface, and the configured velocity range), causing outliers in the data. The outliers of the velocity data were identified during velocity calculations.

### *3.2. Longitudinal Mixing Measurements*

A rhodamine WT solution with a concentration of 100,000 PPB was injected into the inlet pipe for 4 s using a peristaltic pump with a 40 mL/min flow rate. The injection signal activated the peristaltic pump using an Arduino IDE, and the data collection was started 20 s before the injection signal was sent. A series of Cyclops-7 fluorometers (From Turner Designs, San Jose, CA, USA) were used for capturing the tracer concentrations at four stations along the canopy. In each station, one fluorometer was mounted at the mid-height of the canopy, while the other fluorometer was mounted mid-height above the canopy (Figure 2) to measure the longitudinal dispersion in two vertical locations. Some plastic straws around the fluorometers were removed to provide a clear measurement space in front of the fluorometers, and the canopy arrangement was kept consistent throughout the tests. All fluorometers were fixed with an inclination rather than keeping them vertical to provide an additional clearance space and reduce the formation of air bubbles around the sensor head. All instruments, including top and bottom fluorometers and the ADV, were kept in the same positions whenever the tracer tests were conducted.

### *3.3. Calculation of the Coefficient of Longitudinal Dispersion from the N-Zone Model*

#### 3.3.1. Calculating the Shear Stresses

The viscous stress was calculated using Equation (5),

$$\tau_v = \rho\nu\frac{\partial u}{\partial z} \tag{5}$$

where $\rho$ is the density of the fluid and $\nu$ is the kinematic viscosity of the fluid.

The turbulent shear stress at a given location can be expressed by the Reynolds stresses. For longitudinal dispersion in an open channel flow, the $(x, z)$ plane dominates. Hence, Equation (6) can be used for deriving turbulent stress,

$$\tau_r = -\rho\overline{u'w'} \tag{6}$$

where $u'$ and $w'$ were the deviations of instantaneous velocities from the temporal mean values ($u$ and $w$), respectively.

3.3.2. Calculating Diffusivity

From the force balance [25] and by assuming isotropy [46], the horizontal and vertical diffusivity ($D_x$ and $D_z$) at each location can be evaluated using Equation (7), which is valid under the Reynolds analogy and assuming a turbulent Schmidt number equal to unity ($S_{cT}$ = 1),

$$D_x = D_z = \frac{\tau/\rho}{\frac{du}{dz}} \tag{7}$$

where $\tau$ is the total shear stress at any given location, which was calculated by adding the viscous and turbulent shear stress components.

3.3.3. Calculating the Coefficient of Longitudinal Dispersion

The longitudinal dispersion in open channel flow with submerged vegetation can be numerically explained using first principles [25] as shown in Equation (8),

$$D = -\frac{1}{d_c}\int_0^d u'' \int_0^z \frac{1}{D_z}\int_0^z u''dz\,dz\,dz \tag{8}$$

where $u''$ is the deviation of velocity from the cross-sectional mean and $D_z$ is the vertical diffusivity.

Alternatively, the N-zone model, which is presented in Equation (9), can be used for quantifying the longitudinal dispersion [46],

$$D(N) = \sum_{j=1}^{N-1}\left(q_1+q_2+\ldots+q_j\right)^2\left[1-\left(q_1+q_2+\ldots+q_j\right)\right]^2 \times \frac{\left[u_{12\ldots j}-u_{(j+1)\ldots N}\right]^2}{b_{j(j+1)}} + \sum_{j=1}^{N} q_j D_{xj} \tag{9}$$

where $q$ is the dimensionless height of each zone, $u_{12\ldots j}$ is the average velocity of the first $j$ zones, and $u_{(j+1)\ldots N}$ is the average velocity of the last $N-j$ zones. $b_{j(j+1)}$ is the exchange coefficient between any adjacent pair of zones and can be evaluated using Equation (10) [46],

$$b_{j(j+1)} = \frac{2D_{zj(j+1)}}{h^2\left(q_j+q_{j+1}\right)}\ (j = 1, 2, \ldots, N-1) \tag{10}$$

where $D_{zj(j+1)}$ is the vertical diffusivity at the location in consideration, which is the boundary between the $j$ and $(j+1)$ zones.

## 4. Results

### *4.1. Velocity Profile*

Many theoretical models exist for calculating streamwise velocity profiles in vegetated flows, and a few of them were used in this study for re-evaluating a matching velocity profile. The models could not reproduce the exact shape of the profile due to several reasons, including differences in canopy density. Therefore, the model presented by Tang, (2019) [47] was used for obtaining an approximated best-fit line for the velocity profile with few empirical adjustments, so that the normalised root-mean-square error (NRMSE) remains low. The velocity values measured at the "weak spot" were considered outliers

and they were ignored when the NRMSE was calculated. The equation for NRMSE is given in Equation (11),

$$\text{NRMSE} = \frac{\text{RMSE}}{\overline{\overline{u}}} = \frac{1}{\overline{\overline{u}}}\sqrt{\frac{\sum_{z=i}^{n}(u_i - \overline{u})^2}{n}} \tag{11}$$

where $u_i$ is the measured velocity, $\overline{u}$ is the velocity calculated from the model, and $\overline{\overline{u}}$ is the depth averaged mean velocity calculated based on the flow rate.

The unavailability of velocity measurements in the upper part of the water column is a limitation of this study due to the nature of the ADV. Therefore, the line drawn for the available data points was extrapolated to obtain an approximate estimation of the velocities in that region. When the flow rates were compared to the velocity measurements, it was suggested that larger velocity values, such as the ones extrapolated, should prevail in the upper part of the water column to sustain the flow rates. Figures 3a and 4a present the measured and fitted velocity profiles for different tested flow rates. When the velocity profiles between the two canopy conditions are compared, the velocity profile from the canopy height at 0.2 m consists of a larger velocity shear towards the top of the canopy.

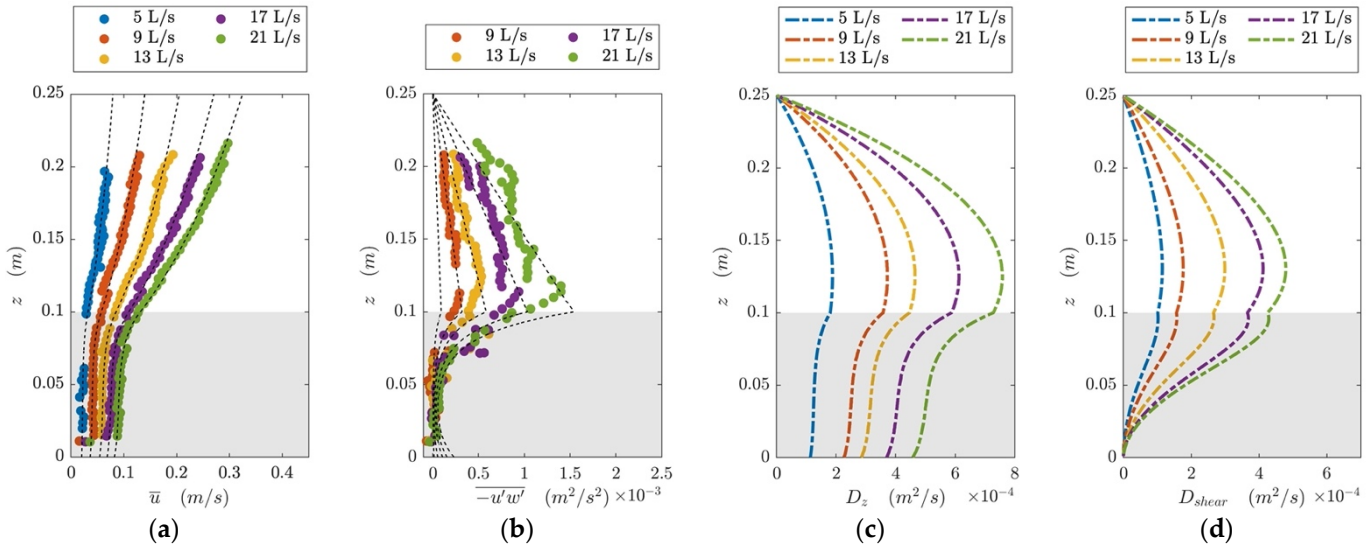


**Figure 3.** Hydrodynamics of the water column in the presence of the canopy of 0.1 m height: (**a**) measured and fitted velocity profiles for the tested flow conditions; (**b**) measured and fitted profile of $-\overline{u'w'}$; (**c**) estimated diffusivity profiles for the tested flow conditions; and (**d**) estimated contribution from each zone in the water column on shear dispersion.

### *4.2. Shear Stress Profile*

Viscous stress component $(\tau_v)$ was added to the turbulent stress component $(\tau_r)$ to obtain the shear stress $(\tau)$. However, the turbulent stress component dominated the magnitude of the shear stress in the tested flow conditions.

When calculating the viscous shear stress, the kinematic viscosity was chosen based on the water temperature measured with the ADV. The velocity gradient was calculated from the fitted velocity profile obtained from the velocity model explained in Section 4.1.

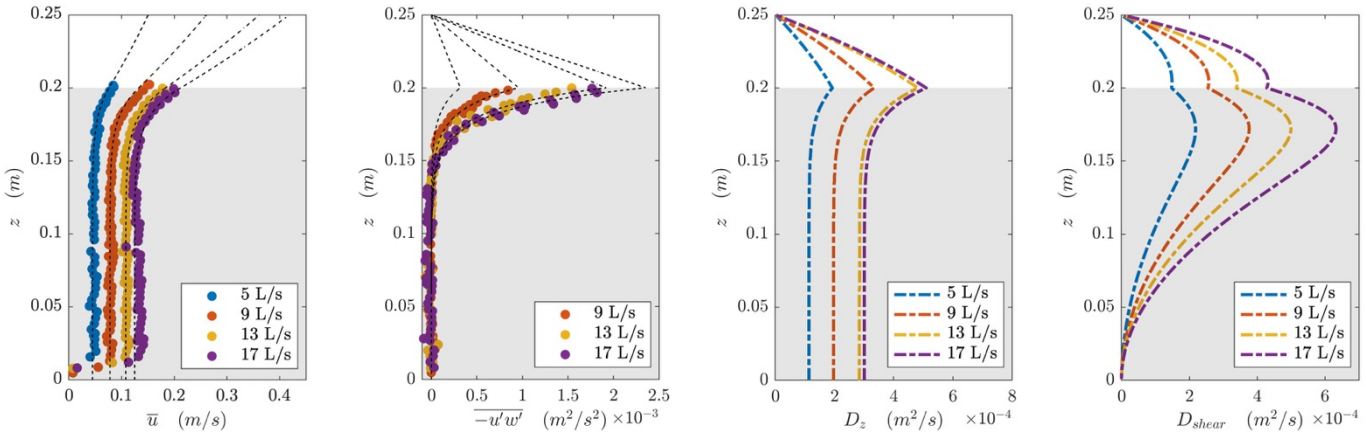


(**a**) (**b**) (**c**) (**d**)

**Figure 4.** Hydrodynamics of the water column in the presence of the canopy of 0.2 m height: (**a**) measured and fitted velocity profiles for the tested flow conditions; (**b**) measured and fitted profile of $-\overline{u'w'}$; (**c**) estimated diffusivity profiles for the tested flow conditions; and (**d**) estimated contribution from each zone in the water column on shear dispersion.

The turbulent shear stress was obtained from the Reynolds stress. A mixing length approach was used for modelling the turbulent stress profile inside the canopy. The velocity measurements in the "weak spot" were ignored when calculating the Reynolds stress profile and the mixing length.

Several mixing length theories are available in the literature. Equation (12) [48] indicates that the turbulent shear stress is related to the velocity gradient,

$$\tau_r = -\rho\overline{u'w'} = \rho\left[l^2\right]\left(\left|\frac{\partial u}{\partial z}\right|\frac{\partial u}{\partial z}\right) \tag{12}$$

where $l$ is the mixing length.

Equation (13) [49] shows that the turbulent shear stress is related to the first and second derivatives of the velocity profile with respect to $z$,

$$\tau_r = -\rho\overline{u'w'} = \rho\kappa^2\left(\frac{\partial u}{\partial z}\right)^4 \Big/ \left(\frac{\partial^2 u}{\partial z^2}\right)^2 \tag{13}$$

where $\kappa$ is the von-Karman constant.

Equation (14) [47,50,51] depicts that the Reynolds stress is related to the velocity and velocity gradient,

$$\tau_r = -\rho\overline{u'w'} = \rho\lambda\left(u\frac{du}{dz}\right) \tag{14}$$

where $\lambda$ is a characteristic turbulent length scale.

The turbulent stresses measured inside the canopy and the functions of the velocity derivatives were plotted to verify the applicability of Equations (12)–(14). It was observed that the gradient corresponding to mixing length $\lambda$ in Equation (14) remains constant throughout the region inside the canopy, while the gradient corresponding to mixing length $l$ in Equation (12) varies along the canopy. Equation (13) was unable to produce accurate estimations for the tested conditions. It was also observed that the magnitude of $\lambda$ remains consistent for different flow rates when the canopy properties remain unchanged. This observation complements previous findings on the magnitude of $\lambda$ being dependent only on water depth and vegetation height [47,51]. For a constant water depth of 0.25 m and canopy height of 0.1 m, the averaged mixing length $(\lambda)$ is 5.6 mm, with an NRMSE of 6.7%. For a canopy height of 0.2 m, the average mixing length $(\lambda)$ is 2.5 mm, with an NRMSE of 3.3%.

Figure 5 presents the calculated $\lambda$ values for each canopy submergence vs. canopy height in each test condition, $h_c = 0.1$ m and $h_c = 0.2$ m. There are few empirical estimations of $\lambda$ in the literature. The first empirical relationship (ER1) mentions that the mixing length can be approximated with $0.0144\sqrt{hh_c}$ [51]. The second empirical relationship (ER2) states that the mixing length can be approximated with $h_w/20$ [52]. The third empirical relationship (ER3) suggests that the mixing length can be approximated with $0.03\sqrt{h_w h_c}$ [47]. The mixing lengths obtained for different canopy heights from these three empirical relationships are also plotted in Figure 5 for a constant water depth of 0.25 m. According to Figure 5, the three empirical equations produce close estimations when the submergence ratio is low ($h_c = 0.2$ m). For the canopy height of 0.1 m, $\lambda$ values derived from empirical relationships vary from those calculated from the measurements. Given that this study was conducted only for two canopy heights and one water depth, herein, the attempts are not made to suggest an empirical relationship for $\lambda$.

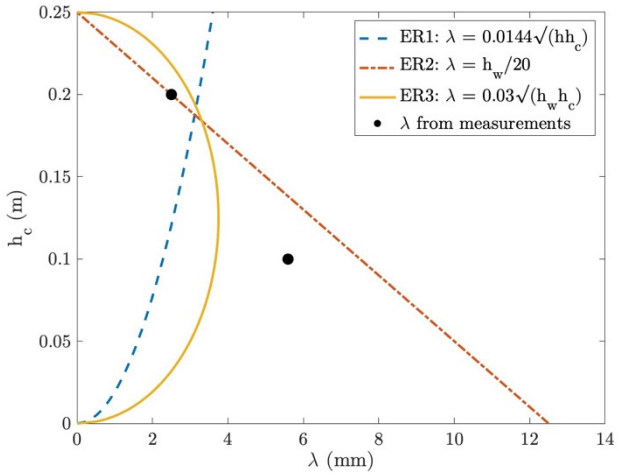


**Figure 5.** Variation of $\lambda$ with vegetation canopy height for a constant water depth of 0.25 m.

Once $\lambda$ is established, the turbulent shear stress inside the canopy was evaluated using Equation (8). The turbulent shear stress above the canopy was calculated using existing knowledge; the maximum shear occurs at the top of the vegetation canopy and linearly decays to zero at the air-water interface. Figures 3b and 4b present the measured and fitted profiles of $-\overline{u'w'}$ for the tested flow rates. The shear stress is negligible inside a canopy of 0.2 m; however, it drastically peaks at the top to reach a higher value when compared to a canopy of 0.1 m.

### *4.3. Longitudinal Dispersion Measurements*

The coefficient of longitudinal dispersion $(D)$ was experimentally derived based on the temporal variance of the injected tracer cloud measured along the distance through the canopy, using Equation (3). The average velocity of the cloud $(u)$ was calculated based on the time taken for the centroid of the tracer cloud to move from the first station to the fourth. Figure 6 presents a typical tracer measurement, where Figure 6a denotes the concentration measurements collected using the fluorometers located inside the canopy, and Figure 6b indicates the concentration measurements above the canopy for the canopy height of 0.1 m. The concentration time series measured inside the canopy consists of more scatter compared to the concentration time series measured above the canopy. The peak concentrations measured using the fluorometers inside the canopy are slightly lower than those measured above the canopy, as the bottom fluorometers might miss the solute movement in the upper part of the water column.

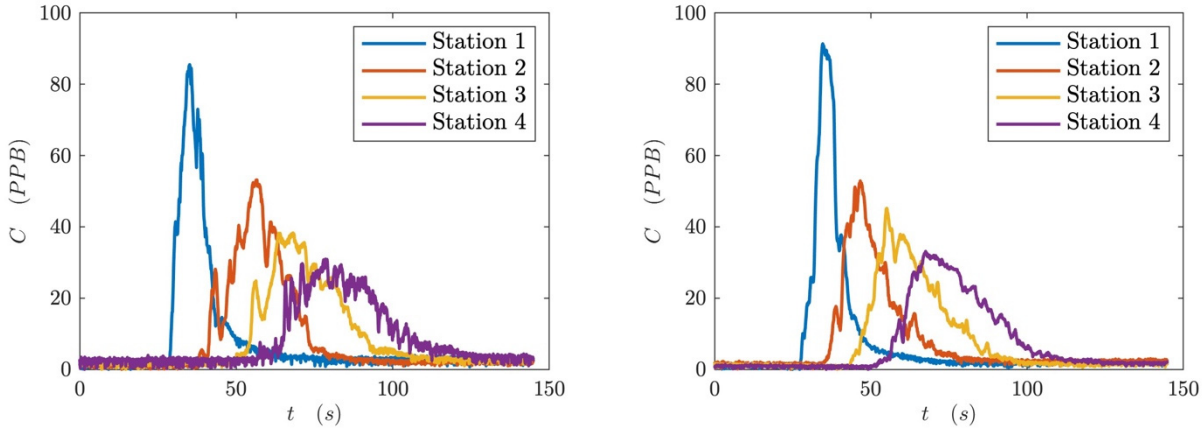


**Figure 6.** A typical tracer concentration measurement along the channel (the data corresponds to the flow rate of 17 L/s when the canopy height is 0.1 m): (**a**) from the fluorometers inside the canopy; and (**b**) from the fluorometers above the canopy.

Table 1 presents the magnitudes of $\lambda$ and the coefficients of longitudinal dispersion derived inside $(D_b)$ and above $(D_t)$ the canopy for different vegetated flow conditions. Five repeat injections were conducted for each test condition, and the average and variance of the longitudinal dispersion coefficients were reported. Here, $D_b$ does not provide a dispersion coefficient for the whole cross-section as the fluorometers inside the canopy miss out on some of the tracer movements above the canopy. Therefore, $D_b$ may only be used for discussing the magnitude of the vertical mixing in each canopy configuration.

**Table 1.** Experimentally derived characteristic mixing length scale and coefficient of longitudinal dispersion for different flow conditions.

| $h_c$(m) | $Q$ (l/s) | $\lambda$ (mm) | Measured inside the Canopy | | Measured above the Canopy | | Calculated $D(N)$ from the N-Zone Model ($\times 10^{-2}$m$^2$/s) |
|---|---|---|---|---|---|---|---|
| | | | Average $D_b$ ($\times 10^{-2}$m$^2$/s) | $\sigma^2$ of $D_b$ ($\times 10^{-6}$m$^4$/s$^2$) | Average $D_t$ ($\times 10^{-2}$m$^2$/s) | $\sigma^2$ of $D_t$ ($\times 10^{-6}$m$^4$/s$^2$) | |
| 0.1 | 5 | - | 1.23 | 3.35 | 1.75 | 1.39 | 1.69 |
| | 9 | 6.2 | 2.02 | 5.71 | 2.84 | 5.37 | 2.61 |
| | 13 | 5.2 | 2.69 | 7.10 | 3.79 | 5.45 | 4.41 |
| | 17 | 5.4 | 4.06 | 22.97 | 5.55 | 3.97 | 6.09 |
| | 21 | 5.5 | 5.20 | 24.69 | 7.10 | 9.96 | 7.09 |
| 0.2 | 5 | - | 0.47 | 0.77 | 1.97 | 1.13 | 2.56 |
| | 9 | 2.5 | 0.71 | 0.72 | 3.65 | 27.73 | 4.37 |
| | 13 | 2.6 | 0.80 | 2.87 | 5.06 | 5.61 | 5.80 |
| | 17 | 2.4 | 1.40 | 14.89 | 7.37 | 64.98 | 7.34 |

Figure 7 presents the data in Table 1 against the depth-averaged mean velocity $(\overline{\overline{u}})$: $D_b$ is plotted in Figure 7a and $D_t$ is plotted in Figure 7b. The coefficient of longitudinal dispersion measured in control tests without vegetation is also plotted to comprehend the effect of vegetation (in the absence of canopies, a single tracer measurement was collected for each cross-section at the mid-water depth). The best-fit lines are drawn through the origin, as the magnitude of molecular diffusion is negligible compared to the magnitudes of turbulent diffusion and shear dispersion. According to Figure 7, the magnitude of $D_b$ is smaller than $D_t$ for both canopy heights. This observation is expected, as the fluorometers inside the canopy observe a reduced velocity and turbulence compared to the upper part of the water column. This observation confirms that vertical mixing is not strong enough to create a uniform solute distribution throughout the cross-section [32]. All longitudinal dispersion measurements in vegetated conditions ($D_b$ and $D_t$) are significantly greater than those measured in open channel flow. Here, the longitudinal dispersion measurements $(D_t)$ for the canopy heights of 0.1 m and 0.2 m are ~12 and 15 times the longitudinal dispersion coefficients obtained for open channel flow, respectively. This observation complements the

increased shear dispersion in vegetated flows compared to open channel flow. The canopy height of 0.2 m causes the highest value of $D_t$, and the canopy height of 0.1 m produces the highest value of $D_b$, when the two canopies are compared. Even though the canopy height of 0.2 m has increased the longitudinal dispersion in the cross-section, this enhancement does not seem to be uniform over the water depth.

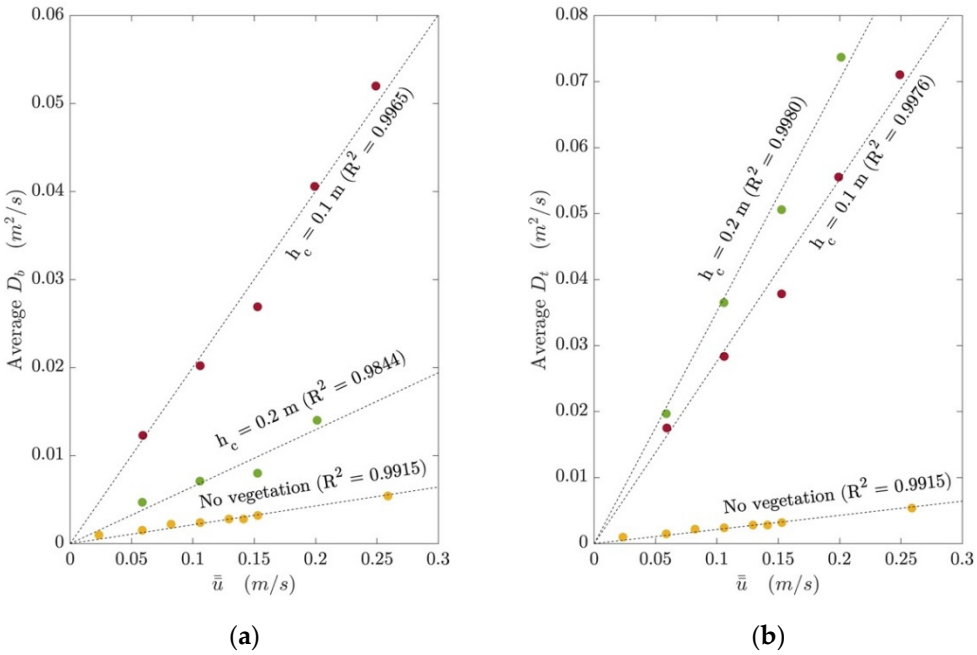


**Figure 7.** Measured averaged coefficient of longitudinal dispersion for different flow conditions (with and without a canopy) plotted against the depth averaged mean velocity: (**a**) measured inside the canopy; and (**b**) measured above the canopy.

Figure 8 compares $D_b$ and $D_t$ with each other for two tested canopies, and $D_t$ remains consistently proportional to $D_b$ at different flow rates. $D_t/D_b$ depend on the canopy height: 1.4 for $h_c$ = 0.1 m ($h/h_c = 2.5$), and 5.4 for $h_c$ = 0.2 m ($h/h_c = 1.25$), despite the constant 0.125 m distance between the top and bottom fluorometers. It is generally observed that the variance of $D_t$ and $D_b$ is high when the measuring point is located near the canopy edge. The complexity of flow dynamics in canopy boundaries may cause this behaviour. The presence of vortices can affect the tracer movement, and the tracer can also become trapped at the surface of canopy elements and eventually be released into the flow, which might not be precisely repeatable. Hence, repeated testing is recommended for dispersion measurements in the boundaries of different flow regimes, as a practical measure even for consistent vegetation canopies.

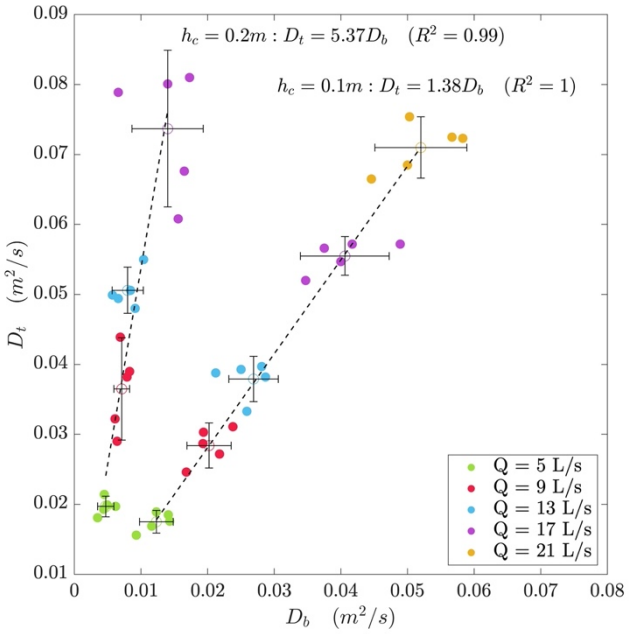


**Figure 8.** Comparison of $D$ evaluated from the measurements above the canopy with $D$ evaluated from the measurements inside the canopy.

### *4.4. Application of the N-Zone Model*

#### 4.4.1. Obtaining Horizontal and Vertical Diffusivity Profiles

The diffusivities were calculated using Equation (7) assuming a turbulent Schmidt number equal to unity ($S_{cT}$ = 1). Since isotropy is assumed, the magnitudes of horizontal and vertical diffusivities were similar. The vertical diffusivity profiles obtained for the tested flow conditions are plotted in Figures 3c and 4c. Since the diffusivities are approximate estimations calculated based on velocity measurements, the profiles were plotted using dotted lines. The diffusivity profiles consist of sharp edges in their shape as they inherit the imperfections of the assumptions made when fitting the velocity models. The diffusivities reach a maximum slightly above the canopy ($h_c = 0.1$ m) or at the top of the canopy ($h_c = 0.2$ m) and gradually decrease when going into the canopy. Overall, the magnitude of the vertical diffusivity at $h_c = 0.1$ m is higher than that at $h_c = 0.2$ m.

#### 4.4.2. Calculating the Coefficient of Longitudinal Dispersion

When the diffusivity and the velocity profile were known, the coefficient of longitudinal dispersion was calculated using Equations (9) and (10). The first term in Equation (9) calculates the longitudinal dispersion occurring due to the velocity shear, i.e., differential advection. The second term calculates the longitudinal dispersion occurring due to turbulent diffusion.

When calculating the diffusivity and applying the N-zone model, the fitted velocity profiles (shown in Figures 3a and 4a) and the fitted shear stress profiles (shown in Figures 3b and 4b) were used for obtaining the velocity gradient, diffusivity, and the velocity in each cell. If scattered raw measurements of the velocity profiles were used in the N-zone model to evaluate longitudinal dispersion, it would be interpreted as higher velocity gradients between zones, resulting in overestimations of shear dispersion. Here, a calculated velocity model and a shear stress profile based on a calibrated mixing length were used to avoid overestimating the shear dispersion. For the test conditions, the shear dispersion was three orders of magnitude larger than the turbulent diffusion in each cell. Therefore, the turbulent diffusion is not presented here, and the contribution from each zone in the water column for shear dispersion is presented in Figures 3d and 4d. The profiles were plotted using dotted lines because they are only approximate estimations. Here, the shear dispersion is maximum in the middle region of the water column, roughly

around the upper part of the vegetation canopy, where the velocity gradient is also at its maximum.

Table 1 summarises the coefficients of longitudinal dispersion estimated using the N-zone model $(D(N))$. $D(N)$, which is evaluated using the N-zone model, is compared with the coefficient of longitudinal dispersion measured above the canopy $(D_t)$ in Figure 9. The N-zone model has produced acceptable estimations, with an average overestimation of 6.4%.

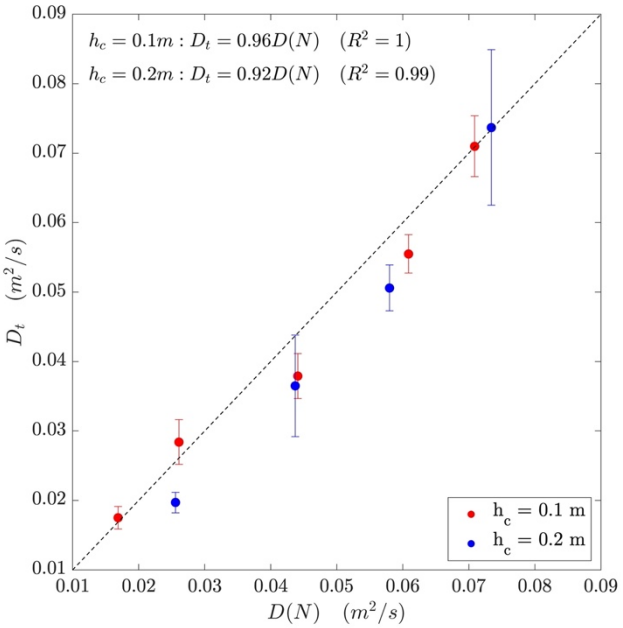


**Figure 9.** Comparison of $D$ evaluated from the measurements above the canopy with $D$ $(N)$ evaluated from the N-zone model.

## 5. Discussion

### *5.1. Vertical Mixing in the Presence of Submerged Canopies*

Vertical diffusivity contributes to the first term in Equation (9) which is the shear dispersion. Shear dispersion is significantly larger than turbulent diffusion (second term in Equation (9)) which depends on horizontal diffusivity. According to Figures 3 and 4, the vertical diffusivity is generally higher throughout the cross-section for the canopy height of 0.1 m, compared to the canopy height of 0.2 m. This suggests that better cross-sectional mixing occurs when the canopy height is 0.1 m, and this observation on diffusivity profiles generated based on velocity measurements complements the experimental observations from tracer measurements. According to Figure 8, for a 0.1 m canopy height, the magnitude of longitudinal dispersion obtained from tracer measurements inside the canopy is very close to that measured above. However, the longitudinal dispersion measured from tracer measurements inside the canopy of 0.2 m is one-fifth of that measured above the canopy.

Previous research on submerged vegetation discusses the occurrence of a vertical mixing layer in the upper part of the submerged canopy. The rate of vertical transport in the bottom part of the canopy is dominated by stem-wake turbulence [28], which is an order of magnitude lower than the rate of vertical transport in the upper part of the canopy [23]. The thickness of the vertical exchange zone in the upper part of the canopy $(\delta_e)$ can be approximated with $(0.23 \pm 0.06)/(C_D a)$ when $C_D a h \geq 0.1$ [30], where $C_D$ is the drag coefficient and $a$ is the leaf area index of the canopy. Taking $C_D \approx 1$, the thickness of the vertical exchange zone is given by 53 mm $\leq \delta_e \leq$ 91 mm for the tested canopy layout in this study. This suggests that the vertical mixing layer reaches beyond the bottom fluorometer when the canopy height is 100 mm as the fluorometer is located 50 mm below the top of the canopy. However, for the canopy height of 200 mm where the fluorometer is

located 100 mm below the top of the canopy, the vertical mixing layer does not reach the position of the bottom fluorometer.

### *5.2. Longitudinal Dispersion in the Presence of Submerged Canopies*

Figures 3 and 4 provide a comprehensive description in terms of the hydrodynamic conditions and shear dispersion for the two tested submerged canopies. Overall, the velocities in the canopy are lower, compared to the velocities in the free-flowing region above the canopy, for both canopy conditions. When compared, the peaks in the velocity profile and the shear stress profile of the canopy height of 0.1 m do not reach as high as the canopy height of 0.2 m, even though they comprise noticeable magnitudes throughout the water column. Accordingly, the vertical diffusivities are significantly higher for the canopy height of 0.1 m. Based on the velocity profile, the canopy height of 0.2 m creates the highest differential advection. In addition, the shear stresses are minimal inside the canopy height of 0.2 m before it increases with a steep gradient to reach a huge peak at the top of the canopy. Accordingly, the vertical diffusivities are lower for the canopy height of 0.2 m, resulting in increased shear dispersion.

### *5.3. Applicability of the N-Zone Model into Submerged Vegetation*

The basis for the N-zone model was the slow-zone model, which divides the flow into two zones: a slow zone and a fast zone [53]. The advantage of the N-zone model over the two-zone model is its ability to fit complex shapes of the velocity profiles by increasing the number of zones. In addition, the contribution from each location in the water column for longitudinal mixing can be obtained using the N-zone model, which can be beneficial in managing environmental pollution problems. Only a limited number of studies have been conducted on the N-zone model to determine the longitudinal dispersion in vegetated flows, and one such study was conducted for natural vegetation [35]. The limited number of studies with the N-zone model might be due to the challenges in deriving accurate values for velocities and turbulent shear stresses in vegetated flows. The benefit of the N-zone model is its ability to link the velocity profile with the mixing characteristics, even when the information for other critical parameters of the canopy, such as the drag coefficient or the characteristics of the mixing layer, is unknown.

During this study, we evaluated the applicability of the N-zone model for two canopy submergences representing two conditions. For $h_c = 0.1$ m $(h/h_c = 2.5)$, the vertical exchange zone reaches a significant distance into the canopy resulting in an enhanced cross-sectional uniformity of the solute. For $h_c = 0.2$ m $(h/h_c = 1.25)$, the vertical exchange zone has limited development, causing a higher shear dispersion in the cross-section. Even though these two canopy geometries provided insight into the effect of submergence on longitudinal dispersion, test results from a series of different canopy heights for a constant water depth would provide a better understanding of the optimum canopy height which provides the maximum shear dispersion. If the velocity data were available for different canopy heights, the turbulent stress data can be used for obtaining the mixing length for each canopy condition using the Reynolds analogy, and an empirical relationship for $\lambda$ can be obtained, which will increase the applicability of the N-zone model in future even when turbulence data are unavailable.

The coefficient of longitudinal dispersion is a bulk transport coefficient which includes all the physical processes of the cross-section of the flow. When applying the N-zone model, the flow is assumed to be two-dimensional, ignoring the three-dimensional effect of the flow due to the walls. The unavailability of velocity measurements in the upper part of the water column is also a limitation here, as the three-dimensional effect of the flow might be visible in the velocity and turbulent stress profiles near the air–water interface. This study represents a three-dimensional flow in a simplified two-dimensional model to obtain a bulk transport coefficient which is used in the context of a depth-averaged one-dimensional model. Therefore, the results of this study can be extended using future studies consisting of different aspect ratios of the channels with different wall roughness.

The relatively high error in the velocity measurements at the lower flow rates can affect the accuracy of the estimations of $\lambda$. Since the N-zone model relies on the velocity profile and diffusivities, improvements in calculating accurate velocity profiles and mixing lengths will increase the applicability of the N-zone model. For example, if the diffusivity can be presented as a function of the velocity gradient (as shown in [54,55]), it will be possible to use the N-zone model with more reliable diffusivity values, once the mean velocity profile and velocity gradients are established. The tested canopies in this study were rigid, and tests on flexible canopies will also help with understanding the applicability of the N-zone model for flexible canopies, especially when very flexible canopies obstruct the vertical continuity of the water column.

## 6. Conclusions

The effect of submerged vegetation on longitudinal dispersion measured in two locations in the water column: inside and above the canopy was experimentally evaluated for two canopy submergences. The longitudinal dispersion measurements for the canopy heights of 0.1 m and 0.2 m are approximately 12 and 15 times the longitudinal dispersion coefficients obtained for open channel flow, due to the increased shear dispersion that resulted from the increased differential velocities of the water column in the presence of submerged vegetation. The coefficient of longitudinal dispersion measured above the canopies is 1.4 and 5.4 times that measured inside the canopies for the canopy heights of 0.1 m and 0.2 m, respectively. This behaviour complements the previous findings, which suggest that a higher canopy submergence results in better vertical mixing within the canopy. To calculate the coefficient of longitudinal dispersion, a mixing length was evaluated based on Reynolds stress measurements for each canopy configuration, the diffusivity profiles were calculated based on the shear stress profiles, and the velocity and diffusivity profiles were applied to the N-zone model. The coefficient of longitudinal dispersion calculated using the N-zone model based on velocity measurements provides a good agreement with the coefficient of longitudinal dispersion measured using the tracer measurements along the vegetated channel. The canopy height of 0.2 m resulted in comparatively smaller vertical diffusivities and a better longitudinal shear dispersion, which is explained by the increased velocity gradients and the increased shear stresses observed towards the top of the canopy. The benefit of this methodology for calculating the coefficient of longitudinal dispersion in the presence of submerged canopies is its ability to produce accurate estimations based on the velocity measurements even when the specific characteristics of the canopy such as the density or flexibility are unknown.

**Author Contributions:** Conceptualisation, M.G.N.O. and J.P.; methodology, M.G.N.O. and J.P.; software, M.G.N.O.; validation, M.G.N.O.; formal analysis, M.G.N.O.; investigation, M.G.N.O.; resources, M.G.N.O. and J.P.; data curation, M.G.N.O.; writing—original draft preparation, M.G.N.O.; writing—review and editing, M.G.N.O. and J.P.; visualisation, M.G.N.O.; supervision, J.P.; project administration, J.P.; funding acquisition, J.P. All authors have read and agreed to the published version of the manuscript.

**Funding:** This research is a part of the PhD of Nipuni Odara Merenchi Galappaththige, which was funded by Engineering and Physical Science Research Council (EPSRC) Doctoral Training Partnership award from the School of Engineering, University of Warwick under grant reference number: EP/N509796/1 (1924369).

**Data Availability Statement:** The data presented in this study are available on request from the corresponding author.

**Acknowledgments:** The authors acknowledge the support received from the former and current members of the technical support team of the Warwick Water Lab during setup construction and data collection.

**Conflicts of Interest:** The authors declare no conflict of interest.

## References


1. Green, E.P.; Short, F. *World Atlas of Seagrasses*; University of California Press: Berkeley, CA, USA, 2003; Volume 47. [CrossRef]
2. Westlake, D.F. Aquatic macrophytes and the oxygen balance of running water. *SIL Proc. 1922–2010* **1961**, *14*, 499–504. [CrossRef]
3. Carpenter, S.R.; Lodge, D.M. Effects of submersed macrophytes on ecosystem processes. *Aquat. Bot.* **1986**, *26*, 341–370. [CrossRef]
4. Moore, K.A. Influence of Seagrasses on Water Quality in Shallow Regions of the Lower Chesapeake Bay. *J. Coast. Res.* **2004**, *10045*, 162–178. [CrossRef]
5. Kadlec, R.H.; Wallace, S.D. *Treatment Wetlands*; CRC Press: Boca Raton, FL, USA, 2008.
6. Abdelrhman, M. Effect of eelgrass Zostera marina canopies on flow and transport. *Mar. Ecol. Prog. Ser.* **2003**, *248*, 67–83. [CrossRef]
7. Chambers, P.; Prepas, E. Nutrient dynamics in riverbeds: The impact of sewage effluent and aquatic macrophytes. *Water Res.* **1994**, *28*, 453–464. [CrossRef]
8. Schulz, M.; Kozerski, H.-P.; Pluntke, T.; Rinke, K. The influence of macrophytes on sedimentation and nutrient retention in the lower River Spree (Germany). *Water Res.* **2002**, *37*, 569–578. [CrossRef]
9. Butcher, R.W. Studies on the Ecology of Rivers: I. On the Distribution of Macrophytic Vegetation in the Rivers of Britain. *J. Ecol.* **1933**, *21*, 58. [CrossRef]
10. Harrod, J.J. The Distribution of Invertebrates on Submerged Aquatic Plants in a Chalk Stream. *J. Anim. Ecol.* **1964**, *33*, 335. [CrossRef]
11. Gambi, M.; Nowell, A.; Jumars, P. Flume observations on flow density dynamics in Zosteramarina (eelgrass) beds. *Mar. Ecol. Prog. Ser.* **1990**, *61*, 159–169. [CrossRef]
12. Koch, E.W.; Ackerman, J.D.; Verduin, J.; van Keulen, M. Fluid Dynamics in Seagrass Ecology—From Molecules to Ecosystems. In *Seagrasses: Biology, Ecologyand Conservation*; Springer: Dordrecht, The Netherlands, 2006; pp. 193–225. [CrossRef]
13. Gregg, W.W.; Rose, F.L. The effects of aquatic macrophytes on the stream microenvironment. *Aquat. Bot.* **1982**, *14*, 309–324. [CrossRef]
14. Sand-Jensen, K.; Mebus, J.R. Fine-Scale Patterns of Water Velocity within Macrophyte Patches in Streams. *Oikos* **1996**, *76*, 169. [CrossRef]
15. López, F.; García, M.H. Mean Flow and Turbulence Structure of Open-Channel Flow through Non-Emergent Vegetation. *J. Hydraul. Eng.* **2001**, *127*, 392–402. [CrossRef]
16. Winant, C.D.; Browand, F.K. Vortex pairing: The mechanism of turbulent mixing-layer growth at moderate Reynolds number. *J. Fluid Mech.* **1974**, *63*, 237–255. [CrossRef]
17. Nepf, H.M.; Vivoni, E.R. Flow structure in depth-limited, vegetated flow. *J. Geophys. Res. Oceans* **2000**, *105*, 28547–28557. [CrossRef]
18. Ghisalberti, M.; Nepf, H.M. Mixing layers and coherent structures in vegetated aquatic flows. *J. Geophys. Res. Atmos.* **2002**, *107*, 3-1–3-11. [CrossRef]
19. Nepf, H.M. Flow and Transport in Regions with Aquatic Vegetation. *Annu. Rev. Fluid Mech.* **2012**, *44*, 123–142. [CrossRef]
20. Nepf, H.M. Flow Over and Through Biota. In *Treatise on Estuarine and Coastal Science*; Elsevier: Amsterdam, The Netherlands, 2011; Volume 2, pp. 267–288.
21. von Kármán, T. *Mechanical Similitude and Turbulence—Reprint from Nachrichten von der Gesellschaft der Wissenschaften zu Göttingen, 1930*; National Advisory Committee on Aeronautics: Washington, DC, USA, 1931.
22. Okamoto, T.-A.; Nezu, I. Spatial evolution of coherent motions in finite-length vegetation patch flow. *Environ. Fluid Mech.* **2013**, *13*, 417–434. [CrossRef]
23. Ghisalberti, M.; Nepf, H. Mass Transport in Vegetated Shear Flows. *Environ. Fluid Mech.* **2005**, *5*, 527–551. [CrossRef]
24. Ikeda, S.; Kanazawa, M. Three-Dimensional Organized Vortices above Flexible Water Plants. *J. Hydraul. Eng.* **1996**, *122*, 634–640. [CrossRef]
25. Fischer, H.B.; List, E.J.; Koh, R.C.Y.; Imberger, J.; Brooks, N.H. Chapter 4: Shear Flow Dispersion. In *Mixing in Inland and Coastal Waters*; Academic Press Inc. (London) Ltd.: London, UK, 1979; pp. 81–102.
26. Elder, J.W. The dispersion of marked fluid in turbulent shear flow. *J. Fluid Mech.* **1959**, *5*, 544–560. [CrossRef]
27. Fonseca, M.S.; Kenworthy, W. Effects of current on photosynthesis and distribution of seagrasses. *Aquat. Bot.* **1987**, *27*, 59–78. [CrossRef]
28. Murphy, E.; Ghisalberti, M.; Nepf, H. Model and laboratory study of dispersion in flows with submerged vegetation. *Water Resour. Res.* **2007**, *43*, W05438. [CrossRef]
29. Ghisalberti, M.; Nepf, H.M. The limited growth of vegetated shear layers. *Water Resour. Res.* **2004**, *40*, W07502. [CrossRef]
30. Nepf, H.; Ghisalberti, M.; White, B.; Murphy, E. Retention time and dispersion associated with submerged aquatic canopies. *Water Resour. Res.* **2007**, *43*, W04422. [CrossRef]
31. Fischer, H.B. The Mechanics of Dispersion in Natural Streams. *J. Hydraul. Div.* **1967**, *93*, 187–216. [CrossRef]
32. Patil, S.; Li, X.; Li, C.; Tam, B.Y.F.; Song, C.Y.; Chen, Y.P.; Zhang, Q. Longitudinal dispersion in wave-current-vegetation flow. *Phys. Oceanogr.* **2009**, *19*, 45–61. [CrossRef]
33. Fischer, H.B.; List, E.J.; Koh, R.C.Y.; Imberger, J.; Brooks, N.H. Chapter 2: Fickian Diffusion. In *Mixing in Inland and Coastal Waters*; Academic Press Inc (London) Ltd.: London, UK, 1979.

34. Shucksmith, J.D.; Boxall, J.B.; Guymer, I. Effects of emergent and submerged natural vegetation on longitudinal mixing in open channel flow. *Water Resour. Res.* **2010**, *46*, W04504. [CrossRef]
35. Shucksmith, J.D.; Boxall, J.B.; Guymer, I. Determining longitudinal dispersion coefficients for submerged vegetated flow. *Water Resour. Res.* **2011**, *47*, W10516. [CrossRef]
36. Noori, R.; Ghiasi, B.; Sheikhian, H.; Adamowski, J.F. Estimation of the Dispersion Coefficient in Natural Rivers Using a Granular Computing Model. *J. Hydraul. Eng.* **2017**, *143*, 04017001. [CrossRef]
37. Noori, R.; Mirchi, A.; Hooshyaripor, F.; Bhattarai, R.; Haghighi, A.T.; Kløve, B. Reliability of functional forms for calculation of longitudinal dispersion coefficient in rivers. *Sci. Total Environ.* **2021**, *791*, 148394. [CrossRef]
38. Lowe, R.J.; Koseff, J.R.; Monismith, S.G. Oscillatory flow through submerged canopies: 1. Velocity structure. *J. Geophys. Res. Atmos.* **2005**, *110*, C10016. [CrossRef]
39. Augustin, L.N.; Irish, J.L.; Lynett, P. Laboratory and numerical studies of wave damping by emergent and near-emergent wetland vegetation. *Coast. Eng.* **2009**, *56*, 332–340. [CrossRef]
40. Thuy, N.B.; Tanimoto, K.; Tanaka, N.; Harada, K.; Iimura, K. Effect of open gap in coastal forest on tsunami run-up—Investigations by experiment and numerical simulation. *Ocean Eng.* **2009**, *36*, 1258–1269. [CrossRef]
41. Liu, P.L.-F.; Chang, C.-W.; Mei, C.C.; Lomonaco, P.; Martin, F.L.; Maza, M. Periodic water waves through an aquatic forest. *Coast. Eng.* **2015**, *96*, 100–117. [CrossRef]
42. Abdolahpour, M.; Ghisalberti, M.; Lavery, P.; McMahon, K. Vertical mixing in coastal canopies. *Limnol. Oceanogr.* **2017**, *62*, 26–42. [CrossRef]
43. Abdolahpour, M.; Hambleton, M.; Ghisalberti, M. The wave-driven current in coastal canopies. *J. Geophys. Res. Oceans* **2017**, *122*, 3660–3674. [CrossRef]
44. Luhar, M.; Coutu, S.; Infantes, E.; Fox, S.; Nepf, H. Wave-induced velocities inside a model seagrass bed. *J. Geophys. Res. Atmos.* **2010**, *115*, C12005. [CrossRef]
45. Thomas, R.E.; Schindfessel, L.; McLelland, S.J.; Creëlle, S.; De Mulder, T. Bias in mean velocities and noise in variances and covariances measured using a multistatic acoustic profiler: The Nortek Vectrino Profiler. *Meas. Sci. Technol.* **2017**, *28*, 075302. [CrossRef]
46. Chikwendu, S.C. Calculation of longitudinal shear dispersivity using an N-zone model as $N \rightarrow \infty$. *J. Fluid Mech.* **1986**, *167*, 19–30. [CrossRef]
47. Tang, X. A mixing-length-scale-based analytical model for predicting velocity profiles of open-channel flows with submerged rigid vegetation. *Water Environ. J.* **2019**, *33*, 610–619. [CrossRef]
48. Prandtl, L. 7. Bericht über Untersuchungen zur ausgebildeten Turbulenz. *ZAMM—J. Appl. Math. Mech. /Z. Für Angew. Math. Und Mech.* **1925**, *5*, 136–139. [CrossRef]
49. Schlichting, H.; Gersten, K. *Boundary-Layer Theory*; Springer: Berlin/Heidelberg, Germany, 2016. [CrossRef]
50. Klopstra, D.; Barneveld, H.J.; van Noortwijk, J.M.; van Velzen, E.H. Analytical model for hydraulic roughness of submerged vegetation. In Proceedings of the Theme A, Managing Water: Coping with Scarcity and Abundance: The 27th Congress of the International Association for Hydraulic Research, San Francisco, CA, USA, 10–15 August 1997; pp. 775–780.
51. Meijer, D.G.; Van Velzen, E.H. Prototype-scale flume experiments on hydraulic roughness of submerged vegetation. In Proceedings of the 28th IHAR World Congress, Graz, Austria, 22–27 August 1999.
52. Baptist, M.J.; Babovic, V.; Uthurburu, J.R.; Keijzer, M.; Uittenbogaard, R.; Mynett, A.; Verwey, A. On inducing equations for vegetation resistance. *J. Hydraul. Res.* **2007**, *45*, 435–450. [CrossRef]
53. Chikwendu, S.C.; Ojiakor, G.U. Slow-zone model for longitudinal dispersion in two-dimensional shear flows. *J. Fluid Mech.* **1985**, *152*, 15–38. [CrossRef]
54. Boghi, A.; Di Venuta, I.; Gori, F. Passive scalar diffusion in the near field region of turbulent rectangular submerged free jets. *Int. J. Heat Mass Transf.* **2017**, *112*, 1017–1031. [CrossRef]
55. Di Venuta, I.; Boghi, A.; Angelino, M.; Gori, F. Passive scalar diffusion in three-dimensional turbulent rectangular free jets with numerical evaluation of turbulent Prandtl/Schmidt number. *Int. Commun. Heat Mass Transf.* **2018**, *95*, 106–115. [CrossRef]

water

MDPI

*Article*

# Seasonality of Water Exchange in the Northern South China Sea from Hydrodynamic Perspective

**Lingbo Cui [1], Mingyu Li [1], Tingting Zu [2,*] and Zhongya Cai [1,3,*]**

[1] State Key Laboratory of Internet of Thing for Smart City, Department of Ocean Science and Technology, University of Macau, Macau 999078, China
[2] State Key Laboratory of Tropical Oceanography, South China Sea Institute of Oceanology, Chinese Academy of Sciences, Guangzhou 510301, China
[3] Center for Ocean Research in Hong Kong and Macau (CORE), Hong Kong 999077, China
* Correspondence: author: zutt@scsio.ac.cn (T.Z.); zycai@um.edu.mo (Z.C.)

**Abstract:** In this study, we utilized exposure time ($\overline{\theta}$) as a key metric to investigate water exchange and its spatiotemporal variations in the Northern South China Sea (NSCS). The Eulerian adjoint method and Lagrangian tracking were adopted to capture a comprehensive view of water exchange in coastal regions. Our findings reveal distinct spatial and seasonal variations in $\overline{\theta}$. Spatially, a long $\overline{\theta}$ (exceeding 150 days) appears in the coastal region, and the largest values occur in the Beibu Gulf (300 days). Temporally, $\overline{\theta}$ exhibits clear seasonal patterns across the extensive shelf area, influenced by the seasonal monsoon which induced seasonally reversing shelf current and results in symmetrical distribution patterns of $\overline{\theta}$ across the board shelf during both winter and summer months. $\overline{\theta}$ is longer in winter than in summer. The study also revealed pronounced vertical contrasts in cross-isobath transport over the NSCS shelf, though significant vertical variations in net exchange time were noted only in specific locations, including the northeast side of Hainan Island, the Beibu Gulf mouth, and along the west side of Taiwan Island. The Beibu Gulf emerged as a critical factor in the NSCS's water exchange dynamics in both seasons. In summer, it impacts more than 20% of the water exchange over adjacent areas, particularly through its westward transport against typical northeastward shelf currents. This highlights the combined effect of the westward spread of the Pearl River freshwater and the stable slope current on regional hydrodynamics. In winter, the Gulf's retention characteristics profoundly affected even distant areas, contributing to up to 50% of water exchange, showing its broad impact on the NSCS's water dynamics throughout the year.

**Keywords:** exposure time; Northern South China Sea; lagrangian and eulerian methods; seasonality; hydrodynamics



**Citation:** Cui, L.; Li, M.; Zu, T.; Cai, Z. Seasonality of Water Exchange in the Northern South China Sea from Hydrodynamic Perspective. *Water* **2024**, *16*, 10. https://doi.org/10.3390/w16010010

Academic Editor: Wencheng Guo

Received: 11 November 2023
Revised: 3 December 2023
Accepted: 11 December 2023
Published: 20 December 2023



## 1. Introduction

Coastal waters serve as critical interfaces where terrestrial and marine ecosystems intersect, playing an essential role in global material cycles. These waters, influenced by the confluence of rivers and oceans, are subject to dynamic processes shaped by tides, winds, buoyancy waters and ocean circulation [1–4]). Meanwhile, the functioning of coastal ecosystems is increasingly threatened by anthropogenic impacts and climate change, leading to detrimental effects such as eutrophication, harmful algal blooms, and hypoxia exacerbated by inadequate water exchange [5,6]. These ecological disturbances highlight the importance of understanding water exchange processes, as they are fundamental in determining the transport and fate of water quality indicators [7,8].

Over the Northern South China Sea (NSCS), the shelf circulation and water movement experience complex dynamics driven by wind, tides, the Kuroshio intrusion, freshwater discharge from the Pearl River Estuary (PRE), and modulated by the local topography [9,10]. The alternate variation of northeasterly winter monsoon to southwesterly summer monsoon induces contrasting seasonally changed southwestward to northeastward shelf current and

a strong seasonal difference in rainfall over southern China and related buoyant discharge into the NSCS, which together impacts water exchange rates and thus the ecological balance of the region [11,12]. Under the interaction of topography and summer southwesterly wind, extensive upwelling was generated at the coastal region of NSCS and brings cold, salty, nutrient-rich deep waters to the surface and therefore, improves the primary production in these regions [9,13,14]. Although previous studies have recognized the influence of the East Asia Monsoon on the NSCS's hydrodynamic processes, indicating substantial seasonal variability [15–17], the specific seasonal patterns of water exchange, the major hydrodynamic processes, and their cumulative impacts remain poorly understood.

Transport timescales and water exchange rates, crucial for evaluating the distribution of properties critical to marine ecosystems and climate, are significantly affected by seasonality of the seasonally contrasting shelf current. Metrics such as exposure time, water age, and flushing time, offer a high-resolution understanding of these variations and have proven effective for assessing coastal water exchange capacities, particularly in tidal regions where water reentry is a key factor [1,18]. These timescales are vital benchmarks in complex dynamic settings and provide insight into how varying conditions impact the transport of phytoplankton biomass and contaminants [19–22]. Earlier research on water exchange in the NSCS primarily concentrated on coastal regions, specifically estuarine areas, for instance, Ren et al. (2014) [23] found riverine influence plays a crucial role in water exchange in the Pearl River Estuary, with tides affecting the fluctuation range of water exchange. Wind predominantly impacts the vertical structure of water exchange during winter [24]. It is also noticed that the large-scale coastal controls the seasonal pattern of bay-shelf exchanges [25]. Over the shelf, research mainly focuses on the cross isobath water motions, such as Liu et al.'s [26] study highlighted that southwesterly wind induced flows in the Taiwan Strait sustained northeastward upwelling currents near the Pearl River Estuary, promoting the extensive upslope movement of deep shelf waters. Therefore, investigation into the seasonal patterns of water exchange in the NSCS and the related hydrodynamic processes could provide valuable information for the effective management and improvement of coastal environments, emphasizing the critical nature of seasonal dynamics in coastal water that is influenced by monsoon.

Following this introduction, Section 2 introduces the numerical model, adjoint model, and tracking model used in this study. Section 3 discusses the spatial-temporal characteristics of water exchange. Finally, Section 4 summarizes the study.

## 2. Methodology

### *2.1. Ocean Model*

To accurately simulate estuarine and shelf circulation with high resolution, this study utilized a hierarchically nested modeling approach based on the Regional Ocean Modeling System [27]. The model's domain encompasses the NSCS shelf (Figure 1), with horizontal grid spacing that finely transitions from approximately 1 km in the coastal proximity to 3 km across the broader NSCS shelf area. Employing the terrain-following s-coordinate system [28], the vertical structure of the water column was discretized into 60 levels to enhance resolution and a higher resolution was used in both the surface and bottom boundary layers. To solve the turbulent mixing and diffusion in the water column, we utilized the level-2.5 turbulence-closure scheme of Mellor and Yamada (1982) [29]. The model incorporates atmospheric forcing including wind, heat flux, and precipitation, provided by the ERA5 atmospheric reanalysis data from the European Center for Medium-Range Weather Forecasts (ECMWF). River discharge data were provided by the Ministry of Water Resources of China. Along the open boundary, the model was nested with the Hybrid Coordinate Ocean Model and the Navy Coupled Ocean Data Assimilation (HYCOM + NCODA) global 1/12° analysis (GLBv0.08; https://www.hycom.org/), with a 3-hourly temporal interval. We imposed nine major constituents of the semidiurnal (i.e., $M_2$, $S_2$, $K_2$, and $N_2$) and diurnal (i.e., $K_1$, $O_1$, $P_1$, and $Q_1$) tides, as well as one of the $M_4$ tide from the nonlinearity of the $M_2$. These harmonic constants were inverted from remotely sensed

long-term sea-level anomaly (SLA) variations using the Oregon Tide Inverse Software (Egbert & Erofeeva, 2002; https://www.tpxo.net/otps) [30] of T. T. Zu et al. (2008) [31]. This modeling system has been previously validated for its efficacy in exploring climate influences and the interannual variability of shelf currents in the NSCS [32]. In this study, the daily results of velocity $(u, v, w)$ and the diffusion coefficient $(k)$ between 1994–2018 were saved to conduct the adjoint simulation under complex hydrodynamic conditions, detailed in the following contents.

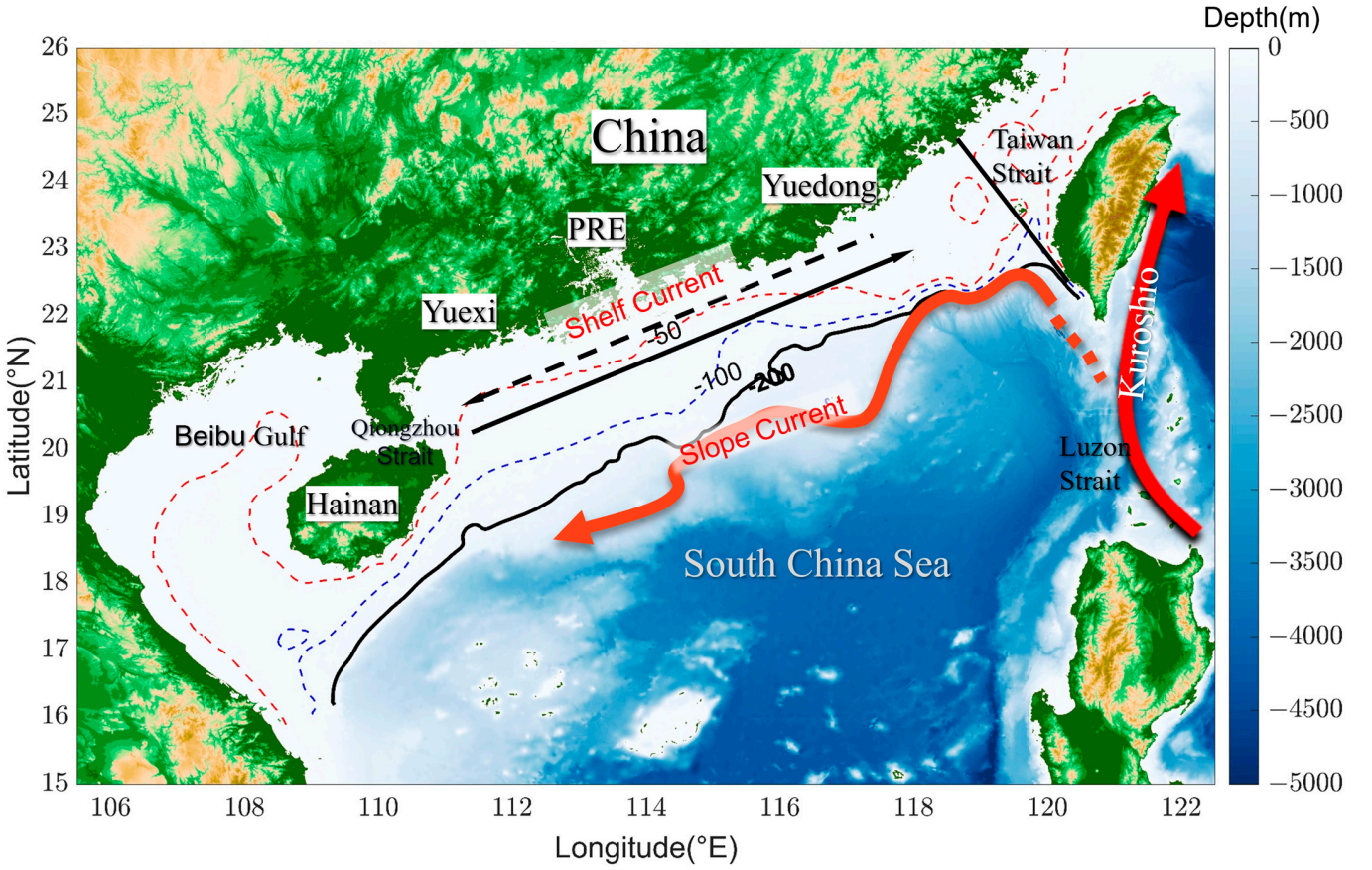


**Figure 1.** Topography (m) and diagrammatic sketch of circulation in the NSCS. The black solid/dashed arrow over the shelf indicates the summer/winter current. The black solid lines and 200 m isobath define the region of $\omega$ in the calculation of exposure time.

### *2.2. Exposure Time Model and Lagrangian Particle Tracking*

To examine the water exchange capacity, the exposure time $(\overline{\theta})$ [33], which was defined as the time required for the released substance to leave the domain of interest $(\omega)$ was used as it showed high-resolution temporal and spatial variations. To resolve the dependence of $\overline{\theta}$ on the initial release location and release time, the adjoint method [34,35] was used.

$$\frac{\partial \overline{\theta}}{\partial t} + \delta_\omega + \vec{v} \cdot \nabla \overline{\theta} + \nabla \left( k \cdot \nabla \overline{\theta} \right) = 0 \tag{1}$$

where $\overline{\theta}$ is the exposure time, $\vec{v}$ is the three-dimensional velocity vector and $k$ is the turbulent diffusion coefficient obtained from the hydrodynamic model, and $\delta_\omega$ is the characteristic function of the domain of interest $\omega$ that $\delta_\omega = \begin{cases} 1 \ (x, y, z) \in \omega \\ 0 \ (x, y, z) \notin \omega \end{cases}$.

In this study, $\omega$ covers the region from Beibu Gulf to the Taiwan Strait. It is bounded by the 200-m isobath (Figure 1). In this study, the saved daily results of velocity $(u, v, w)$ and the diffusion coefficient $(k)$ were used to calculate the $\overline{\theta}$ offline. In the calculation, the initial value of $\overline{\theta}$ is set to zero in the computational domain and it was integrated backward

in time (from the present to the past) with the reversed flow [35,36]. Along the boundary of simulation domain, the $\overline{\theta}$ was set as zero, which indicates that after leaving the simulation domain, the water does not come back.

Besides using the $\overline{\theta}$, to reveal the transport pattern, the Lagrangian TRANSport model (LTRANS v.2b), which is a popular off-line three-dimensional particle tracking module [37–39] was used to track the motion of water parcels in a Lagrangian manner to identify the areas where water parcels gather. The fourth-order Runge–Kutta scheme was applied for particle advection and reflective boundary conditions were used to treat the particles that hit the solid boundaries. The effects of vertical and horizontal turbulence are considered by the random displacement model using the diffusivity coefficient from the hydrodynamic simulation [40,41]. Particles were released on each computational grid every 5 days during the simulation.

## 3. Results and Discussion

### *3.1. Shelf Circulation*

In order to gain a comprehensive understanding of the hydrodynamic factors influencing water exchanges, we first examined the circulation patterns within the computational domain, focusing on climatologically averaged conditions for the distinct periods of summer and winter (Figure 2). The hydrodynamic variations between these seasons are pivotal for interpreting the mechanisms driving water exchange.

The circulation patterns in the NSCS shelf exhibit marked seasonal variations, closely linked to monsoonal influences and regional geomorphological features (Figure 2), meanwhile the Kuroshio intrusion through the Luzon Strait fosters a cyclonic slope current that serves as the dynamic boundary delineating the shelf circulation [42]. During the summer, the shelf current is directed northeastward under the influences of the southwesterly monsoon. Along the Yuexi coast that to the west of PRE, the northwestward coastal current to the west of PRE was largely reduced under the influence of the westward expanded plume from PRE. The river plume that comes from the PRE is mainly affected by the winds that drive currents along the coast. Additionally, the natural buoyancy within the plume plays a crucial role in altering the circulation of water both along the shore and across the shelf, especially in the upper layers of the water column. At the estuary mouth, the interaction of Pearl River Plume and shelf current induced the intrusion of shelf current [43,44]. It is also noticed that, during summer, the cyclonic slope current intruded into the shelf through the region to the southeast of Hainan Island and joined the shelf current (Figure 2a). On the surface, the complicated cross-isobath transport patterns occur around Hainan Island, but the bottom onshore intrusion prevails over the shelf due to the flow-topography interaction [10,45] (Figure 2c,d). Conversely, during winter, the shelf current intensifies and assumes a southwestward flow. Associated with the intensified northeast wind, the surface water mainly features the onshore intrusion, while the strong bottom offshore transport covers the whole shelf (Figure 2e,f), particularly to the southeast of Hainan Island. The cross-shelf velocities are instrumental in establishing the dynamic connection between the shelf current and the basin-wide circulation [26,46], and these velocities, combined with the observed seasonal circulation patterns, emphasize the complex interplay between shelf and basin dynamics in the region.

The Beibu Gulf, linked to the broader shelf via the Qiongzhou Strait, presents a less clear picture. The majority of evidence suggests a predominance of cyclonic and anticyclonic gyres controlling the circulation within the gulf [47,48]. However, during summer, currents weaken considerably, leading to a reduced water exchange capacity within the Beibu Gulf, contrasting with the well-defined gyres of winter. The complexity of these seasonal circulation patterns underscores the need for nuanced understanding when considering hydrodynamic impacts on water exchanges in the NSCS.

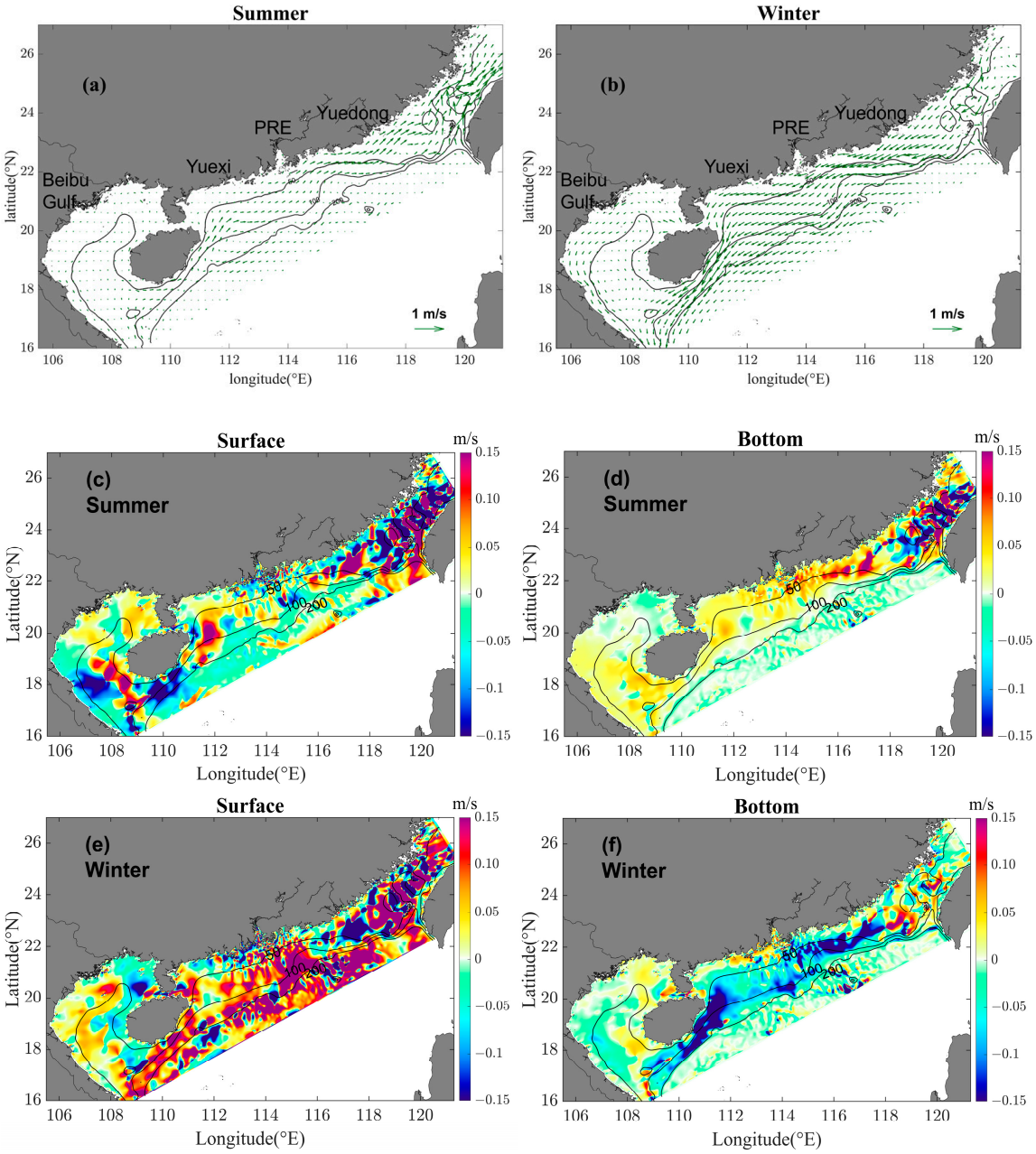


**Figure 2.** (**a**) Horizontal map of the depth-averaged shelf current in summer. (**b**) Same as (**a**), but for winter. (**c**,**d**) Summer cross isobath velocity (m/s) in surface and bottom, respectively, positive and negative values indicate the onshore and offshore motions, respectively. (**e**,**f**) Same as (**c**,**d**) but for winter.

### *3.2. Seasonal Variability of the* $\overline{\theta}$

The Figure 3a depicts the spatial pattern of the annual mean $\overline{\theta}$ in the NSCS. Generally, the longest $\overline{\theta}$ with the magnitude of ~300 days is observed in the nearshore areas of the Beibu Gulf and the Yuexi shelf, where the circulation is relatively weaker (Figure 2a,b). Then it gradually decreases towards the outer shelf which correlates inversely with water depth and decreases northeastwardly from Beibu Gulf towards the Yuedong regions. In order to comprehensively examine the variability of $\overline{\theta}$, we conducted an Empirical Orthogonal Function (EOF) analysis. The dominant mode (Figure 3b), referred to as EOF-01, emerges as particularly significant, accounting for a substantial portion (47.5%) of the overall variance. In contrast, the subsequent modes each make relatively modest contributions, with each of them accounting for less than 15% of the total variance.

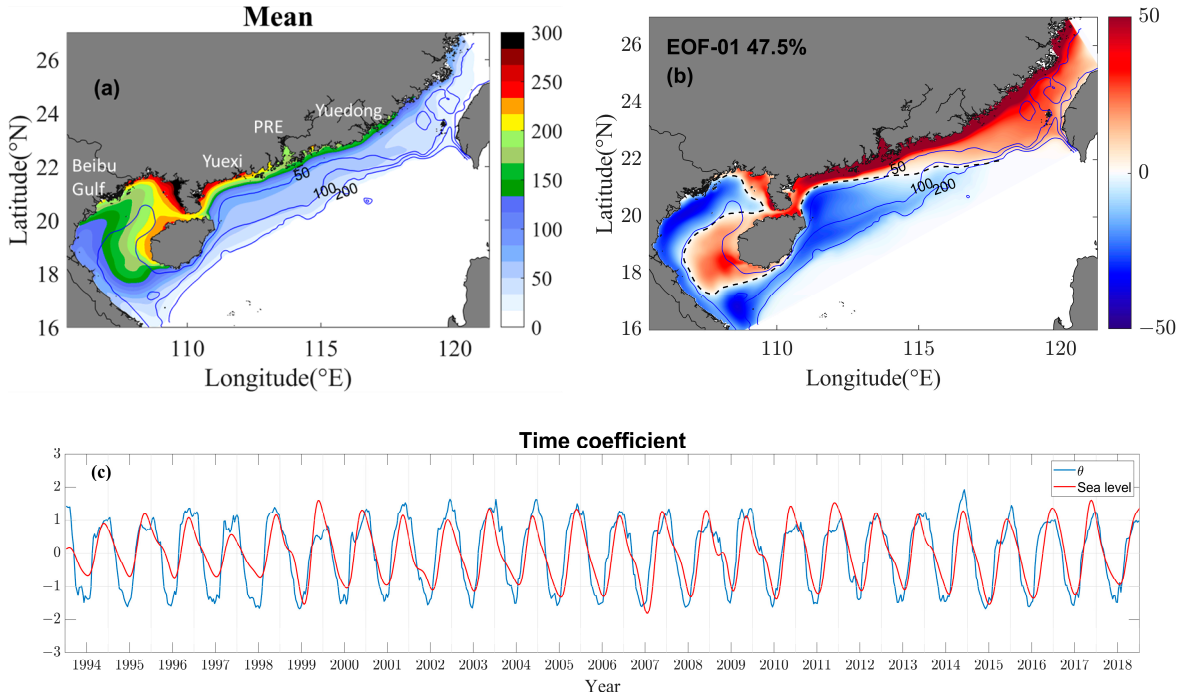


**Figure 3.** (**a**) The annual mean distribution of the depth-averaged $\overline{\theta}$ in NSCS. (**b**) EOF leading mode of $\overline{\theta}$. (**c**) Time coefficient of the leading mode of $\overline{\theta}$ and time coefficient of the leading mode of sea level.

The magnitude of $\overline{\theta}$ anomalies exhibit an increasing trend, transitioning from the outer shelf towards the inner shelf and coastal areas, particularly in the Beibu Gulf. It is also noted that a positive anomaly appears in the northeast corner of the Beibu Gulf, mirroring the anomaly observed in the coastal region of the shelf. This suggests a potential connection of circulations between the Beibu Gulf and the broader shelf region. Temporally, the time coefficient associated with EOF-01 exhibits clear seasonal fluctuations on an annual scale (Figure 3c). Compared with the time coefficient of the EOF-01 of sea level in NSCS, there is minimal time lag, indicating an almost immediate response of the water exchange rate to the hydrodynamic conditions. Seasonal variations in $\overline{\theta}$ are marked by lower values during the summer, in line with decreased sea levels, and higher values during the winter, corresponding with elevated sea levels.

To check the seasonality of the $\overline{\theta}$ in the NSCS, it was averaged in the summer and winter time during the simulation period. During the summer months, the robust northeastward shelf current initiates an active water exchange (Figure 2a), the substance released in the northeast shelf can leave the NSCS rapidly through the Taiwan Strait, thus diminishing $\overline{\theta}$ values along the northeast shelf. From the Taiwan Strait, there is a notable southwestward increase to approximately 200 days near Qiongzhou Strait (Figure 4a). The Beibu Gulf experiences complex interactions between anti-cyclonic circulation in its southern reaches and cyclonic circulation in the north (Figure 2a), causing $\overline{\theta}$ values to rise from the mouth of the bay toward the gulf's northeast and reach the largest exceeding 300 days. Meanwhile, the water motion is relatively weak, and induces the larger values $\overline{\theta}$ at the top of the Beibu Gulf.

In contrast, during winter, the distribution of $\overline{\theta}$ exhibits roughly opposite patterns (Figure 4b). The southwestward coastal current carries water into the Beibu Gulf via the Qiongzhou Strait (Figure 2b), resulting in a zonal distribution along the coastline of Guangdong Province. In the Beibu Gulf, a gulf-scale cyclonic circulation that is nested with a cyclonic gyre in the southern gulf emerges in winter [49]. The southwestward shelf current formed a strong jet at the southeast of Hainan Island and flow westward, then, it enters the Beibu gulf from the southwest side of Hainan Island and exits through the southern coastal region of Vietnam (Figure 2b), consequently, this circulation leads to low values of $\overline{\theta}$

along the eastern coast of Vietnam. Furthermore, the gulf-scale cyclonic gyre, extending northeastward, facilitates the transport of substances released in the northwest coast region of Hainan Island to the northern Gulf, where they may persist for an extended period.

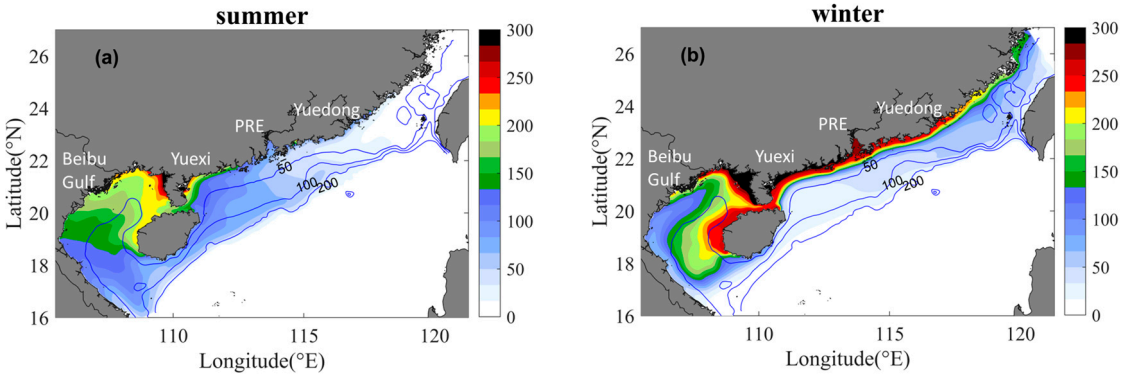


**Figure 4.** (**a**) Depth averaged exposure time in summer ($\bar{\theta}$, Days). (**b**) Depth averaged exposure time in winter ($\bar{\theta}$, Days).

The cross-isobath transport plays a pivotal role in establishing hydrodynamic connections between the open ocean and coastal regions, which shows quite significant vertical changes in coastal regions (Figure 2c–f), thus may have different contribution to the water/mass cycle vertically. The $\bar{\theta}_{VD}$ ($\bar{\theta}_{bottom} - \bar{\theta}_{surface}$) serves as a more direct and effective indicator for illustrating the cumulative effects of vertically varying cross-shore motions and displays the clear seasonality.

During summer with prevailing southwest wind forcing, the coastal region experiences substantial surface offshore transport and bottom onshore intrusion (Figure 2c,d). While, despite the prevalence of strong vertically contrasting cross-isobath transport over the shelf, most locally intensified cross-isobath motions do not lead to significant changes in the water exchange rate in the water column. Mainly over the region to the east of Hainan Island and the mouth of Beibu Gulf, the bottom intrusion induces the net increase of the $\bar{\theta}$ (Figure 5a). Over those regions, the bottom water spends approximately 50 days longer time in the NSCS than surface water.

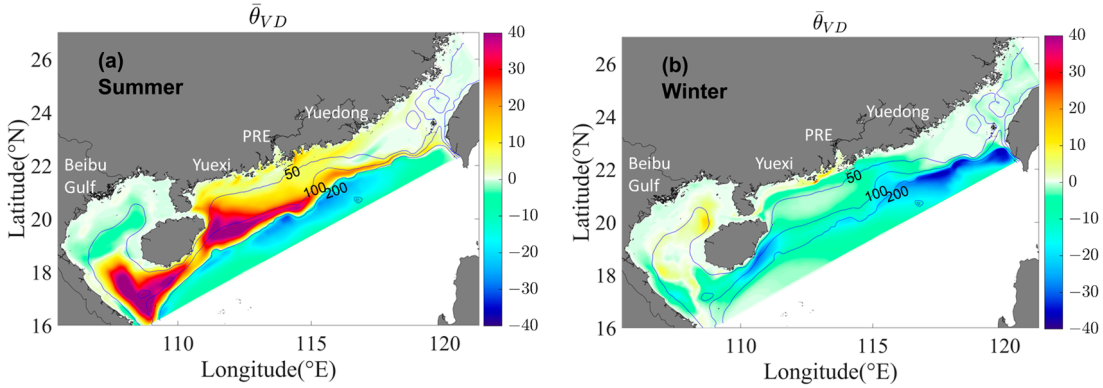


**Figure 5.** (**a**,**b**) horizontal distribution of $\bar{\theta}_{VD}$ (day) in summer and winter, respectively.

In contrast, during winter with northeast wind forcing and intensified southwest shelf current, it mainly features the surface onshore intrusion and bottom offshore transport, particularly over the southeast of Hainan Island and shelf out of PRE. Thus, the downwelling results in the exchange rate of the bottom water being slightly faster than the surface water with the negative $\bar{\theta}_{VD}$ over the whole shelf NSCS (Figure 5b). However, although the magnitude of the cross-isobath transport is stronger in comparison with the summer, the magnitude of the negative $\bar{\theta}_{VD}$ is much smaller. The large $\bar{\theta}_{VD}$ is only observed near the 200 m isobath and southeast side of Hainan Island.

### 3.3. Transport Pattern Inferred from $\overline{\theta}_i$

To further check how water moves in the entire NSCS, we examined the time spent in various subdomains before the water finally leaves the NSCS. Based on the topographic and hydrodynamic features, the NSCS was divided into four regions: The Beibu Gulf region (Region A), the semi-closed gulf separated from the vast shelf by Hainan Island. Yuexi region (Region B), the hydrodynamic structure is largely influenced by interaction of the monsoon and Pearl River Plume. PRE region (Region C), where the Pearl River pours fresh water into the NSCS. Yuedong region (Region D), with widen shelf and active Yuedong upwelling (Figure 6). Then, $\overline{\theta}_A - \overline{\theta}_D$, which represents the time of water spent in the four subdomains, was calculated based on Equation (1) by setting $\delta_\omega$ to 1 in each subdomain [50].

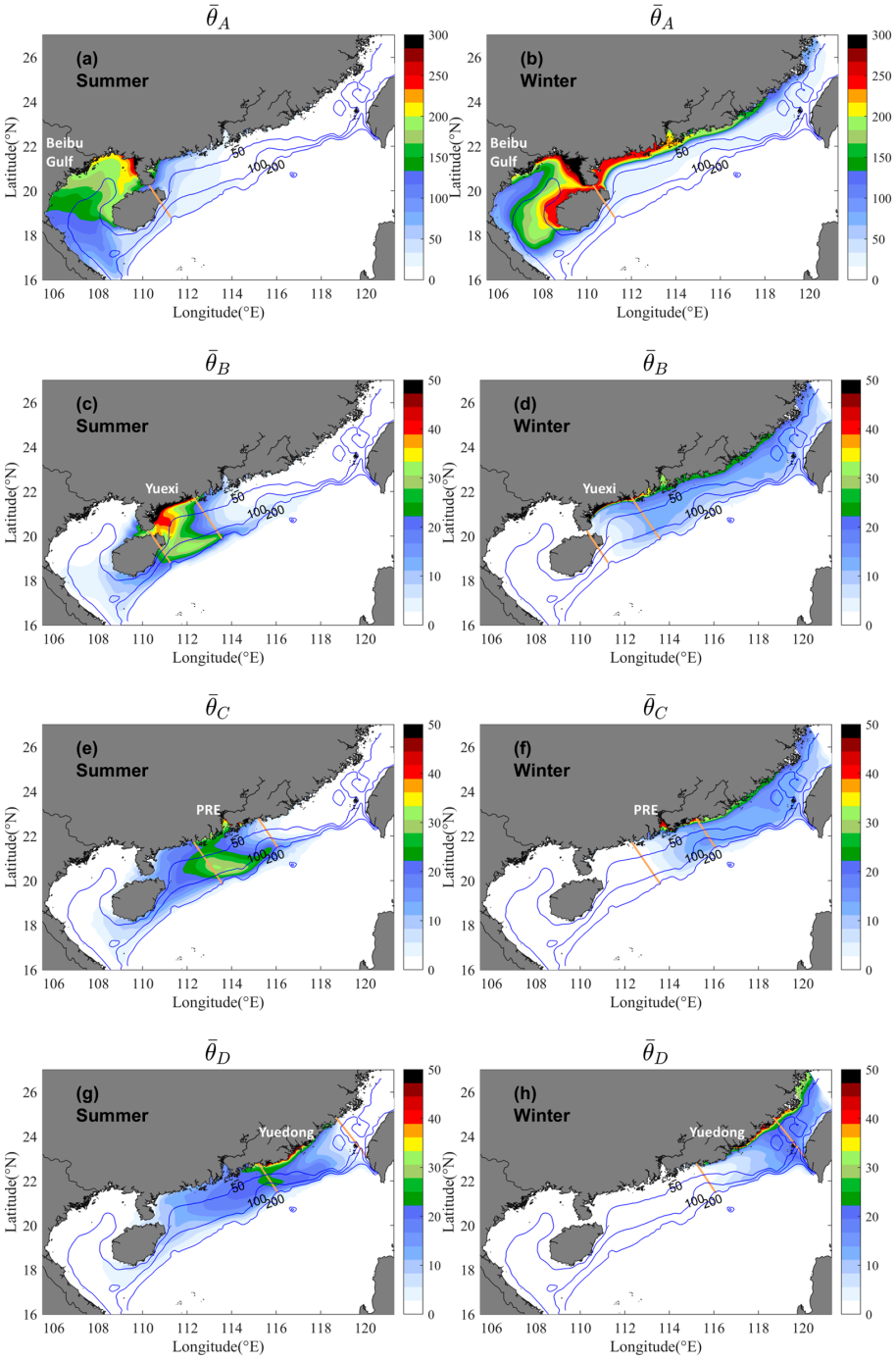


**Figure 6.** Depth-averaged partial exposure time in summer and winter, respectively ($\overline{\theta}_A - \overline{\theta}_D$, day).

As shown in Figure 6, in the semi-closed Beibu Gulf, the water motions are limited and water exchange rate are relatively low, thus lead to a pronounced increase of $\overline{\theta}_A$, which indicates the time of water stayed in Beibu Gulf is relatively long than the other regions. The $\overline{\theta}_A$ increases from 50 days at the mouth of the gulf to exceed 300 days in the northeast (Figure 6a,b) in both summer and winter, and it has larger contribution to the total $\overline{\theta}$. Outside the Beibu Gulf, in summer, there is an extension of $\overline{\theta}_A$ (~50 days) towards the PRE, potentially indicates a southwestward movement along the coast that against summer wind. Another branch of extension of $\overline{\theta}_A$ expanded along the 100 isobath, indicates the westward transport due to the stable slope current. In winter, high values of $\overline{\theta}_A$ could spread to the coastal areas of Region D, which suggests that, by overriding the shelf current, waters from distant coastal region can arrive the Beibu Gulf.

In Region B-D, the magnitude of the $\overline{\theta}_B \sim \overline{\theta}_D$ is generally shorter than 50 days which represent a much stronger exchanging rate with the open ocean. Spatially, they exhibit a similar pattern, with their magnitudes progressively escalating from the outer shelf towards the inner shelf, and the highest values primarily concentrated along the coastal areas. There is also notably seasonality of $\overline{\theta}_i$ that under the influence of the northeasterly/southwesterly monsoon during summer/winter, non-zero regions of the $\overline{\theta}_B \sim \overline{\theta}_D$ appear in the upstream regions. Besides, it is also noted that during summertime, the $\overline{\theta}_B$ and $\overline{\theta}_C$ have high values on the vicinity of the 100-m isobath line on the outer shelf, although there are quite close to the boundary of NSCS. It suggests a notable onshore exchange of water between the outer shelf and the coastal zones in region B and C during summertime.

Based on the values of $\overline{\theta}_i$ in regions A–D, we could examine the contribution of each $\overline{\theta}_i$ to the overall $\overline{\theta}$ (Figure 7). The $x$ axis and $y$ axis of the bar charts in Figure 7 indicates the different subdomain and the various $\overline{\theta}_i$, respectively. During summer (Figure 7a), generally, it shows substantial contribution of the initial release locations, which means the substance released on the shelf trends to stay in the initial release locations for longer time. Such as the contribution of $\overline{\theta}_A$ exceeds 80% in region A itself. The large contribute of $\overline{\theta}_A$ in Region B and C illustrates a quite strong westward transport, contrary to the prevailing wind and shelf current direction. Even under the northeastward wind forcing and shelf current, the $\overline{\theta}_A$ accounts for approximately 30% and 20% in regions B and C, respectively. In winter (Figure 7b), the strong southwestward shelf current significantly influences the distribution. The $\overline{\theta}_A$ which means the time stay inside the Beibu Gulf, has a significant contribution to all the subdomains, with ratios exceeding 50% in regions B and C and. Even in the region D that quite away from Beibu Gulf, contributions from $\overline{\theta}_A$ reaches 50%. This illustrates the extensive interaction facilitated by shelf circulation, suggesting that the Beibu Gulf marine environment could be affected by the entire NSCS shelf regions.

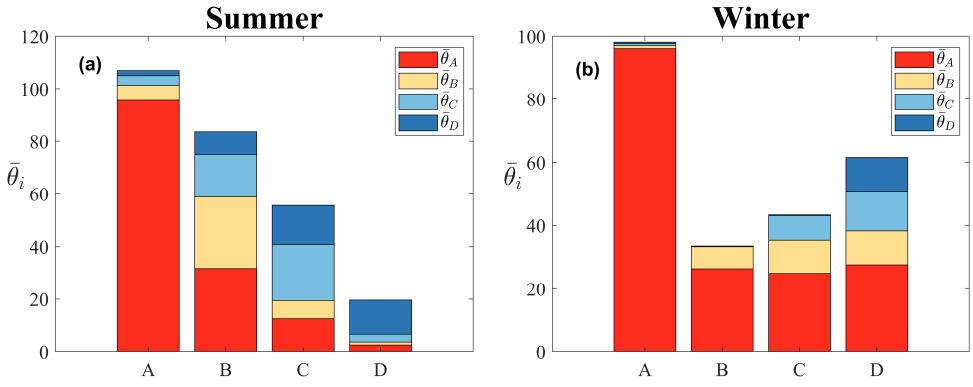


**Figure 7.** (**a**) Contribution of $\overline{\theta}_A - \overline{\theta}_D$ in different subdomains. Region A is the Beibu Gulf, Region B is the Yuexi Region, Region C is the PRE region, and Region D is the Yuedong Region. (**b**) Same as (**a**) but for winter.

To confirm the westward transport against the wind during summer, we checked the detailed distribution of summer $\overline{\theta}_A$ over the shelf of NSCS. Two branches of extension

of $\overline{\theta}_A$ can be identified (Figure 8a): the first branch extends from the Qiongzhou Strait and eventually reaches to the PRE under the influence of plume, and the second branch expands roughly along100–200 m isobaths which shows the influences of slope current. The Lagrangian tracking provides an alternative perspective for observing the transport structure and connectivity within the NSCS, particularly the westward transport during summer. Figure 8b shows the examples of the summertime trajectories that were released in PRE regions. Along the coast, the expansion of the Pearl River Plume could carry the particles westward, passing through the Yuexi region and finally entering the Beibu Gulf through the Qiongzhou Strait even under the southwest summer wind. Simultaneously, parts of particles released on the vast shelf flow southwestward carried by the slope current (Figure 2a). However, as they approach Hainan Island, some of these particles change direction, move shoreward and eventually become entrapped by the plume. Those particles entered the Beibu Gulf through the Qiongzhou Strait. The remaining particles continue their westward trajectory along the cyclonic slope current and enter the Beibu Gulf from the southern side of Hainan Island. As shown in the previous studies, the ADCP observation and the drifter derived velocity illustrate the southwestward velocity over slope during summer [51,52], which give indirect evidence of this westward transport.

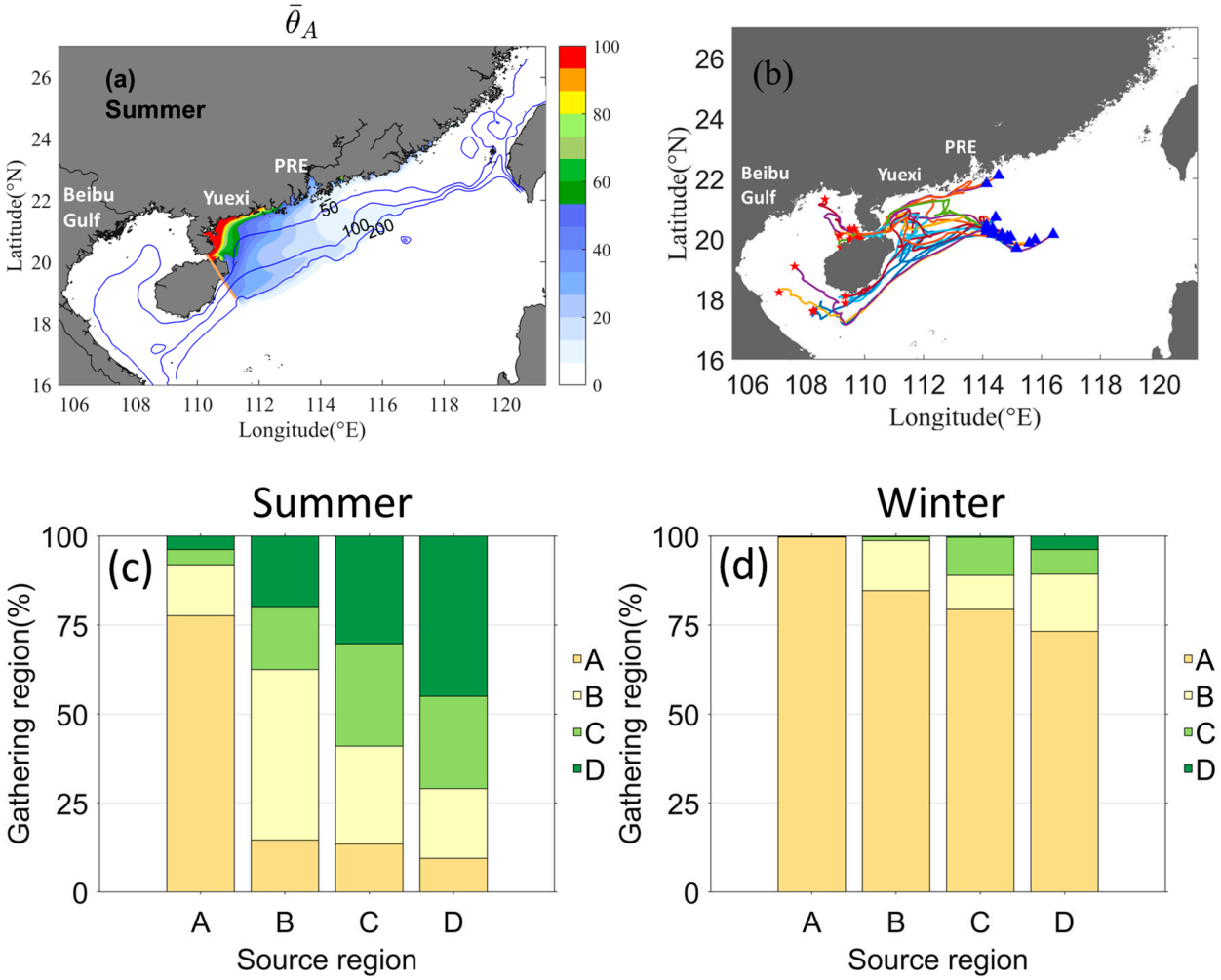


**Figure 8.** (**a**) Depth-averaged $\overline{\theta}_A$ in summer but ignored the values in Beibu Gulf. (**b**) The trajectories of particles released in the summer. The blue triangles and red stars denote the locations of particles on the 0, 60 days after their release, respectively. (**c**,**d**) Distribution of the particles that released from different regions during summer and winter.

Utilizing the outcomes from Lagrangian tracking, we conducted a statistical analysis of the distribution of particles initially released in different regions (Figure 8c,d). Similar as that obtained from $\overline{\theta}_i$ (Figure 7), during summer with a northeastward shelf current, the particles tend to accumulate in their original release regions and downstream areas. Notably, some particles from Regions B and C ultimately migrate and settle in the Beibu Gulf, following the westward transport pathways depicted in Figure 8b. During the winter, Lagrangian tracking similarly indicates that the majority of particles in the NSCS eventually move to the Beibu Gulf. The distributions of released particles (Figure 8c,d) differ somewhat from the contributions of $\overline{\theta}_i$ (Figure 7) in each subdomain. However, they exhibit a quite similar pattern, suggesting that the results based on exchange times can effectively reveal the predominant transport structures under complicated hydrodynamical processes.

## 4. Conclusions

In this study, we investigated the spatio-temporal variability of three-dimensional water exchanges under the complex hydrodynamic conditions in NSCS and explored the connectivity among the shelf. Spatially, the annual mean exposure time $\overline{\theta}$ increased from ~30 days over the 200 m isobath to more than 150 days in the coastal region (<50 m), with the largest values occurring at the north of the Beibu Gulf. Seasonally, the water exchange rate shows an immediate response to hydrodynamic conditions. Driven by the monsoon, the strong shelf current triggered a vigorous exchange of water on the northwestern shelf, the horizontal distribution of $\overline{\theta}$ on the board shelf except Beibu Gulf during winter and summer. The distribution of $\overline{\theta}$ in the Beibu Gulf was affected by the seasonally varying cyclonic circulation in the Gulf. However, the largest values in the northeast of the Beibu Gulf were maintained despite of the seasons due to its semi-enclosed nature and restricted water motions. This contrasts with the regions outside the gulf where the water exchange rate is higher, with lower $\overline{\theta}$ suggesting a more dynamic interaction with the open ocean. Vertically, the local vertical contrasting cross-isobath transport did not induce strong vertical changes in net water exchanges, except in several particular regions. Summer months are dominated by substantial surface offshore transport against a counteracting bottom onshore intrusion, while significant positive $\overline{\theta}_{VD}$ (~50 days) mainly occurs east of Hainan Island and at the Beibu Gulf's mouth. During winter, however, the dynamic reverses under the influence of the northeast winds and the intensified southwest shelf current, promoting slightly faster bottom water exchange rates.

Both in summer and winter, the contribution ratio of $\overline{\theta}$ in Beibu Gulf to the NSCS shelf is conspicuous. This area significantly affects adjacent regions, hinting at westward movement against typical currents in summer. Notably, the westward transport is important for water exchange throughout the NSCS, contributing to more than 20% of the time of water exchange over almost the entire shelf, which illustrates the potential influence of the westward spreading of the Pearl River freshwater conjunction with the stable slope current. In winter, the Gulf's influence extends across all regions, with its retention characteristics contributing up to 50% even to distant areas, showing its broad impact on the NSCS's water dynamics throughout the year. It should be noted that the exposure time is a measure of the overall effect of water movement processes, and the research would benefit from including actual measurements. It would enhance our understanding of water exchange rates and transport patterns.

**Author Contributions:** Conceptualization, T.Z. and Z.C.; Data curation, L.C. and M.L.; Investigation, L.C. and M.L.; Methodology, T.Z.; Supervision, Z.C.; Writing—original draft, L.C.; Writing—review & editing, T.Z. and Z.C. All authors have read and agreed to the published version of the manuscript.

**Funding:** This work was funded by the Science and Technology Development Fund, Macau SAR (File/Project no. 0093/2020/A2 and SKL-IOTSC-2021-2023; SKL-IoTSC(UM)-2021-2023/ORPF/A20/2022); National Natural Science Foundation of China (NSFC) under Project (42076026), Independent Research Project Program of State Key Laboratory of Tropical Oceanography (LTOZZ2102).

**Data Availability Statement:** The data used during the current study is available from the corresponding author on reasonable request.

**Acknowledgments:** This work is supported by CORE which is a joint research centre for ocean research between Laoshan Laboratory and HKUST. This work was performed in part at the SICC, which is supported by the SKL-IOTSC, University of Macau. This work is partly supported by COASTAL-SOS, a project endorsed by UN Decade of Ocean Science for Sustainable Development.

**Conflicts of Interest:** The authors declare no conflict of interest.

## References

1. Cai, Z.; Liu, G.; Liu, Z.; Gan, J. Spatiotemporal variability of water exchanges in the Pearl River Estuary by interactive multiscale currents. *Estuar. Coast. Shelf Sci.* **2022**, *265*, 107730. [CrossRef]
2. Zu, T.; Gan, J. A numerical study of coupled estuary–shelf circulation around the Pearl River Estuary during summer: Responses to variable winds, tides and river discharge. *Deep Sea Res. Part II Top. Stud. Oceanogr.* **2015**, *117*, 53–64. [CrossRef]
3. Lai, W.; Pan, J.; Devlin, A.T. Impact of tides and winds on estuarine circulation in the Pearl River Estuary. *Cont. Shelf Res.* **2018**, *168*, 68–82. [CrossRef]
4. Shang, J.; Sun, J.; Tao, L.; Li, Y.; Nie, Z.; Liu, H.; Chen, R.; Yuan, D. Combined Effect of Tides and Wind on Water Exchange in a Semi-Enclosed Shallow Sea. *Water* **2019**, *11*, 1762. [CrossRef]
5. Hart, J.A.; Phlips, E.J.; Badylak, S.; Dix, N.; Petrinec, K.; Mathews, A.L.; Green, W.; Srifa, A. Phytoplankton biomass and composition in a well-flushed, sub-tropical estuary: The contrasting effects of hydrology, nutrient loads and allochthonous influences. *Mar. Environ. Res.* **2015**, *112 Pt A*, 9–20. [CrossRef]
6. Ryther, J.H.; Dunstan, W.M. Nitrogen, Phosphorus, and Eutrophication in the Coastal Marine Environment. *Science* **1971**, *171*, 1008–1013. [CrossRef] [PubMed]
7. Li, D.; Gan, J.; Hui, C.; Yu, L.; Liu, Z.; Lu, Z.; Kao, S.; Dai, M. Spatiotemporal Development and Dissipation of Hypoxia Induced by Variable Wind-Driven Shelf Circulation off the Pearl River Estuary: Observational and Modeling Studies. *J. Geophys. Res. Oceans* **2021**, *126*, e2020JC016700. [CrossRef]
8. Li, D.; Gan, J.; Hui, R.; Liu, Z.; Yu, L.; Lu, Z.; Dai, M. Vortex and Biogeochemical Dynamics for the Hypoxia Formation Within the Coastal Transition Zone off the Pearl River Estuary. *J. Geophys. Res. Oceans* **2020**, *125*, e2020JC016178. [CrossRef]
9. Shu, Y.; Wang, D.; Feng, M.; Geng, B.; Chen, J.; Yao, J.; Xie, Q.; Liu, Q. The Contribution of Local Wind and Ocean Circulation to the Interannual Variability in Coastal Upwelling Intensity in the Northern South China Sea. *J. Geophys. Res. Oceans* **2018**, *123*, 6766–6778. [CrossRef]
10. Gan, J.; Cheung, A.; Guo, X.; Li, L. Intensified upwelling over a widened shelf in the northeastern South China Sea. *J. Geophys. Res.* **2009**, *114*, C09019. [CrossRef]
11. Ou, S.; Zhang, H.; Wang, D.-X. Dynamics of the buoyant plume off the Pearl River Estuary in summer. *Environ. Fluid Mech.* **2009**, *9*, 471–492. [CrossRef]
12. Pan, J.; Gu, Y.; Wang, D. Observations and numerical modeling of the Pearl River plume in summer season. *J. Geophys. Res. Oceans* **2014**, *119*, 2480–2500. [CrossRef]
13. Shi, W.; Huang, Z.; Hu, J. Using TPI to Map Spatial and Temporal Variations of Significant Coastal Upwelling in the Northern South China Sea. *Remote Sens.* **2021**, *13*, 1065. [CrossRef]
14. Jiang, R.; Wang, Y.-S. Modeling the ecosystem response to summer coastal upwelling in the northern South China Sea. *Oceanologia* **2018**, *60*, 32–51. [CrossRef]
15. Dong, L.; Su, J.; Ah Wong, L.; Cao, Z.; Chen, J.-C. Seasonal variation and dynamics of the Pearl River plume. *Cont. Shelf Res.* **2004**, *24*, 1761–1777. [CrossRef]
16. Gao, J.; Shi, M.; Chen, B.; Guo, P.; Zhao, D. Responses of the circulation and water mass in the Beibu Gulf to the seasonal forcing regimes. *Acta Oceanol. Sin.* **2014**, *33*, 1–11. [CrossRef]
17. Quan, Q.; Liu, Z.; Sun, S.; Cai, Z.; Yang, Y.; Jin, G.; Li, Z.; Liang, X.S. Influence of the Kuroshio Intrusion on Deep Flow Intraseasonal Variability in the Northern South China Sea. *J. Geophys. Res. Oceans* **2021**, *126*, e2021JC017429. [CrossRef]
18. Gao, X.; Zhao, G.; Zhang, C.; Wang, Y. Modeling the exposure time in a tidal system: The impacts of external domain, tidal range, and inflows. *Environ. Sci. Pollut. Res.* **2018**, *25*, 11128–11142. [CrossRef]
19. Cucco, A.; Umgiesser, G. Modeling the Venice Lagoon residence time. *Ecol. Model.* **2006**, *193*, 34–51. [CrossRef]
20. Du, J.; Shen, J. Water residence time in Chesapeake Bay for 1980–2012. *J. Mar. Syst.* **2016**, *164*, 101–111. [CrossRef]
21. Liu, Z.; Wei, H.; Liu, G.; Zhang, J. Simulation of water exchange in Jiaozhou Bay by average residence time approach. *Estuar. Coast. Shelf Sci.* **2004**, *61*, 25–35. [CrossRef]
22. Deleersnijder, E.; Campin, J.-M.; Delhez, E.J. The concept of age in marine modelling: I. Theory and preliminary model results. *J. Mar. Syst.* **2001**, *28*, 229–267. [CrossRef]
23. Ren, Y.; Lin, B.; Sun, J.; Pan, S. Predicting water age distribution in the Pearl River Estuary using a three-dimensional model. *J. Mar. Syst.* **2014**, *139*, 276–287. [CrossRef]
24. Cui, L.; Cai, Z.; Liu, Z. Water exchange and transport pathways in estuary-shelf region of Pearl River Estuary under multiple forcings. *Cont. Shelf Res.* **2023**, *266*, 105099. [CrossRef]

25. Zhang, H.; Cheng, W.; Chen, Y.; Shi, Z.; Gong, W.; Liu, S. Importance of large-scale coastal circulation on bay-shelf exchange and residence time in a subtropical embayment, the northern South China Sea. *Ocean Coast. Manag.* **2019**, *168*, 72–89. [CrossRef]
26. Liu, Z.; Zu, T.; Gan, J. Dynamics of cross-shelf water exchanges off Pearl River Estuary in summer. *Prog. Oceanogr.* **2020**, *189*, 102465. [CrossRef]
27. Shchepetkin, A.F.; McWilliams, J.C. The regional oceanic modeling system (ROMS): A split-explicit, free-surface, topography-following-coordinate oceanic model. *Ocean Model.* **2005**, *9*, 347–404. [CrossRef]
28. Song, Y.; Haidvogel, D. A semi-implicit ocean circulation model using a generalized topography-following coordinate system. *J. Comput. Phys.* **1994**, *115*, 228–244. [CrossRef]
29. Mellor, G.L.; Yamada, T. Development of a turbulence closure model for geophysical fluid problems. *Rev. Geophys.* **1982**, *20*, 851–875. [CrossRef]
30. Egbert, G.D.; Erofeeva, S.Y. Efficient inverse modeling of barotropic ocean tides. *J. Atmos. Ocean. Technol.* **2002**, *19*, 183–204. [CrossRef]
31. Zu, T.; Gan, J.; Erofeeva, S.Y. Numerical study of the tide and tidal dynamics in the South China Sea. *Deep Sea Res. Part I Oceanogr. Res. Pap.* **2008**, *55*, 137–154. [CrossRef]
32. Deng, Y.; Liu, Z.; Zu, T.; Hu, J.; Gan, J.; Lin, Y.; Li, Z.; Quan, Q.; Cai, Z. Climatic Controls on the Interannual Variability of Shelf Circulation in the Northern South China Sea. *J. Geophys. Res. Oceans* **2022**, *127*, e2022JC018419. [CrossRef]
33. Brauwere, A.d.; de Brye, B.; Blaise, S.; Deleersnijder, E. Residence time, exposure time and connectivity in the Scheldt Estuary. *J. Mar. Syst.* **2011**, *84*, 85–95. [CrossRef]
34. Delhez, É.J.M.; Deleersnijder, É. The boundary layer of the residence time field. *Ocean Dyn.* **2006**, *56*, 139–150. [CrossRef]
35. Delhez, É.J.M.; Heemink, A.W.; Deleersnijder, E. Residence time in a semi-enclosed domain from the solution of an adjoint problem. *Estuar. Coast. Shelf Sci.* **2004**, *61*, 691–702. [CrossRef]
36. Zhang, D.Q.; Tan, S.K.; Gersberg, R.M. Municipal solid waste management in China: Status, problems and challenges. *J. Environ. Manag.* **2010**, *91*, 1623–1633. [CrossRef] [PubMed]
37. North, E.W.; Adams, E.E.; Schlag, Z.; Sherwood, C.R.; He, R.; Hyun, K.H.; Socolofsky, S.A. Simulating Oil Droplet Dispersal from the Deepwater Horizon Spill with a Lagrangian Approach. In *Monitoring and Modeling the Deepwater Horizon Oil Spill: A Record-Breaking Enterprise*; American Geophysical Union: Washington, DC, USA, 2011; pp. 217–226. [CrossRef]
38. Chu, N.; Liu, G.; Xu, J.; Yao, P.; Du, Y.; Liu, Z.; Cai, Z. Hydrodynamical transport structure and lagrangian connectivity of circulations in the Pearl River Estuary. *Front. Mar. Sci.* **2022**, *9*, 996551. [CrossRef]
39. Liang, J.-H.; Liu, J.; Benfield, M.; Justic, D.; Holstein, D.; Liu, B.; Hetland, R.; Kobashi, D.; Dong, C.; Dong, W. Including the effects of subsurface currents on buoyant particles in Lagrangian particle tracking models: Model development and its application to the study of riverborne plastics over the Louisiana/Texas shelf. *Ocean Model.* **2021**, *167*, 101879. [CrossRef]
40. North, E.; Hood, R.; Chao, S.-Y.; Sanford, L. Using a random displacement model to simulate turbulent particle motion in a baroclinic frontal zone: A new implementation scheme and model performance tests. *J. Mar. Syst.* **2006**, *60*, 365–380. [CrossRef]
41. Zhong, L.J.; Li, M. Tidal energy fluxes and dissipation in the Chesapeake Bay. *Cont. Shelf Res.* **2006**, *26*, 752–770. [CrossRef]
42. Shu, Y.; Wang, Q.; Zu, T. Progress on shelf and slope circulation in the northern South China Sea. *Sci. China Earth Sci.* **2018**, *61*, 560–571. [CrossRef]
43. Shu, Y.; Chen, J.; Yao, J.; Pan, J.; Wang, W.; Mao, H.; Wang, D. Effects of the Pearl River plume on the vertical structure of coastal currents in the Northern South China Sea during summer 2008. *Ocean Dyn.* **2014**, *64*, 1743–1752. [CrossRef]
44. Gan, J.; Li, L.; Wang, D.; Guo, X. Interaction of a river plume with coastal upwelling in the northeastern South China Sea. *Cont. Shelf Res.* **2009**, *29*, 728–740. [CrossRef]
45. Gan, J.; Wang, J.; Liang, L.; Li, L.; Guo, X. A modeling study of the formation, maintenance, and relaxation of upwelling circulation on the Northeastern South China Sea shelf. *Deep Sea Res. Part II Top. Stud. Oceanogr.* **2015**, *117*, 41–52. [CrossRef]
46. Brink, K.H. Cross-Shelf Exchange. *Annu. Rev. Mar. Sci.* **2016**, *8*, 59–78. [CrossRef] [PubMed]
47. Gao, J.; Chen, B.; Shi, M. Summer circulation structure and formation mechanism in the Beibu Gulf. *Sci. China Earth Sci.* **2014**, *58*, 286–299. [CrossRef]
48. Wu, D.; Wang, Y.; Lin, X.; Yang, J. On the mechanism of the cyclonic circulation in the Gulf of Tonkin in the summer. *J. Geophys. Res. Atmos.* **2008**, *113*, C09029. [CrossRef]
49. Gao, J.; Wu, G.; Ya, H. Review of the circulation in the Beibu Gulf, South China Sea. *Cont. Shelf Res.* **2017**, *138*, 106–119. [CrossRef]
50. Lin, L.; Liu, Z. Partial residence times: Determining residence time composition in different subregions. *Ocean Dyn.* **2019**, *69*, 1023–1036. [CrossRef]
51. Fang, W.; Guo, P.; Liu, C.; Fang, G.; Li, S. Observed sub-inertial current variability and volume transport over the continental shelf in the northern South China Sea. *Estuar. Coast. Shelf Sci.* **2015**, *157*, 19–31. [CrossRef]
52. Huang, G.; Zhan, H.; He, Q.; Wei, X.; Li, B. A Lagrangian study of the near-surface intrusion of Pacific water into the South China Sea. *Acta Oceanol. Sin.* **2021**, *40*, 15–30. [CrossRef]

water

MDPI

*Article*

# Influence of Spring Water Residence Time on the Irrigation Water Stability in the Hani Rice Terraces

**Kun Wei [1], Yuanmei Jiao [1,*], Guilin Zhang [2], Ying Wang [1] and Hua Zhang [3]**

[1] Provincial Key Laboratory of Plateau Geographic Processes and Environmental Change, Faculty of Geography, Yunnan Normal University, Kunming 650500, China; wwwweikun95@163.com (K.W.)
[2] School of Metallurgy and Materials, Wenshan University, Wenshan 663099, China
[3] Key Laboratory of Geohazard Forecast and Geoecological Restoration in Plateau Mountainous Area Plateau mountains, Ministry of Natural Resources of the People's Republic of China, Yunnan Institute of Geo-Environment Monitoring, Kunming 650216, China
* Correspondence: ymjiao@sina.com

**Abstract:** The stability of irrigation water is critical for the sustainability of alpine agriculture. Based on monthly precipitation and terraced field water and spring water samples obtained between 2015 and 2016, the study used the mean residence time and isotope mixing model to analyze the influence of spring water residence time on irrigation water stability in the Hani Rice Terraces. The results indicate that: (1) The mean residence time of precipitation and terraced field water in spring water was 2.46 years and 1.55 years, respectively, implying that the terraced field's irrigation water source could be refilled by spring water recharged 1.5–2.5 years ago. (2) The mean residence time of precipitation in ascending and descending springs was 2.73 years and 1.95 years, respectively. The mean residence time of terraced field water in ascending and descending springs was 1.54 years and 1.04 years, respectively. The ascending spring's recharge water residence time is 0.5–0.8 years longer than that of the descending spring, indicating that the spring water exhibits intra-seasonal and inter-seasonal staggered peak recharging. At the same time, the total recharge period of the ascending–descending spring is extended to 1–3 years, which means the terraced fields have a drought resistance of three years. (3) The mean residence time of precipitation and terraced field water at higher altitudes in the ascending spring is 2.52 times and 3.73 times, respectively, while in the descending spring, it is 3.36 times and 6.49 times to the lower altitude region. This means that the mean residence time of the recharge water source in the lower terraced fields was shorter, and the elevation difference between ascending and descending springs was smaller, thereby regulating the spatial homogeneous distribution of recharge water sources in the terraced fields.

**Keywords:** Hani Rice Terraces; hydrogen and oxygen isotopes; mean residence time; spring recharge-discharge ratio; the stability of irrigation water sources



**Citation:** Wei, K.; Jiao, Y.; Zhang, G.; Wang, Y.; Zhang, H. Influence of Spring Water Residence Time on the Irrigation Water Stability in the Hani Rice Terraces. *Water* **2024**, *16*, 804. https://doi.org/10.3390/w16060804

Academic Editor: Giuseppe Oliveto

Received: 3 February 2024
Revised: 28 February 2024
Accepted: 5 March 2024
Published: 8 March 2024



## 1. Introduction

Groundwater is an important freshwater resource for ecosystems and human survival [1], but it is at risk of being depleted and is difficult to regenerate as a result of the effects of global climate change, over-abstraction by humans, and pollution, especially in mountainous and irrigated agricultural areas where water resources are scarce [2–4]. Therefore, in order to achieve effective management and sustainable utilization of groundwater resources, a comprehensive scientific understanding of the sources of groundwater recharge, the transportation and transformation process of groundwater flow, and understanding the transit time of groundwater and its renewal capacity are critical to solving the above problems.

The stable isotope of hydrogen and oxygen, as a natural tracer, can be efficiently applied in the study of the water cycle [5–7]. Mean residence time (MRT) is the average time water spends in a subsurface system before it emerges as surface flow [8]. Because

biogeochemical reactions are time-dependent, MRT can provide valuable insights into the hydro-chemical systems within a watershed and the effects of the catchment recharge-discharge of water on human activities. MRT can also serve as an effective indicator of water storage, flow path, and sources [9,10]. Currently, studies on the residence time of groundwater based on stable isotopes of hydrogen and oxygen are currently being conducted to examine the interactions between various water bodies, such as surface water to groundwater, precipitation to groundwater, and soil water to groundwater. The factors influencing these interactions, including watershed area, slopes, soil depth, and physicochemical properties of the soils, have also been analyzed [8,11–16]. Generally speaking, the smaller the watershed area, the steeper the slope, and the thinner the soil layer, the shorter the water residence time and the longer the time [17].

The Honghe Hani Rice Terraces are the only rice terraces in southern China that were inscribed on the UNESCO World Heritage of Cultural Landscapes in 2013. It is mainly located in the Quanfuzhuang watershed on the leeward slopes of the southern portion of the Ailao Mountain in the southwestern region of China [18–22]. The basin has abundant precipitation with two main east–west tributaries, and the groundwater is mainly exposed by crevice springs formed by rock fissures, which is of high socio-ecological value. The rice farming system has been around for over 1300 years, and water is a key factor in sustaining the longevity of the entire farming system. The Hani terrace irrigation process is not a single rain-fed agricultural irrigation, but a composite agricultural irrigation consisting of precipitation, ditch diversion, upstream terrace water, and spring water [23–28]. However, with the globalization of society and the economy, the transformation and upgrading of the terrace industry, and the rapid development of tourism in the Hani Rice Terraces, the contradiction between people and land has become more and more obvious [19,20]. Due to the influence of global warming, precipitation in the Hani Rice Terraces decreases during the rainy season, and the terraces' primary source of water replenishment during the dry season is groundwater recharge. Local residents indiscriminately cut down the upstream forests and plant understorey cash crops under the forest's water source or economic forests such as cedar trees for the sake of economic benefits, resulting in a decline in the ability of the forest to conserve water [26–28]. However, upstream forested areas can effectively store groundwater, which will have a significant impact on groundwater recharge to terraces in midstream terrace areas [23–25]. The primary issue facing the locals is figuring out how to divide and manage water resources sensibly in order to provide water to terraced agriculture and sustain the steady growth of terraced rice growing.

Currently, research on the stability of irrigation water sources in the Hani terrace agricultural system has been carried out. Liu et al. [19], in conjunction with the local cycle of agricultural activities, indicated that high-intensity rice farming activities in the Hani Rice Terraces would increase the supply of terraced water to groundwater, thus ensuring the sustainability of rice cultivation in the terraces during the dry season. Wang et al. [24] analyzed Hani terrace structure, soil water holding capacity, and topsoil productivity, revealing that drainage of paddy terraces along with associated changes in crop and field management led to an increase in soil productivity, but degradation of terrace structures and a decrease in water holding capacity will inhibit restoration to paddy terraces. In fact, analyzed from the perspective of the water cycle, there is a time-lag effect in the process of irrigation water recharge in the Hani terraces [8–10], especially in the process of groundwater recharge-discharge. In other words, a major component affecting groundwater circulation is the periodic time or residence time of groundwater recharge sources. There are not many studies on the MRT of different water bodies in the Hani terraces. Ma et al. [25] analyzed the soil moisture residence time in the forested area of the Hani terraces and concluded that the primary determinants of the water residence time in the Hani terraces are soil depth and non-capillary porosity (macropores). However, analyzing all sources of groundwater recharge, including precipitation, surface water, and soil water, and then recharging local farmland through spring outcrops to ensure the stability of farmland water sources and the

impact of the discharge time of different spring types on the recharge of agricultural water sources has not yet been reported.

In this study, the influence of spring water residence time on irrigation water stability in the Hani Rice Terraces was the objective of the study, which was analyzed by using MRT and the isotope mixing model. The main concerns include (1) characteristics of stable hydrogen and oxygen isotopes in the various water bodies of the Hani Rice Terraces, (2) how the stability of irrigation water sources in the Hani Rice Terraces is affected by the MRT of spring recharge water sources, and (3) how the MRT of spring recharge water sources in the Hani Rice Terraces is affected by the ratio of recharge to discharge of spring water. This will offer insightful concepts for the development and use of regional water resources as well as a deeper understanding of how the water cycle process affects terraced agriculture irrigation.

## 2. Materials and Methods

### *2.1. Study Area*

The Quanfuzhuang River Basin is located in the upper reaches of the Malizhai River basin in Yuanyang County, Yunnan Province [18–24], with a latitude and longitude range of 23°05′20″–23°13′18″ N, 102°43′16″–102°50′39″ E (Figure 1a), which receives abundant precipitation and has developed two main east–west tributaries. The terraces are mainly located in the Quanfuzhuang watershed between 1475 and 1737 m above sea level. The aquifers in the basin can be divided into two categories: pore aquifers and bedrock weathering fissure aquifers. The pore aquifer is dominated by clayey soil, with pore diving and weak water enrichment, and is the relative water barrier in the area. The bedrock weathering fissure aquifer, with joints and fissures developed in the rock body and loose structure, is endowed with network fissure diving and is the main aquifer in the area. Fissure water is widely exposed in the area and there are several springs [25–28].

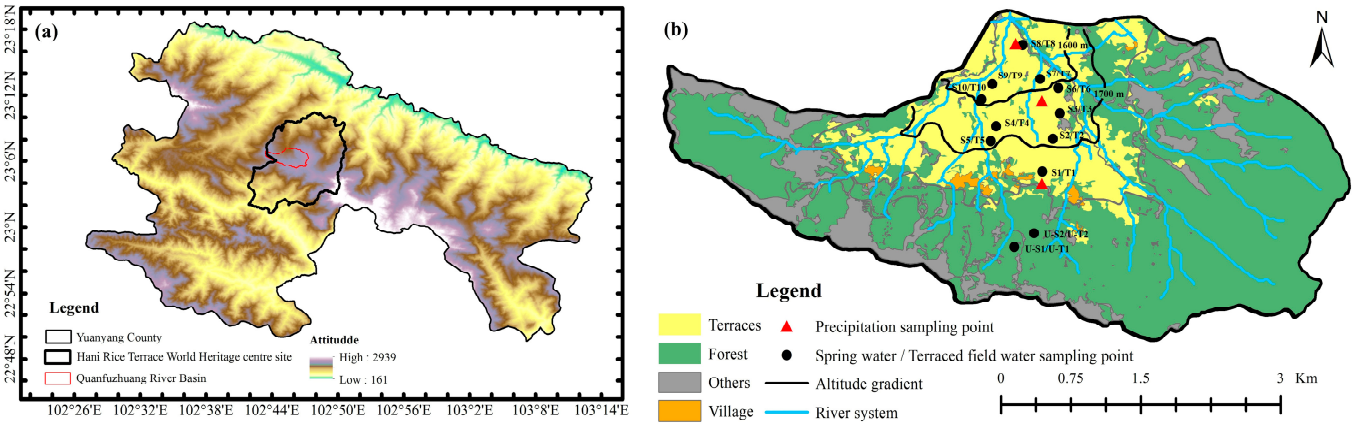


**Figure 1.** (**a**) Location and altitude of the study area; (**b**) Study area and distribution of sampling points.

### *2.2. Sample Collection and Testing*

Based on the results of our field investigations and taking into account the water isotope sampling criteria and precautions, we laid out sampling points in the terraced area at altitudes ranging from 1475 m to 1720 m above sea level. Sampling sites were selected based on the principle of selecting areas with springs and corresponding water terraces on different elevation gradient bands, while precipitation collection buckets were installed at 1508 m, 1698 m, and 1872 m near the spring sampling sites. Samples of precipitation, terrace water, and springs were collected at the end of each month from May 2015 to April 2016 (Figure 1b). Water samples were collected using 100 mL plastic bottles. The spring/terrace water samples were collected by firstly washing the sampling bottles three times with spring/terrace water, placing the sampling bottles 3–5 cm underwater, filling

them quickly, making sure that there were no air bubbles in the bottles, sealing them with sealant, labelling them, and recording the location and time of collection. Precipitation samples were collected, firstly, from reformed rain gauges (using a 15 L plastic bucket with the top converted into a plastic funnel with ping pong balls), and secondly, at the end of each month from the reformed rain gauges, in the same way that the spring/terrace water samples were collected. The hydrogen and oxygen isotope tests were conducted in the Key Laboratory of Plateau Lake Ecology and Global Change, Yunnan Normal University. Using a Picarro L2130-i ultra-high precision liquid water and moisture isotope analyzer, the measurement accuracy of $\delta^{18}O$ and $\delta^{2}H$ was ±0.1‰ and ±0.5‰, respectively [19,23]. In this study, according to the hydrodynamic nature of the springs in the terraced area when they were exposed [29,30], the exposed springs were classified into ascending springs (S3, S9, S10), which showed an upward movement under hydrostatic pressure, and descending springs (S1, S2, S4, S5, S6, S7, S8), which were overflowed and formed under the action of gravity.

### 2.3. Mean Residence Time (MRT)

With a watershed area of roughly 13.92 $km^2$ and a slope ranging from 17° to 58°, the Hani Rice Terraces are primarily composed of rice soils with thick soil layers and brief residence times for various water bodies. Therefore, sine-wave curves are used in this study, which favor the estimation of the MRT of younger water bodies. The MRT in the local water circulation system was estimated from the amplitude and phase lag difference of seasonal changes in $\delta^{18}O$ in different water bodies [17,31]. The time series of its distribution can then be described as:

$$\delta^{18}O = X + A^{*}\cos(ct - \theta) \quad (1)$$

where $\delta^{18}O$ denotes the projected oxygen isotope values of precipitation, terraced field water, and spring water; X represents the interannual mean values of measured oxygen isotopes of precipitation, terraced field water, and spring water; A is the yearly amplitude of precipitation, terraced field water, and spring water of $\delta^{18}O$ (‰); c is the annual fluctuation radial frequency (0.017214 rad·$d^{-1}$); t is the actual sample sampling time (d); and θ is the phase lag.

$$MRT = c^{-1}[(A_{z1}/A_{z2})^{-2} - 1]^{0.5} \quad (2)$$

where MRT represents the mean residence time of water in the water circulation system; $A_{z1}$ represents the amplitude of the input signal (the amplitude of $\delta^{18}O_{\text{spring water}}$); and $A_{z2}$ represents the amplitude of the output signal (the amplitude of $\delta^{18}O_{\text{precipitation}}$/the amplitude of $\delta^{18}O_{\text{terraced field water}}$).

### 2.4. End Member Mixing Analysis

A spring is a natural outcrop of groundwater, a phenomenon that occurs when groundwater gushes from an aquifer or a water-bearing channel outcropping the surface of the ground. Ascending springs are subjected to hydrostatic pressure so that the water in the confined aquifer is in an upward movement, while descending springs are subjected to a downward movement under the influence of the shallow aquifer [32,33]. Therefore, we constructed a formula for the recharge sources of ascending and descending springs in the terraced area, and the formula is as follows:

$$\delta^{18}O_{A\text{-}S} = f_{P}\delta^{18}O_{P} + f_{T}\delta^{18}O_{T} + f_{L}\delta^{18}O_{L} \quad (3)$$

$$\delta^{2}H_{A\text{-}S} = f_{P}\delta^{2}H_{P} + f_{T}\delta^{2}H_{T} + f_{L}\delta^{2}H_{L} \quad (4)$$

$$1 = f_{P} + f_{T} + f_{L} \quad (5)$$

where $f_{P}$, $f_{T}$, and $f_{L}$, respectively, denote the percentage of precipitation, terraced field water, and lateral groundwater recharge; $\delta^{18}O_{A\text{-}S}$, $\delta^{18}O_{P}$, $\delta^{18}O_{T}$, and $\delta^{18}O_{L}$ denote oxygen isotope values of ascending spring water, precipitation, terraced field water, and

lateral groundwater, respectively; and $\delta^2H_{A\text{-}S}$, $\delta^2H_P$, $\delta^2H_T$, and $\delta^2H_L$ denote hydrogen isotope values of ascending spring water, precipitation, terraced field water, and lateral groundwater, respectively.

$$\delta^{18}O_{D\text{-}S} = f_P\delta^{18}O_P + f_T\delta^{18}O_T \quad (6)$$

$$\delta^2H_{D\text{-}S} = f_P\delta^2H_P + f_T\delta^2H_T \quad (7)$$

$$1 = f_P + f_T \quad (8)$$

where $f_P$ and $f_T$, respectively, denote the percentage of precipitation and terraced field water recharge; $\delta^{18}O_{D\text{-}S}$, $\delta^{18}O_P$, and $\delta^{18}O_T$ denote oxygen isotope values of descending spring water, precipitation, and terraced field water, respectively; and $\delta^2H_{D\text{-}S}$, $\delta^2H_P$, and $\delta^2H_T$ denote hydrogen isotope values of descending spring water, precipitation, and terraced field water, respectively.

This study was based on the research background of the influence of spring water residence time on the irrigation water stability in the Hani Rice Terraces. The MRT of spring water in the Hani terraces was considered the dependent variable in this study, with precipitation, terrace water, and groundwater recharge serving as the independent variables. On the independent and dependent variables, correlation analysis, linear regression analyses, and significance tests were carried out using SPSS 13.0 statistical software.

## 3. Results

### *3.1. Spatial and Temporal Characteristics of Hydrogen and Oxygen Stable Isotopes in Springs and Their Recharge Water Sources*

During the observation period, the stable isotope data of the precipitation yield the local meteoric water line (LMWL) equation: $\delta D = 8.36\delta^{18}O + 22.01$ ($R^2 = 0.98$, $n = 36$) (Figure 2a). The slope and intercept are larger than those of the global meteoric water line (GMWL) equation $\delta D = 8\ \delta^{18}O + 10$ ($R^2 = 0.98$). The results indicate that the study area is subject to the subtropical monsoon climate and precipitation in the region consists mainly of humid oceanic air masses. Nevertheless, the local terraced field water line (LTWL) is: $\delta D = 6.10\ \delta^{18}O - 3.90$ ($R^2 = 0.86$, $n = 120$), indicating that there is evaporative fractionation during the process of precipitation and groundwater recharge to the terraced field water. The local spring water line (LSWL) is: $\delta D = 4.95\ \delta^{18}O - 15.22$ ($R^2 = 0.92$, $n = 120$), and its slope and intercept are significantly smaller than LMWL and LTWL, indicating a stronger evaporative fractionation process during the process of recharging groundwater and then outgrowth from springs by precipitation and terraced field water.

We chose $\delta^{18}O$ for our systematic analyses because of the correlation between hydrogen and oxygen isotopes [5–7]. Figure 2b,c illustrates seasonal fluctuations in the monthly mean $\delta^{18}O$ of springs. The $\delta^{18}O$ of spring water varied from −9.65‰ to −3.01‰, with a mean value of −7.29‰. Spring water's $\delta^{18}O$ varies seasonally, forming a soft "S" shape with an upward trend from May to August, a slow fall from August to January, and a slow upward trend from January to April. In terms of different spring types, ascending springs have higher temperatures and faster $\delta^{18}O$ fractionation than descending springs due to hydrostatic pressure, resulting in more positive isotopic values. The isotopic anti-elevation effect of spring water was observed in November and January in the ascending springs and from December to February in the descending springs, which was related to the local farming cycle. With the harvesting of terraced rice at the end of October, local farmers ploughed and rebuilt the terraces, artificially destroying the impermeable/weakly permeable layer in the terraced fields and allowing terraced field water to enter the subsurface more rapidly. This caused a rapid enrichment of groundwater $\delta^{18}O$, and the response to this phenomenon was more sensitive in the ascending springs than in the descending springs.

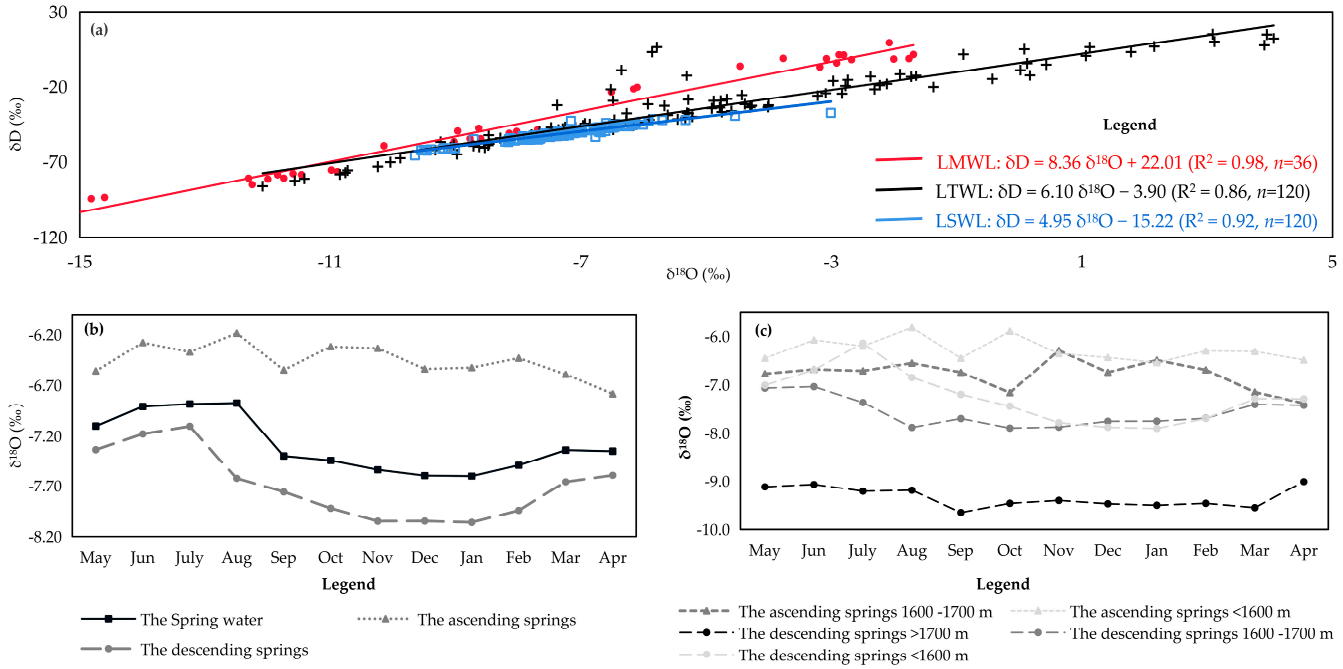


**Figure 2.** (**a**) Local meteoric water line (LMWL), Local terraced field water line (LTWL) and Local spring water line (LSWL) for the study area; (**b**) the temporal distributions of $\delta^{18}O$ in ascending and descending springs; (**c**) the spatial distributions of $\delta^{18}O$ in ascending and descending springs.

### *3.2. Effect of MRT of Spring Recharge Water Sources on the Stability of Irrigation Water Sources in the Hani Rice Terraces*

Based on Equation (2), the mean multi-year residence time of spring recharge sources in the Hani terrace area was calculated (Table 1 and Figure 3). As shown in the table, the inter-annual residence time of precipitation and terraced field water in springs was 2.46 years and 1.54 years, respectively, indicating that the springs in May 2015–April 2016 were influenced by 2.46 years of former precipitation and 1.54 years of former terraced field water. In other words, both the precipitation from 2.46 years ago and the terraced field water from 1.54 years ago were able to effectively recharge the water used for agriculture in the terraces in that year. This explains the drought event that occurred in the whole province of Yunnan Province in 2015 under the influence of the El Niño event, but the drought event did not affect the sustainable development of rice agriculture in the Hani Rice Terraces that year.

We discovered that different types of springs had distinct emergence timings, allowing for staggered refilling of terraced water sources. The time it took for precipitation and terraced field water to be transited and exposed as ascending/descending springs in the terraced area was 2.73 years and 1.95 years, and 1.55 years and 1.04 years, respectively. The MRT of ascending springs was about half a year longer than that of descending springs, implying that ascending and descending springs can be staggered to recharge the terraced field water.

At higher elevations, precipitation and terraced field water residence in ascending and descending springs took 2.52 and 3.73 times longer to emerge from terraces, and 3.36 and 6.49 times longer than at lower levels. This means that the lower the altitude, the shorter the MRT of the recharge water source, and the elevation gradient of the ascending spring is smaller than that of the descending spring. It further illustrates that the ascending springs regulate the temporal distribution of the terrace recharge water sources, while the descending springs regulate the spatial distribution of the terrace recharge water sources, demonstrating that the Hani Rice Terraces are a relatively stable agroecosystem.

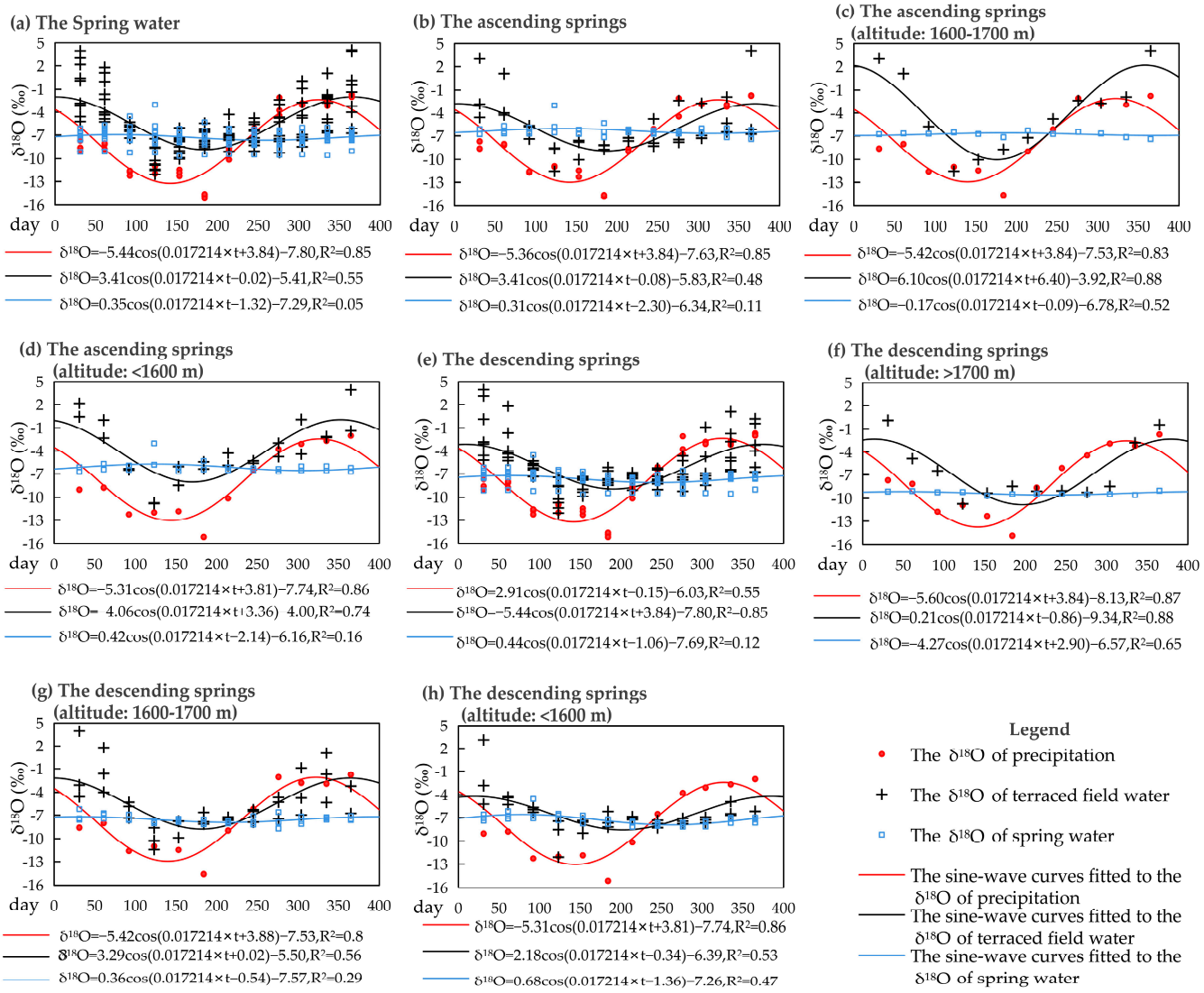


**Figure 3.** Seasonal oxygen-18 variations in Precipitation, Terraced field water, and Spring water at the Hani terraced fields; raw data and sine-wave curves fitted to data.

**Table 1.** The MRT of spring recharge water sources in the Hani Rice Terraces.

| Type of Springs | Altitude | Intersubstance Transport Processes | MRT (a) |
|---|---|---|---|
| The Spring water | | Precipitation → Spring water | 2.46 |
| | | Terraced field water → Spring water | 1.54 |
| The ascending springs | 1600–1700 m | Precipitation → Spring water | 2.73 |
| | | Terraced field water → Spring water | 1.55 |
| | <1600 m | Precipitation → Spring water | 5.03 |
| | | Terraced field water → Spring water | 5.67 |
| | | Precipitation → Spring water | 2.00 |
| | | Terraced field water → Spring water | 1.52 |
| The descending springs | >1700 m | Precipitation → Spring water | 1.95 |
| | | Terraced field water → Spring water | 1.04 |
| | 1600–1700 m | Precipitation → Spring water | 4.17 |
| | | Terraced field water → Spring water | 3.18 |
| | <1600 m | Precipitation → Spring water | 2.37 |
| | | Terraced field water → Spring water | 1.43 |
| | | Precipitation → Spring water | 1.24 |
| | | Terraced field water → Spring water | 0.49 |

## 4. Discussion

### *4.1. Effects of the Spring Recharge-Discharge Ratio on the Stability of Irrigation Water Sources in the Hani Terraced Fields*

According to Equations (3)–(8), the recharge-discharge ratios of ascending and descending springs in the Hani terrace area were obtained (Figure 4). As a whole, groundwater in the terraced area is distinguished by short recharge routes, in situ recharge, and in situ discharge, and its quantity is directly tied to topography [34]. The ascending spring percolates upward in a confined aquifer, thus lateral groundwater supplies more than half of its recharge; the descending spring's primary recharge source is shallow groundwater, which is influenced by precipitation and terraced field water. The ascending springs in the terraced area follow the rule that the lower the elevation, the greater the proportion of lateral groundwater recharge; the descending springs obey the rule that the lower the elevation, the greater the ratio of terraced field water recharge. This suggests that the upstream–downstream recharge relationship of groundwater in the terraced area is critical to ensuring the stability of the terraced water source.

To effectively explain the effect of the spring water recharge ratio on the periodicity of Hani terrace irrigation water sources, this study used linear regression to explore the relationship between precipitation, the terraced field water recharge ratio, and the MRT of spring water in different water bodies (Table 2). It has been discovered that there is a significant correlation between the ratio of field water recharge to springs in the Hani terraces and the MRT of field water in springs. Among these, there is a substantial negative connection for descending springs, indicating that the ratio of terraced field water recharge will influence the MRT of spring water on the Hani terraces. This suggests that local agricultural activities on the terraces will effectively interfere with shallow groundwater, thus affecting the MRT of groundwater and ensuring the ongoing recharge of descending springs to the terraced water. The ratio of precipitation recharging the springs, on the other hand, has a correlation with the MRT of springs but is not significant. It demonstrates that the process of direct recharging of precipitation to springs is reduced, and the ratio of precipitation recharge to springs is not a key factor determining the MRT of springs by precipitation.

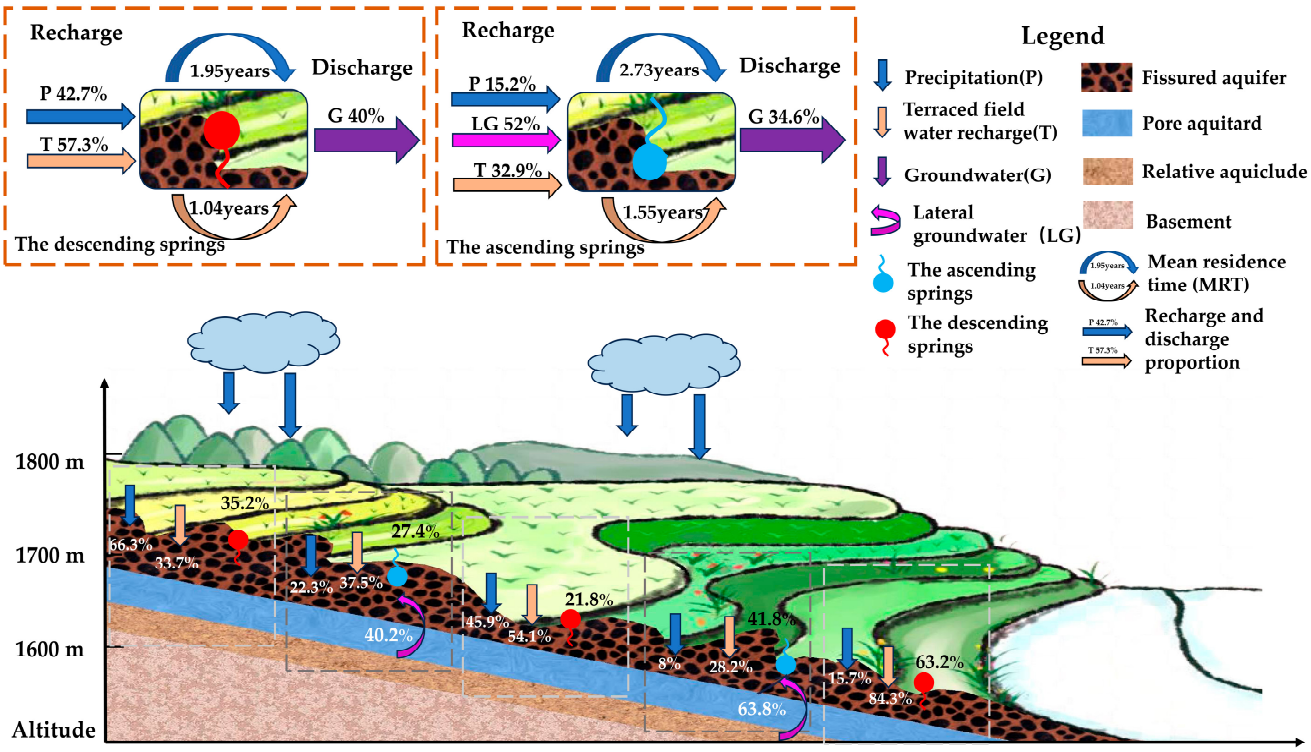


**Figure 4.** Ratio of recharge/discharge from ascending/descending springs at different altitudes in the Hani Rice Terraces.

**Table 2.** The relationship between precipitation, the terraced field water recharge ratio, and the MRT of spring water in different water bodies.

| Type of Springs | Intersubstance Transport Processes | Pearson Correlation | Linear Regression Equation | $R^2$ |
|---|---|---|---|---|
| The Spring water | Precipitation → Spring water | 0.21 | - | - |
| | Terraced field water → Spring water | −0.70 * | MRT = 10.18 T − 13.90 $T^2$ | 0.77 ** |
| The ascending springs | Precipitation → Spring water | −0.92 | - | - |
| | Terraced field water → Spring water | 0.96 | - | - |
| The descending springs | Precipitation → Spring water | 0.56 | - | - |
| | Terraced field water → Spring water | −0.92 ** | MRT = −7.56 T + 2.33 $T^2$ + 4.79 | 0.85 * |

Notes: * indicate the *p*-value is less than 0.05 (5%); ** indicate the *p*-value is less than 0.01 (1%).

### *4.2. Effect of MRT of Spring Water and Its Influencing Factors on the Stability of Irrigation Water Sources*

Table 3 summarizes the residence times of various types of water bodies in different regions of the globe, with precipitation residence in surface water ranging from 0.5 to 1.5 years, precipitation residence in groundwater from 1.1 to 1.3 years, surface water residence in groundwater from 0.41 to 3.15 years, precipitation residence in 0.15 to 0.55 years for soil water, and soil water residence in rock water from 0.06 to 1.15 years. Globally, water residence time is not only related to the hydraulic gradient of the watershed, but also closely related to the catchment area, soil depth, and land use type [11–18,26]. Generally speaking, the smaller the watershed area, the steeper the slope, and the thinner the soil layer, the shorter the water residence time, and the longer the time. Despite the small watershed area (13.92 $km^2$) and steep slope (17°−58°) of the Hani terrace area, its water residence time is longer than that of other watersheds around the globe due to its thick soil layer, which is dominated by rice soil, and the plow pan is effective in isolating the water [35,36], implying that the terraces function as a source of water conservation.

From a global perspective, different locations maintain water resource stability in terraced agricultural systems in different ways, with different transmission cycles and their influencing factors [37–41]. For irrigated terraced agriculture in semi-arid areas, the construction of terraces can effectively improve the soil erosion phenomenon of sloping arable land, increase the residence time of rainwater on the ground, and improve the infiltration of soil moisture, guaranteeing the stability of water sources in the region [37]. Rice terrace agriculture in the humid zone is distinguished by flooded fields throughout the year, and springs are essential for preserving the stability of water sources in the terraces [19–23,38–41]. Previously, some scholars have found that the recharge of terrace irrigation water sources has the characteristics of alternating seasons and spatial staggered distribution of spring and rainwater, and that the terrace irrigation water source is most stable when recharged by spring water [19]. However, we found that precipitation and terraced field water are transited for about half a year longer in the ascending springs than in the descending springs, implying that different spring types have different discharge times in the same area and that different types of springs can be staggered to recharge the terraced field water to maintain the stability of the terraced rice agriculture. This suggests that the Hani terraces' spring irrigation water source is not only multi-temporal but also spatially heterogeneous. This also explains why the Hani terraces can maintain the stability of water resources in the rice farming system even during drought years.

The current study examines the time scale of the spring water cycle, concentrating on the impact of spring water residence time on irrigation water stability in the Hani Rice Terraces. However, we did not account for the effect of soil water on spring water residence time. In the future, we need to focus on quantitative research on the effect of soil factors in the Hani terraces based on the soil's physicochemical properties, so as to systematically and comprehensively reveal the mechanism of irrigation, recharge, and discharge transformation of the Hani terraced irrigation water source, as well as its impact on the sustainability of terraced agriculture, and to provide effective scientific basis for the protection of the Hani terraces.

**Table 3.** The residence times of various types of water bodies in different regions of the globe.

| Region | The Intersubstance Transport Processes | MRT (a) | The Influence Factor | Sampling Time Period |
|---|---|---|---|---|
| Tuojiang river [16] | Precipitation → Surface water | 0.95–1.35 year | Topography; Catchment area; Soil type; Land use type | 2018.5–2019.4 |
| The Abay/Upper Blue Nile [14] | Precipitation → Surface water | 0.34 year, 0.5 year | | 2008.8–2011.8 |
| Upper Indus River Basin [11] | Precipitation → Surface water | 0.5–1.03 year | The steep gradient of stream profile; Flowpath length; Landscape physiography | 2007.11–2009.1 |
| Redondo Peak, located in the Valles Caldera, New Mexico, United States [13] | Precipitation → Surface water | 0.34 year | Topographical features (such as flow path length, slope gradient, aspect and elevation) | 2007.3–2007.8 |
| Two forested basins in West Virginia and one in Pennsylvania [17] | Precipitation → Spring water; Precipitation → Stream water | The Fernow watersheds: 1.1–1.3 year; The Benner Run: 1.4–1.6 year | Catchment area; Slope; Soil depth | 1989.3–1990.3 |
| The Tianguer River and Duowang Rive, in Yilan, Taiwan [9] | Surface water → Groundwater | 0.41 year, 3.15 year | | 2018.10–2020.4 |
| The Honghe Hani Terraces [25] | Precipitation → Soil water | The forest land: 0.15–0.26 year; The shrubland: 0.21–0.39 year | Land use type; non-capillary porosity | 2015.7–2015.12 |
| Jeju Island [15] | Precipitation → Soil water | 30 cm depth: 0.14 year, 60 cm depth: 0.44 year, 80 cm depth: 0.55 year | Soil depth; The boundary between the upper fine-grained soil and the lower coarse-grained soil | 2002.11–2003.11 |
| Huanjiang County of northwest Guangxi, southwest China [8] | Soil water → Spring water | 0.06–1.15 year, 0.98 year | Soil thickness; Epikarst | 2011.4–2013.4 |

## 5. Conclusions

In this study, the influence of spring water residence time on the irrigation water stability in the Hani Rice Terraces was assessed using MRT and the isotope mixing model based on monthly samples of precipitation, terrace water, and spring water collected between 2015 and 2016. The results show that:

(1) All inter-water body transformations between precipitation recharge to terraced field water, recharge to the subsurface, and spring water outcropping to the surface have undergone varying degrees of evaporative fractionation. The $\delta^{18}O$ of the springs in

the terraced area showed a gentle "S" shape, with ascending springs having more positive isotopic values than descending springs. The isotopic anti-elevation effect of spring water was observed in the ascending springs from November to January and in the descending springs from December to February, which was related to the local farming cycle, and the ascending springs were more sensitive to the response to the farming cycle than the descending springs.

(2) The residence time of precipitation and terraced field water in springs was 2.46 years and 1.54 years, respectively, indicating that the springs were affected by 2.46 years of previous precipitation and 1.54 years of previous terraced field water. When analyzed in terms of different spring types, the time for precipitation and terraced field water to be transited and exposed as ascending/descending springs in the terraced area was 2.73 years and 1.95 years, and 1.55 years and 1.04 years, respectively, where the residence time of ascending springs was about half a year longer than that of descending springs, indicating that the ascending springs and the descending springs can be staggered to recharge the terraced field water. From different elevations, the lower the elevation, the shorter the MRT of the recharge water source, and the elevation difference of the MRT of the ascending spring is smaller than that of the descending spring, indicating that the ascending spring regulates the temporal distribution of the recharge water source of the terraces, while the descending spring regulates the spatial distribution.

(3) Groundwater in the terraced area has short recharge routes, in situ recharge, and in situ discharge, and its quantity is strongly tied to topography. The ascending spring percolates upward in a confined aquifer, thus lateral groundwater supplies more than half of its recharge; the descending spring's primary recharge source is shallow groundwater, which is influenced by precipitation and terraced field water. The ascending springs in the terraced area follow the rule that the lower the elevation, the higher the ratio of lateral groundwater recharge; the descending springs obey the rule that the lower the elevation, the higher the ratio of terraced field water recharge.

**Author Contributions:** Conceptualization, Y.J.; methodology, Y.J. and K.W.; software, K.W.; validation, Y.W., G.Z. and H.Z.; formal analysis, K.W.; investigation, G.Z.; resources, Y.J. and G.Z.; data curation, Y.J.; writing—original draft preparation, K.W.; writing—review and editing, Y.J.; visualization, K.W. and Y.W.; supervision, Y.J.; project administration, Y.J.; funding acquisition, Y.J. All authors have read and agreed to the published version of the manuscript.

**Funding:** This study was funded by Yunnan Provincial Basic Research Project—Key Project (202201AS070024), 2023's Promotion Project of Scientific Research by Faculty of Geography in Yunnan Normal University (01300205020516083/022), the National Natural Science Foundation of China (grant numbers 41271203, 41761115), Yunnan Province Reserve Talent Program for Young and Middle-aged Academic and Technical Leaders (202205AC160014, 202305AC160083), The Natural Science Foundation of Yunnan Province of China (202101AT070052).

**Data Availability Statement:** The data presented in this study are available on request from the corresponding author.

**Acknowledgments:** The authors thank Hucai Zhang and Wenxiang Zhang of Yunnan University for the lab experiment with the water samples.

**Conflicts of Interest:** The authors declare no conflicts of interest. The funders had no role in the design of the study; in the collection, analyses, or interpretation of data; in the writing of the manuscript; or in the decision to publish the results.

## References

1. Gleeson, T.; Cuthbert, M.; Ferguson, G.; Perrone, D. Global groundwater sustainability, resources, and systems in the Anthropocene. *Annu. Rev. Earth Planet. Sci.* **2020**, *48*, 431–463. [CrossRef]
2. Leduc, C.; Pulido-Bosch, A.; Remini, B. Anthropization of groundwater resources in the Mediterranean region: Processes and challenges. *Hydrogeol. J.* **2017**, *25*, 1529–1547. [CrossRef]

3. Nikolaou, G.; Neocleous, D.; Christou, A.; Kitta, E.; Katsoulas, N. Implementing Sustainable Irrigation in Water-Scarce Regions under the Impact of Climate Change. *Agronomy* **2020**, *10*, 1120. [CrossRef]
4. Guermazi, E.; Milano, M.; Reynard, E.; Zairi, M. Impact of climate change and anthropogenic pressure on the groundwater resources in arid environment. *Mitig. Adapt. Strateg. Glob. Chang.* **2019**, *24*, 73–92. [CrossRef]
5. Kløve, B.; Margrethe, H.; Kvitsand, L.; Pitkänen, T.; Gunnarsdottir, M.J.; Gaut, S.; Gardarsson, S.M.; Rossi, P.M.; Miettinen, I. Overview of groundwater sources and water-supply systems, and associated microbial pollution, in Finland, Norway and Iceland. *Hydrogeol. J.* **2017**, *25*, 1033. [CrossRef]
6. Qiu, X.L.; Wang, Y.; Wang, Z.Z.; Regenauer-Lieb, K.; Zhang, K.; Liu, J. Determining the origin, circulation path and residence time of geothermal groundwater using multiple isotopic techniques in the Heyuan Fault Zone of Southern China. *J. Hydrol.* **2018**, *567*, 339–350. [CrossRef]
7. Xiao, Y.; Shao, J.; Cui, Y.; Zhang, G.; Zhang, Q. Groundwater circulation and hydrogeochemical evolution in Nomhon of Qaidam Basin, northwest China. *J. Earth Syst. Sci.* **2017**, *126*, 26. [CrossRef]
8. Hu, K.; Chen, H.; Nie, Y.; Wang, K. Seasonal recharge and mean residence times of soil and epikarst water in a small karst catchment of southwest China. *Sci. Rep.* **2015**, *5*, 10215. [CrossRef]
9. Kuo, C.H.; Li, P.Y.; Lin, J.Y.; Chen, Y.L. Integrating Stable Isotopes with Mean Residence Time Estimation to Characterize Groundwater Circulation in a Metamorphic Geothermal Field in Yilan, Taiwan. *Water* **2022**, *14*, 97. [CrossRef]
10. Xia, C.C.; Liu, G.D.; Zhou, J.; Meng, Y.; Chen, K.; Gu, P.; Yang, M.; Huang, X.; Mei, J. Revealing the impact of water conservancy projects and urbanization on hydrological cycle based on the distribution of hydrogen and oxygen isotopes in water. *Environ. Sci. Pollut. Res.* **2021**, *28*, 40160–40177. [CrossRef]
11. Lone, S.A.; Jeelani, G.; Deshpande, R.D.; Bhat, M.S.; Padhya, V. Assessing the hydrological controls on spatio-temporal patterns of streamwater in glacierized mountainous Upper Indus River Basin (UIRB), western Himalayas. *J. Hydrol.* **2023**, *619*, 129310. [CrossRef]
12. Jeelani, G.; Kumar, U.S.; Kumar, B. Variation of δ18O and δD in precipitation and stream waters across the Kashmir Himalaya (India) to distinguish and estimate the seasonal sources of stream flow. *J. Hydrol.* **2013**, *481*, 157–165. [CrossRef]
13. Broxton, P.D.; Troch, P.A.; Lyon, S.W. On the role of aspect to quantify water transit times in small mountainous catchments. *Water Resour. Res.* **2009**, *45*, W08427. [CrossRef]
14. Tekleab, S.; Wenninger, J.; Uhlenbrook, S. Identifying residence times and streamflow generation processes using $\delta^{18}$ O and $\delta^{2}$ H in meso-scale catchments in the Abay/Upper Blue Nile, Ethiopia. *Hydrol. Earth Syst. Sci.* **2013**, *10*, 10333–10377.
15. Lee, K.S.; Kim, J.M.; Lee, D.R.; Kim, Y.; Lee, D. Analysis of water movement through an unsaturated soil zone in Jeju Island, Korea using stable oxygen and hydrogen isotopes. *J. Hydrol.* **2007**, *345*, 199–211. [CrossRef]
16. Zhou, J.; Liu, G.; Meng, Y.; Xia, C.; Chen, K.; Chen, Y. Using stable isotopes as tracer to investigate hydrological condition and estimate water residence time in a plain region, Chengdu, China. *Sci. Rep.* **2021**, *11*, 2812. [CrossRef] [PubMed]
17. DeWalle, D.R.; Edwards, P.J.; Swistock, B.R.; Aravena, R.; Drimmie, R.J. Seasonal isotope hydrology of three Appalachian forest catchments. *Hydrol. Process.* **1997**, *11*, 1895–1906. [CrossRef]
18. Jiao, Y.M.; Liu, C.J.; Liu, Z.L.; Ding, Y.; Xu, Q. Impacts of moisture sources on the temporal and spatial heterogeneity of monsoon precipitation isotopic altitude effects. *J. Hydrol.* **2020**, *583*, 124576. [CrossRef]
19. Liu, C.; Jiao, Y.; Zhao, D.; Ding, Y.; Liu, Z.; Xu, Q. Effects of Farming Activities on the Temporal and Spatial Changes of Hydrogen and Oxygen Isotopes Present in Groundwater in the Hani Rice Terraces, Southwest China. *Water* **2020**, *12*, 265. [CrossRef]
20. Bai, Y.; Min, Q.; Liu, M.; Yuan, Z.; Xu, Y.; Cao, Z.; Li, J. Resilience of the Hani Rice Terraces System to extreme drought. *J. Food Agric. Environ.* **2013**, *11*, 2376–2382.
21. Gu, H.; Jiao, Y.; Liang, L. Strengthening the socio-ecological resilience of forest-dependent communities: The case of the Hani Rice Terraces in Yunnan, China. *For. Policy Econ.* **2012**, *22*, 53–59. [CrossRef]
22. Ma, Z.; Song, W.; Ma, J.; Ma, J.; He, X. Dynamic Change Characteristics of Soil Moisture and Its Relationship with Precipitation in Hani Rice Terraces Water Source Area. *Water* **2022**, *14*, 2690. [CrossRef]
23. Liu, C.; Jiao, Y.; Xu, Q.; Liu, Z.; Ding, Y. Temp-Spatial Heterogeneity of Water Recharge and Its Stable Mechanisms of the Mountainous Rice Terraces in East Asia Monsoon Region. *Water* **2022**, *14*, 4110. [CrossRef]
24. Wang, M.; Rong, L.; Li, Y.; Huang, J.; Jiao, Y.; Wei, X. Drainage of paddy terraces impacts structures and soil properties in the globally important agricultural heritage of Hani Paddy Terraces, China. *Int. Soil Water Conserv. Res.* **2024**, *12*, 64–76. [CrossRef]
25. Ma, J.; Song, W.; Wu, J.; Liu, Z.; Wei, Z. Identifying the mean residence time of soil water for different vegetation types in a water source area of the Yuanyang Terrace, southwestern China. *Isot. Environ. Health Stud.* **2019**, *55*, 272–289. [CrossRef]
26. Jiao, Y.M.; Liu, C.J.; Gao, X.; Xu, Q.E.; Ding, Y.P.; Liu, Z.L. Impacts of moisture sources on the isotopic inverse altitude effect and amount of precipitation in the Hani Rice Terraces region of the Ailao Mountains. *Sci. Total Environ.* **2019**, *687*, 470–478. [CrossRef] [PubMed]
27. Gao, X.; Roder, G.; Jiao, Y.; Ding, Y.; Liu, Z.; Tarolli, P. Farmers' landslide risk perceptions and willingness for restoration and conservation of world heritage site of Honghe Hani Rice Terraces, China. *Landslides* **2020**, *17*, 1915–1924. [CrossRef]
28. Ding, Y.P.; Liu, Z.L.; Jiao, Y.M.; Hu, T. Response and Its Mechanism of Hani Terraces to El Nino Extreme Drought Events. *J. Soil Water Conserv.* **2021**, *35*, 161–171.
29. Kresic, N. Chapter 2—Types and Classifications of Springs. In *Groundwater Hydrology of Springs*; Kresic, N., Stevanovic, Z., Eds.; Butterworth-Heinemann: Oxford, UK, 2010; pp. 31–85. ISBN 9781856175029.

30. Lynne, B.Y.; Campbell, K.A.; Moore, J.; Browne, P. Origin and evolution of the Steamboat Springs siliceous sinter deposit, Nevada, USA. *Sediment. Geol.* **2008**, *210*, 111–131. [CrossRef]
31. Bliss, C.L. *Statistics in Biology*; McGraw Hill: New York, NY, USA, 1970; Volume 2.
32. Kazemi, G.A.; Lehr, J.H.; Perrochet, P. *Groundwater Age*; John Wiley & Sons: Hoboken, NJ, USA, 2006.
33. Strauch, G. Isotope methods for dating old groundwater. *Isot. Environ. Health Stud.* **2014**, *50*, 566–568. [CrossRef]
34. Tien Bui, D.; Talebpour Asl, D.; Ghanavati, E.; Al-Ansari, N.; Khezri, S.; Chapi, K.; Amini, A.; Pham, B.T. Effects of Inter-Basin Water Transfer on Water Flow Condition of Destination Basin. *Sustainability* **2020**, *12*, 338. [CrossRef]
35. Yang, L.; Liu, M.; Lun, F.; Yuan, Z.; Zhang, Y.; Min, Q. An Analysis on Crops Choice and Its Driving Factors in Agricultural Heritage Systems—A Case of Honghe Hani Rice Terraces System. *Sustainability* **2017**, *9*, 1162. [CrossRef]
36. Jiao, Y.M. *Natural and Cultural Landscape Ecology of Hani T Erraces*; Chinese Environmental Science Press: Beijing, China, 2009; pp. 75–112.
37. Xu, Y.X.; Zhu, G.F.; Wan, Q.Z.; Yong, L.; Ma, H.; Sun, Z.; Zhang, Z.; Qiu, D. Effect of terrace construction on soil moisture in rain-fed farming area of Loess Plateau. *J. Hydrol. Reg. Stud.* **2021**, *37*, 100889. [CrossRef]
38. Sintayehu, D.W. Impact of climate change on biodiversity and associated key ecosystem services in Africa: A systematic review. *Ecosyst. Health Sustain.* **2018**, *4*, 225–239. [CrossRef]
39. Dang, K.B.; Burkhard, B.; Windhorst, W.; Müller, F. Application of a hybrid neural-fuzzy inference system for mapping crop suitability areas and predicting rice yields. *Environ. Model. Softw.* **2019**, *114*, 166–180. [CrossRef]
40. Jiang, Y.; Li, S.; Cai, D.; Chen, W.; Liu, Y.; Yu, Z. The genesis and paleoenvironmental records of Longji agricultural terraces, southern China: A pilot study of human–environment interaction. *Quat. Int.* **2014**, *321*, 12–21. [CrossRef]
41. Guo, X.; Feng, Q.; Si, J.; Xi, H.; Zhao, Y.; Deo, R.C. Partitioning groundwater recharge sources in multiple aquifers system within a desert oasis environment: Implications for water resources management in endorheic basins. *J. Hydrol.* **2019**, *579*, 124212. [CrossRef]

water

MDPI

*Article*

# The General Relationship between Mean Dissolved Oxygen Concentrations and Timescales in Estuaries

**Jian Shen [1,*] and Qubin Qin [2]**

[1] Virginia Institute of Marine Science, William & Mary, Gloucester Point, VA 23062, USA
[2] Coastal Studies Institute, East Carolina University, Wanchese, NC 27981, USA; qinq23@ecu.edu
* Correspondence: shen@vims.edu

**Abstract:** The onset of hypoxia is a consequence of the competition between oxygen replenishment, production, and consumption. Dissolved oxygen (DO) levels inside an estuary depend on the balance between physical processes that transport oxygen-rich water into the estuary, including upstream freshwater advection, gravitational circulation, and vertical mixing, and biochemical processes that produce and consume oxygen, such as photosynthesis, respiration, and organic decomposition. We propose a general relationship between the physical and biochemical processes with a Lagrangian perspective to interpolate mean DO concentrations at local and system levels to assess the onset of hypoxia in an estuary. Simple parameters using timescales are proposed for cross-system comparison of hypoxia and anoxia conditions. Our study demonstrates that the hypoxia of an estuary system is determined by the timescales of vertical exchange, freshwater and saltwater transport, and DO consumption. When the vertical exchange timescale is shorter than the residence time in a system, vertical exchange dominates DO replenishment, while shorter residence time enhances advection, which quickly inputs DO-rich water to regulate hypoxia. The interplay between DO consumption and dynamic DO replenishment is the primary determinant of hypoxia in an estuary.

**Keywords:** hypoxia and anoxia; cross-system comparison; transport timescales; vertical exchange time; residence time; Chesapeake Bay



**Citation:** Shen, J.; Qin, Q. The General Relationship between Mean Dissolved Oxygen Concentrations and Timescales in Estuaries. *Water* **2024**, *16*, 969. https://doi.org/10.3390/w16070969

Academic Editor: Giuseppe Oliveto

Received: 28 February 2024
Revised: 21 March 2024
Accepted: 21 March 2024
Published: 27 March 2024



## 1. Introduction

Hypoxia and anoxia are phenomena characterized by dissolved oxygen (DO) levels falling below 2 g $O_2$ $m^{-3}$ and reaching zero, respectively. Persistent seasonal hypoxia occurs in many stratified or partially mixed estuaries and shelf regions worldwide [1–4]. It causes water degradation, which is harmful to living resources, kills fish, and causes the deterioration of water quality [1,4]. Hypoxia and anoxia occur when oxygen consumption exceeds oxygen production and replenishment within an aquatic environment. In the context of an estuary, DO replenishment occurs through vertical and lateral mixing processes, advection of upstream freshwater, or gravitational circulation (exchange flow) that transports DO-rich water into the estuary [2,3]. Conversely, oxygen production/consumption mainly result from phytoplankton photosynthesis/respiration, nitrification, organic matter decomposition, and bottom sediment oxygen demand (SOD). Because of the persistence of estuarine stratification, hypoxia often develops in sub-pycnocline water when the DO consumption rate of biochemical processes surpasses the oxygen supply [2]. Hypoxia occurs in rivers and coastal waters, and its frequency of occurrence appears to be increasing and is most likely accelerated by human activities [1,4]. The phenomenon of low-DO conditions in aquatic ecosystems has captured the interest of researchers and managers. Understanding the causes of hypoxia and effectively managing them is an urgent need and it requires a multidisciplinary approach.

Because the transport and mixing processes play a crucial role in modulating DO, physical oceanographers have become increasingly interested in the dynamics of oxygen

variations and how they modulate DO dynamics. In the Chesapeake Bay, it has been found that freshwater discharge is a major factor in regulating stratification [5], which is a predictor of summertime hypoxic volume due to high nutrient input during spring runoff [6]. Kuo and Neilson [3] analyzed DO budgets in the Virginia tributary estuaries of the Chesapeake Bay. They pointed out the importance of gravitational circulation in modulating DO in these tributaries. In addition to gravitational circulation, Sanford et al. [7] showed the importance of the lateral exchange of DO between the surface and sub-pycnocline water due to lateral circulations. Scully [8] demonstrated that wind plays a crucial role in modulating hypoxia in the Chesapeake Bay through lateral circulation. Because of the complicity of dynamics, this makes cross-system comparison challenging.

The approach of using timescales for understanding the overall effect of dynamics and transport processes has been used for cross-system comparison under a common currency [9–12]. Shen et al. [10] provided a simplified two-layer theoretical model, for which the bottom DO concentration can be interpolated by the timescales of vertical exchange time ($\tau_v$), horizontal transport time (saltwater age), and DO consumption time. The timescale approach was verified by a three-dimensional model in the Chesapeake Bay [13]. Recently, Fennel and Testa [14] proposed a non-dimensional number that relates the hypoxia timescale and water residence time to guide the cross-system comparison, which provides a convenient method of cross-system comparison. However, the water residence time does not account for the vertical exchange that is a key parameter for DO replenishment [2,7] when the water residence time is long [10]. The competition between vertical and horizontal transport needs to be quantified and included to fully account for the DO dynamics.

The purpose of this study is to provide a general relationship between DO and transport timescales in estuaries, using a Lagrangian perspective, to quantify the effects of physical and biochemical processes on the mean DO at both local and system scales, which can be used to assess the onset of hypoxia in an estuary and enable cross-system comparisons. While the simplified approach is based on an idealized estuary, it provides insights into understanding DO dynamics. This study demonstrates that the hypoxia of an estuary system can be effectively quantified by timescales, which can be used for cross-system comparison.

## 2. Methods

In this section, a general case that is applicable to both rivers and estuaries is introduced to understand the relationship between physical and biochemical processes that influence the average DO levels in these environments. We derived simple relationships between mean DO and DO replenishment/net consumption in a river or estuary with the ultimate objective of describing the interplay between physical and biological processes while acknowledging that the various processes influencing DO variation in an estuary are inherently spatially and temporally variable over finer scales.

### *2.1. DO Variation along a River or Estuary*

To study DO variation along a river or an estuary and the relationship between DO variation and timescales, we assume that the estuary or river can be represented by a rectangle channel with the constant cross-section area A ($m^2$) and depth H (m) for simplicity without losing generalization. The mass balance of DO (tidally averaged for estuary), which is similar to the salt balance, can be expressed as [15–17]:

$$O_t + \frac{1}{A}(uAO)_x + (wO)_z = \frac{1}{A}(k_H O_x A)_x + (k_z O_z)_z + P - R\,, \quad (1)$$

where $O$ (g $O_2$ $m^{-3}$) is the DO concentration at a specific location ($x$, $z$) and time ($t$), $u$ and $w$ (m $s^{-1}$) are the horizontal and vertical velocities at location ($x$, $z$), respectively; $k_H$ and $k_z$ ($m^2$ $s^{-1}$) are the horizontal and vertical diffusivity, respectively; and $P$ and $R$ (g $O_2$ $m^{-3}$ $s^{-1}$) are DO production and total consumption rates, respectively. Using the boundary conditions

$k_z \frac{dO}{dz}(z=0) = \theta_s$ and $k_z \frac{dO}{dz}(z=-H) = \theta_b$, where $\theta_s$ and $\theta_b$ are the surface and bottom DO fluxes (g $O_2$ $m^{-2}$ $s^{-1}$), respectively [17], the vertical mean DO can be expressed as:

$$\overline{O_t} + \frac{1}{A}\left(\overline{u}A\overline{O}\right)_x + \frac{1}{A}\left(\overline{u'O'}A\right)_x = \frac{1}{A}\left(k_H\overline{O_x}A\right)_x + \overline{P} - \overline{R} + \frac{1}{H}\left(\theta_s - \theta_b\right). \quad (2)$$

Under the steady-state assumption (i.e., $\overline{O_t} = 0$), and assuming that $\frac{1}{A}\left(k_H\overline{O_x}A\right)_x$, and $\frac{1}{A}\left(\overline{u'O'}A\right)_x \ll \frac{1}{A}\left(\overline{u}A\overline{O}\right)_x$, the dominant advection terms of the vertical mean $\overline{O}$ can be expressed as (hereafter, we dropped the over bar of all variables for convenience):

$$uO_x = P - \left(R + \frac{\theta_b}{H}\right) + \frac{1}{H}\theta_s\,. \quad (3)$$

Using the boundary condition and assuming $k_z$ is independent of depth, $\theta_s$ can be approximated as follows:

$$\frac{\theta_s}{k_z} = \frac{dO}{dz} \approx \frac{O_s - O}{h}, \quad (4)$$

Here, we scaled the flux $\theta_s$ by using the difference between DO at the surface ($O_s$) and mean $O$ at the water depth of $h$ below the surface at location $x$. $O_s$ can be higher, lower, or equal to saturation DO. Using Equation (4), the last term of Equation (3) can be written as $\frac{k_z}{Hh}(O_s - O)$. Note that $Hh/k_z$ is a vertical mixing timescale. Although $h$ is not readily determined, the mixing scale can be obtained from model simulations of surface water age [10], which will be further discussed. We refer to this timescale as vertical exchange time ($\tau_v$), $\tau_v = Hh/k_z$, which quantifies how long it will take for surface water with high DO to be transported to the location $x$. By substituting Equation (4) into Equation (3), Equation (3) can be written as:

$$\frac{dO}{dx} + \frac{O}{u\tau_v} = -\frac{R_N}{u} + \frac{O_s}{u\tau_v}\,, \quad (5)$$

where $R_N = \left(R + \frac{\theta_b}{H} - P\right)$, in which $R_N$ is the net DO consumption rate, resulting from water column respiration, production, and bottom sediment oxygen demand [10]. Note that $-R_N$ is net ecosystem metabolism (NEM) and $R_N$ can be either positive or negative, which can be estimated through measurements. A positive $R_N$ indicates that respiration is larger than production and vice versa. If we assume the upstream boundary $O = O_u$ at $x = 0$, the solution of Equation (5) is:

$$O = [O_u - (O_s - \tau_v R_N)]e^{\frac{-\tau_u}{\tau_v}} + O_s - \tau_v R_N \quad (6)$$

where $\tau_u = x/u$ is the time required for freshwater travel from the upstream boundary to the location $x$ (i.e., residence time [9,18,19]), which can be estimated by freshwater age [18,19]. The first term on the right side of Equation (6) is the deficit of DO consumption due to upstream DO advection, and the last term is the DO consumed during the period of vertical transport. Equation (6) indicates that the mean DO concentration at location $x$ is a superimposition of DO advection from the upstream and vertical mixing. When $\tau_u$ is large (slow-moving water), the first term vanishes, indicating that the DO-rich water transported from the upstream boundary has been depleted and has less impact on DO dynamics at the present location.

In estuaries, DO-rich water can also enter from the outside through gravitational circulation [3]. The DO input with saltwater has the same effect as freshwater on DO. Therefore, the general solution can be expressed as the superimposition of the horizontal DO transport from the upper stream, downstream, and surface as:

$$O = O_s - \tau_v R_N + [O_u - (O_s - \tau_v R_N)]e^{\frac{-\tau_u}{\tau_v}} + [O_d - (O_s - \tau_v R_N)]e^{\frac{-\tau_d}{\tau_v}} \quad (7)$$

where $\tau_d = x/u_e$ is the time required for saltwater to be transported to the location x in the estuary, which can be estimated by saltwater age [10]; $u_e$, is the exchange flow; $O_d$ is the DO concentration at the downstream boundary; and $\tau_R = 1/R_N$ is the timescale for net DO consumption. Note that DO transport from the upstream or downstream boundary is modulated by the vertical exchange timescale. If $\tau_v$ is relatively short ($\tau_v \ll \tau_u$ or $\tau_d$ , i.e., slow horizontal transport), the effect of the transport of DO-rich water from the upper stream and downstream becomes negligible. When $\tau_v \gg \tau_u$ or $\tau_d$ , DO transported from the upstream or downstream boundary dominates the DO replenishment. By introducing timescales, we presented the solution from a Lagrangian perspective, where DO can be assessed at each observational location using a common currency [9]. Therefore, DO concentration can be expressed by the horizontal freshwater and saltwater ages, vertical exchange times of water, and net DO consumption time at the observational locations.

For a special case when $O_u = O_d = O_s = O_{sa}$, i.e., when DO concentrations at the boundaries are all equal to the saturated *DO* concentration ($O_{sa}$), Equation (7) can be simplified as:

$$O = O_{sa} - O_{sa}\tau_v/\tau'_R(1 - e^{\frac{-\tau_u}{\tau_v}} - e^{\frac{-\tau_d}{\tau_v}}). \quad (8)$$

The normalized *O* distribution is

$$\frac{O}{O_{sa}} = 1 - \frac{1}{\tau^*_R}(1 - e^{-\tau^*_{eu}} - e^{-\tau^*_{ed}}), \quad (9)$$

where we define $\tau'_R = \frac{O_{sa}}{R_N}$ as a timescale for net DO consumption and the dimensionless timescale parameters $\tau^*_{eu} = \frac{\tau_u}{\tau_v}$, $\tau^*_{ed} = \frac{\tau_d}{\tau_v}$, $\tau^*_R = \frac{\tau'_R}{\tau_v}$. Figure 1 shows the contours of DO variations with respect to $\tau^*_{ed}$ and $\tau^*_R$ (there is a similar DO distribution for the upper boundary $\tau^*_{eu}$ and $\tau^*_R$). A decrease in $\tau^*_R$ (i.e., an increase in DO consumption rate) increases the chance of hypoxia, while an increase in gravitational circulation or freshwater discharge (i.e., a decrease in $\tau^*_{eu}$ or $\tau^*_{ed}$) improves DO conditions inside the estuary for a given $\tau_v$ (Figure 1a). The onset of hypoxia depends on the ratio of DO consumption and vertical exchange and horizontal transport times. DO concentrations at the boundary affect DO concentrations inside the estuary, and incoming water with low DO concentration (e.g., $O_d$ = 0.5 $O_{sa}$) results in a decrease in estuarine DO concentrations (Figure 1b). This impact varies with saltwater age. When saltwater age is low at a location, either due to a short distance from the downstream boundary or a high exchange flow, low-DO water at the mouth of the estuary is transported into the location quickly, and the incoming water with lower DO concentrations significantly decreases DO concentrations at that location. However, DO at the downstream boundary has a low impact on local DO dynamics at a location where saltwater age is high, as most incoming DO from the downstream boundary has been consumed before reaching that location.

### *2.2. Timescales Controlling Hypoxia in a System*

If we assume the waterbody is well mixed with a volume V ($m^3$) and surface area A ($m^2$), it has one principal opening to transport water out. Inflows to the system occur through estuarine circulation that moves water into the system from its opening. DO input to the system can be from the upstream and downstream boundaries as well as through the surface exchange, and DO consumption is proportional to the volume of the waterbody. We acknowledge that this is an overly simplified system. The purpose of this analysis is to understand the interplay between physical transport processes and DO consumption at a system-wide scale. With these assumptions, the vertical-averaged mass balance under the steady state over a specified averaging period T (e.g., T = tidal cycle, or day) can be simplified under the steady state and can be written as follows [11]:

$$(Q_{in} + Q_r)O_{sa} - Q_e O - R_N V + \frac{k_z}{h}(O_{sa} - O)A = 0\,, \quad (10)$$

where $O$ is the mean oxygen of the waterbody (g $O_2$ $m^{-3}$) and $O_{sa}$ is DO saturation (g $O_2$ $m^{-3}$). Here, we use $O$ as the system mean DO for convenience rather than the DO at location x as in Equation (5). $Q_{in}$ is the inflow ($m^3$ $d^{-1}$) at the downstream boundary, $Q_r$ is the freshwater discharge, $Q_e$ is the outflow ($m^3$ $d^{-1}$) at the downstream boundary, and $Q_e = Q_{in} + Q_r$ [11]. Here, we assume the DO inputs from upstream, downstream, and the surface are at saturation. The first two terms are advection terms. $R_N$ is the net respiration rate (g $O_2$ $m^{-3}$ $d^{-1}$) as defined before. The last term of Equation (10) is the approximation of DO exchange between the waterbody and surface water with a DO concentration equal to $O_{sa}$ (Equation (4)). Assuming that volume does not change, Equation (10) can be written as:

$$Q_e(O_{sa} - O)/V - R_N + \frac{k_z}{Hh}(O_{sa} - O) = 0\,. \tag{11}$$

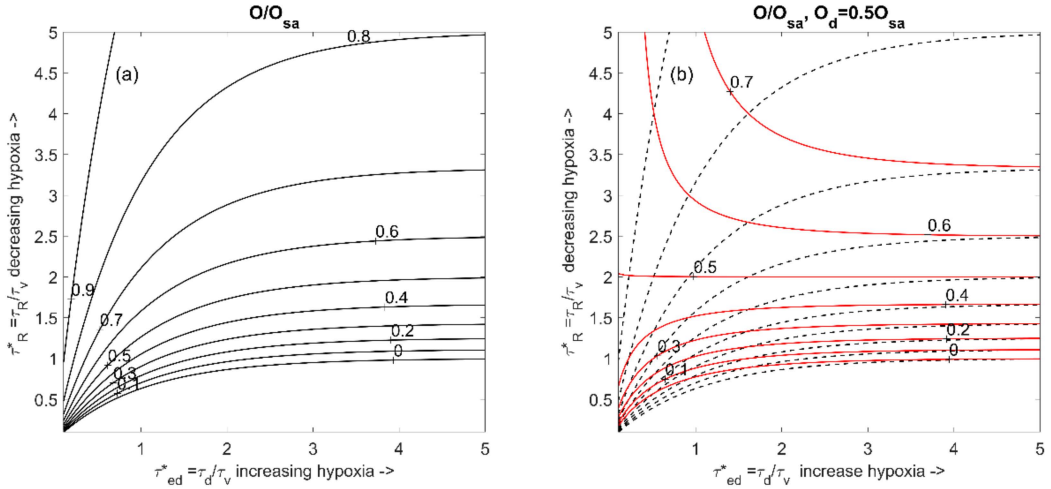


**Figure 1.** Change in normalized DO with respect to non-dimensional physical and biological timescale parameters (only shows DO influence from the mouth, $\tau^*_{ed}$). Panel (**a**) shows that an increase in net DO consumption rate (decreased $\tau^*_R$) increases the chance of hypoxia, while an increase in gravitational circulation (decreased $\tau^*_{ed}$) improves the DO conditions inside the river or estuary for a given vertical exchange time. Panel (**b**) shows that when DO outside of a waterbody is low, it can affect the DO inside the estuary, resulting in a decrease in DO concentrations (red lines).

Note that the term $V/Q_e$ is the residence time [11,20]. Let $\tau = V/Q_e$, and $\tau_v = Hh/k_z$ as the residence and vertical exchange times, respectively. Equation (11) can be expressed as:

$$O(\frac{1}{\tau} + \frac{1}{\tau_v}) = O_{sa}\left(\frac{1}{\tau} + \frac{1}{\tau_v}\right) - R_N\,. \tag{12}$$

The mean DO in the waterbody can be expressed as

$$O = O_{sa} - R_N\left(\frac{\tau_v}{1 + \frac{\tau_v}{\tau}}\right) \text{ or } O = O_{sa} - R_N\left(\frac{\tau}{1 + \frac{\tau}{\tau_v}}\right). \tag{13}$$

Equation (13) shows two typical cases, for which $O = O_{sa} - R\tau_v$ if $\tau_v \ll \tau$, or $O = O_{sa} - R\tau$ if $\tau \ll \tau_v$. For a large waterbody in which $\tau$ is much longer than $\tau_v$, such as the Chesapeake Bay, DO is mainly controlled by $\tau_v$, except in the regions near the headwater or near the mouth. For a small waterbody with a short residence time, DO can be renewed by transporting DO-rich water from its boundaries, either from its upper stream or downstream. Although the system is simplified, the result (Equation (13)) provides the key relationship between DO transport and net DO consumption. Given $R_N$, $\tau_v$, and $\tau$, the hypoxic condition of a waterbody can be determined. Although the model

is derived for the whole system, the relationship is applicable to a segment of a river or estuary to assess local DO in a sub-region, which provides a more accurate estimation.

### *2.3. Compute Vertical Exchange Time and Water Ages*

To demonstrate the use of timescales to determine DO, we used the Chesapeake Bay as an example. The Environmental Fluid Dynamics Code (EFDC) [21,22] was applied to the Chesapeake Bay to simulate hydrodynamics and transport timescales. The EFDC uses a boundary-fitted curvilinear grid model in the horizontal and sigma grids in the vertical. This model was calibrated for the surface elevation, current, and salinity of the Chesapeake Bay [13]. The model produced reliable stratification and destratification responses temporally and spatially in both wet and dry years. The grid is shown in Figure 2a. The model is forced by the interpolated observed tide at the open boundary (http://tidesandcurrents.noaa.gov, accessed on 20 March 2024), freshwater discharges of eight main tributaries (http://waterdata.usgs.gov/nwis/, accessed on 20 March 2024), and wind obtained from the North America Regional Reanalysis (NARR) produced at the National Center for Environmental Prediction (https://psl.noaa.gov/data/gridded/data.narr.html, accessed on 23 March 2024). The climatology salinity data were used at the open boundary.

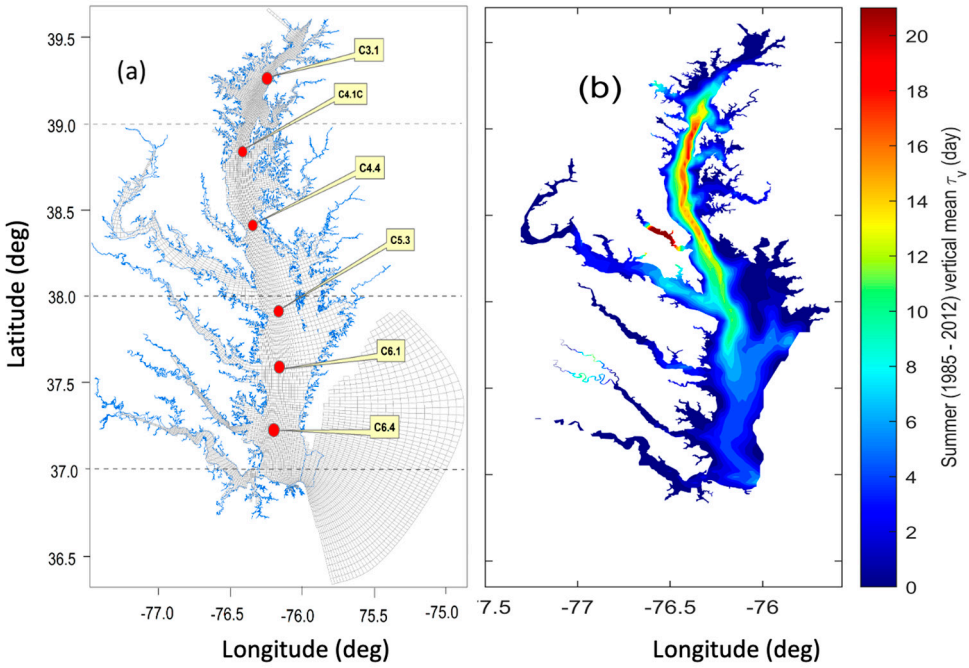


**Figure 2.** (**a**) Model grid of the Chesapeake Bay and observational stations (red dots). (**b**) Average summer (1985–2012) vertical mean transport time ($\tau_v$).

The Constitutional-oriented Age and Residence Time Theory (CART) [18,19] was applied to compute various water ages corresponding to vertical exchange time, $\tau_v$, freshwater transport time (freshwater age $\tau_u$), and saltwater transport time (saltwater age $\tau_d$). The $\tau_v$ was computed using the water age of the surface water by continuously releasing dye at the surface and setting the age concentration to be zero at the surface [23]. The transport time of freshwater and saltwater from the open boundary was computed by releasing dye at the freshwater inflows and open boundary, respectively [24]. The age at freshwater inflow location and open boundary are set to be zero, respectively. It should be noted that $\tau_v$ represents the age of water parcels that can be transported vertically and laterally, and can come from both upstream freshwater and saltwater when the water parcels touch the surface during the transport. Every time, the age is set to zero when the water parcels touch the surface. Therefore, the $\tau_v$ is the elapsed time since the last time that the parcels contact the surface [23]. Different from $\tau_v$, the ages of water parcels do not change even when they

contact the surface, as we need to use the freshwater and saltwater ages to represent DO transport from the boundaries.

## 3. Results

### *3.1. Transport Timescales*

The averaged summer vertical mean $\tau_v$ distribution from 1985 to 2012 is shown in Figure 2b. $\tau_v$ distribution shows that long $\tau_v$ occurs in the deep change in the upper portion of the Bay. It takes approximately 20 d for the surface DO-rich water to be transported to the lower layer on average in summer in the deep channel. The area with longer $\tau_v$ is coincident with the Bay hypoxic zone [25]. Figure 3 depicts the monthly mean ages in July for the wet flow year of 1998 and the mean flow year of 2000, respectively, for freshwater, saltwater, and surface water ($\tau_v$). It can be seen that age varies under different flow years. The freshwater age becomes shorter near the surface during the wet year than the mean flow year (Figure 3a,b). With a higher freshwater input during the wet year, saltwater age also becomes shorter compared to the mean flow year (Figure 3c,d). During the wet year, the estuary becomes more stratified, and $\tau_v$ increases compared to the mean flow year (Figure 3e,f).

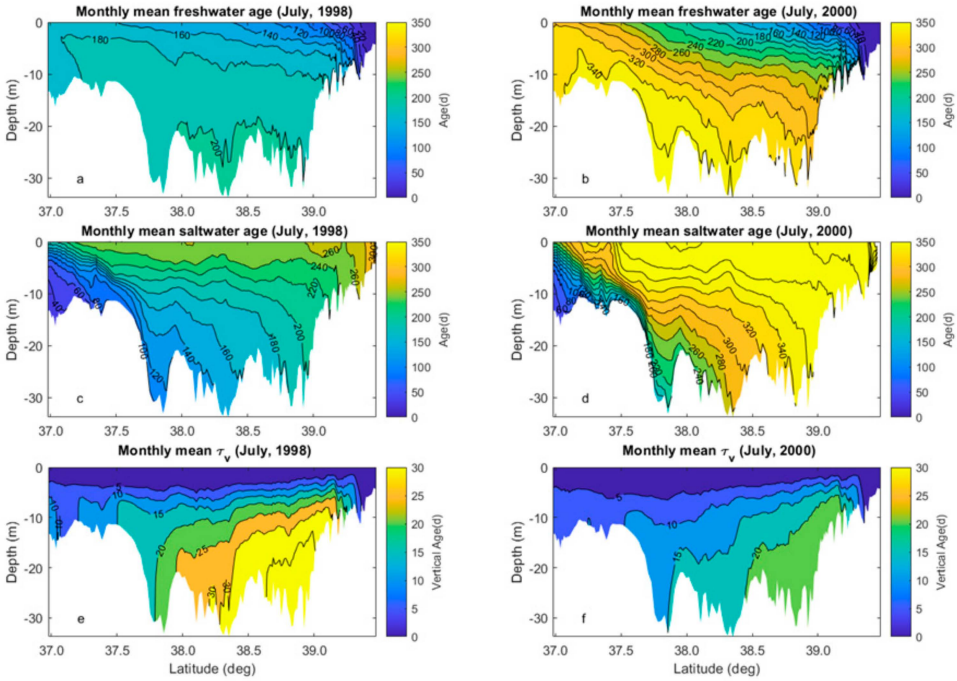


**Figure 3.** An example of model-simulated monthly mean water ages in July for a wet flow year (1998) and a mean flow year (2000) ((**a**,**b**) show freshwater age, (**c**,**d**) show saltwater age, and (**e**,**f**) show vertical exchange time, $\tau_v$).

Figure 4 shows the mean vertically averaged ages for freshwater, saltwater, and surface water ($\tau_v$) between 1985 and 2012 in summer along the deep channel together with their variations with one standard deviation. It takes more than 250 d for the freshwater to be transported out of the estuary. The short freshwater age (<50 d) is only located in a small region with a short distance from the discharge location in summer. It takes more than 200 d for the saltwater to be transported to the upstream in summer. $\tau_v$ longer than 15 d is located in the region from a 38-degree to 39.25-degree latitude. The longest $\tau_v$ is located near Station 4.1C.

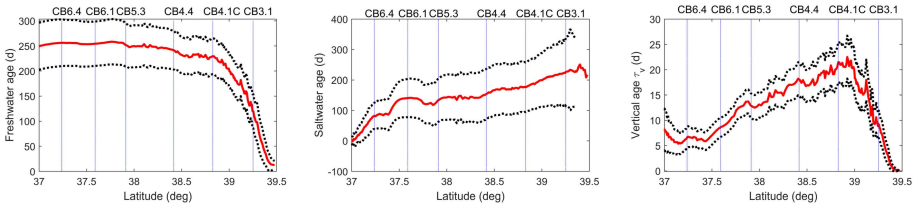


**Figure 4.** Mean vertically averaged water ages during the summer months of June to August from 1985 to 2012 (black dashed lines are one standard deviation, and station locations are marked with dashed vertical lines).

### *3.2. Dissolved Oxygen*

Figure 5 shows the comparison of observed DO and modeled DO concentrations using Equation (8) at selected stations. Observational DO are monthly observations obtained from the Chesapeake Bay Program. Observation stations are shown in Figure 2. DO saturation was computed using observed temperature and salinity at each station near the surface. The net consumption rate was computed as $R = R^{20}\,\theta^{T-20}$, where $R^{20}$ is the net respiration rate at 20 °C, $\theta = 1.03$ [26], and $T$ is temperature. The net DO consumption rate can be estimated as the sum of SOD and water column respiration, using an SOD value of 1.0 g $O_2$ $m^{-2}$ $d^{-1}$ for the mainstem of the Bay. This value is slightly higher than the measured high value of 0.86 g $O_2$ $m^{-2}$ $d^{-1}$ reported by Cowan and Boynton [27] but is lower than the value reported by Boynton and Kemp [28]. The mean concentration of dissolved organic carbon (DOC) in the mainstem of the Bay is about 2.0 g $m^{-3}$ to 4.0 g $m^{-3}$. We used 2.0 g $m^{-3}$, a mean DOC decay rate of 0.05 $d^{-1}$, and a depth of 20 m [10,29]; the oxygen consumption rate was approximately 0.32 g $O_2$ $m^{-3}d^{-1}$, or 0.013 g $O_2$ $m^{-3}h^{-1}$at 20 °C. This value is within the range of measured values for the Chesapeake Bay between 0.01 and 0.04 g $O_2$ $m^{-3}h^{-1}$ [29]. We estimated the mean respiration rate $R^{20}$ based on the minimum root-mean-square error (RMSE) between observed and modeled DO. The estimated net consumption rate at 20 °C ranges from 0.15 to 0.36 g $O_2$ $m^{-3}d^{-1}$. Higher respiration rates are located in the upper Bay. The results are within the same range of observations [29]. The results show a good agreement between the modeled DO and observations, with a mean RMSE ranging from 0.73 to 0.92. The difference between modeled DO and observations can be attributed to the use of constant net consumption rate of $R^{20}$. Because of interannual variations of nutrient loadings, $R^{20}$ has a high interannual version, which is highly correlated with the nutrient loading [13]. It is expected that the modeled DO will be improved if temporally varying net consumption rates are used.

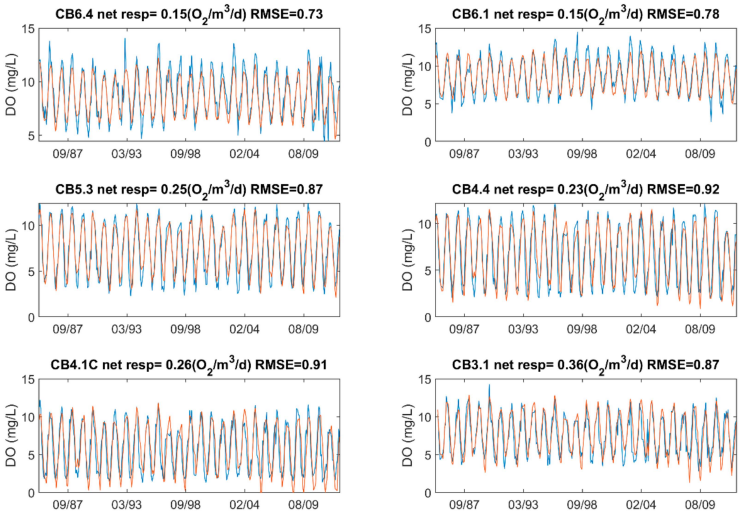


**Figure 5.** Comparisons of model results of vertical mean DO against observations at selected stations (blue lines are observations and red lines are model results).

## 4. Discussion

### *4.1. Transport Timescales*

The simplified models provide a Lagrangian perspective on DO variations. DO at a location can be estimated as the superimposition of the DO transport from the upper stream and downstream, and from the surface (Equation (7)). In the context of a water parcel, the impact on DO due to transport can be divided into three components: transport from the surface ($Q_v$, $\tau_v$), upstream freshwater ($Q_u$, $\tau_u$), and downstream saltwater ($Q_d$, $\tau_d$), as depicted in Figure 6. In particular, the computation of $\tau_v$ encompasses all water parcels that have encountered the surface since the last time during the transport, which may result from direct vertical mixing, lateral transport due to lateral circulation, and transport from both the upstream and downstream locations. When water parcels enter the estuary through upstream or downstream boundaries, only a fraction of the water parcels are transported to the specified location without encountering the surface, and the rest of them reach the surface during the transport process. Upon contact with the surface, the DO of the water parcels is mixed up with the DO near the surface, and the age of the water parcels resets to zero. Subsequently, these water parcels are treated as the surface water parcels in the calculation. By understanding the pathways and the transport times of these three water ages, we can estimate the DO consumption during their transport, thus estimating DO at each location. Our simplified equation captures these distinctions among water parcels, despite being derived from a simplified model. DO consumption is quantified by freshwater, saltwater, and vertical transport ages to represent these three types of water parcels.

We computed the water age using CART, which provides an accurate estimate of the water age including all the dynamic processes, variations of bathymetry, and forcings. In practice, the characteristics of these timescales can also be estimated based on mean dynamic conditions or characteristics. The freshwater age at location x can be estimated by $x/u_{A,}$ where $u_A$ is the cross-section averaged mean velocity (i.e., Q/A, where Q is discharge and A is cross-section area). The exchange flow can be scaled by the gravitational flow $U_E$ and estimated as $(L - x)/U_E$, where $L$ is the length of the estuary, $U_E = \frac{g\beta S_x H^3}{48K_M}$ [15], $S_x$ is the horizontal salinity gradient, $K_M$ is vertical eddy viscosity, $H$ is depth, and $\beta = 7.7 \times 10^{-4}$. $K_M$ can be estimated as $K_M = K(1 + 10R_i)^{-1/2} \approx 0.316$ K, $K = C_D HU$, where $C_D$ is the drag coefficient, $U$ is the tidal averaged velocity, and $R_i$ is the Richardson number [30]. The vertical exchange time can be estimated as $\tau_v = H^2/K_s$ [30], where $K_s = K(1 + 3.3R_i)^{-1/2} \approx 0.167$ K.

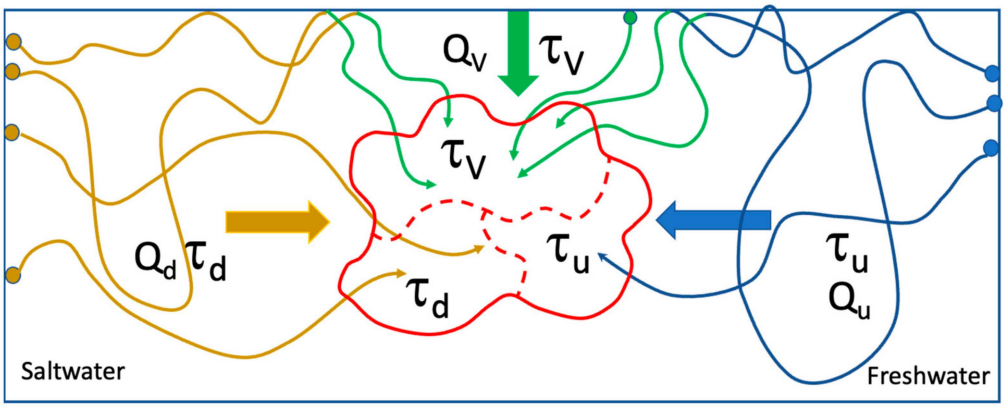


**Figure 6.** A diagram illustrating the pathways of water parcels during transport.

*4.2. Hypoxia Assessment*

If we assume that the DO at the boundaries and surface reaches saturation, $O_{sa}$, then Equation (7) can be written as:

$$O = O_{sa} - \tau_v R_N (1 - e^{\frac{-\tau_u}{\tau_v}} - e^{\frac{-\tau_d}{\tau_v}}) \quad (14)$$

We can define a combined timescale $\tau_T = \tau_v (1 - e^{\frac{-\tau_u}{\tau_v}} - e^{\frac{-\tau_d}{\tau_v}})$, and the DO concentration at location $x$ can be expressed as:

$$O(x) = \max((O_{sa}(x) - \tau_T(x) R_N(x)),\ 0) \quad (15)$$

where all variables vary with location. If water moves much faster than $\tau_v$ ($\tau_d$ or $\tau_u \ll \tau_v$), DO will approach saturation conditions (or DO conditions at the boundary), and there is not enough consumption time for DO to be depleted.

If hypoxia is defined as less than 2 g $O_2$ $m^{-3}$, the combined transport timescale should satisfy the following condition without hypoxia:

$$\tau_T \leq \frac{O_{sa} - 2}{R_N} \quad (16)$$

This equation provides a simple assessment of DO conditions at any location. For example, if $O_{sa}$ = 7 g $m^{-3}$ in summer, $R_N$ is on the order of 0.3 per day [13] and requires $\tau_T \leq 16.67$ days to satisfy the conditions without hypoxia. The mean $\tau_T$ is about 20 d at Station CB4.1C and is about 14 d at Station CB5.2 (Figure 4). This suggests that the mean DO is less than 2 g $O_2$ $m^{-3}$ at Station CB4.1C, but it is larger than 2.0 g $O_2$ $m^{-3}$ at Station 5.3.

Fennel and Testa [14] compared the residence time and timescales of oxygen consumption and introduced a simple scale for hypoxia conditions as follows: $\tau_{hyp} = \frac{O_{ini}}{R}$ and $\gamma = \frac{\tau_{hyp}}{\tau}$ ($O_{ini}$ is the initial waterbody DO concentration that can be assumed to be under saturation, $R$ is the net DO consumption rate, and $\tau$ is residence time). They suggest that a waterbody under hypoxia conditions requires $\gamma < 1$. This scale provides a convenient way to evaluate hypoxia conditions in a waterbody. However, this criterion is for anoxia and overlooks the difference between residence time and vertical exchange time when controlling DO replenishment. It works for a small waterbody with a short residence time or a system where the residence time is on the same order of $\tau_v$. For a large estuary with long residence times, vertical replacement is the dominant method of DO replacement through physical transport processes, such as the Chesapeake Bay (mean $\tau$ = 180 d [31]) and the James River (mean $\tau$ = 90 d [32]). Therefore, the residence time $\tau$ needs to be carefully defined. For example, in the James River, a tributary of the Chesapeake Bay, the average net DO consumption rate in the water column is about 0.3 g $O_2$ $m^{-3}d^{-1}$ [10], mean residence time is 90 d, and the residence time during high flow is about 40 d [32]. Assuming that summer saturation DO concentration is 7 g $O_2$ $m^{-3}$, and residence time is 40 d, it gives $\gamma < 0.58 < 1$, indicating a condition favoring hypoxia according to the scaling by Fennel and Testa's criteria [14]. However, hypoxia does not occur in the James River due to short vertical exchange time and the presence of strong gravitational circulation near the mouth [3], which suggests that using residence time as a measure is not adequate for large estuaries.

Using Equation (13), we can find the required conditions when DO is zero (O = 0, anoxia condition), and $\gamma$ can be written as

$$\gamma = \frac{O_{sa}}{R\tau_v} = \frac{1}{1 + \frac{\tau_v}{\tau}} < 1 \text{ if } \tau_v << \tau \text{ or } \gamma = \frac{O_{sa}}{R\tau} = \frac{1}{1 + \frac{\tau}{\tau_v}} < 1\ \tau << \tau_v \quad (17)$$

This gives $\gamma < 1$ for anoxia conditions. It can be seen that a more accurate estimation is to use different timescales with consideration of dominant hydrodynamic conditions causing low DO when using this criterion. Note that $\tau_v$ is about 10 d in the James [10], which

is less than residence time $\tau$ in the James. Using the same values of $R_N$ (0.3 g $O_2$ $m^{-3}d^{-1}$) and saturation DO concentration (7.0 g $O_2$ $m^{-3}$), we obtain $\gamma = 2.3 > 1$. This suggests there are no anoxia conditions in the James.

For hypoxia conditions defined as DO concentration $\leq 2$ g $O_2$ $m^{-3}$, a criterion for hypoxia can be expressed as:

$$\gamma' = \frac{O_s - 2}{R\tau_v} =< 1 \text{ or } \gamma' = \frac{O_s - 2}{R\tau} < 1. \quad (18)$$

This criterion can also be applied to a section of an estuary. For example, in the middle of Chesapeake Bay where influence from both upstream and downstream are minimum, $R \approx 0.3$ g $O_2$ $m^{-3}d^{-1}$, $\tau_v$ is about 20 d, and $\tau > 100$ d in summer (Figure 5, Stations CB4.4 and CB4.1C), so that $\gamma\prime = 0.83$, which indicates that hypoxia is favored. On the other hand, in the lower Bay (Figure 5, Stations CB6.4, CB6.1, and CB5.3), $\tau_v$ is less than 10 d, and $\tau$ is less than 50 d, leading to $\gamma\prime > 1$, which indicates that hypoxia is not favored if measured by the mean DO concentration.

It should be noted that the criteria presented here are for assessing the vertically averaged DO conditions for a system. Since the vertically mean DO concentration is typically higher than the bottom DO concentration, the bottom water can experience hypoxia conditions if the estuary is stratified at a certain location even though the mean DO concentration is high. For the estimation of bottom DO concentration in an estuary, the vertical exchange time at the bottom should be used in Equations (17) and (18) based on the two-layer model developed by Shen et al. [10]. On the other hand, if the gradational circulation is strong at the location near the mouth, which is shorter than vertical exchange time, Equation (16) should be used for the assessment of DO conditions at the location of concern.

## 5. Conclusions

To understand the impact of hydrodynamics and biochemical processes on hypoxia in rivers and estuaries, we introduced timescales representing these processes to quantify variations in DO concentrations. These timescales serve as a common currency [9] for assessing the onset of hypoxia and enable cross-system comparisons. Derived from a simple model, these timescales offer insights into the intricate interplay between DO consumption and dynamic replenishment without sacrificing generality. The resulting relationship provides a Lagrangian perspective, enhancing our understanding of the physical processes involved in DO consumption and replenishment.

Water parcels at a specific location are categorized into three components: those transported from the surface, from upstream freshwater, and from downstream saltwater. In particular, the component of surface-transported water parcels encompasses all water parcels that have encountered the surface during transport, which may result from direct vertical mixing, lateral transport due to lateral circulation, and transport from both the upstream and downstream locations. Water parcels transported from upstream and downstream boundaries without contacting the surface are classified as freshwater and saltwater parcels, respectively. Water ages are computed to represent the transport timescales for these three types of water parcels based on CART, providing accurate estimates of transport times that account for all the dynamic transport processes. The estimation of DO concentration at a location of concern is achieved based on the established relationships, computed water ages, and estimated net DO consumption rates. Applying the simple model with timescales computed for the Chesapeake Bay, our results demonstrate accurate predictions of DO levels over 26 years at multiple stations. With an appropriate estimate of temporal variations of the net DO consumption rate, DO estimation can be improved.

We have introduced a simple model aimed at providing a general understanding of the key processes controlling hypoxia in estuaries while acknowledging the many assumptions inherent in the model. To address specific ecological problems and answer management questions, complex ecosystem models are needed for different temporal

and spatial scales. However, our simple model approach provides criteria that allow us to conduct cross-system comparisons for the potential formation of hypoxia conditions. Criteria for cross-system comparison to determine hypoxia and anoxia are established based on transport timescales, highlighting the critical importance of these timescales in using such criteria. Our study reveals that the hypoxia/anoxia status of a river or estuary system is determined by the timescales of vertical exchange, freshwater transport, saltwater transport, and net DO consumption rate. The shortest timescale that determines the DO replenishment is the dominant factor physically controlling DO dynamics in estuaries. The interplay between DO consumption and dynamic replenishment emerges as the primary determinant of hypoxia in an estuarine environment.

**Author Contributions:** Conceptualization, J.S.; Methodology, J.S. and Q.Q.; Investigation, J.S. and Q.Q.; Writing—original draft, J.S.; Writing—review & editing, J.S. and Q.Q. All authors have read and agreed to the published version of the manuscript.

**Funding:** This research received no external funding.

**Data Availability Statement:** The observation DO data is available at https://www.chesapeakebay.net/what/downloads/cbp-water-quality-database-1984-present (accessed on 20 March 2024). The processed age data refer to reference [13]. No new data was generated.

**Acknowledgments:** We thank Lisa Lucas for many constructive discussions. We are grateful to Jiabi Du for providing model results for age calculations in the Chesapeake Bay. We thank the two anonymous reviewers for their constructive comments and suggestions that have improved the manuscript.

**Conflicts of Interest:** The authors declare no conflicts of interest.

## References

1. Diaz, R.J. Overview of hypoxia around the world. *J. Environ. Qual.* **2001**, *30*, 275–281. [CrossRef] [PubMed]
2. Officer, C.B.; Biggs, R.B.; Taft, J.L.; Cronin, L.E.; Tyler, M.A.; Boynton, W.R. Chesapeake bay anoxia: Origin, development, and significance. *Science* **1984**, *223*, 22–27. [CrossRef]
3. Kuo, A.Y.; Neilson, B.J. Hypoxia and salinity in Virginia estuaries. *Estuaries* **1987**, *10*, 277–283. [CrossRef]
4. Cloern, J. Our evolving conceptual model of the coastal eutrophication problem. *Mar. Ecol. Prog. Ser.* **2001**, *210*, 223–253. [CrossRef]
5. Boicourt, W.C. Influence of circulation processes on dissolved oxygen in the Chesapeake Bay. In *Oxygen Dynamics in Chesapeake Bay: A Synthesis of Recent Research*; Smith, D.E., Leffler, M., Mackiernan, G., Eds.; Maryland Sea Grant Publication: College Park, MD, USA, 1992; pp. 7–59.
6. Hagy, J.D.; Boynton, W.R.; Keefe, C.W.; Wood, K.V. Hypoxia in Chesapeake Bay, 1950–2001: Long-term change in relation to nutrient loading and river flow. *Estuaries* **2004**, *27*, 634–658. [CrossRef]
7. Sanford, L.P.; Sellner, K.G.; Breitburg, D.L. Covariability of dissolved oxygen with physical processes in the summertime Chesapeake Bay. *J. Mar. Res.* **1990**, *48*, 567–590. [CrossRef]
8. Scully, M.E. Wind modulation of dissolved oxygen in Chesapeake Bay. *Estuaries Coasts* **2010**, *33*, 1164–1175. [CrossRef]
9. Lucas, L.V.; Deleersnijder, E. Timescale methods for simplifying, understanding and modeling biophysical and water quality processes in coastal aquatic ecosystems: A review. *Water* **2020**, *12*, 2717. [CrossRef]
10. Shen, J.; Hong, B.; Kuo, A.Y. Using timescales to interpret dissolved oxygen distributions in the bottom waters of Chesapeake Bay. *Limnol. Oceanogr.* **2013**, *58*, 2237–2248. [CrossRef]
11. Shen, J.; Du, J.; Lucas, L.V. Simple relationships between residence time and annual nutrient retention, export, and loading for estuaries. *Limnol. Oceanogr.* **2022**, *67*, 918–933. [CrossRef]
12. Lucas, L.V.; Thompson, J.K.; Brown, L.R. Why are diverse relationship observed between phytoplankton biomass and transport time? *Limnol. Oceanogr.* **2009**, *54*, 381–390. [CrossRef]
13. Du, J.; Shen, J. Decoupling the influence of biological and physical processes on the dissolved oxygen in the Chesapeake Bay. *J. Geophys. Res. Oceans* **2015**, *120*, 78–93. [CrossRef]
14. Fennel, K.; Testa, J.M. Biogeochemical controls on coastal hypoxia. *Annu. Rev. Mar. Sci.* **2018**, *11*, 105–130. [CrossRef]
15. Hansen, D.V.; Rattray, M. Gravitational circulation in straits and estuaries. *J. Mar. Res.* **1965**, *23*, 104–122. [CrossRef]
16. MacCready, P. Toward a unified theory of tidally-averaged estuarine salinity structure. *Estuaries* **2004**, *27*, 561–570. [CrossRef]
17. Lin, J.; Xie, L.; Pietrafesa, L.J.; Shen, J.; Mallin, M.A.; Durako, M.J. Dissolved oxygen stratification in two micro-tidal partially-mixed estuaries. *Estuar. Coast. Shelf Sci.* **2006**, *70*, 423–437. [CrossRef]
18. Deleersnijder, E.; Campin, J.-M.; Delhez, E.J. The concept of age in marine modelling: I. Theory and preliminary model results. *J. Mar. Syst.* **2001**, *28*, 229–267. [CrossRef]

19. Delhez, É.; Lacroix, G.; Deleersnijder, É. The age as a diagnostic of the dynamics of marine ecosystem models. *Ocean Dyn.* **2004**, *54*, 221–231. [CrossRef]
20. Vollenweider, R.A. Input-output models with special reference to the phosphorus loading concept in limnology. *Schweiz. Z. Hydrol.* **1975**, *37*, 53–84.
21. Hamrick, J.M. *A Three-Dimensional Environmental Fluid Dynamics Computer Code: Theoretical and Computational Aspects*; Special Report in Applied Marine Science and Ocean Engineering. No. 317; Virginia Institute of Marine Science, College of William and Mary: Williamsburg, VA, USA, 1992.
22. Hong, B.; Wang, G.; Xu, H.; Wang, D. Study on the transport of terrestrial dissolved substances in the Pearl River Estuary Using Passive Tracers. *Water* **2020**, *12*, 1235. [CrossRef]
23. Gustafsson, K.E.; Bendtsen, J. Elucidating the dynamics and mixing agents of a shallow fjord through age tracer modelling. *Estuar. Coast. Shelf Sci.* **2007**, *74*, 641–654. [CrossRef]
24. Deleersnijder, E.; Draoui, I.; Lambrechts, J.; Legat, V.; Mouchet, A. Consistent boundary conditions for age calculations. *Water* **2020**, *12*, 1274. [CrossRef]
25. Da, F.; Friedrichs, M.A.M.; St-Laurent, P. Impacts of atmospheric nitrogen deposition and coastal nitrogen fluxes on oxygen concentrations in Chesapeake Bay. *J. Geophys. Res. Ocean.* **2018**, *123*, 5004–5025. [CrossRef]
26. Thomann, R.V.; Mueller, J.A. *Principles of Surface Water Quality Modeling and Control*; Harper and Row: Manhattan, NY, USA, 1987.
27. Cowan, J.L.W.; Boynton, W.R. Sediment-water oxygen and nutrient exchanges along the longitudinal axis of Chesapeake Bay: Seasonal patterns, controlling factors and ecological significance. *Estuaries* **1996**, *19*, 562–580. [CrossRef]
28. Boynton, W.; Kemp, W. Nutrient regeneration and oxygen consumption by sediments along an estuarine salinity gradient. *Mar. Ecol. Prog. Ser.* **1985**, *23*, 45–55. [CrossRef]
29. Smith, E.; Kemp, W. Seasonal and regional variations in plankton community production and respiration for Chesapeake Bay. *Mar. Ecol. Prog. Ser.* **1995**, *116*, 217–231. [CrossRef]
30. Munk, W.H.; Anderson, E.R. Notes on the theory of the thermocline. *J. Mar. Res.* **1948**, *7*, 276–295.
31. Nixon, S.W.; Ammerman, J.W.; Atkinson, L.P.; Berounsky, V.M.; Billen, G.; Boicourt, W.C.; Boynton, W.R.; Church, T.M.; DiToro, D.M.; Elmgren, R.; et al. The fate of nitrogen and phosphorus at the land-sea margin of the North Atlantic Ocean. *Biogeochemistry* **1996**, *35*, 141–180. [CrossRef]
32. Shen, J.; Lin, J. Modeling study of the influences of tide and stratification on age of water in the tidal James River. *Estuar. Coast. Shelf Sci.* **2006**, *68*, 101–112. [CrossRef]

water

MDPI

*Article*

# Timescales of Ecological Processes, Settling, and Estuarine Transport to Create Estuarine Turbidity Maxima: An Application of the Peter–Parker Model

**Lilian Engel * and Mark Stacey**

Department of Civil and Environmental Engineering, University of California, Berkeley, CA 94720, USA; mstacey@berkeley.edu

* Correspondence: lmengel@berkeley.edu

**Abstract:** The estuarine exchange flow increases the longitudinal dispersion of passive tracers and trap sinking particles, potentially creating an estuarine turbidity maximum (ETM): a localized maximum of suspended particulate matter concentration in an estuary. The ETM can have many implications: dead zones due to increased turbidity or hypoxia from organic matter decomposition, naval navigation challenges, and other water quality problems. Using timescales, we investigate how the interaction between exchange flow and particle sinking leads to ETMs by modeling a sinking tracer in an idealized box model of the Total Exchange Flow (TEF) first developed by **Parker** MacCready. Results indicate that the balance of particle sinking and vertical mixing is critical to determining ETM size and location. We then focus on the role of ecology in ETM formation through the use of the Peter–Parker Model, a new biophysical model which combines the TEF box model with a Nutrient–Phytoplankton–Zooplankton–Detritus (NPZD) model, the likes of which were first developed by **Peter** J.S. Franks. Detritus sinking rates similarly influence detritus peak concentration and location (an ETM), but detritus ETMs occur in a different location than the sinking tracer due to the influence of biological factors, which create a time lag of about 1 day. Lastly, we characterize the flow of the models with a dimensionless parameter that compares timescales and summarizes the dynamics of the sinking tracer in ETM formation and that can be used across systems.

**Keywords:** estuarine turbidity maxima; Total Exchange Flow; physical–biological interactions; planktonic ecosystem



**Citation:** Engel, L.; Stacey, M. Timescales of Ecological Processes, Settling, and Estuarine Transport to Create Estuarine Turbidity Maxima: An Application of the Peter–Parker Model. *Water* **2024**, *16*, 2084. https://doi.org/10.3390/w16152084

Academic Editor: Chin H Wu

Received: 20 June 2024
Revised: 17 July 2024
Accepted: 19 July 2024
Published: 24 July 2024



## 1. Introduction

Estuarine exchange flow, driven directly by longitudinal density gradients [1] and indirectly by tidally asymmetric flows [2], provides the foundational circulation and transport for estuaries and fjords (Figure 1). These flows carry freshwater seaward, typically in an upper surface layer, with dense saline waters replacing those outflows at depth. This exchange produces flushing and dispersion of river-sourced scalars. Sinking particles, whether they are biotic or abiotic, can result in trapping and retention within the estuary [2], forming the estuarine turbidity maximum (ETM), a localized maximum of suspended particulate matter concentration in an estuary. While naturally occurring, ETMs are frequently associated with deteriorated ecological and physical conditions, including ecological dead zones due to either decreased light or increased organic matter decomposition, naval navigation challenges, and other water quality problems [3]. This study aims to investigate this sinking particle trapping phenomenon and how it relates to ETMs by looking at both a sinking tracer in isolation and sinking detritus within a planktonic ecosystem.

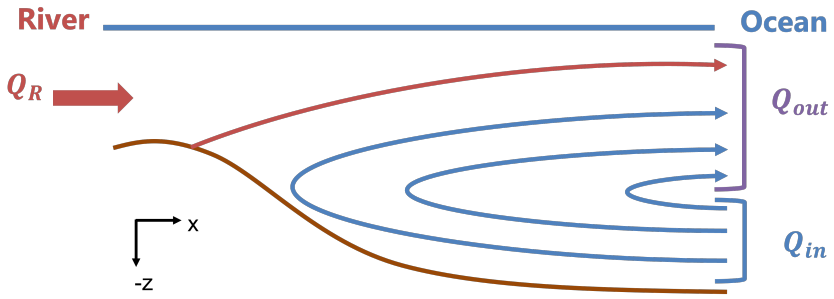


**Figure 1.** Schematic of longitudinal exchange. $Q_r$ is the river flow, $Q_{in}$ is the flow into the estuary, and $Q_{out}$ is the cumulative outflow consisting of the inflow and the river flow. Replicated with slight modifications from [2].

ETMs have been the subject of modeling studies for several decades. In 1978, ref. [4] used an idealized numerical model to investigate ETM formation and found it to be a function of settling velocity and the strength of the estuarine circulation. In 1980, researchers began to realize that ETMs could also be tidally caused [5]. Later studies found that there may be seasonal effects driving ETMs, especially for sediments deposited during large flooding events from winter storms [6]. While some estuaries develop ETMs from bathymetry or lateral trapping processes, most basic ETM dynamics can be described using a constant settling velocity [4,5,7]. A summary is provided in the review in [3], where one of their concluding thoughts is that more fundamental research in suspended particulate matter (SPM) dynamics is needed to be able to classify estuaries by their ETMs. Further, one of the main remaining questions those authors found in their review is, "How do the fast dynamics of SPM in the water column and the slow dynamics of the bottom pool interact to determine ETM locations and variability, and what processes govern the dynamics of the mobile bottom pool?" [3]. The analyses presented in this paper are motivated in part by this call for additional research on ETMs and how sinking particles contribute to these accumulations.

Sinking detritus can lead to hypoxic (low-oxygen) regions of the estuary, in addition to ETMs. For example, the Hood Canal section of the Puget Sound has seasonal periods of low dissolved oxygen [8], leading to fish kills and other ecosystem impacts [9]. One of the causes of hypoxic regions is the sinking of dead organic material that originally grew in the high-irradiance surface layer and is then decomposed at depth by aerobic microorganisms that use up the oxygen. Field studies have detected patchiness in dissolved oxygen levels in the depths of the Hood Canal [10]. An investigation of the interaction of detritus sinking with estuarine exchange flow will help to develop an understanding of the physical and biological processes that lead to oxygen depletion in the Hood Canal and other similar fjordic and estuarine systems. While we do not study the formation of hypoxia directly, it serves as a motivation for this work, which we hope will inform the further study of sinking decaying matter that leads to hypoxic regions via biological oxygen demand.

In order to capture dynamics similar to those in Puget Sound, we simulate a partially mixed estuarine system, with a density-driven circulation dominating the along-estuary net transport, which is reflective of the fjord-like systems of the Puget Sound region [2,9]. The exchange flow increases the longitudinal dispersion of passive tracers but traps sinking particles that enter the lower layer [2]. This study aims to investigate this sinking particle trapping phenomena and how it relates to ETMs/sinking particle/detritus accumulation, as well as to look to the future to understand how physical changes to the estuary will alter these ETMs.

The tool of this study is a numerical model of a two-layer estuary that divides the estuary into longitudinal compartments. This model was originally used by [11] to investigate residence times in the Salish Sea estuary by advecting a passive, non-sinking tracer. We expanded the box model in [11] with a sinking tracer to understand the relationship between particle sinking and exchange flow. First, we explore the implications

of varying parameters in this model for estuarine turbidity maximum/sinking particle accumulation in a system inspired by, but not strictly tied to, the Puget Sound. We next assess the planktonic ecosystem impacts of sinking detritus with the Peter–Parker Model, which adds a biological component that tracks nutrients, phytoplankton, zooplankton, and detritus (NPZD) [12] concentrations through time with the Total Exchange Flow (TEF) box model [11]. Then, we break apart the mechanisms leading to these accumulations by using a timescale analysis and compare the accumulations of systems with and without biology. Lastly, we characterize the flow of the model with a dimensionless parameter that summarizes the dynamics of the sinking tracer and can be used across systems.

## 2. Methods

### *2.1. Base: Total Exchange Flow Box Model*

The fundamental model in this study is a box model for Total Exchange Flow (TEF), as developed by **Parker** MacCready [11]. TEF is defined as the "sub-tidal volume flux integrated over a salinity range" [13]. For our system of study, we assume a two-layer exchange flow consisting of a shallow and deep layer [13]. River flow drives the shallow layer seaward, and the density gradient brings in the deep oceanic layer. Tidal currents then mix these shallow and deep layers vertically. Together, these processes comprise the TEF [13]. In this work, the advective fluxes are quantified by the Knudsen relation [14] (as in the original TEF framework from [13]), and the mixing between the shallow and deep layers is quantified by the Cokelet and Stewart efflux/reflux method [15]. The salinity distribution, which drives this TEF model, is obtained from the Chatwin solution [16] and follows the paradigm that the flow is predominantly density driven while tidal effects are limited to mixing. Note that there have been earlier similar box models of estuarine circulation [17], but this paper utilizes the approach in [11], which slightly modifies the grid staggering and utilizes the efflux/reflux method.

The box model reinterpretation of TEF for a tracer $C$ is defined in Figure 2 and as follows:

$$\begin{aligned} \frac{dC_s^i dV_s}{dt} &= (1 - a_s^{i-1}) q_s^{i-1} C_s^{i-1} - Q_s^i C_s^i + a_d^{i+1} q_d^{i+1} C_d^i + q_r^i C_{riv} \\ \frac{dC_d^i dV_d}{dt} &= (1 - a_d^{i+1}) q_d^{i+1} C_d^{i+1} - Q_d^i C_d^i + a_s^{i-1} q_s^{i-1} C_s^i \end{aligned} \tag{1}$$

$C$ is the general tracer concentration in either the shallow ($C_s$) or deep ($C_d$) layer at $x$-location $i$, $dV$ is the volume per box in the shallow ($s$) or deep ($d$) layer, $Q$ is the flow (defined in Equation (3) with units of $m^3 s^{-1}$), $q_s$ and $q_d$ are the rate of volume transport, which are a fraction of the flows calculated using the Cokelet and Stewart efflux–reflux theory (defined in Equation (2), from [15], also with units of $m^3 s^{-1}$) using $a_s$ and $a_d$, which are fractions of the flow solved to ensure mass and volume conservation (defined in Equation (4) [15]), $aq$ is a flow rate in which both the fraction ($a_s$ or $a_d$) and the total possible flow rate ($q_s$ or $q_d$) vary according the details given below, and $C_{riv}$ is the concentration of the scalar from the river transported by the rate of freshwater volume transport ('river flux') $q_r^i$ (units $m^3 s^{-1}$). As written, the river can input concentration into the estuary at any x-location. For this study, we only implement the river flux at $X = 0$ km, so, at all other locations, $q_r^i = 0$ $m^3 s^{-1}$. The exchanges in Equation (1) are illustrated in Figure 2. The flows/fluxes are related by Cokelet and Stewart salt and volume conservation [11,15]. The Cokelet and Stewart method separates the vertical fluxes as efflux and reflux, where efflux is the flow upward from the deep layer to the shallow layer ($a_d^{i+1} q_d^{i+1}$ in Figure 2) and reflux is the flow downward from the shallow to the deep layer ($a_s^{i-1} q_s^{i-1}$ in Figure 2). The net transport from longitudinal and vertical mixing only (no river flow) sums to

$$\begin{aligned} Q_s^i &= \left(1 - a_s^{i-1}\right) q_s^{i-1} + a_d^{i+1} q_d^{i+1} \\ Q_d^i &= \left(1 - a_d^{i+1}\right) q_d^{i+1} + a_s^{i-1} q_s^{i-1} \end{aligned} \tag{2}$$

where $Q_s^i$ and $Q_d^i$ combine the flow of the efflux or reflux, respectively, and the remaining longitudinal flow in each respective layer in Figure 2 [11]. Figure 3 shows the efflux/reflux method and how the flows in Equation (2) fit together. Note that the flows are located on the faces of the boxes, whereas the concentrations are at the center.

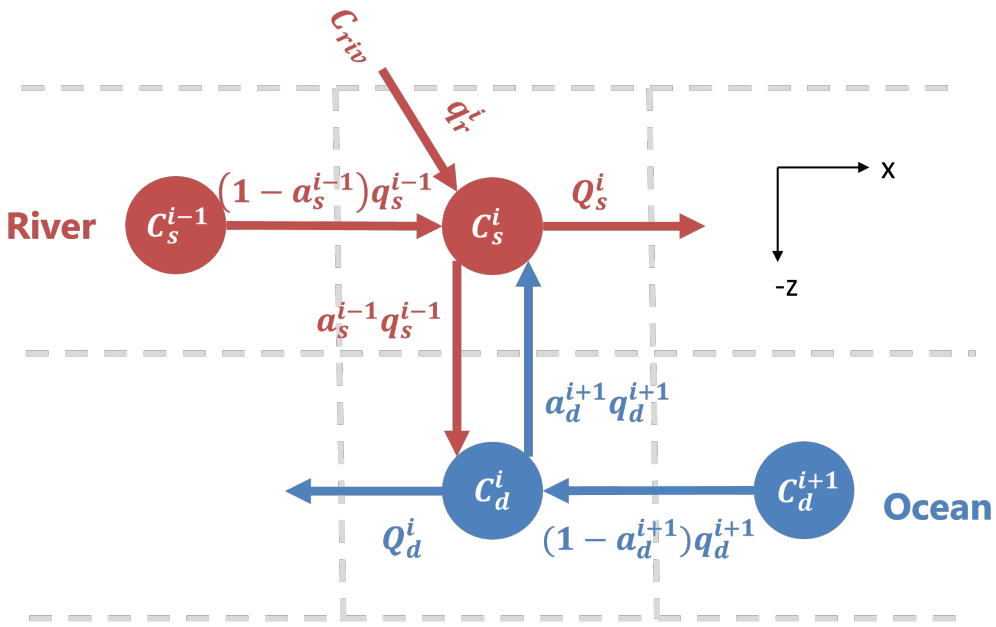


**Figure 2.** Simplification taken for the box model experiment, showing only three x-locations and vertical separation denoted by the dashed gray line. Reproduced with modification from [11]. For explanation, see Equation (1).

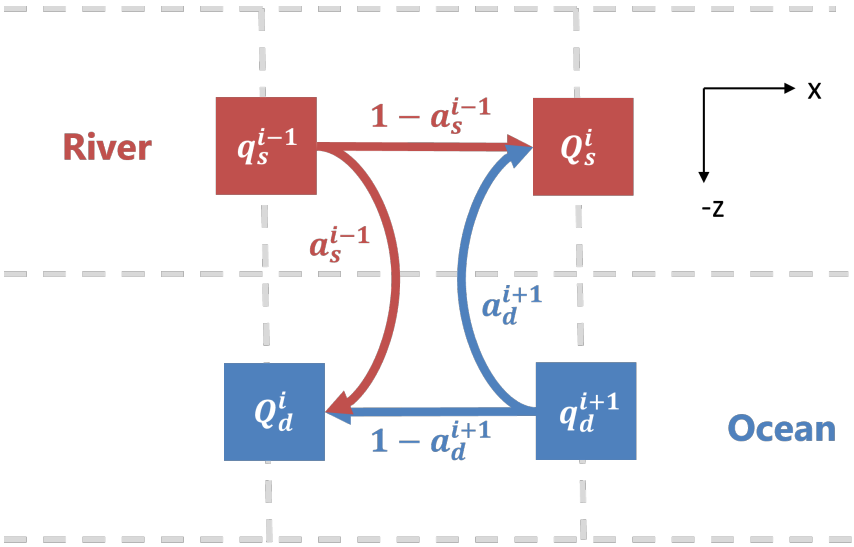


**Figure 3.** Flows and the efflux/reflux method used in the TEF box model (Figure 2) recreated with modification from [11]. For explanation, see Equation (2).

These flows depend on both the salinity distribution and the river flow. The flow divisions, with $Q_s$ being in the direction toward the ocean (shallow) and $Q_d$ being toward the river head (deep), are based on the Knudsen relation [13,14]:

$$Q_s^i = Q_r \frac{S_d^i}{S_d^i - S_s^i},\ Q_d^i = Q_r \frac{S_s^i}{S_d^i - S_s^i} \tag{3}$$

where $S^i$ is salinity (distinct from the tracer studied, $C^i$) at location $i$ either in the shallow (subscript $s$) or deep (subscript $d$) layer of the estuary and $Q_r$ is the cumulative river flow along x. The following flow ratios ($a_s$ and $a_d$) determine how much of the flow in Equation (3) mixes vertically as determined by the Cokelet Stewart method:

$$a_s^i = \frac{S_s^i}{S_d^i}\frac{S_d^{i+1} - S_d^i}{S_d^{i+1} - S_s^i},\ a_d^i = \frac{S_d^i}{S_s^i}\frac{S_s^i - S_s^{i-1}}{S_d^i - S_s^{i-1}} \tag{4}$$

where $S$ is the salinity either heading longitudinally in (deep, $d$) or longitudinally out (shallow, $s$) of the estuary at x-locations denoted in the superscripts [15]. Note that, to match the stencil in Figure 2, the superscripts would need to be incremented accordingly. The along-estuary salinity distribution is externally specified and defined by the Chatwin solution [16]. Equation (4) results in vertical exchanges that are roughly equal and opposite and approach zero near the ocean boundary (Figure 4). Approaching the upstream boundary, the upwards efflux approaches the upstream lower layer flux as is required by mass conservation, and the downwards reflux quickly approaches zero at the boundary.

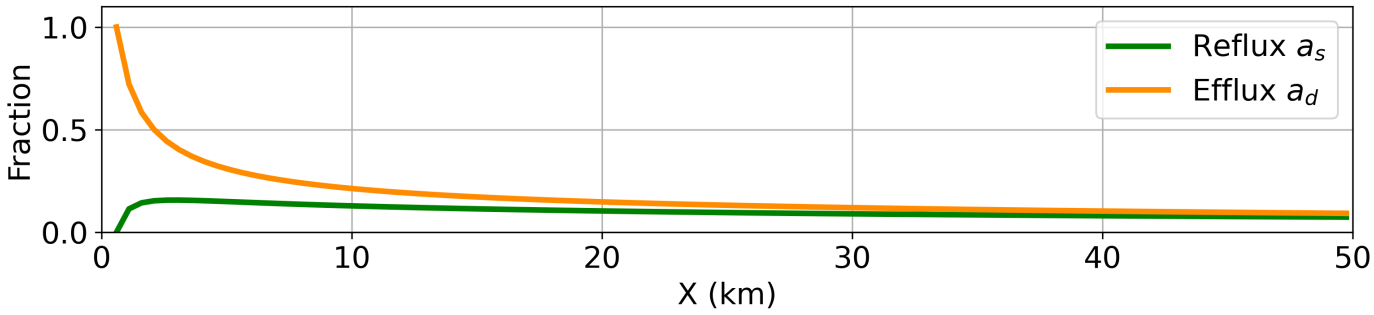


**Figure 4.** Efflux (up)/reflux (down) fractions throughout the estuary for the test cases presented in this study. For explanation, see Equation (4).

### *2.2. Variation 1: Sinking Tracer Model*

To investigate particle sinking, we added another flux in the base TEF model from the shallow layer to the deep layer, making the passive tracer now a sinking tracer. Thus, Equation (1) changes to the following:

$$\begin{aligned}\frac{dC_s^i dV_s}{dt} &= (1 - a_s^{i-1})q_s^{i-1}C_s^{i-1} - Q_s^i C_s^i + a_d^{i+1}q_d^{i+1}C_d^i + q_r^i C_{riv} - Q_{set}C_s^i \\ \frac{dC_d^i dV_d}{dt} &= (1 - a_d^{i+1})q_d^{i+1}C_d^{i+1} - Q_d^i C_d^i + a_s^{i-1}q_s^{i-1}C_s^i + Q_{set}C_s^i\end{aligned} \tag{5}$$

where $Q_{set}$ is the settling flow rate, $C_s^i$ is the tracer concentration in the surface layer at x-location $i$, and $C_d^i$ is the tracer concentration in the deep layer at x-location $i$. To numerically implement this in the box model, the sinking rate is applied to a surface area through which the tracer is settling. In other words,

$$Q_{set} = w_s A_s \tag{6}$$

where $A_s$ is shallow surface area and $w_s$ is the sinking speed. The sinking terms are not denoted in Figure 2, but act to increase the downwards reflux (or counteract the upwards efflux). In the deep layer, we assume that all mass is retained in the water column, with no accumulation in the bed. This is equivalent to assuming that particles that reach the bed are immediately re-suspended. As a result, no sinking flux needs be specified out of the lower layer. At the upstream boundary, we do not allow settling from the most-upward estuary cell in the upper layer because such settling would add mass to an inactive cell in

the lower layer due to the staggering of cells in the upper and lower layer (see Figure 2). Thus, there is no deposition, but this is consistent with the simplicity of the model.

We set the depth of each layer ($h_s$, $h_d$) to 20 m each, the spacing in x in the numerical model or the length of each box ($dx$) is 500 m, and the length of the estuary ($L$) is set to 50 km. The width ($B$) is the dimension into and out of the page in Figure 2 and does not vary longitudinally or vertically. Thus, the box volumes are defined as $dV_s = B * h_s * dx$ in the shallow layer and $dV_d = B * h_d * dx$ in the deep layer, giving $n = 2 * 100$ grid cells.

For the sinking tracer study we examined cases with a tracer input of 1 µM (0.0645 $gL^{-1}$) at the river ($C_{riv}$ = 1 µM) enforced with a Dirichlet boundary condition. A Dirichlet boundary condition is also applied at the ocean ($C_{ocn}$ = 0), so this study only looks at the effects of a terrestrially sourced sinking tracer in the estuary. These parameters are summarized in Table 1.

**Table 1.** Model parameters, separated between parameters in the base model: parameters in the sinking tracer model only (Variation 1), parameters in both models (1 and 2), and parameters in the Peter–Parker Model only (Variation 2). Most biological parameter values obtained from [12].

| Model | Name | Units | Value/Definition | Description |
|---|---|---|---|---|
| Base | $dV_s$ | $m^3$ | $BH_s dx$ | Volume shallow box |
| | $dV_d$ | $m^3$ | $BH_d dx$ | Volume deep box |
| | $V_s$ | $m^3$ | $BH_s L$ | Volume shallow section |
| | $V_d$ | $m^3$ | $BH_d L$ | Volume deep section |
| | $dx$ | m | 501.54 | Length each box |
| | $L$ | km | 50 | Length entire estuary |
| | $H_s$ | m | 20 | Depth shallow layer |
| | $H_d$ | m | 20 | Depth deep layer |
| | $B$ | km | 3 | Estuary width |
| | $q_s$ | $m^3 s^{-1}$ | Equation (2) | Shallow layer rate of volume transport |
| | $q_d$ | $m^3 s^{-1}$ | Equation (2) | Deep layer rate of volume transport |
| | $Q_s$ | $m^3 s^{-1}$ | Equation (3) | Shallow layer flow |
| | $Q_d$ | $m^3 s^{-1}$ | Equation (3) | Deep layer flow |
| | $a_s$ | | Equation (4) | Fraction of flow refluxed down |
| | $a_d$ | | Equation (4) | Fraction of flow effluxed up |
| | $q_r$ | $m^3 s^{-1}$ | 1000 | River rate of volume transport |
| | $Q_r$ | $m^3 s^{-1}$ | 6500 | Cumulative river flow |
| 1 | $C_{riv}$ | µM $N$ | 1 | Sinking tracer river loading concentration |
| | $C_{ocn}$ | µM $N$ | 0 | Sinking tracer ocean loading concentration |
| 1 and 2 | $w_s$ | m $d^{-1}$ | Variable | Tracer or $D$ sinking speed |
| | $n_{days}$ | d | 200 | Simulation time |
| 2 | $\mu_{inst}$ | $d^{-1}$ | Equation (8) | Instantaneous $P$ growth rate |
| | $\mu_0$ | $d^{-1}$ | 2.2 | Max inst. $P$ growth rate |
| | $k_s$ | µM $N$ | 4.6 | Half-saturation $N$ uptake by $P$ |
| | $\alpha$ | $(Wm^{-2})^{-1}$ $d^{-1}$ | 0.06 | Initial slope growth-light curve |
| | $E$ | $W m^{-2}$ | Equation (10) | Photosynthetically available radiation |
| | $E_0$ | $W m^{-2}$ | 200 | Maximum light |
| | $att_{sw}$ | $m^{-1}$ | 0.13 | Light attenuation seawater |
| | $att_P$ | $m^{-1}$ (µM $N$)$^{-1}$ | 0.018 | Light attenuation by $P$ |
| | $m$ | $d^{-1}$ | 0.1 | Non-grazing $P$ mortality |
| | $I$ | $d^{-1}$ | Equation (9) | $Z$ ingestion of $P$ |
| | $I_0$ | $d^{-1}$ | 4.8 | Max $Z$ ingestion rate of $P$ |
| | $K_s$ | µM $N$ | 3 | Half-saturation $Z$ ingestion of $P$ |
| | $\xi$ | $d^{-1}$(µM $N$)$^{-1}$ | 2.0 | $Z$ mortality |
| | $\epsilon$ | | 0.3 | $Z$ growth efficiency |
| | $f_{egest}$ | | 0.5 | Fraction losses $Z$ egested |
| | $r$ | $d^{-1}$ | 0.1 | Remineralization rate |
| | $N_{riv}$ | µM $N$ | 5 | River nutrients |
| | $N_{ocn}$ | µM $N$ | 0 | $N$ ocean boundary condition |
| | $P_{riv}$ | µM $N$ | 0.01 | $P$ river seed population |
| | $P_{ocn}$ | µM $N$ | 0.01 | $P$ ocean seed population |
| | $Z_{riv}$ | µM $N$ | 0.01 | $Z$ river seed populations |
| | $Z_{ocn}$ | µM $N$ | 0.01 | $Z$ ocean seed populations |
| | $D_{riv}$ | µM $N$ | 0 | $D$ river boundary conditions |
| | $D_{ocn}$ | µM $N$ | 0 | $D$ ocean boundary conditions |

### 2.3. Variation 2: The Peter–Parker Model

To study the ecological impact of ETMs, we implemented a Nutrient–Phytoplankton–Zooplankton–Detritus (NPZD) model into the base TEF box model, with settling only active for the detritus component of the model. We used the NPZD model from [12], which is a variation of the Nutrient-Phytoplankton-Zooplankton idealized models first developed by **Peter** Franks [18]. This particular model includes a detritus box and is tuned for the pacific northwest [12]. The NPZD model provides a basic ecosystem structure with nutrients being taken up by phytoplankton, which is, in turn, grazed by zooplankton. Detritus provides a mechanism for waste to return to the nutrient pool. The nutrient component of the model should be based on whatever nutrient is limiting to phytoplankton growth; in our implementation, we consider this to be nitrogen, reflective of the limiting factor in the Salish Sea [12,19]. Figure 5 summarizes the NPZD relationships written in Equation (7): nutrients are taken up by phytoplankton and allow for growth, phytoplankton excrete nutrients and become detritus due to reasons other than grazing, phytoplankton are consumed by zooplankton grazing, but a fraction of the phytoplankton are lost to detritus due to "messy eating" of the zooplankton, zooplankton become detritus, and the detritus sinks and remineralizes back to nutrients.

The equations for the dynamics shown in Figure 5 are as follows:

$$\begin{aligned}
\frac{dN}{dt} &= -\mu_{inst}(E(t,z),N)P + (1-\epsilon)(1-f_{egest})I(P)Z + rD \\
\frac{dP}{dt} &= \mu_{inst}(E(t,z),N)P - I(P)Z - mP \\
\frac{dZ}{dt} &= \epsilon I(P)Z - \xi Z^2 \\
\frac{dD}{dt} &= (1-\epsilon)f_{egest}I(P)Z + mP + \xi Z^2 - rD - w_s\frac{dD}{dz}
\end{aligned} \tag{7}$$

where $\mu_{inst}$ is the instantaneous phytoplankton growth rate, which depends on irradiance and nutrients, $E$ is photosynthetically available radiation (irradiance) and is time and depth dependent, $\epsilon$ is zooplankton growth efficiency, $f_{egest}$ is the fraction of losses egested of phytoplankton by zooplankton ("messy eating"), $I$ is zooplankton ingestion/grazing of phytoplankton, $r$ is remineralization rate of detritus to nutrients, $m$ is non-grazing phytoplankton mortality, $\xi$ is zooplankton mortality, and $w_s$ is detritus sinking rate [12]. The growth ($\mu_{inst}$) and grazing ($I$) rates are parameters that change in time based on available resources:

$$\mu_{inst}(E,N) = \mu_0 \frac{N}{k_s + N} \frac{\alpha E}{\sqrt{\mu_0^2 + \alpha^2 E^2}} \tag{8}$$

where $\mu_0$ is maximum instantaneous growth rate, $k_s$ is half-saturation for nitrate uptake, and $\alpha$ is the initial slope of the growth-light curve. Further,

$$I(P) = \frac{I_0 P^2}{K_s^2 + P^2} \tag{9}$$

where $I_0$ is maximum ingestion rate and $K_s$ is half-saturation for ingestion. Irradiance ($E$) is time-dependent to reflect the day/night light cycle:

$$E(t) = \frac{E_0}{2}(1 + cos(2\pi t)) \tag{10}$$

$E_0$ is maximum light, and $t$ is in days.

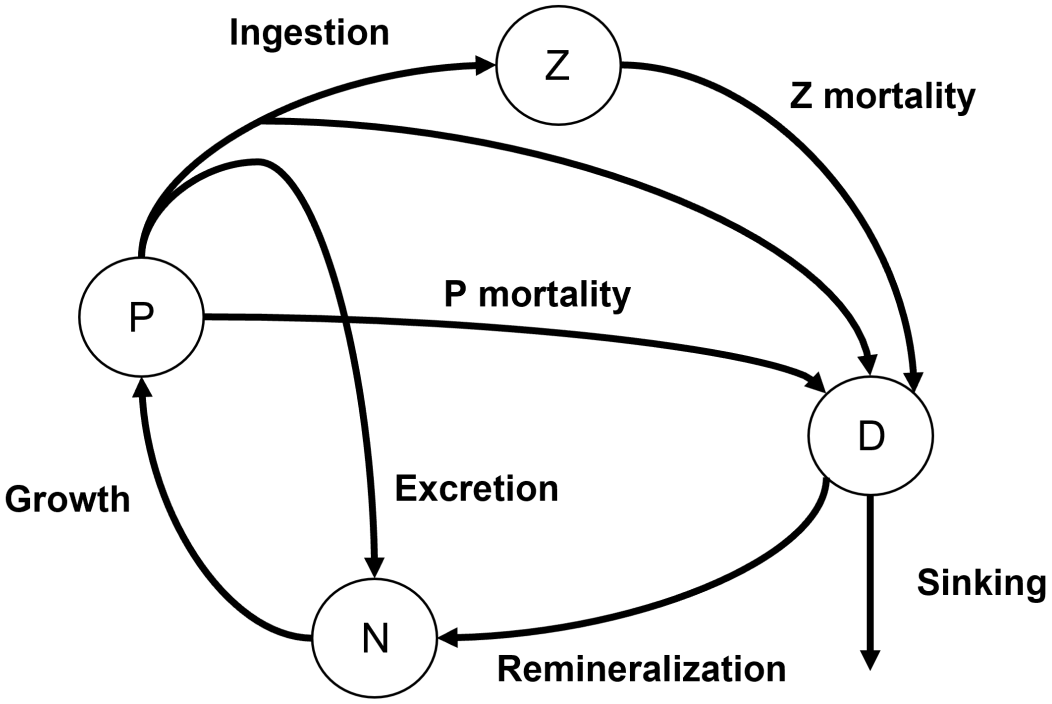


**Figure 5.** Nitrogen flow diagram to phytoplankton, zooplankton, and detritus (NPZD) summarized in Equation (7). Recreated with slight modification from [12].

So, treating $N$, $P$, $Z$, and $D$ as passive scalars, we put the Peter Model (NPZD, Equation (7)) into the Parker Model (TEF, Equation (1)) to form **the Peter–Parker Model**:

$$\begin{aligned}
\frac{d(N_s^i dV_s)}{dt} &= (1-a_s^{i-1})q_s^{i-1}N_s^{i-1} - Q_s^i N_s^i + a_d^{i+1}q_d^{i+1}N_d^i + q_r^i N_{riv} \\
&\quad + dV_s\left(-\mu_{inst}^i(E_s,N_s^i)P_s^i + (1-\epsilon)(1-f_{egest})I^i(P_s^i)Z_s^i + rD_s^i\right) \\
\frac{d(N_d^i dV_d)}{dt} &= (1-a_d^{i+1})q_d^{i+1}N_d^{i+1} - Q_d^i N_d^i + a_s^{i-1}q_s^{i-1}N_s^i \\
&\quad + dV_d\left(-\mu_{inst}^i(E_d^i,N_d^i)P_d^i + (1-\epsilon)(1-f_{egest})I^i(P_d^i)Z_d^i + rD_d^i\right) \\
\frac{d(P_s^i dV_s)}{dt} &= (1-a_s^{i-1})q_s^{i-1}P_s^{i-1} - Q_s^i P_s^i + a_d^{i+1}q_d^{i+1}P_d^i \\
&\quad + dV_s\left(\mu_{inst}^i(E_s,N_s^i)P_s^i - I^i(P_s^i)Z_s^i - mP_s^i\right) \\
\frac{d(P_d^i dV_d)}{dt} &= (1-a_d^{i+1})q_d^{i+1}P_d^{i+1} - Q_d^i P_d^i + a_s^{i-1}q_s^{i-1}P_s^i \\
&\quad + dV_d\left(\mu_{inst}^i(E_d^i,N_d^i)P_d^i - I^i(P_d^i)Z_d^i - mP_d^i\right) \\
\frac{d(Z_s^i dV_s)}{dt} &= (1-a_s^{i-1})q_s^{i-1}Z_s^{i-1} - Q_s^i Z_s^i + a_d^{i+1}q_d^{i+1}Z_d^i \\
&\quad + dV_s\left(\epsilon I^i(P_s^i)Z_s^i - \xi\left(Z_s^i\right)^2\right) \\
\frac{d(Z_d^i dV_d)}{dt} &= (1-a_d^{i+1})q_d^{i+1}Z_d^{i+1} - Q_d^i Z_d^i + a_s^{i-1}q_s^{i-1}Z_s^i \\
&\quad + dV_d\left(\epsilon I^i(P_d^i)Z_d^i - \xi\left(Z_d^i\right)^2\right) \\
\frac{d(D_s^i dV_s)}{dt} &= (1-a_s^{i-1})q_s^{i-1}D_s^{i-1} - Q_s^i D_s^i + a_d^{i+1}q_d^{i+1}D_d^i - Q_{set}D_s^i \\
&\quad + dV_s\left((1-\epsilon)f_{egest}I^i(P_s^i)Z_s^i + mP_s^i + \xi\left(Z_s^i\right)^2 - rD_s^i\right) \\
\frac{d(D_d^i dV_d)}{dt} &= (1-a_d^{i+1})q_d^{i+1}D_d^{i+1} - Q_d^i D_d^i + a_s^{i-1}q_s^{i-1}D_s^i + Q_{set}D_s^i \\
&\quad + dV_d\left((1-\epsilon)f_{egest}I^i(P_d^i)Z_d^i + mP_d^i + \xi\left(Z_d^i\right)^2 - rD_d^i\right)
\end{aligned} \tag{11}$$

where all the parameters are the same as in Equations (1) and (7). The values we used for the parameters are summarized in Table 1.

The boundary conditions for the biological components of the Peter–Parker Model are as follows. First, the nutrients are only supplied in the river ($N_{riv} = 5$ μM $N$) and the ocean nutrients boundary condition is 0. The tests all had initial phytoplankton and zooplankton concentrations of 0.01 μM $N$ throughout the estuary as a starting population and boundary condition. We assumed no river or ocean sourcing of phytoplankton, zooplankton, or detritus. The model is solved with an explicit forward Euler numerical method with Dirichlet boundary conditions on $N$, $P$, $Z$, and $D$. While this upwind scheme does introduce slight numerical diffusion, in this study, comparative data are more important than absolute accuracy. We ran the model to an approximate steady state before analysis, to be discussed below (200 days).

We allow the shallow layer detritus to sink to the deep layer; the sinking detritus progresses directly from the shallow concentration to the deep due to the same settling flux $Q_{set}$ as above (Equation (6)). We assume that detritus that reaches the bed is re-suspended (no net flux).

The light availability for the deep phytoplankton is limited based on the water above and the shading caused by the shallow population. This changes Equation (10) to the following:

$$\begin{aligned} E_s(t) &= \frac{E_0}{2}(1 + cos(2\pi t)) \\ E_d^i(t) &= \frac{E_0}{2}(1 + cos(2\pi t))e^{-att_{sw}H_s - att_P P_s^i(t_p)H_s} \end{aligned} \tag{12}$$

where $E_s$ is irradiance in the shallow layer, $E_d^i$ is irradiance in the deep layer at location $i$, $att_{sw}$ is the light attenuation of seawater, $att_P$ is the light attenuation by phytoplankton, $P_s^i(t_p)$ is the phytoplankton location in the shallow layer at location $i$ from the previous time step $t_p$, and $H_s$ is the depth of the shallow layer.

## 3. Results: Effects of Sinking Speed on Tracer or Detritus Accumulation

We first present concentration results from a sinking tracer in the TEF box model (Equation (1)) without any biological considerations (Variation 1 above). We then present the effects of detritus sinking as it interacts with the ecosystem with results from the Peter–Parker Model (Variation 2 above).

The tracer concentration profiles results for varying sinking while holding all other parameters constant (Figure 6) indicate that there is accumulation of the sinking tracer near the river ($X = 0$ km) in both the shallow and deep layer for certain sinking speeds. We define accumulation as when the concentration surpasses the river input value of 1 μM. Without sinking, $w_s = 0$ md$^{-1}$; the tracer advects out or mixes down from its box and does not get above the river input concentration. Interestingly, the peak concentration increases with increased sinking rate to reach an inflection point at around 15 md$^{-1}$ in both the shallow and the deep layer, after which the peak grows unbounded at $X = 0$ km (does not reach steady state within the 200 days of simulation time). In the deep layer, there is accumulation regardless of sinking speed, but the amount increases and becomes unbounded above the same sinking speed as the shallow layer. The deep layer always has a higher peak concentration than the shallow layer. Also, the locations of these peak concentrations shift toward the river with increasing sinking speed in both layers.

Why do sinking particles (Figure 6) lead to accumulation in the estuary? Following one particle starting in the shallow layer of the box model (Figure 2), as it sinks out of the shallow layer into the deep, it then is pushed back towards the river ($X = 0$ km). This happening to a group of particles leads to high concentration in the deep layer up-estuary ($X = 0$ km). Some of that accumulated concentration is moved back into the shallow layer via efflux. The balance between the sinking and efflux creates a type of vertical circular eddy motion, which maintains the tracer concentration at a higher value than the river

input of 1 µM in both the shallow and deep layer at $X = 0$ km. The peak also occurs near $X = 0$ km because that is where there is increased vertical mixing activity via efflux (Figure 4). When sinking passes a certain threshold of around 15 md$^{-1}$, the effects of the efflux are diminished in the shallow layer as the efflux is no longer sufficient to balance the sinking flux anywhere in the estuary and the system grows unbounded (does not reach steady state within the simulation time of 200 days).

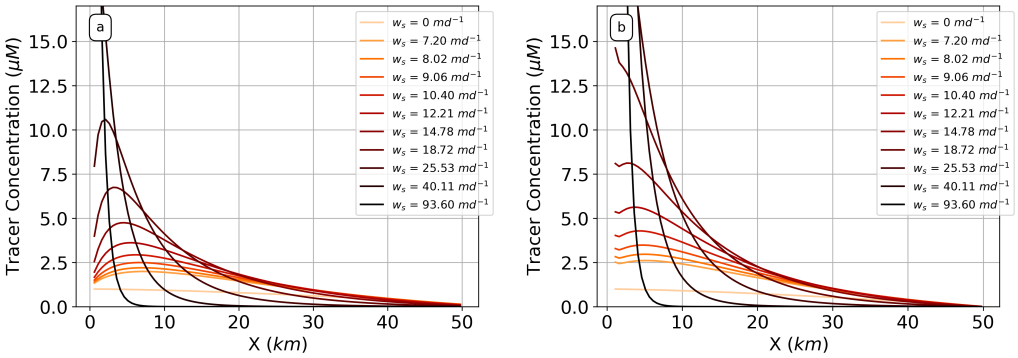


(**a**) Shallow layer tracer concentration with variable sinking speed ($w_s$).

(**b**) Deep layer tracer concentration with variable sinking speed ($w_s$).

**Figure 6.** Concentration of tracer distributed along the estuary after 200 days with varying sinking rates ($w_s$). The lines of a lighter shade correspond to concentrations obtained with lower detritus sinking speeds. This shade increases in darkness with increasing detritus sinking speed.

For large settling velocities, the peak concentration is constrained spatially by the up-estuary boundary condition at $X = 0$ km and the mass conservation of the system: as tracer is not allowed to leave the system, it is pushed against $X = 0$ with higher sinking speeds, resulting in narrower peaks. For sinking speeds less than 15 md$^{-1}$, steady state is reached, and the peak appears downstream of the boundary. Note that 15 md$^{-1}$ is quite low; marine snow can be 36 md$^{-1}$ [20]. If we compare the sinking speed to a ratio of the sinking flux to the vertical mixing flux, $\frac{Q_{set}}{a_d q_d}$, where $Q_{set}$ is the sinking flux (defined in Equation (6)) and $a_d q_d$ is the vertical flux (arrow pointing from deep to shallow in Figure 2), sinking speeds greater than 15 md$^{-1}$ correspond to when the ratio of settling flux to vertical flux is greater than 0.5. Thus, this balance of sinking and vertical flux is determining when the system accumulates unboundedly: the sinking flux must be at most 50% of the vertical flux to reach steady state.

Peak concentrations move closer to the river ($X = 0$ km) because that is where the sinking tracer concentration is being sourced. So, the faster a particle sinks, the closer it will sink to its source because it is sinking faster than the estuarine flow, which otherwise would move it further from its source. This is further investigated with timescales in the following section.

When incorporating a biological model to evaluate sinking detritus, we also see this phenomenon with the peak detritus concentration in the estuary (Figure 7). Increasing detritus sinking speed leads to an increased detritus peak concentration that moves closer to the river end of the estuary ($X = 0$ km). Also, the detritus grows unbounded (does not reach steady state) with a sinking speed above $w_s = 40$ md$^{-1}$.

Increasing the sinking rate ($w_s$) of detritus from the shallow to the deep layer leads to an increase in phytoplankton ($P$) concentration in both the shallow and deep layer (Figure 8a,b) for all sinking speeds. $P$ concentration reaches a maximum in both the shallow and deep layer at around $X = 8$ km and the location of this peak does not significantly change with increasing sinking speed, contrary to the peak detritus concentration. Nutrient concentration follows a similar pattern: increasing detritus sinking speed leads to increased nutrient concentrations with peaks that do not move with increased sinking speed. Peak nutrient concentration occurs between 0 and 5 km.

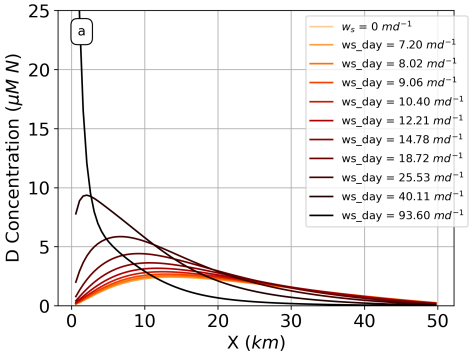


(**a**) Shallow layer detritus concentration with variable detritus sinking speed ($w_s$).

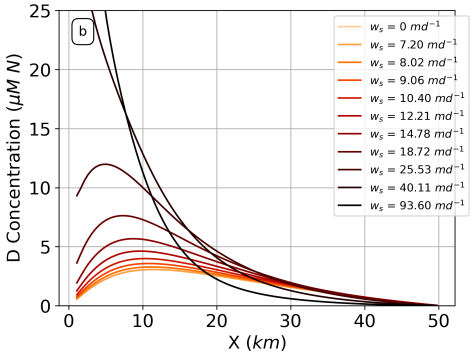


(**b**) Deep layer detritus concentration with variable detritus sinking speed ($w_s$).

**Figure 7.** Varying detritus sinking speed effects on detritus concentration profiles after 200 days of simulation time. $X = 0$ km marks where the river enters the estuary and $X = 50$ km marks the ocean. An increasing value of each sinking speed is denoted with a darker shade of orange line. The left-hand panel is for the shallow layer; the right-hand panel is for the deep layer.

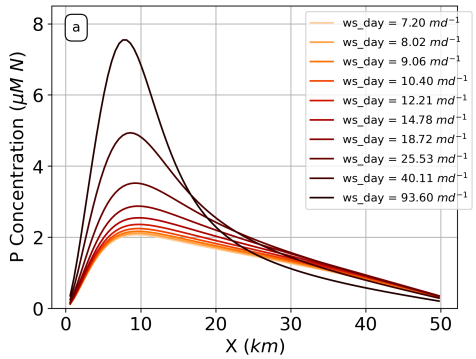


(**a**) Shallow layer phytoplankton concentration with variable detritus sinking speed ($w_s$).

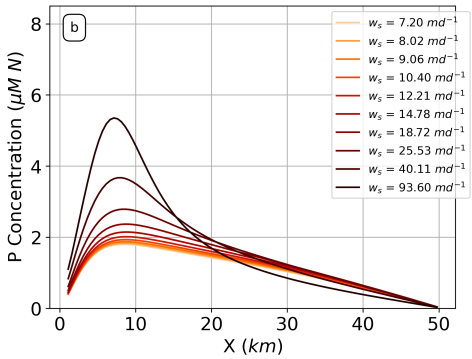


(**b**) Deep layer phytoplankton concentration with variable detritus sinking speed ($w_s$).

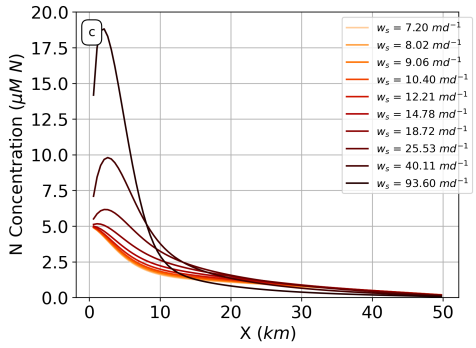


(**c**) Shallow layer nutrient concentration with variable detritus sinking speed ($w_s$).

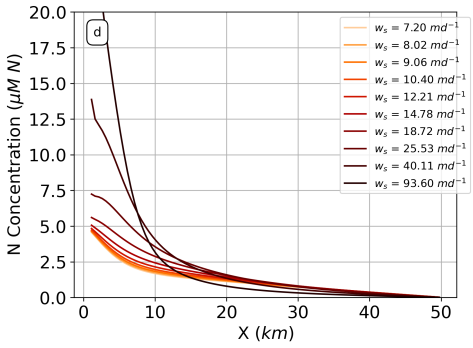


(**d**) Deep layer nutrient concentration with variable detritus sinking speed ($w_s$).

**Figure 8.** Varying detritus sinking speed effects on phytoplankton (**a**,**b**) and nutrient (**c**,**d**) concentration profiles after 200 days of simulation time. $X = 0$ km marks where the river enters the estuary and $X = 50$ km marks the ocean. Increasing value of each parameter denoted with a darker shade of orange line. The left-hand panel is for the shallow layer; the right-hand panel is for the deep layer.

Increased detritus influences phytoplankton and nutrient peak concentration because more detritus accumulating in one spot of the estuary leads to more nutrients available to the phytoplankton via remineralization. As long as the location of the nutrients does not

change, which is the case with increasing detritus sinking speed and constant remineralization rate (Figure 8c,d), the location of the phytoplankton will not change. Increasing nutrient concentration does not change the rate of nutrient uptake by the phytoplankton and, thus, does not change the location of the peak. But their peaks themselves increase with the increase in detritus/nutrient supply.

As demonstrated above, the passive tracer accumulates indefinitely for sinking speeds greater than 15 $md^{-1}$ due to the balance of the sinking and vertical mixing flux. With biology, however, there are additional fluxes keeping the concentration from growing indefinitely (growth, grazing, remineralization, etc.). Thus, detritus and nutrients grow unboundedly for sinking speeds greater than 40 $md^{-1}$ in the deep layer, but phytoplankton does not grow unboundedly regardless of sinking speed. This is because there is a carrying capacity represented in the Michaelis–Menten phytoplankton growth expression (Equation (8)), which restricts unlimited phytoplankton growth even with unlimited nutrients $\left(\frac{N}{k_s+N}\right)$, where $k_s$ is half-saturation $N$ uptake by $P$. We explore the interplay of these physical–biological interactions in the following timescales section.

Interestingly, the peak detritus location moves closer to the river with higher detritus sinking speeds even though we only source nutrients in the river, not detritus. Phytoplankton will follow nutrients due to its nutrient-dependent growth rate, and zooplankton will then follow the phytoplankton. Detritus concentration is high where concentrations of phytoplankton and zooplankton are high. Where the detritus is formed via biological processes is then the source of the sinking tracer, as in Figure 6, and, as occurs with the sinking tracer, the interaction of the detritus sinking and exchange flow leads to accumulation. Figure 9 shows the biological contribution to $\frac{dD}{dt}$, which includes sources from zooplankton "messy eating", phytoplankton and zooplankton mortality, and sinks from remineralization (Equations (7) and (11)). This demonstrates that the source for the detritus is shifted 8–15 km downstream of the river mouth and distributed over a broader reach of the estuary, as compared to the river-sourced sinking tracer considered in the previous section. Regardless, the peak detritus is positioned based on a balance between efflux and sinking, which occurs near $X = 0$ km, especially for larger sinking speeds. This results in a location for the peak detritus concentration that moves upstream as sinking increases. This is further explored with the timescale analysis in the following section.

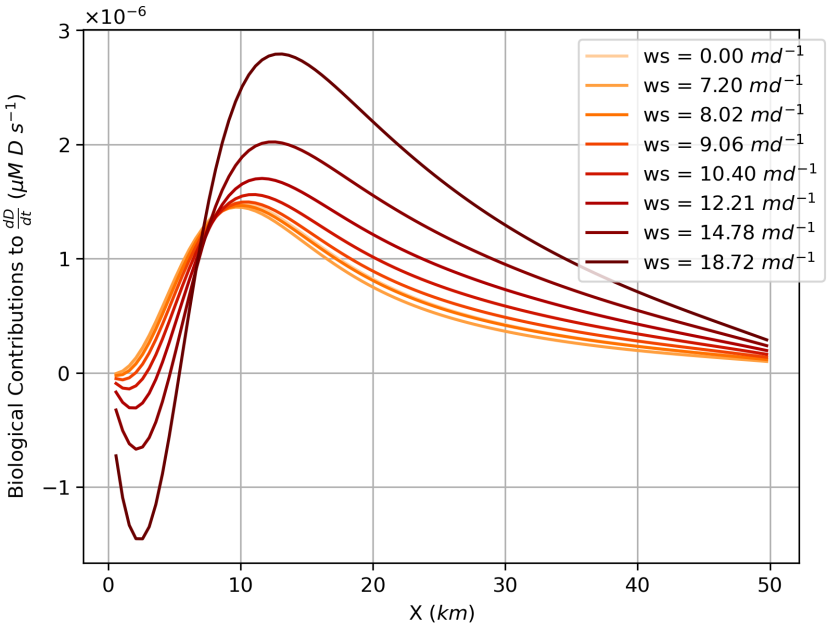


**Figure 9.** Distribution of the biological contributions to $\frac{dD}{dt}$ in the shallow layer for a variety of sinking speeds. Biological contributions include sources from zooplankton "messy eating", phytoplankton and zooplankton mortality, and sinks from remineralization—see Equations (7) and (11).

## 4. Discussion: Timescale Analysis

To understand the processes that lead to the different concentration states, we perform a timescales analysis similar to those reviewed in [21]. For this discussion, we focus on the cases that reach steady state.

### *4.1. Timescales Definitions*

We introduce the following timescales that are used in the analysis of the sinking tracer and sinking detritus in the estuary. The timescales are detailed below and summarized in Table 2. We use the timescales to directly compare the processes that contribute to the sinking tracer and detritus concentration. A faster timescale means that a process is the fastest to occur and is dominant in determining the ETM.

**Table 2.** Summary of timescales to understand behavior as written in Equations (13)–(22).

| Name | Process | Formula |
|---|---|---|
| Sinking | Time for concentration to sink from the shallow to deep layer | $\tau_{sink} = \frac{h_s}{w_s}$ |
| Vertical Mixing | Time for concentration to efflux to shallow from deep ($\tau_{eff}$) or reflux to deep from shallow ($\tau_{ref}$) at location $i$ | $\tau^i_{eff} = \frac{dV_s}{\lvert -q_s^{i-1} * a_s^{i-1} + q_d^{i+1} * a_d^{i+1} \rvert}$<br>$\tau^i_{ref} = \frac{dV_d}{\lvert q_s^{i-1} * a_s^{i-1} - q_d^{i+1} * a_d^{i+1} \rvert}$ |
| Longitudinal Exchange | Time for concentration to flow out towards the ocean ($\tau_{out}$) or in towards the river ($\tau_{in}$) at location $i$ | $\tau^i_{out} = \frac{dV_s}{Q^i_s}$<br>$\tau^i_{in} = \frac{dV_d}{Q^i_d}$ |
| Estuarine Dispersion | Time for concentration peak to be reduced by the longitudinal and vertical mixing at location $i$ as described in Equations (16)–(18) | $\tau^i_{disp} = \frac{V\left(a_s^{i-1} q_s^{i-1} + a_d^{i+1} q_d^{i+1}\right)}{c_{disp}\left((1-a_s^{i-1}) q_s^{i-1} + (1-a_d^{i+1}) q_d^{i+1}\right)^2}$ |
| Messy Eating | Time for the fraction of phytoplankton missed by zooplankton to become detritus | $\tau^i_{messy,s} = \frac{1}{(1-\epsilon) f_{egest} I^i_s}$<br>$\tau^i_{messy,d} = \frac{1}{(1-\epsilon) f_{egest} I^i_d}$ |
| P Mortality | Time for phytoplankton to become detritus from methods other than grazing | $\tau_{Pmort} = \frac{1}{m}$ |
| Z Mortality/Higher Predation | Time for zooplankton to become detritus due to mortality or higher predation | $\tau^i_{Zmort,s} = \frac{Z^i_s}{\zeta}$<br>$\tau^i_{Zmort,d} = \frac{Z^i_d}{\zeta}$ |
| Remineralization | Time for detritus to become nutrients | $\tau_{remin} = \frac{1}{r}$ |

We first introduce a sinking timescale based on the time it takes for the concentration to sink from the shallow to the deep layer:

$$\tau_{sink} = \frac{h_s}{w_s} \tag{13}$$

where $h_s$ is the depth of the shallow layer and $w_s$ is the sinking speed. Next are timescales for the vertical mixing, or the time for concentration to efflux up to the shallow from the deep layer ($\tau_{eff}$) and the time for concentration to reflux down from the shallow layer to the deep ($\tau_{ref}$). These timescales are calculated at each box and, thus, are determined at location $i$:

$$\begin{aligned} \tau^i_{eff} &= \frac{dV_s}{Q_{eff_{net}}} = \frac{dV_s}{\lvert -q_s^{i-1} * a_s^{i-1} + q_d^{i+1} * a_d^{i+1} \rvert} \\ \tau^i_{ref} &= \frac{dV_d}{Q_{ref_{net}}} = \frac{dV_d}{\lvert q_s^{i-1} * a_s^{i-1} - q_d^{i+1} * a_d^{i+1} \rvert} \end{aligned} \tag{14}$$

where $Q_{eff_{net}}$ is the net flow from the deep to the shallow layer, $Q_{ref_{net}}$ is the net flow from the shallow to the deep layer, and the remaining variables are defined as in Equations (2) and (4). There are also timescales for the flow of the estuary, or the time for the concentration to flow out towards the ocean ($\tau_{out}$) and the time for the concentration to flow in towards

the river ($\tau_{in}$) at location $i$. We calculated these timescales using the volume of each box over the flow at those boxes:

$$\begin{aligned} \tau^i_{out} &= \frac{dV_s}{Q^i_s} \\ \tau^i_{in} &= \frac{dV_d}{Q^i_d} \end{aligned} \tag{15}$$

where the variables are as defined in Equation (3). Lastly, we introduce an estuarine dispersion timescale ($\tau_{disp}$), or the time for the concentration peak to be reduced by longitudinal and vertical mixing alone at location $i$. We start with a definition for the timescale [22]:

$$\tau^i_{disp} = \frac{L^2}{c_{disp} K^i_{disp}} \tag{16}$$

where $L$ is the length of the estuary, $K_{disp}$ is the estuarine dispersion coefficient, and $c_{disp}$ is a dispersion multiplication factor, which usually ranges from 30 to 120 [22,23]. For this study, we set $c_{disp} = 1$ to focus on some direct comparisons of processes in the system. We solve for $K_{disp}$ using the following equations:

$$\begin{aligned} K_{disp} &= \frac{u^2 H^2}{K_z} \\ u &= \frac{\Delta Q_x}{BH} \approx \frac{Q_{in_{net}} + Q_{out_{net}}}{BH} \\ K_z &= \frac{Q_z H}{BL} \approx \frac{\left(Q_{eff} + Q_{ref}\right) H}{BL} \\ K_{disp} &= \frac{\left(Q_{in_{net}} + Q_{out_{net}}\right)^2}{\left(Q_{eff} + Q_{ref}\right)} \frac{L}{BH} \\ K^i_{disp} &= \frac{\left((1 - a^{i-1}_s) q^{i-1}_s + (1 - a^{i+1}_d) q^{i+1}_d\right)^2}{\left(a^{i-1}_s q^{i-1}_s + a^{i+1}_d q^{i+1}_d\right)} \frac{L}{BH} \end{aligned} \tag{17}$$

where $u$ is the velocity in the estuary in the x-direction, $H$ is the total depth of the estuary, $\Delta Q_x$ is the difference in horizontal flow, $Q_{in_{net}}$ is the net flow moving into the estuary (the fraction not being effluxed up in Figure 3), $Q_{out_{net}}$ is the net flow moving out of the estuary (the fraction not refluxed down in Figure 3), $K_z$ is vertical eddy diffusivity, $Q_z$ is all vertical flow, $Q_{eff}$ is the flow moving upwards (the fraction effluxed up in Figure 3), and $Q_{ref}$ is the flow moving downwards (the fraction refluxed down in Figure 3). Then we plug the $K_{disp}$ equation into Equation (16):

$$\tau^i_{disp} = \frac{V\left(a^{i-1}_s q^{i-1}_s + a^{i+1}_d q^{i+1}_d\right)}{c_{disp}\left((1 - a^{i-1}_s) q^{i-1}_s + (1 - a^{i+1}_d) q^{i+1}_d\right)^2} \tag{18}$$

where $V$ is the total volume of the estuary ($V = BHL$) and $a$ and $q$ are defined as in Equations (2)–(4).

For the detritus analysis, we take biological timescales from the Peter–Parker Model that relate to detritus only ($D$ equations in Equation (7) [12]) in addition to the same timescales as above. We start with the messy eating timescale, or the time it takes for bits of phytoplankton missed by zooplankton to become detritus:

$$\tau^i_{messy,(s,d)} = \frac{1}{(1 - \epsilon) f_{egest} I^i_{s,d}} \tag{19}$$

where the variables are as defined in Equation (9). The time for phytoplankton to die from causes other than grazing (mortality timescale) is

$$\tau_{Pmort} = \frac{1}{m} \tag{20}$$

Similarly, the time for zooplankton to die from higher predation or other mortality is

$$\tau_{Zmort,(s,d)} = \frac{Z^i_{s,d}}{\xi} \tag{21}$$

This timescale depends on the current concentration of zooplankton to accommodate the units of $\xi$. Lastly, the remineralization timescale or the time for detritus to turn into nutrients is

$$\tau_{remin} = \frac{1}{r} \tag{22}$$

### *4.2. Sinking Tracer Timescales*

Looking at the timescales while changing the sinking speed of the tracer only (Figure 10), the fastest (smallest-value) timescale is the longitudinal exchange in the shallow layer when $w_s \approx 7$–$30$ md$^{-1}$. In the deep layer, the longitudinal exchange timescale is the fastest timescale up to $w_s = 15$ md$^{-1}$, after which it abruptly increases. This means that the dominant process leading to the concentration profile at these sinking speeds is longitudinal exchange. In the shallow layer, the sinking timescale becomes faster with increasing sinking speed but is always the second fastest timescale. In the deep layer, the sinking timescale approaches the reflux timescale when $w_s > 15$ md$^{-1}$, which also corresponds to when the system no longer reaches a steady state. Thus, the balance between vertical mixing, advection, and settling is critical in determining when the model reaches a steady state. In the shallow layer, the vertical mixing timescale decreases with increasing sinking speed and becomes closer in value to the sinking and longitudinal exchange timescales, so vertical mixing becomes more important with increasing sinking speed. The dispersion timescale increases with increasing sinking speed, reflecting a reduction in the contribution of longitudinal dispersion that results in the more "peaky" concentration distributions in Figure 6.

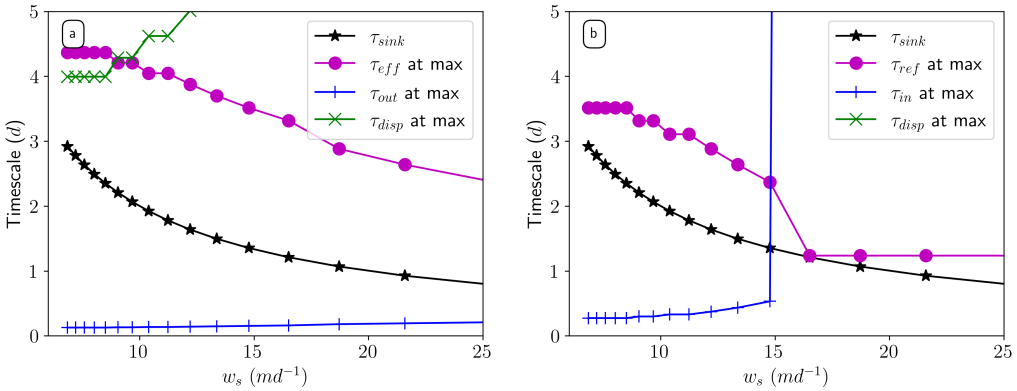


(**a**) Shallow layer with variable sinking. (**b**) Deep layer with variable sinking.

**Figure 10.** Timescales ($d$) for each case shown in Figure 6 taken at the location of the peak concentration. Black stars represent sinking timescales, purple dots are vertical mixing timescales, blue pluses are longitudinal exchange (advection) timescales, and green crosses are dispersion timescales. We intentionally truncated the y-axis at 5 days, to focus on the interactions of the fastest timescales and the x-axis at 25 md$^{-1}$ to focus on the cases which reach steady state. Timescales defined as in Table 2.

### *4.3. Sinking Detritus Timescales*

In the shallow layer, $Z$ mortality and longitudinal exchange are the fastest timescales for detritus sinking speeds less than 40 md$^{-1}$ (Figure 11a). The sinking timescale decreases with increasing sinking speed, however, and therefore increases with influence on the detritus concentration. This highlights the interplay of sinking speed and the $D$ concentration. A smaller sinking speed corresponds to a larger sinking timescale, which means that there is more time for the peak concentrations to spread out and results in a larger dispersion timescale. In the deep layer (Figure 11b), $Z$ mortality and advection timescales are the fastest until $w_s \approx 25$ md$^{-1}$, after which sinking and vertical mixing are the fastest timescales. Above $w_s = 25$ md$^{-1}$, physical processes are the most significant for detritus concentration in the deep layer. Conversely, biological processes in the shallow layer play an important role in detritus formation for all sinking speeds shown.

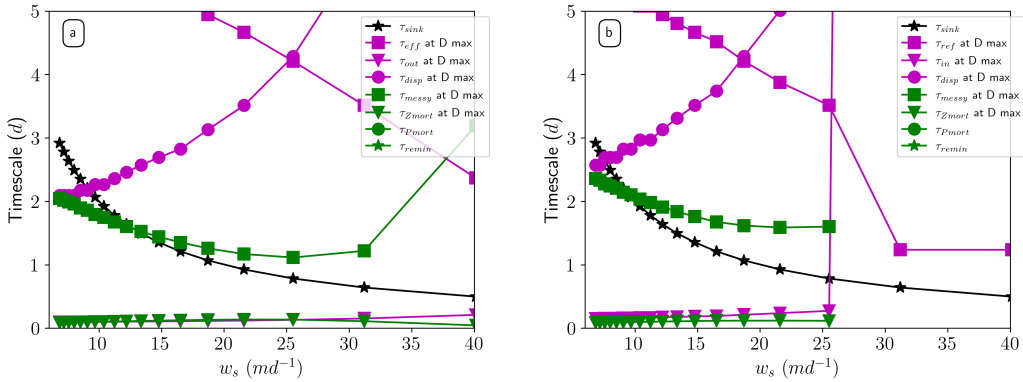


(**a**) Shallow layer with variable detritus sinking speed.

(**b**) Deep layer with variable detritus sinking speed.

**Figure 11.** Timescales ($d$) for each case shown in Figure 7. Purple markers/lines denote physical processes, green denotes biological, and black denotes sinking. Marker type denotes the timescale: purple squares are for the vertical mixing timescale, purple triangles are for the longitudinal exchange (advection) timescale, purple circles are for the dispersion timescale, green squares are messy eating, green upside-down triangles are Z mortality, green circles are P mortality, green stars are remineralization, and black stars are sinking. Each of the timescales which have x-dependence were calculated at the location of the peak $D$ concentration for each case. We intentionally truncated the y-axis at 5 days, to focus on the interactions of the fastest timescales and the x-axis at 40 md$^{-1}$ to focus on the cases which reach steady state. Timescales defined as in Table 2.

### *4.4. Sinking Tracer vs. Sinking Detritus*

Several differences occur between the accumulation of sinking tracers or detritus, as discussed in the previous section. For one, the lack of a settling velocity ($w_s = 0$ md$^{-1}$) does not mean that there is no detritus accumulation (Figure 7) like it does for the non-biological sinking tracer (Figure 6) because there are other sources that can lead to detritus accumulation other than just sinking ($P$ mortality, messy eating, etc.). Also, detritus accumulates and reaches a steady state up to a sinking speed of 40 md$^{-1}$, whereas the sinking speed of the sinking tracer accumulates unboundedly for sinking speeds greater than $w_s = 15$ md$^{-1}$. This shows that sinking detritus has a larger range of sinking speeds, which accumulate in the estuary before growing unboundedly, than a sinking tracer due to how detritus interacts in an ecosystem in addition to sinking via zooplankton/phytoplankton sources or nutrient remineralization losses (Equation (7)).

In addition, the peak locations of tracer and detritus accumulations differ with the same sinking speed (Figure 12). In this example, the sinking tracer peak location is closer to the river end of the estuary ($X = 0$ km) than the peak detritus (for $w_s = 8$ md$^{-1}$). If settling velocity were to be increased (or decreased), the peaks would shift up-estuary (down-estuary) due to the vertical cycling between the two layers and the required balance

between efflux and settling for the peak to establish. In all cases, however, the detritus peak is shifted down-estuary due to the fact that its source is distributed along the upper layer through phytoplankton and zooplankton populations (Figure 9). The longitudinal shift in peak concentration (shown in Figure 12) introduces a new timescale that describes the characteristic ecosystem cycling time, as the system converts nutrients to phytoplankton to zooplankton and then into the detritus pool (acknowledging that some detritus is also formed directly from the phytoplankton). From the perspective of a water parcel that enters at the river, these ecological processes can be thought of as a time-lag in the creation of detritus.

We further quantify the difference in these peak locations with the following timescale:

$$\tau_{diff} = \frac{(X_{D_{max}} - X_{C_{max}})BL}{Q_{flush}} \tag{23}$$

where $\tau_{diff}$ is the lag timescale, which leads to the difference between the peak locations at the same sinking speed, $X_{D_{max}}$ is the $X$ location of the peak $D$ (detritus) concentration, and $X_{C_{max}}$ is the $X$ location of the peak $C$ (tracer) concentration. $\tau_{diff}$ can be interpreted as a characteristic cycling time for the ecosystem.

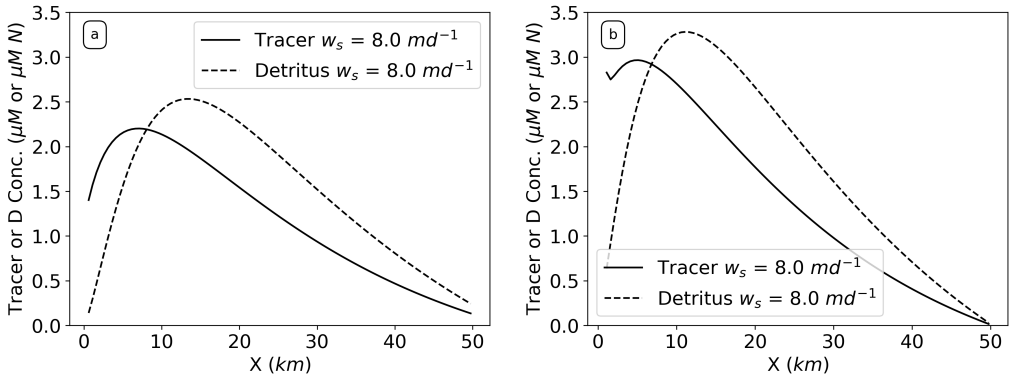


(**a**) Shallow layer. (**b**) Deep layer.

**Figure 12.** Sinking tracer (solid line, units μM) and sinking detritus (dashed line, units μM $N$) concentrations with the same sinking speed ($w_s = 8$ md$^{-1}$) in the shallow (**a**) and deep (**b**) layer.

We see in Figure 13 that, in the shallow layer, this timescale is clustered around 1.2 days, but then decreases as the settling velocity increases beyond the steady-state transition. For these larger settling velocities, the peak concentration of both detritus and sinking tracer is constrained by the boundary at $X = 0$ km and, thus, this transport timescale is no longer relevant. For the cases with a steady-state and well-defined peak in detritus (settling velocity less than about 30 md$^{-1}$), it is clear that the ecosystem cycles from nutrients through phytoplankton and zooplankton into detritus with a characteristic timescale of a little over 1 day. At the same time, large settling velocities are able to reduce the longitudinal difference in the location of the peak (between detritus and non-biological setting tracers) due to the tight cycling between the upper and lower layers at the upstream end of the estuary (Figure 4).

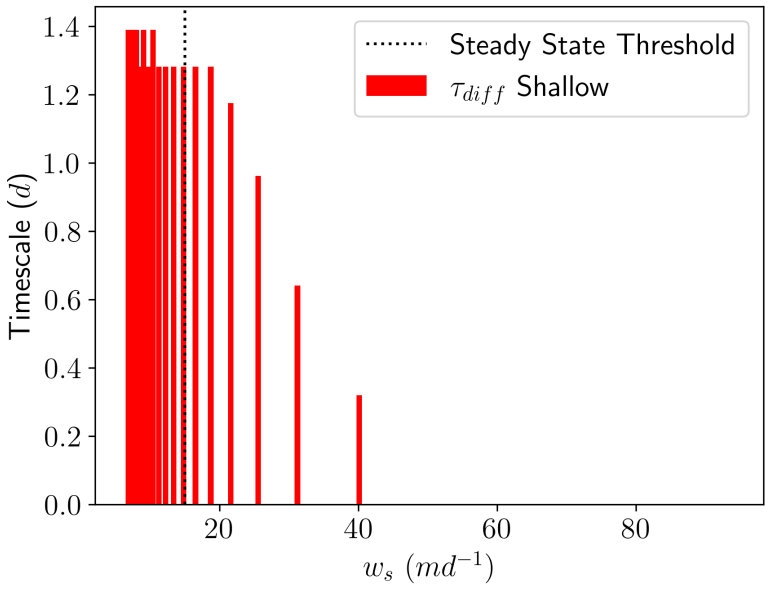


**Figure 13.** Values of the introduced timescale $\tau_{diff}$, which quantifies the lag leading to the difference in peak *D* and *C* locations. Red bars correspond to $\tau_{diff}$ in the shallow layer and and vertical line corresponds to the steady-state threshold of the system when run to 200 days.

## 5. Summarizing the Behavior with a Dimensionless Group

Through some further evaluations of varying sinking speed ($w_s$), estuarine flushing rate ($Q_{flush}$), estuary width ($B$), and river flow rate ($Q_r$), we found that increasing sinking speed and width and decreasing flushing rate and river flow lead to increased ETM magnitude, but only up to certain values of each parameter before the system does not reach a steady state (see Appendix A for additional details). Through dimensional analysis, we obtained the following dimensionless group:

$$\left(\frac{w_s BL}{Q_r}\right)^{-0.50}\left(\frac{Q_{flush}}{Q_r}\right)^{0.75} = \left(\frac{\tau_{sink}}{\tau_{flush}}\right)^{0.5}\left(\frac{\tau_{riv}}{\tau_{flush}}\right)^{0.25} \tag{24}$$

using general timescales $\tau_{riv} = \frac{V}{Q_r}$, $\tau_{sink} = \frac{h}{w_s}$, and $\tau_{flush} = \frac{V}{Q_{flush}}$, where $V = BLh$ is total estuary volume and $h$ is depth. We validated this group by using the estuary length ($L$) as a constant parameter and dimensionless concentration $C^* = \frac{\int C_s}{\int C_{total}}$, which represents the integrated shallow layer concentration normalized to the total integrated concentration (shallow+deep) (Figure 14). $C^*$ focuses on the strength of the concentration peak in the estuary while taking away the x-dependence of the ETMs. The dimensionless concentration $C^*$ increases as the shallow and total integrated concentrations approach each other. Thus, $C^*$ alone does not tell us the location of the peak concentration, but allows us to compare the state of concentration in the estuary. We performed this dimensionless analysis on both the sinking tracer and sinking detritus studies and found the outcomes to be similar, so we present the results from the tracer study only here to reduce redundancies.

Figure 14 shows that varying $Q_{flush}$, $B$, $Q_r$, or $w_s$ will result in the same state in the estuary, $C^*$. This dimensionless group connects three timescales, which represent three fluxes in the system: the estuarine flux, the sinking flux, and the river flux. The ratio of sinking to exchange flow and the ratio of river flow to exchange flow are the two drivers of the system, with the former having a stronger exponential dependence than the latter. As such, increasing flushing has a similar effect as reducing sinking and increasing flushing has a similar effect to reducing river flow. These relationships are not one to one, so increasing flushing has a stronger effect than decreasing river flow or sinking. Flushing has this extra complexity because of how the flow is defined (Equation (3)): the in- and outflow ($Q_s$ and

$Q_d$) depend on a fraction of the river flow that varies with the salinity difference taken at different locations in the estuary. Thus, unlike estuary width, sinking speed, and river flow, this parameter varies in space and cannot be combined with the others as cleanly.

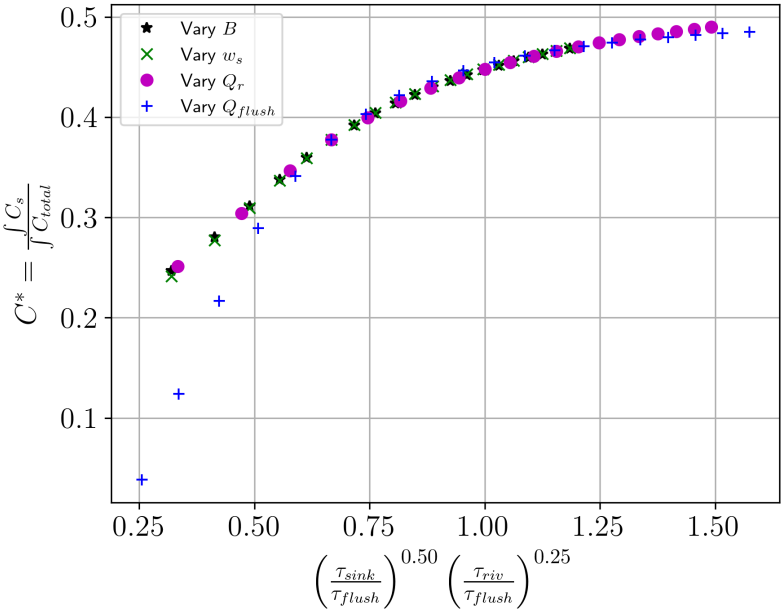


**Figure 14.** Relationship between the dimensionless group $\left(\frac{\tau_{sink}}{\tau_{flush}}\right)^{0.5}\left(\frac{\tau_{riv}}{\tau_{flush}}\right)^{0.25}$ and the dimensionless summary of the shallow layer concentration $\frac{\int C_s}{\int C_{total}}$ ($C^*$). Black stars refer to values obtained by varying estuary width ($B$), green crosses are from varying sinking speed ($w_s$), purple dots are from varying river flow ($Q_r$), and blue pluses are from varying flushing rate ($Q_{flush}$). All of these variations were taken while holding the other parameters constant.

This parameter informs the relative importance of particle sinking, estuary surface area, estuary flow, and river flow for accumulation of scalars in an estuary. As discussed above, particle sinking influences accumulation because of the interplay of sinking and vertical mixing. Varying estuarine flushing ($Q_{flush}$) rate also leads to accumulation because, when the overall advection scheme is slower, the effects of the sinking tracers are more pronounced. In other words, if the estuary is flushing slower, the sinking tracer has more time to accumulate in the bottom layer. Thus, it is able to efflux back upwards with more ease and present more accumulation in both the shallow and deep layers. Accumulation occurs with varying estuarine surface area ($B$) due to similar logic as with reduced flushing rate; when the river flow is held constant but the estuary is larger, the effects of the river on the longitudinal exchange in the estuary are reduced. Thus, the sinking tracer has more time to accumulate in both layers. Lastly, accumulation occurs with decreased river flow ($Q_r$) for the same reason as altering estuary size and flushing; when the river is faster, the tracer has less time to settle and accumulate.

## 6. Conclusions

We would like to highlight several key findings from this work that establish the differences between ETM dynamics when considering a sinking tracer versus sinking detritus in an estuary. In both cases, the concentration of sinking tracer or detritus accumulates in an estuary because the sinking of the tracer is in balance with the vertical mixing (efflux) of the system at some location along the estuary. The peak concentration of a river-sourced sinking tracer moves towards the river with increased sinking speed because it comes into balance with the efflux further upstream and creates a narrower vertical recirculation. The peak concentration of sinking detritus in a system where nutrients are sourced in the river moves towards the river with increased sinking speed as well, but the peak is

displaced down-estuary. This shift in the position of the ETM is a result of the biological processes that govern the creation of detritus, which is tied to the peaks of phytoplankton and zooplankton. This shift in the peak is created by a temporal lag for nutrients to turn into detritus in the biological model. As nutrients are taken up by phytoplankton, which are, in turn, consumed by zooplankton, down-estuary transport in the surface layer means that the source of detritus (whether from messy eating or mortality) is shifted downstream from the river by a distance related to the surface-layer advection and the characteristic cycling timescale of the ecosystem.

Accumulation increases until a distinct sinking speed for both sinking tracer and detritus, after which the peak does not reach a steady state. The sinking speed after which this happens is smaller for sinking tracer than detritus. The peak accumulates unboundedly after the ratio of the sinking flux to the vertical flux surpasses 0.5 due to the retention of mass at the upstream boundary and the rapid recycling of a sinking tracer between the lower and upper layers (a balance between efflux and settling). It is interesting to note that the other components of the ecological model (e.g., phytoplankton) maintain a steady state at the same sinking speed due to the other ecological controls on each component (e.g., grazing by zooplankton).

We break apart the contributions of the processes in our model by analyzing timescales. The fastest timescale indicates the process that is most influential on the concentration profiles. Longitudinal mixing is the shortest timescale for the sinking tracer in the shallow layer. In the deep layer, the shortest timescale switches from longitudinal exchange to vertical mixing and sinking at the same point at which the system switches from steady state to unbounded. With detritus, zooplankton mortality and longitudinal mixing are the fastest timescales in the shallow layer. In the deep layer, zooplankton mortality is also the fastest timescale up to a certain sinking speed and the physical timescales follow similar dynamics as the sinking tracer; this indicates that adding biology to the system influences the processes that determine the concentration in the shallow layer.

The peak concentration occurs at a different location in the estuary at the same sinking speed because of the time lag of biological processes. This time lag is about 1 day for steady-state cases, but it devolves for cases which grow unboundedly because they all peak up-estuary at $X = 0$ km, where vertical mixing activity is the strongest.

Lastly, sinking tracer concentration depends on four different variables, which were summarized in a single nondimensional parameter (Section 5). This parameter allows us to directly compare the impacts of the individual attributes of the estuary on ETMs. For instance, given an estuary of a certain size and river flow rate, we can determine how fast a particle needs to sink to accumulate.

**Author Contributions:** Conceptualization, L.E. and M.S.; methodology, L.E. and M.S.; software, L.E.; validation, L.E.; formal analysis, L.E. and M.S.; investigation, L.E. and M.S.; resources, L.E.; data curation, L.E.; writing—original draft preparation, L.E.; writing—review and editing, M.S.; visualization, L.E.; supervision, M.S.; project administration, M.S.; funding acquisition, L.E. and M.S. All authors have read and agreed to the published version of the manuscript.

**Funding:** L.E. and M.S. would like to acknowledge National Science Foundation Graduate Research Fellowship Program (NSF-GRFP) for funding this work under grant DGE2146752.

**Data Availability Statement:** Data can be reproduced using modeling scripts at the following GitHub repository: lmengel422/The-Peter–Parker-Model, DOI: 10.5281/zenodo.12169937.

**Acknowledgments:** L.E. named the Peter–Parker Model after two great mentors during her PhD, Peter J.S. Franks and Parker MacCready. They were instrumental for inspiration, assistance with model setup, and overall advice; she offers huge thanks to them both. Thanks also to Albert Ruhi and Evan Variano for editorial suggestions to a previous version of this manuscript and to the anonymous reviewers whose suggestions greatly improved this text.

**Conflicts of Interest:** The authors declare no conflicts of interest.

## Abbreviations

The following abbreviations are used in this manuscript:

| | |
|---|---|
| ETM | Estuarine Turbidity Maximum |
| NPZD | Nutrient–Phytoplankton–Zooplankton–Detritus |
| SPM | Suspended Particulate Matter |
| TEF | Total Exchange Flow |

## Appendix A

*Appendix A.1. Varying Flushing, River Flow, and Estuary Surface Area*

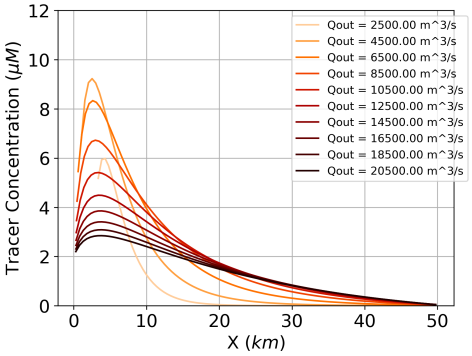


(**a**) Shallow layer tracer concentration with variable estuarine flushing ($Q_{flush}$).

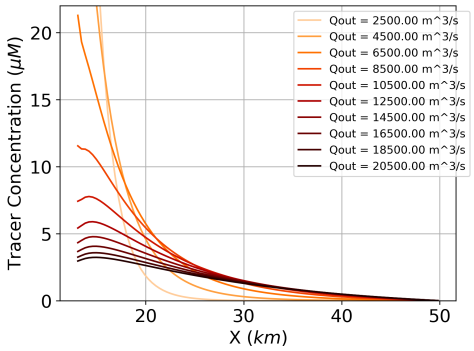


(**b**) Deep layer tracer concentration with variable estuarine flushing ($Q_{flush}$).

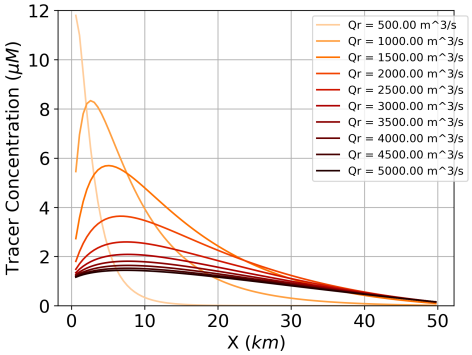


(**c**) Shallow layer tracer concentration with variable river flow ($Q_{riv}$).

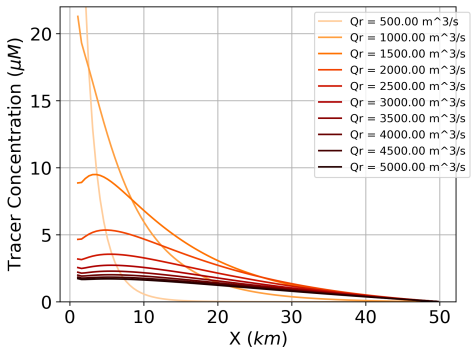


(**d**) Shallow layer tracer concentration with variable river flow ($Q_{riv}$).

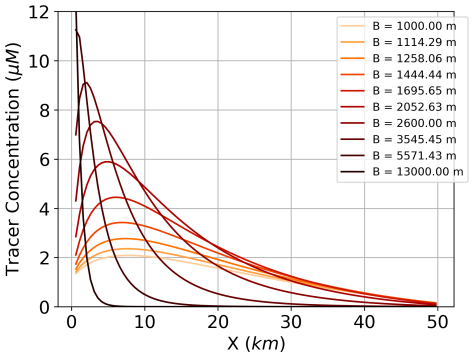


(**e**) Shallow layer tracer concentration with variable estuary surface area ($B$).

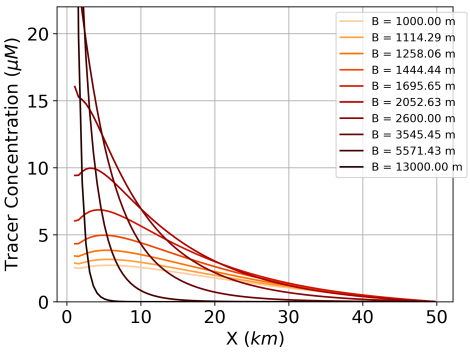


(**f**) Shallow layer tracer concentration with variable estuary surface area ($B$).

**Figure A1.** Sinking tracer concentration profiles when varying one parameter but holding all others constant. Results from this used to develop the dimensionless group in Section 5.

*Appendix A.2. Development of Dimensionless Group*

The results above show that certain sinking speeds, estuarine flushing rate, estuary size (width), and river flow lead to distinct sinking tracer concentrations. We obtain the same concentration profile by varying different parameters of the model and holding others constant. (Specifically, the concentration profiles when altering sinking and B are identical, even though we altered different parameters.) This suggests that there is a relationship among the parameters. We set out to find this relationship by developing a dimensionless group. We know that the model should be able to be described by a finite number of dimensionless groups, based on the way it is formulated.

Thus, using the Buckingham Pi theorem, we define the following dimensionless groups from Equation (1):

$$dim_1 = \frac{B}{L},\ dim_2 = \frac{Q_{flush}}{Q_r},\ dim_3 = \frac{w_s L^2}{Q_r} \tag{A1}$$

We define these dimensionless groups so that no more than two parameters are varying at a time. We next combine these dimensionless groups into one parameter. This parameter informs the relative importance of tracer sinking, estuary surface area, estuary flow, and river flow on accumulation intensity in an estuary. We present the non-dimensional concentration, which we call $C^*$. $C^*$ focuses on the strength of the concentration peak in the estuary while taking away the x-dependence of the ETMs. Thus, it summarizes the state of the estuary in a way that can be easily compared across multiple cases. For $C^*$, we use the relationship of the integral of shallow layer concentration to the total concentration, $C^* = \left(\frac{\int C_s}{\int C_{total}}\right)$. For $C^*$, we non-dimensionalize the concentration of the shallow layer as our metric to compare the different cases, but the results hold for the shallow and the deep layer.

We hypothesize that $C^*$ is determined by a function that is a product of these dimensionless groups, $C^* = \prod_{i=1}^{3} dim_i^{a_i}$. We performed a linear regression on the log of this equation to determine the values of the coefficients ($a_i$) and obtained

$$\begin{aligned} C^* &\approx dim_1^{-0.50} dim_2^{0.75} dim_3^{-0.50} \\ &= \left(\frac{w_s BL}{Q_r}\right)^{-0.50} \left(\frac{Q_{flush}}{Q_r}\right)^{0.75} \end{aligned} \tag{A2}$$

Since $dim_1$ and $dim_3$ had the same coefficient, this suggests that they collapse into their own group.

## References


1. Hansen, D.V.; Rattray, M., Jr. *Gravitational Circulation in Straits and Estuaries*; Technical Report; Department of Oceanography, University of Washington: Seattle, WA, USA, 1966.
2. Geyer, W.R.; MacCready, P. The Estuarine Circulation. *Annu. Rev. Fluid Mech.* **2014**, *46*, 175–197. [CrossRef]
3. Burchard, H.; Schuttelaars, H.M.; Ralston, D.K. Sediment Trapping in Estuaries. *Annu. Rev. Mar. Sci.* **2018**, *10*, 371–395. [CrossRef] [PubMed]
4. Festa, J.F.; Hansen, D.V. Turbidity maxima in partially mixed estuaries: A two-dimensional numerical model. *Estuar. Coast. Mar. Sci.* **1978**, *7*, 347–359. [CrossRef]
5. Allen, G.P.; Salomon, J.C.; Bassoullet, P.; Du Penhoat, Y.; de Grandpré, C. Effects of tides on mixing and suspended sediment transport in macrotidal estuaries. *Sediment. Geol.* **1980**, *26*, 69–90. [CrossRef]
6. Sanford, L.P.; Suttles, S.E.; Halka, J.P. Reconsidering the physics of the Chesapeake Bay estuarine turbidity maximum. *Estuaries* **2001**, *24*, 655–669. [CrossRef]
7. Burchard, H.; Baumert, H. The formation of estuarine turbidity maxima due to density effects in the salt wedge. A hydrodynamic process study. *J. Phys. Oceanogr.* **1998**, *28*, 309–321. [CrossRef]
8. Emmett, R.; Llansó, R.; Newton, J.; Thom, R.; Hornberger, M.; Morgan, C.; Levings, C.; Copping, A.; Fishman, P. Geographic signatures of North American West Coast estuaries. *Estuaries* **2012**, *23*, 765–792. [CrossRef]

9. Babson, A.L.; Kawase, M.; MacCready, P. Seasonal and Interannual Variability in the Circulation of Puget Sound, Washington: A Box Model Study. *Atmos.-Ocean.* **2003**, *44*, 29–45. [CrossRef]
10. Feely, R.A.; Alin, S.R.; Newton, J.; Sabine, C.L.; Warner, M.; Devol, A.; Krembs, C.; Maloy, C. The combined effects of ocean acidification, mixing, and respiration on pH and carbonate saturation in an urbanized estuary. *Estuar. Coast. Shelf Sci.* **2010**, *88*, 442–449. [CrossRef]
11. MacCready, P.; McCabe, R.M.; Siedlecki, S.A.; Lorenz, M.; Giddings, S.N.; Bos, J.; Albertson, S.; Banas, N.S.; Garnier, S. Estuarine Circulation, Mixing, and Residence Times in the Salish Sea. *J. Geophys. Res. Ocean.* **2021**, *126*, e2020JC016738. [CrossRef]
12. Banas, N.S.; Lessard, E.J.; Kudela, R.M.; MacCready, P.; Peterson, T.D.; Hickey, B.M.; Frame, E. Planktonic growth and grazing in the Columbia River plume region: A biophysical model study. *J. Geophys. Res.-Ocean.* **2009**, *114*, C00B13. [CrossRef]
13. MacCready, P. Calculating Estuarine Exchange Flow Using Isohaline Coordinates. *J. Phys. Oceanogr.* **2011**, *41*, 1116–1124. [CrossRef]
14. Burchard, H.; Bolding, K.; Feistel, R.; Graewe, U.; Klingbeil, K.; MacCready, P.; Mohrholz, V.; Umlauf, L.; van der Lee, E.M. The Knudsen theorem and the Total Exchange Flow analysis framework applied to the Baltic Sea. *Prog. Oceanogr.* **2018**, *165*, 268–286. [CrossRef]
15. Cokelet, E.D.; Stewart, R.J. The Exchange of Water in Fjords - the Efflux/reflux Theory of Advective Reaches Separated by Mixing Zones. *J. Geophys. Res.-Ocean.* **1985**, *90*, 7287–7306. [CrossRef]
16. Chatwin, P.C. Some remarks on the maintenance of the salinity distribution in estuaries. *Estuar. Coast. Mar. Sci.* **1976**, *4*, 555–566. [CrossRef]
17. Officer, C.B. Box Models Revisited. In *Estuarine and Wetland Processes: With Emphasis on Modeling*; Hamilton, P., Macdonald, K.B., Eds.; Springer: Boston, MA, USA, 1980; pp. 65–114. [CrossRef]
18. Franks, P.; Wroblewski, J.S.; Flierl, G.R. Behavior of a Simple Plankton Model with Food-Level Acclimation by Herbivores. *Mar. Biol.* **1986**, *91*, 121–129. [CrossRef]
19. Davis, K.A.; Banas, N.S.; Giddings, S.N.; Siedlecki, S.A.; MacCready, P.; Lessard, E.J.; Kudela, R.M.; Hickey, B.M. Estuary-enhanced upwelling of marine nutrients fuels coastal productivity in the U.S. Pacific Northwest. *J. Geophys. Res. Ocean.* **2014**, *119*, 8778–8799. [CrossRef]
20. Asper, V.L. Measuring the flux and sinking speed of marine snow aggregates. *Deep. Sea Res. Part A Oceanogr. Res. Pap.* **1987**, *34*, 1–17. [CrossRef]
21. Lucas, L.V.; Deleersnijder, E. Timescale Methods for Simplifying, Understanding and Modeling Biophysical and Water Quality Processes in Coastal Aquatic Ecosystems: A Review. *Water* **2020**, *12*, 2717. [CrossRef]
22. Fischer, H.B. Mixing and Dispersion in Estuaries. *Annu. Rev. Fluid Mech.* **1976**, *8*, 107–133. [CrossRef]
23. Taylor, G.I. Dispersion of soluble matter in solvent flowing slowly through a tube. *Proc. R. Soc. London. Ser. A Math. Phys. Sci.* **1953**, *219*, 186–203.

water

MDPI

*Article*

# Tidal-Driven Water Residence Time in the Bohai and Yellow Seas: The Roles of Different Tidal Constituents

**Qingjun Fu [1], Huichao Jiang [2], Chen Dong [1], Kangjie Jin [1], Xihan Liu [3] and Lei Lin [1,*]**

[1] College of Ocean Science and Engineering, Shandong University of Science and Technology, Qingdao 266590, China; fuqingjun@sdust.edu.cn (Q.F.); 201901061306@sdust.edu.cn (C.D.); 202383190018@sdust.edu.cn (K.J.)
[2] Shandong Key Laboratory of Marine Ecological Restoration, Shandong Marine Resource and Environment Research Institute & Observation and Research Station of Laizhou Bay Marine Ecosystem, MNR, Yantai 264006, China; jianghuichao2008@163.com
[3] Hebei Technology Innovation Center for Geographic Information Application, Institute of Geographical Sciences, Hebei Academy of Sciences, Shijiazhuang 050011, China; xihanigs@petalmail.com
* Correspondence: llin@sdust.edu.cn; Tel.: +86-0532-86058220

**Abstract:** Water residence time (WRT) is a crucial parameter for evaluating the rate of water exchange and it serves as a timescale for elucidating hydrodynamic processes, pollutant dispersion, and biogeochemical cycling in coastal waters. This study investigates the tidal-driven WRT patterns in the Bohai and Yellow Seas (collectively known as BYS) by employing a tidal model in conjunction with an adjoint WRT diagnostic model and explores the influence of tidal constituents on WRT. The findings indicate that the tidal-driven WRT in the BYS is approximately 2.11 years, exhibiting a significant spatially heterogeneous distribution. The WRT pattern shows a strong correlation with the pattern of tidal-driven Lagrangian residual currents (LRCs). Semidiurnal tides have a more pronounced effect on WRT than diurnal tides. Semidiurnal tides significantly reduce WRT across the entire BYS, while diurnal tides predominantly influence WRT in the Bohai Sea (BS). The $M_2$ tidal constituent is the most influential in decreasing WRT and enhancing water exchange, owing to its dominant energy contribution within the tidal system. In contrast, the $S_2$ tidal constituent has a minimal effect; however, its interaction with the $M_2$ tidal constituent plays a significant role in reducing the WRT. The $K_1$ and $O_1$ constituents exert more localized effects on WRT, particularly in the central BS, where their energy ratios relative to $M_2$ are relatively high. Although the amplitude of the $S_2$ constituent exceeds that of $K_1$ and $O_1$, its contribution to LRC—and consequently to WRT—is limited due to the overlapping tidal wave with $M_2$. This research contributes to a deeper understanding of the influence of tidal dynamics on long-term water transport and associated timescales, which are vital for enhancing predictions of material transport and ecosystem dynamics in tidal-dominated environments.

**Keywords:** water residence time; tidal constituents; Bohai and Yellow Seas; adjoint method; Lagrangian residual currents



Academic Editor: Serafeim E. Poulos

Received: 13 January 2025
Revised: 11 March 2025
Accepted: 14 March 2025
Published: 19 March 2025

**Citation:** Fu, Q.; Jiang, H.; Dong, C.; Jin, K.; Liu, X.; Lin, L. Tidal-Driven Water Residence Time in the Bohai and Yellow Seas: The Roles of Different Tidal Constituents. *Water* **2025**, *17*, 884. https://doi.org/10.3390/w17060884



## 1. Introduction

Water residence time (WRT) is defined as the time required for a water parcel to leave the region of interest for the first time [1–3] and serves as a pivotal timescale parameter for understanding ocean hydrodynamics and marine biogeochemistry cycling [4,5]. In coastal regions, nutrient cycling, primary production, pollutant dispersion, and ecosystem resilience are highly related to the WRT [5–7]. A short WRT promotes water renewal, which

limits pollutant accumulation but may restrict nutrient retention, potentially inhibiting primary production. Conversely, a longer WRT enhances nutrient retention and organic matter sedimentation, thus supporting productivity and increasing the risks of eutrophication and hypoxia [7–9]. Furthermore, WRT can provide insights into ecosystem connectivity and resilience, which is critical for understanding how ecosystems respond to anthropogenic pressures and climate change [5]. Given its significant implications for marine ecology and environmental management, investigating the variability of WRT in coastal waters and its underlying dynamic mechanisms is essential [10,11].

The variability of WRT in coastal waters is influenced by various physical processes and their interactions. For example, seasonal and interannual variations in WRT in the Chesapeake Bay are primarily driven by fluctuations in river discharge and wind [12], with gravitational circulation also playing a significant role [13,14]. Research has indicated that the distribution and seasonal changes of water residence time (WRT) in the BS and Subei Coastal waters are primarily influenced by tidal and wind forces [9,15]. Furthermore, it has been suggested that wind-driven coastal currents and their interactions with tides play a significant role in determining WRT in the eastern shelf seas of China [16]. Tides, as substantial components of coastal hydrodynamics, play essential roles in the hydrodynamic processes and water exchange in coastal regions [17–21]. While previous studies have primarily focused on the overall patterns of WRT influenced by all physical processes in coastal waters, the characteristics of WRT solely driven by tidal forces have not been fully elucidated. In particular, the contributions of various tidal constituents and their differing roles in WRT remain unclear. Due to rising sea levels and changes in the coastline resulting from land reclamation, the coastal tidal system is undergoing significant transformations [22]. Different tidal constituents exhibit varying responses to these changes [23]. Understanding the tidal-driven WRT and the roles of tidal constituents is crucial for assessing the potential future alterations in water exchange capacity in coastal regions, as well as the subsequent impacts on the marine environment and ecology.

This study aims to investigate the patterns of tidal-driven WRT in the Bohai and Yellow Seas (collectively known as BYS), which are typical enclosed shelf seas, and to elucidate the roles of various tidal constituents through three-dimensional tidal simulations and a diagnostic model of WRT. The structure of this paper is organized as follows: Section 2 introduces the tidal simulation methodology, the WRT diagnostic model, and the numerical experimental designs. Section 3 presents the results of the tidal-driven WRT in the BYS and examines the influence of different tidal constituents on WRT. Section 4 discusses the formation of the WRT patterns and the contributions of various tidal constituents by analyzing the tidal-driven Lagrangian residual currents (LRCs). Finally, Section 5 provides a concise conclusion.

## 2. Methods

### 2.1. Study Area

The Bohai and Yellow Seas (collectively known as BYS), characterized by a mean water depth of approximately 40 m and bordered by China and the Korean Peninsula, are typical semi-enclosed coastal seas (Figure 1). The BYS features a strong and complex tidal system, including semidiurnal constituents ($M_2$, $S_2$) and diurnal ones ($K_1$, $O_1$), significantly influencing hydrodynamics and water exchange processes [16,24]. Previous studies utilizing hydrodynamic models have explored the seasonal and spatial variations in WRT driven by various dynamic processes within the BYS. For instance, substantial seasonal fluctuations in WRT in the BS, influenced by wind, tidal forces, and river discharge, were revealed through three-dimensional modeling [15]. Moreover, it has been shown that the WRT pattern and its variability in the BYS as well as the coastal waters of the Yellow Sea (YS) are significantly

affected by the interactions between tides and wind, based on a hydrodynamic model considering complete dynamic processes [9,24]. By comparing various hydrodynamic processes, a previous study by Lin et al. (2020) suggested that tides are the predominant factor influencing the WRT in the BYS [16]. Nonetheless, the patterns of tidal-driven WRT and the roles of different tidal constituents in the BYS remain poorly understood.

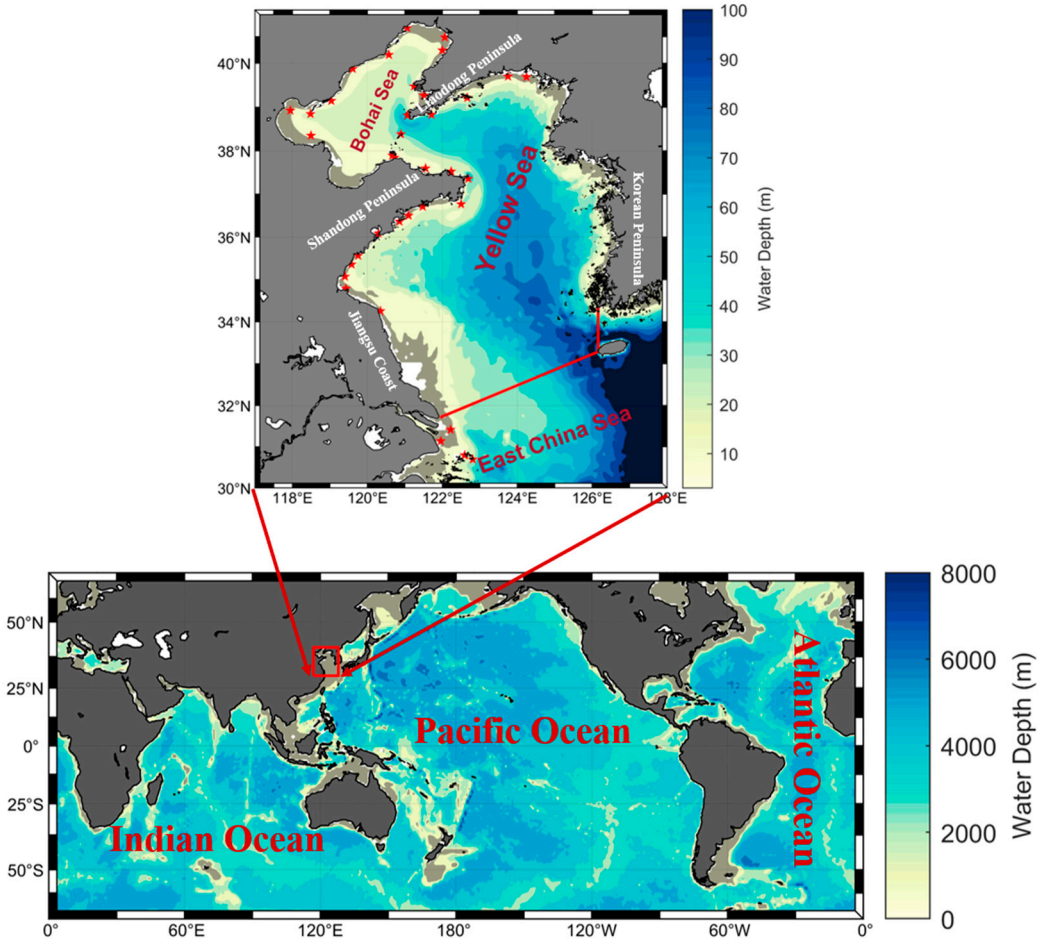


**Figure 1.** Topography and the model domain of the BYS (the upper panel). The red lines denote the prescribed open boundary of the control region for the calculation of the WRT. The red stars represent the locations of the tidal gauge stations.

### *2.2. Tidal Simulation by the MERF Model*

The hydrostatic and barotropic versions of the Marine Environment Research and Forecasting (MERF) ocean model [25] were employed in this study to simulate the tidal process. MERF employed the three-dimensional, primitive, non-hydrostatic equations governing the ocean dynamics, using the Boussinesq approximation and the terrain-following σ-coordinate system [25]. The two-equation turbulence closure model (MY2.5) [26] was implemented in the model to determine the values of the vertical viscosity coefficient and diffusion coefficient.

As shown in Figure 1, the model domain covers the entire BYS. The domain was discretized into a 333 × 333 grid horizontally with a resolution of approximately 3 km (1/30 degree) and into 21 σ-levels vertically. A time step of 30 s was adopted. The model was forced by tidal elevation at the open boundaries, which were calculated based on the tidal amplitudes and epochs of 8 tidal constituents ($M_2$, $S_2$, $K_1$, $O_1$, $N_2$, $K_2$, $P_1$, and $Q_1$). Data for these 8 tidal constituents were obtained from the global ocean tides model TPXO8-atlas TOPEX/Poseidon (https://www.tpxo.net/tpxo-products-and-registration, accessed on 13 June 2022). The tidal model was run for 396 days, starting from 2 December

2019. The simulation results from the last 366 days were output for tidal harmonic analysis and used to drive the WRT model. The amplitudes and epochs of the four primary tidal constituents (i.e., $M_2$, $S_2$, $K_1$, and $O_1$) were validated using data from the 36 tide gauge stations (https://www.chaoxibiao.net/, accessed on 17 August 2023). In the absence of observational data for tidal currents during the simulation period, validation of the modeled tidal currents was conducted by comparing tidal current ellipses with data from the TPXO8 atlas. Meanwhile, given the strong correlation between tidal elevations and currents, validating tidal amplitudes and epochs can serve as an indicator of the accuracy of the modeled tidal currents. Model outputs—including water depth, velocity, and diffusion coefficients—were saved at 30 min intervals and used to drive the WRT model introduced in Section 2.3.

### *2.3. Diagnosis of Water Residence Time*

In this study, WRT is diagnosed using the adjoint method [2] under the framework of the constituent-oriented age and residence time (CART) theory [2,27,28]. By solving the adjoint problem associated with tracer transport, the WRT equation is derived as follows [2]:

$$\frac{\partial \overline{\theta}}{\partial t} + \delta_\omega(x) + \boldsymbol{V} \cdot \nabla \overline{\theta} + \nabla \cdot \left[ \boldsymbol{K} \cdot \nabla \overline{\theta} \right] = 0, \quad (1)$$

where $\overline{\theta}$ represents the WRT, $\boldsymbol{V}$ denotes the three-dimensional velocity field, $\boldsymbol{K}$ is the diffusion tensor, $\delta_\omega(x)$ represents the characteristic function of the control region $\omega$, and $\delta_\omega(x) = \begin{cases} 1 & \forall x \in \omega \\ 0 & \forall x \notin \omega \end{cases}$. The adjoint method enables the calculation of spatiotemporal variations in WRT through a single backward model run.

Based on the adjoint Equation (1), a WRT diagnosis model [29] was applied to determine the spatiotemporal distribution of the WRT in the BYS based on the adjoint method. This model functions as a submodule of the Marine Environment Research and Forecasting model. The governing equations are solved using the finite-difference method, maintaining consistency in grids and vertical layers with the hydrodynamic model. This model has been successfully applied to study WRT in multiple regions, including Jiaozhou Bay [29], the BS [15], the eastern shelf seas of China [16], and the Subei Coastal Water of the YS [9]. These studies showed the high reliability of the WRT model.

In the calculation, the closed boundary is set to $\vec{n} \cdot (\nabla \overline{\theta}) = 0$, with $\vec{n}$ as the outgoing unit vector normal to the boundary. For the open boundary (red lines in Figure 1), a homogeneous Dirichlet boundary condition ($\overline{\theta} = 0$) is imposed, representing the time required for a water parcel to leave the control region for the first time [2,30,31]. The WRT model was executed for a 10-year spin-up period using water depth, velocity, and diffusion coefficients derived from the tidal model. This duration ensured the attainment of a stable WRT variation in the BYS, effectively eliminating the influence of initial conditions on the WRT [12,31]. The WRT values of the 10th year were subsequently utilized for analysis.

### *2.4. Numerical Sensitivity Experiments*

To investigate the impact of different tidal constituents on WRT in the BYS, we conducted two groups of numerical sensitivity experiments. In each experiment, one or several tidal constituents were removed from the tidal model, and then the WRT result was calculated by the WRT model driven by the changed tidal model. Then, the WRT results from different experiments were compared with the control run (i.e., the calculation including all eight tidal constituents) to quantify the impact of various tidal constituents on the WRT in the BYS. In the first group of experiments, we excluded either the semidiurnal or diurnal tidal constituents from the tidal model, separately, and calculated the corresponding WRT

for the two cases (hereinafter referred to as "NoSemidiurnal" and "NoDiurnal" cases, respectively). In addition, we, respectively, excluded the $M_2$ + $S_2$ and $K_1$ + $O_1$ constituents from the tidal model individually to examine the effect of interaction between the primary semidiurnal or diurnal tidal constituents (hereafter referred to as "No$M_2S_2$" and "No$K_1O_1$" cases, respectively). In the second group of experiments, we, respectively, excluded the $M_2$, $S_2$, $K_1$, and $O_1$ constituents from the tidal model individually and then calculated the corresponding WRT values for the six cases (hereafter referred to as "No$M_2$", "No$S_2$", "No$K_1$", and "No$O_1$" cases, respectively).

### *2.5. Lagrangian Residual Currents*

In coastal waters, the Lagrangian residual currents (LRCs) have been recognized as determinants of long-term water transport [32–34]. The tidal-driven Lagrangian residual currents (LRCs) in the BYS were diagnosed and analyzed to help understand the role of tides on the WRT. The LRC is defined as the net displacement of a labeled water parcel over one or multiple tidal cycles, divided by the corresponding time interval, which is calculated using the following equation [32,33]:

$$\mathbf{u}_L(\mathbf{X},\ \tau;\ t_0) = \langle \mathbf{u}[\mathbf{X}_0 + \boldsymbol{\xi}(t;\ \tau),\ t;\ \tau] \rangle = \frac{\boldsymbol{\xi}_{nr}}{nT}, \tag{2}$$

where $\mathbf{u}_L$ represents the LRC; $\mathbf{X}$ denotes the position vector; $\mathbf{X}_0$ represents the initial position vector; $t$ and $\tau$ represent the intra-tidal process-independent time and the inter-tidal process-independent time, respectively; $t_0$ is the initial time at which the water parcel is tracked; $\mathbf{u}(\mathbf{X}_0 + \boldsymbol{\xi}(t;\ \tau))$ is the instantaneous velocity, where $\mathbf{u} = \frac{\partial \boldsymbol{\xi}}{\partial t}$; $\boldsymbol{\xi}(t;\ \tau)$ is the displacement of the water parcel, where $\boldsymbol{\xi} = \mathbf{X} - \mathbf{X_0}$; $\boldsymbol{\xi}_{nr}$ represents the net displacement of the water parcel over $n$ tidal cycles; and $T$ is the tidal period.

Based on Equation (2), we implemented a particle tracking model to determine the net displacement of particles after a period of 30 days (one month). The particle tracking model utilized in this study is derived from open-access code that has been previously employed in other studies, including the calculation of the LRC [15,35]. In the particle tracking model, a spatial linear interpolation method was implemented to derive velocity values at the particle locations, facilitating a smooth transition of velocity values between grid nodes and reducing the discontinuities of the current field. The LRC was calculated by dividing this net displacement by 30 days. At the initial time step, particles were released at the center of each grid cell of the tidal model. We computed the LRC for the sensitivity experiments in Section 2.3 and analyzed the LRC characteristics of tidal constituents. Although we lack data to validate the LRC, the correspondence between the LRC and the WRT presented below may offer some evidence supporting the model's validity.

## 3. Results

### *3.1. Validation of the Tidal Simulation*

The cotidal charts of the four principal tidal constituents ($M_2$, $S_2$, $K_1$, and $O_1$) in the BYS obtained from the tidal model are shown in Figure 2. The simulation results of our tidal model are consistent with the marine atlas of the BS and YS [36], the observations of the satellite altimeter [37], and numerical simulations [38–40], particularly showing high agreement in terms of amphidromic point locations and amplitude distribution. Furthermore, we validated the simulated tidal amplitudes and epochs of the tidal model against observations from tide gauge stations (Figure 3), which show high consistency with each other. The root mean square errors (RMSEs) of the amplitude for the $M_2$, $S_2$, $K_1$, and $O_1$ tidal constituents are 7.4 cm, 4.5 cm, 1.9 cm, and 2.1 cm, respectively, and the RMSE values of the epoch for these constituents are 10.6°, 9.2°, 5.1°, and 5.8°, respectively.

Meanwhile, the modeled tidal current ellipse demonstrates strong consistency with the data from the TPXO8-atlas (Figure 3c,d). Therefore, the tidal model of the BYS established in this study can well represent the tidal characteristics and be reliable for simulating the tidal dynamic processes in the BYS.

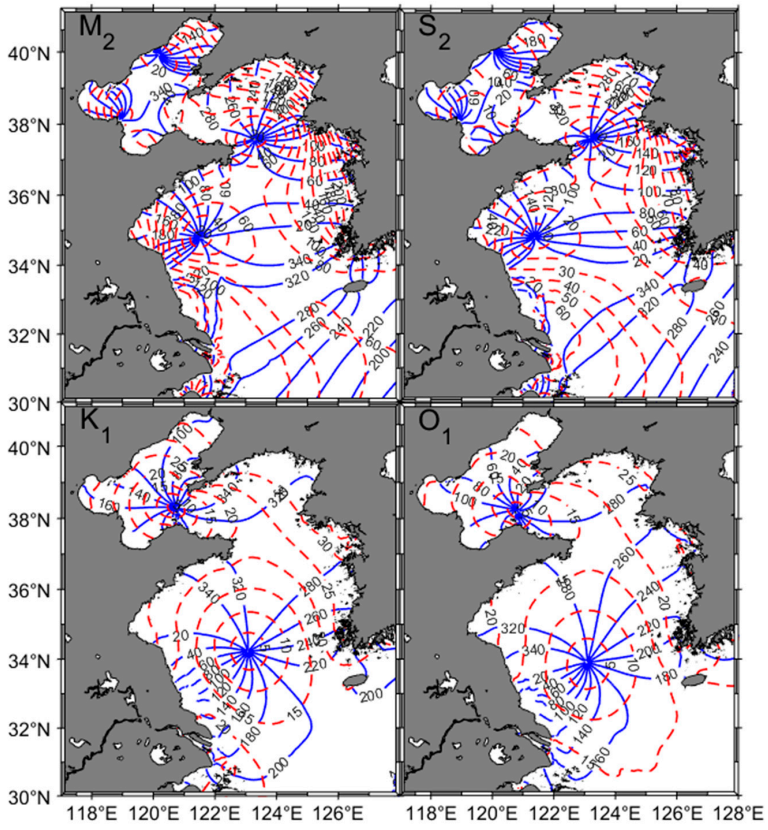


**Figure 2.** Co-tidal charts for the four primary tidal constituents ($M_2$, $S_2$, $K_1$, and $O_1$). The red dashed and blue solid isolines denote the amplitude (cm) and epoch (○) of the tidal constituents, respectively.

### *3.2. Tidal-Driven WRT in the BYS*

Driven by the tides in the BYS, the WRT was diagnosed using the WRT model. The spatially averaged WRT for the BYS, the BS, and the YS are 2.11 years, 2.40 years, and 2.05 years, respectively. Influenced by the tidal cycles, the spatially averaged WRT in the BYS exhibits a semidiurnal tidal variation (Figure 4a) and a spring–neap tidal cycle on a monthly scale (Figure 4b). However, these tidal variations are only approximately 4–6 days, which is small compared to the average WRT of 2.11 years for the BYS. Similarly, although there are significant differences in the WRT values across different experiments, the tidal variation within each experiment is negligible (Figure 4c).

In space, the WRT in the BYS exhibits significant inhomogeneity (Figure 5). Overall, the WRT is longer in the BS and relatively shorter in the YS. Specifically, the central and southern areas of BS, the central YS, and the southern waters off the Korean Peninsula are characterized by longer WRTs, reaching up to 3 to 6 years in the central BS and central YS. This indicates a lower rate of water exchange in these areas. In contrast, the coastal waters of the YS—particularly those of the Liaodong Peninsula, the northwestern side of the Korean Peninsula, the eastern side of the Shandong Peninsula, and along the southern waters of the Jiangsu coast—have shorter residence times, approximately 1 to 2 years, suggesting a faster water exchange in these regions.

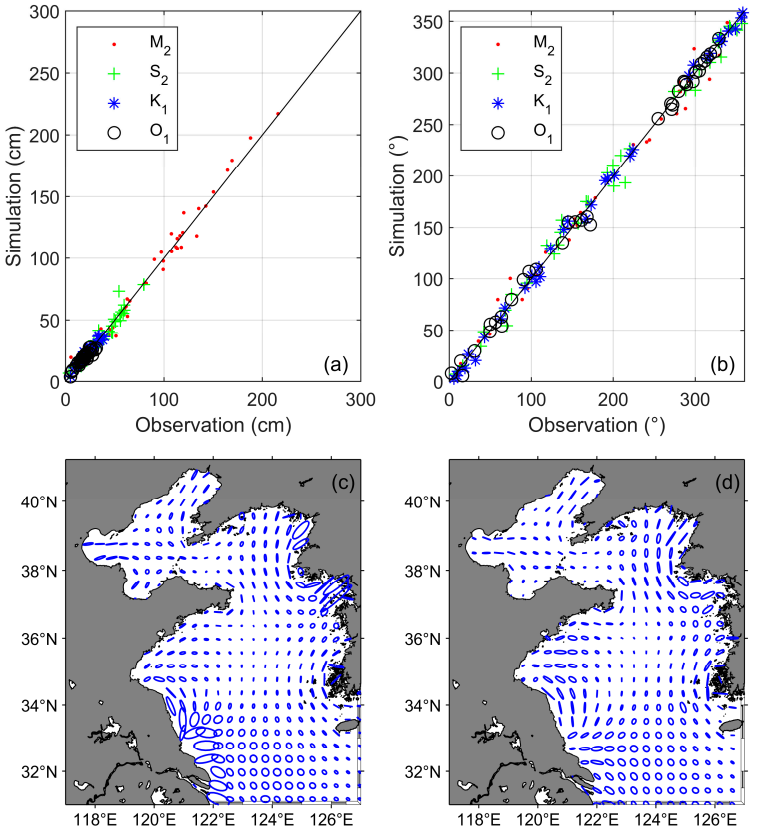


**Figure 3.** Comparison of the simulated values of tidal amplitude (**a**) and epoch (**b**) with the observed values from the tidal gauge stations (Figure 1). Comparison of the modeled $M_2$ tidal current ellipse (**c**) with that from the TPXO8-atlas (**d**), the blue circles represent tidal current ellipses.

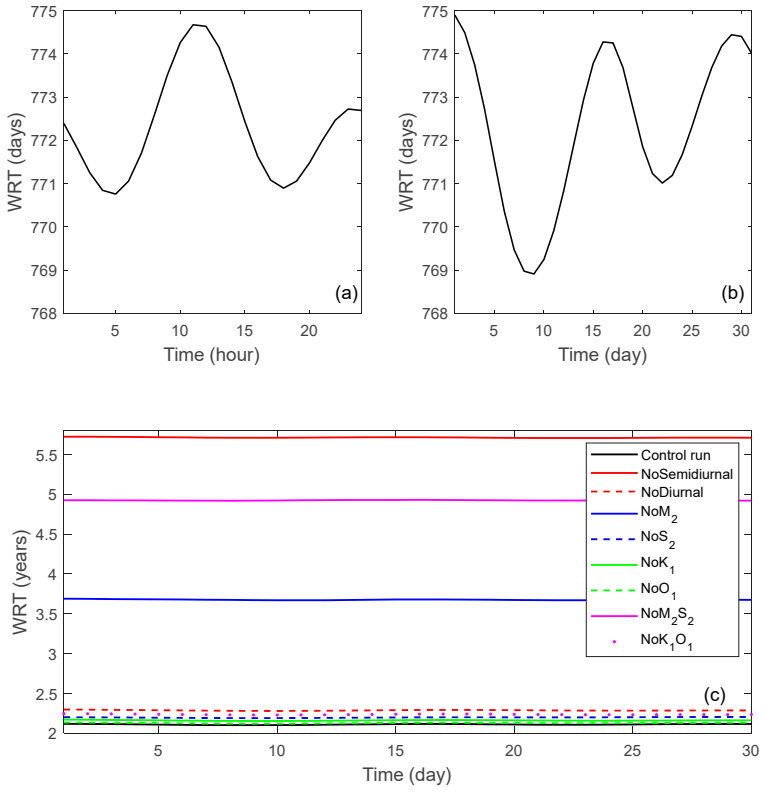


**Figure 4.** The spatially averaged WRTs in the BYS over a month: (**a**) hourly mean, (**b**) daily mean, (**c**) daily mean for the nine cases. Note that (**b**) uses a small range on the Y-axis to show the daily variations in the WRT.

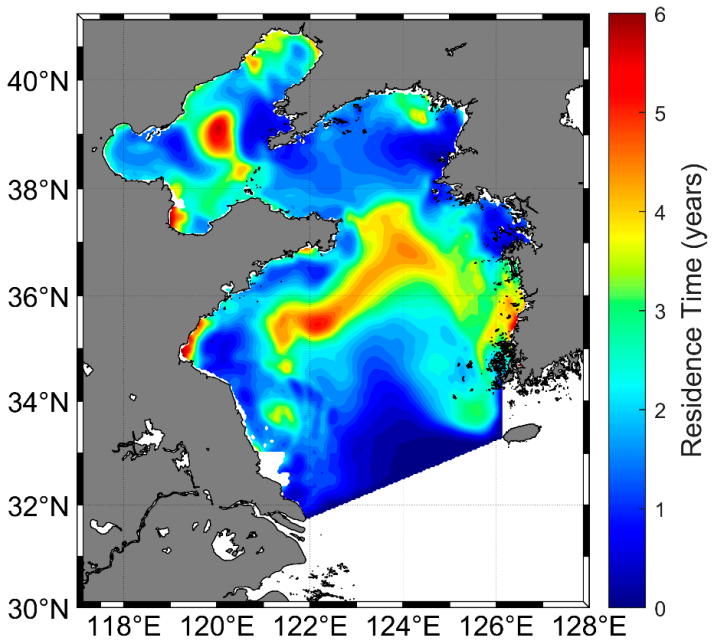


**Figure 5.** The monthly mean of vertically averaged average WRT in the BYS for the control run.

### *3.3. Effects of Tidal Constituents on the WRT*

Using the sensitivity experiments, the effects of different tidal constituents (semidiurnal tides, diurnal tides, and the four primary tidal constituents) on the WRT are investigated. In the NoSemidiurnal case, the average WRT values are 5.71 years in BYS, 3.86 years in BS, and 6.10 years in YS (Table 1). Compared to the control run, the spatially averaged WRT in the BYS increases by 170% (Figure 6a). Figure 6b shows that the absence of semidiurnal tides leads to a significant increase in WRT across most areas of the YS and the center and south of the BS, with increases of up to approximately 3 years. This finding suggests that the semidiurnal tides significantly reduce the WRT and, thus, enhance water exchange in the BYS. In addition, the $NoM_2S_2$ case shows similar WRT and changes to those observed in the NoSemidiurnal case (Table 1 and Figure 6e,f), indicating that the two primary semidiurnal constituents, $M_2$ and $S_2$, could play major roles in the role of semidiurnal tides on the WRT.

**Table 1.** The spatially averaged WRT in various regions for different sensitivity experiments.

| Region | Control Run | NoSemidiurnal | NoDiurnal | $NoM_2S_2$ | $NoK_1O_1$ | $NoM_2$ | $NoS_2$ | $NoK_1$ | $NoO_1$ |
|---|---|---|---|---|---|---|---|---|---|
| BYS (year) | 2.11 | 5.71 | 2.29 | 4.92 | 2.24 | 3.68 | 2.20 | 2.16 | 2.13 |
| BS (year) | 2.40 | 3.86 | 3.09 | 3.42 | 2.93 | 3.08 | 2.40 | 2.73 | 2.67 |
| YS (year) | 2.05 | 6.10 | 2.12 | 5.24 | 2.09 | 3.80 | 2.15 | 2.04 | 2.01 |

In contrast, the NoDiurnal case with WRT values of 2.29 years in BYS, 3.09 years in BS, and 2.12 years in YS (Table 1) in the respective regions has a relatively small difference from the control run. The spatially averaged WRT in the BYS increases by only 8.5% compared to the control run. The spatial distribution of WRT in the NoDiurnal case (Figure 6c) is generally similar to that in the control run (Figure 5). The difference distribution (control run–NoDiurnal, Figure 6d) shows that in the NoDiurnal case, the change in WRT mainly occurs in BS. The change in BS is comparable to that in the $NoM_2$ case. The diurnal tides increase the WRT by 1 to 2 years in the central BS and decrease the WRT by about 3 years in the northwest of the BS. Overall, the semidiurnal tides have a more pronounced effect on the WRT than the diurnal tides, which is related to the stronger amplitude of the

semidiurnal tides, while the effect of diurnal tides is mainly in the BS. Similarly, the two primary semidiurnal constituents, $K_1$ and $O_1$, play major roles in the role of diurnal tides on the WRT (Table 1 and Figure 6g,h).

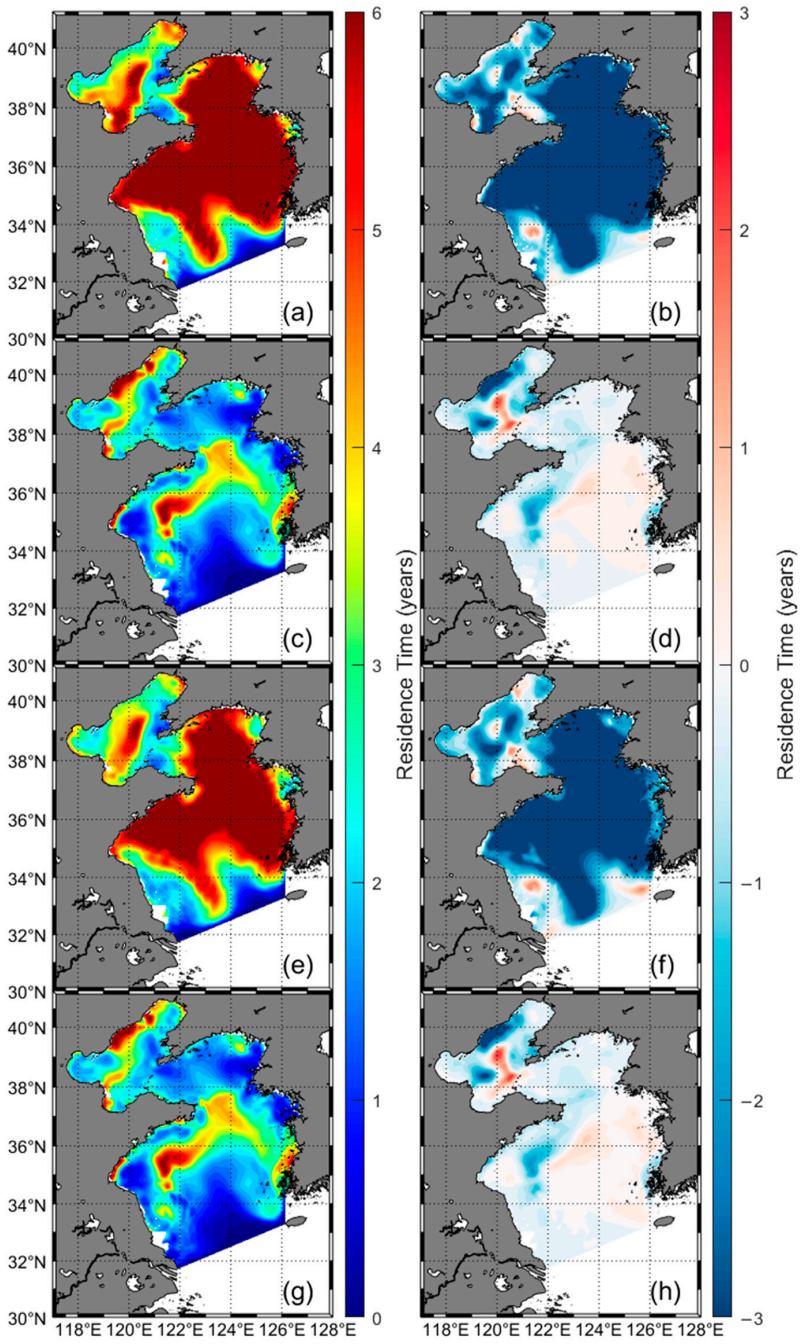


**Figure 6.** The monthly mean of vertically averaged WRT in the BYS for the first group of sensitivity experiments: (**a**) NoSemidiurnal; (**b**) control run-NoSemidiurnal; (**c**) NoDiurnal; (**d**) control run-NoDiurnal; (**e**) $NoM_2S_2$; (**f**) control run-$NoM_2S_2$; (**g**) $NoK_1O_1$; (**h**) control run-$NoK_1O_1$.

The WRT results of the second group of numerical experiments are shown in Figure 7. In the $NoM_2$ case, the WRT in the BYS significantly increased, with a spatial average of 3.68 years, representing a 74.4% increase compared to the control run (Figure 7a). This increase is particularly pronounced in the central YS, where it reaches approximately 3 years. The WRT difference between the control run and the $NoM_2$ case (Figure 7b) further shows that the presence of the $M_2$ tidal constituent significantly reduces the WRT in most areas of the BYS, especially highlighting its crucial role in accelerating the water exchange

of the YS. In the $NoS_2$ case, the spatially averaged WRT is 2.20 years, and the spatial distribution of the WRT (Figure 7c) is very similar to that of the control run. The WRT difference between the control run and $NoS_2$ (Figure 7d) further reveals no significant changes in WRT, suggesting a minimal impact from the $S_2$ tidal constituent. In the $NoK_1$ and $NoO_1$ cases, the spatially averaged WRT values are 2.16 and 2.13 years, respectively, and the spatial distributions of WRT are nearly identical (Figure 7e,g). Their differences with the control run (control run—$NoK_1$, Figure 7f; control run—$NoO_1$, Figure 7h) showed that the effects of the $K_1$ and $O_1$ tidal constituents are relatively strong in the BS, but weak in the YS.

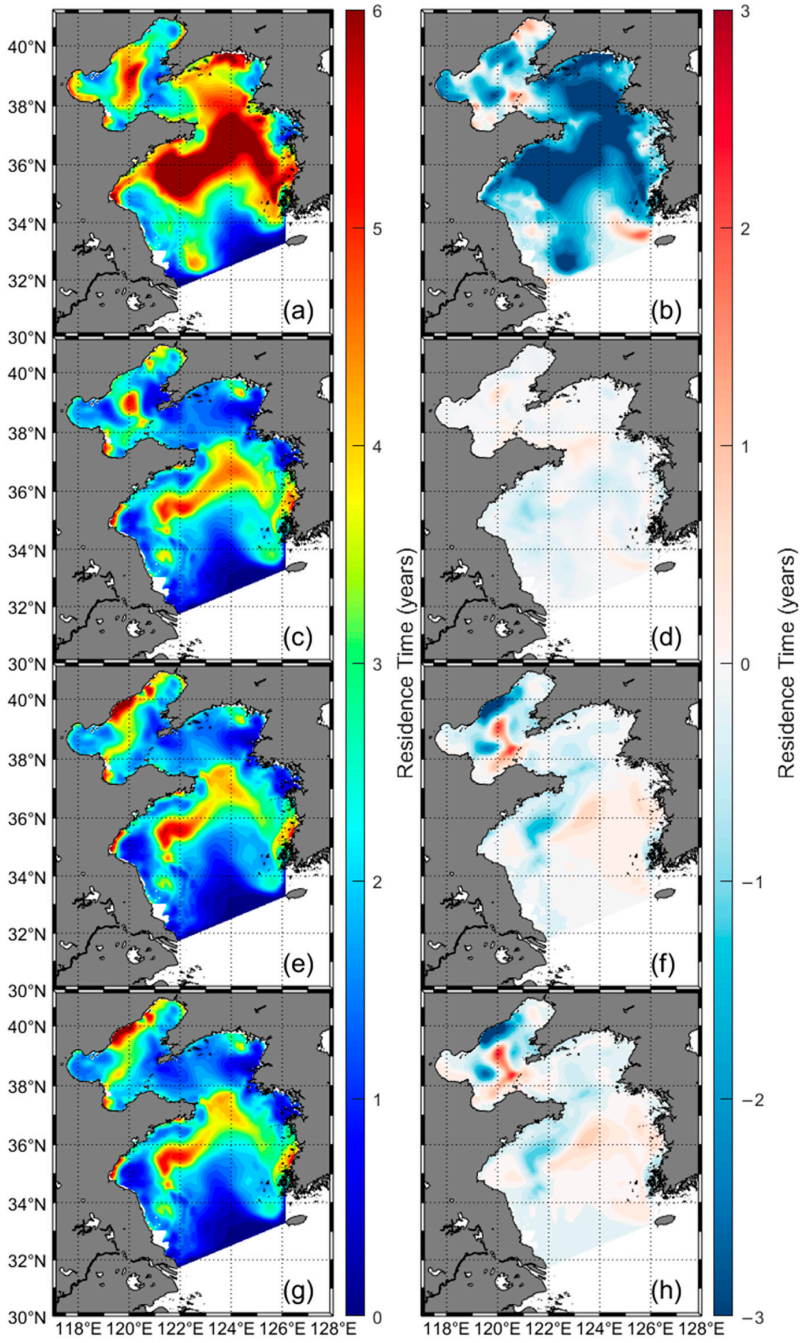


**Figure 7.** The monthly mean of vertically averaged WRT in the BYS for the second group of sensitivity experiments: (**a**) $NoM_2$; (**b**) control run-$NoM_2$; (**c**) $NoS_2$; (**d**) control run-$NoS_2$; (**e**) $NoK_1$; (**f**) control run-$NoK_1$; (**g**) $NoO_1$; (**h**) control run-$NoO_1$.

Furthermore, the combination of the two experimental groups indicated that the WRT in the $NoM_2S_2$ case (4.92 years) is significantly longer than the WRT observed in both the $NoM_2$ (3.68 years) and $NoS_2$ (2.20 years) cases (see Table 1 and Figures 6 and 7). This finding suggests that the interaction between the two primary semidiurnal constituents, M2 and S2, may also be critical in influencing WRT. Overall, the effects of the tidal constituents on the WRT in the BYS exhibit significant differences. The $M_2$ tidal constituent leads to a substantial decrease in the WRT, while the $S_2$, $K_1$, and $O_1$ tidal constituents have relatively minor effects on the WRT. The influence of the K1 and $O_1$ tidal constituents is primarily confined to the central and northern parts of the BS, while the $S_2$ tidal constituent has the least impact on water exchange in the BYS.

## 4. Discussion

### *4.1. Comparison with Previous Studies*

In contrast to previous studies that examined water residence time (WRT) patterns or seasonal variations influenced by various dynamic processes, including tides, wind, and river discharge (e.g., Luo et al. [15]; Lin et al. [16]), the present study specifically investigates the WRT pattern driven solely by tidal forces, with a focus on the roles of different tidal constituents. Although this study employed the same WRT diagnostic methodology as the prior research, it utilized a different boundary for the calculations. Luo et al. [15] and Lin et al. [16] defined their boundaries at the Bohai Strait and the shelf break of the eastern shelf seas of China, whereas this study established its boundary at the interface between the Yellow Sea (YS) and the East China Sea. The variation in boundary definitions is likely to result in differing WRT estimates.

For instance, Lin et al. [16] reported average WRTs of 11.60 years in the Bohai Sea (BS) and 4.95 years in the YS, which are substantially longer than the WRTs found in this study (2.40 years and 2.05 years, respectively). Luo et al. [15] calculated an annual mean WRT of 3.43 years in the BS, slightly higher than the values reported here. This discrepancy may be attributed to the stratification present in the Bohai Sea, which may limit bottom water mixing and exchange, thereby prolonging the WRT.

Moreover, while the tidal-driven WRT exhibited similar values in the BS and YS in this study, Lin et al. [16] observed a significantly higher WRT in the BS compared to the YS. This finding suggests that other hydrodynamic processes, such as wind-driven currents, contribute to the increased disparity in WRT between the YS and BS. In the YS, strong wind-driven coastal currents and the warm current of the Yellow Sea facilitate water exchange. In contrast, in the BS, wind-driven currents may be hindered by shallower water depths and considerable bottom resistance, resulting in a much longer WRT compared to that in the YS [16].

### *4.2. Formation Mechanism of the Tidal-Driven WRT Pattern*

The tidal-driven LRC in the BYS, which represents long-term transport by the tidal currents [33,34], is analyzed to understand the spatial patterns of the tidal-driven WRT. A comparison of the LRC (Figure 8) and the WRT (Figure 5) shows a significant spatial correlation. The LRC (Figure 8) is relatively weak in the central BS and the central YS, with flow speeds generally below 0.005 m/s, corresponding to the higher WRT observed in these areas (Figure 5). The weaker LRC in these regions facilitates water retention, thereby leading to a longer WRT. In contrast, coastal regions, such as the Liaodong Peninsula, Shandong Peninsula, Korean Peninsula, and the Jiangsu Coast, exhibit stronger LRCs, with local speeds reaching up to 0.02 m/s or more, corresponding to a lower WRT. Stronger LRCs in the coastal regions accelerate the water exchange rate, thereby reducing the WRT. In addition, the direction of the LRC also influences the WRT in the BYS. In the central BS

and the central YS, the LRC exhibits eddy structures (Figure 8). These LRC eddies could trap the water inside the eddies to some extent and, thus, significantly extend the WRT in these regions (Figure 5). In nearshore regions, the LRC generally flows outward toward the open sea, such as along the coasts of the Liaodong and Shandong Peninsulas and Jiangsu. The LRC exhibits along-shore flow patterns that facilitate the transport of coastal waters offshore, thereby reducing the WRT in these regions.

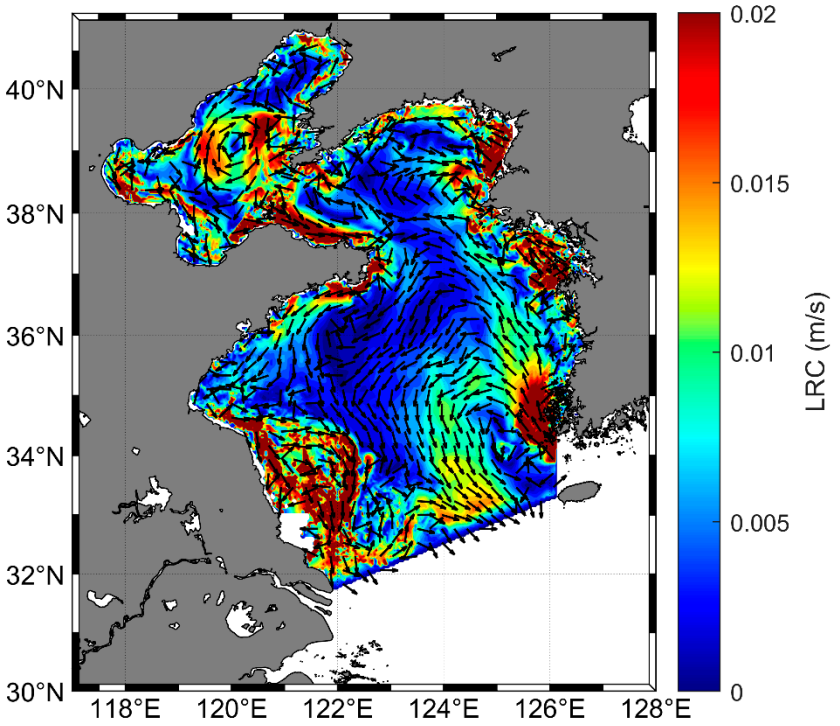


**Figure 8.** Lagrange residual currents (black arrows) for the control run. The color denotes the magnitude of the LRC speed (m/s).

Other processes, such as tidal pumping and tidal dispersion, may also influence water transport, particularly in proximity to topography. In the majority of this study, the terrain is relatively flat, which likely confines their effects primarily to the coastal regions. Furthermore, the spatial scale of the study area is approximately 1000 km, with a mean lateral residual current (LRC) of approximately 0.01 m/s (Figure 8). Consequently, the estimated water residence time (WRT) induced by the LRC is approximately 3.2 years, which closely aligns with the modeled WRT value. This suggests that the LRC is the predominant factor influencing the WRT within the overall system.

### *4.3. Roles of Different Tidal Constituents on the WRT*

In the sensitivity experiments, the changes in the LRC for different tidal constituents can explain the changes in the WRT well. Compared to the control run results (Figure 8), the intensity of LRC in almost the entire BYS weakens in the NoSemidiurnal case (Figure 9a), with the most pronounced reduction occurring in the coastal regions, where the decrease reaches up to 0.02 m/s. The LRC reduction induces a slower water exchange rate and longer WRT (Figure 6a). The LRC induced by the semidiurnal tides (i.e., LRC in control run–NoSemidiurnal, Figure 9b) shows the strong currents along the coast of the BYS, indicating that the semidiurnal tides could facilitate the water export in the BYS mainly by inducing the coastal water transport. In the NoDiurnal case, the LRC is weakened in the central BS, while the LRC in the YS is generally similar to those in the control run (Figures 8 and 9c). The difference in the LRC (control run–NoDiurnal, Figure 9d) indicates that the diurnal

tide has a significant effect on the LRC in the BS, especially on the LRC eddy, and a minimal effect on the LRC in the YS. The diurnal tides enhance the LRC intensity in the coastal BS (Figure 9d), thereby reducing the WRT in the coastal BS. However, the diurnal tides also enhance the LRC eddy in the central BS, which exacerbates the trapping of the water in the central BS and, thus, increases the WRT in the central region (Figure 6d). In summary, both the semidiurnal and diurnal tidal constituents exert an influence on the LRC in the BYS. The semidiurnal tides primarily affect the intensity of the LRC along the coasts of the BYS, as well as the eddy structures in the central BS, thereby influencing the WRT in these regions. In contrast, the diurnal tides have a significant impact on the LRC intensity and eddy structures in the central BS, with minimal effects in other regions.

The significant influence of the interaction between $M_2$ and $S_2$ on the WRT is also supported by the stronger LRC in the $NoM_2S_2$ case compared to both the $NoM_2$ and $NoS_2$ cases. The superposition of $M_2$ and $S_2$ generates the spring–neap tidal cycle. During spring tides, the tidal currents are significantly intensified, leading to enhanced residual currents and water exchange. Although the tidal currents and water exchange are diminished during neap tides, the strengthening effect of spring tides on the water exchange may surpass the weakening effect of neap tides, indicating a non-linear interaction among tidal constituents that influences long-term water transport and WRT.

The LRCs of the $NoM_2$, $NoS_2$, $NoK_1$, and $NoO_1$ sensitivity experiments are shown in Figure 10a,c,e,g, respectively. By subtracting the LRCs of the sensitivity experiments from that of the control run, we can obtain the LRCs induced by $M_2$, $S_2$, $K_1$, and $O_1$ (Figure 10b,d,f,h), respectively. In comparison, $M_2$ induces strong LRCs along the coasts of the BYS and in the central BS (Figure 10b), suggesting the critical role of the $M_2$ tidal constituent in driving water exchange along the coasts of the BYS and in the central BS. Therefore, $M_2$ plays an important role in the long-term water transport and WRT pattern in the BYS. The $S_2$ tidal constituent has a relatively weak influence on the LRC in the entire BYS (Figure 10d) and, thus, a weak influence on the WRT. The $K_1$ and $O_1$ tidal constituents mainly influence the LRC in the BS (Figure 10f,h) and, thus, the WRT in the BS.

The different roles of the tidal constituents on the LRC and WRT could be related to their different tidal energies, as demonstrated by the significant correlation between the tidal energy and change in WRT (Figure 11a). The tidal energy (quantified using the square of the tidal amplitude [41]) of $M_2$ is mainly concentrated in the nearshore and shallow regions of the BYS (Figure 11b), which induces strong coastal tidal currents and LRCs and, thus, facilitates the water export of the BYS. The tidal energies of $S_2$, $K_1$, and $O_1$ are significantly lower than that of the $M_2$ constituent (Figure 11c–e). Because the $M_2$ constituent dominates the tidal energy and dynamics of the BYS (Figures 2 and 11), exerting a primary influence on the WRT. Due to the tidal wave overlap of the $S_2$ with $M_2$, the contribution of the $S_2$ constituent on the LRC and WRT is limited, although the amplitude of $S_2$ is stronger than $K_1$ and $O_1$ (Figure 2). On the contrary, although the amplitudes of $K_1$ and $O_1$ are relatively small, they have a relatively high energy ratio to $M_2$ in the BS, particularly in the central BS around the $M_2$ amphidromic points (Figures 2 and 11) and, thus, they can modulate the LRC in the BS, which can explain the pronounced effects of $K_1$ and $O_1$ on WRT in the BS.

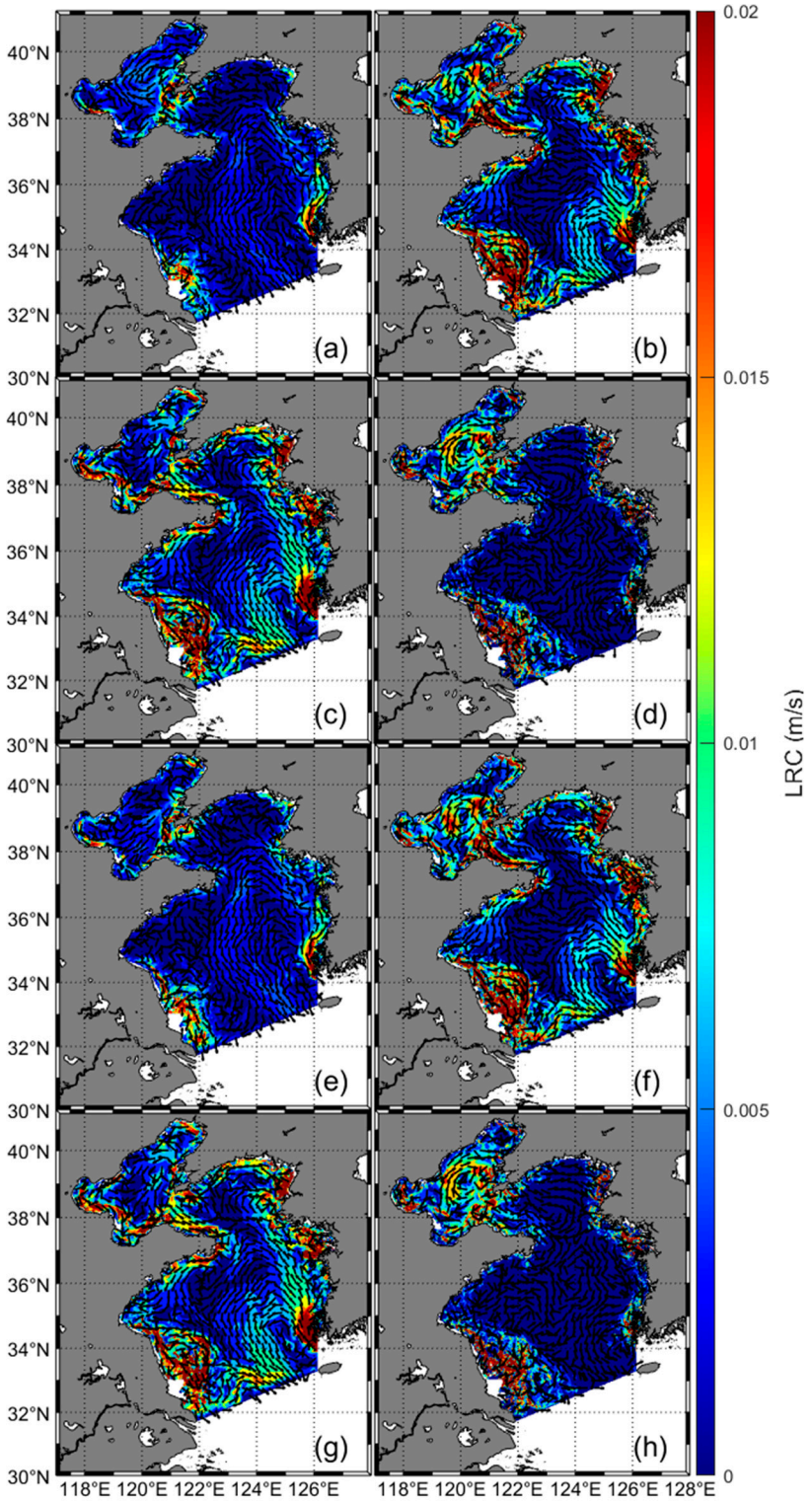


**Figure 9.** Lagrange residual currents (black arrows) for the sensitivity experiments: (**a**) NoSemidiurnal; (**b**) control run-NoSemidiurnal; (**c**) NoDiurnal; (**d**) control run-NoDiurnal; (**e**) $NoM_2S_2$; (**f**) control run-$NoM_2S_2$; (**g**) $NoK_1O_1$; (**h**) Control run-$NoK_1O_1$. The color denotes the magnitude of the LRC speed (m/s).

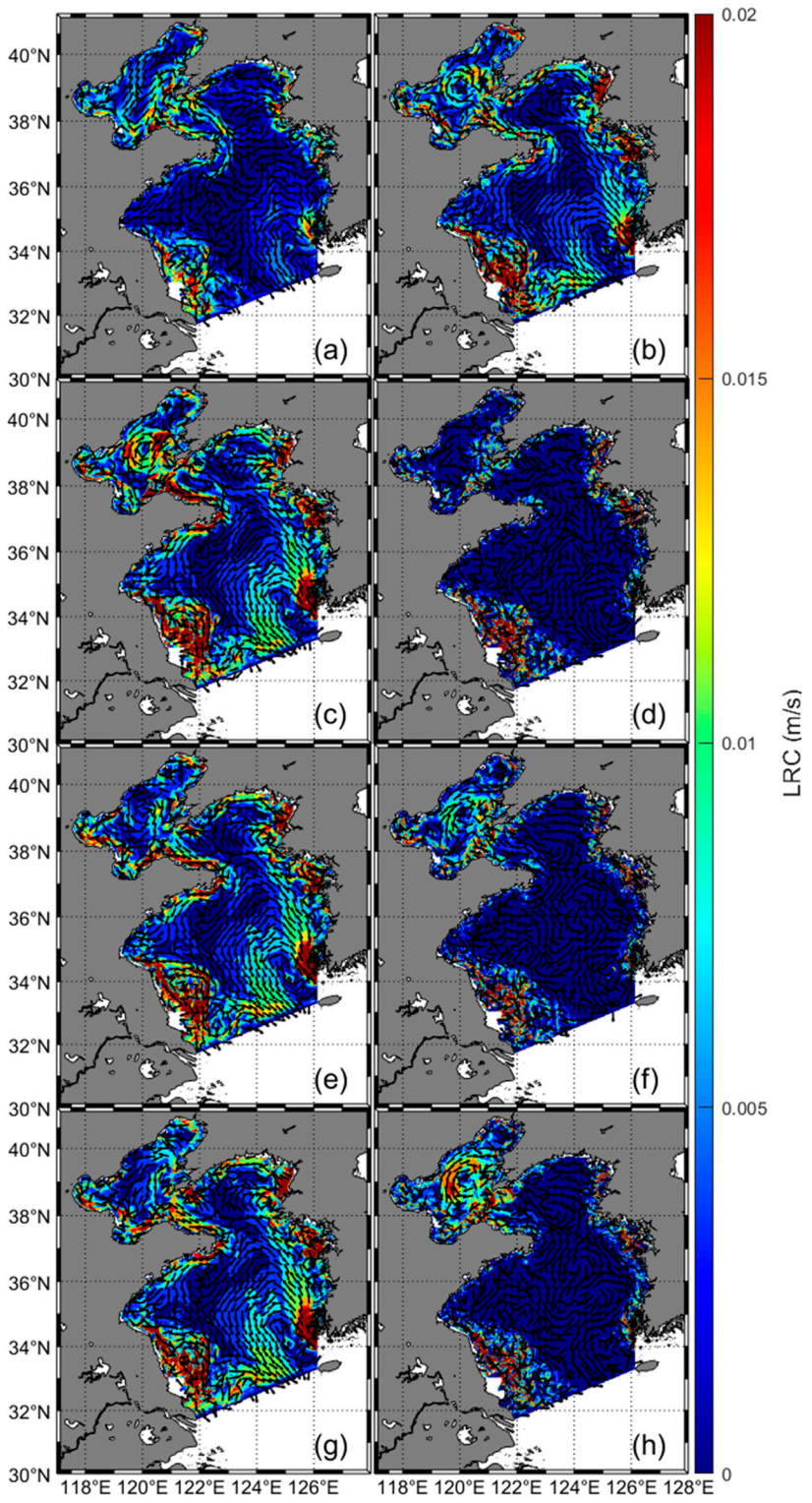


**Figure 10.** Lagrange residual currents (black arrows) for the second group of sensitivity experiments: (**a**) $NoM_2$; (**b**) control run-$NoM_2$; (**c**) $NoS_2$; (**d**) control run-$NoS_2$; (**e**) $NoK_1$; (**f**) control run-$NoK_1$; (**g**) $NoO_1$; (**h**) control run-$NoO_1$. The colors show the patterns of the LRC speed (m/s).

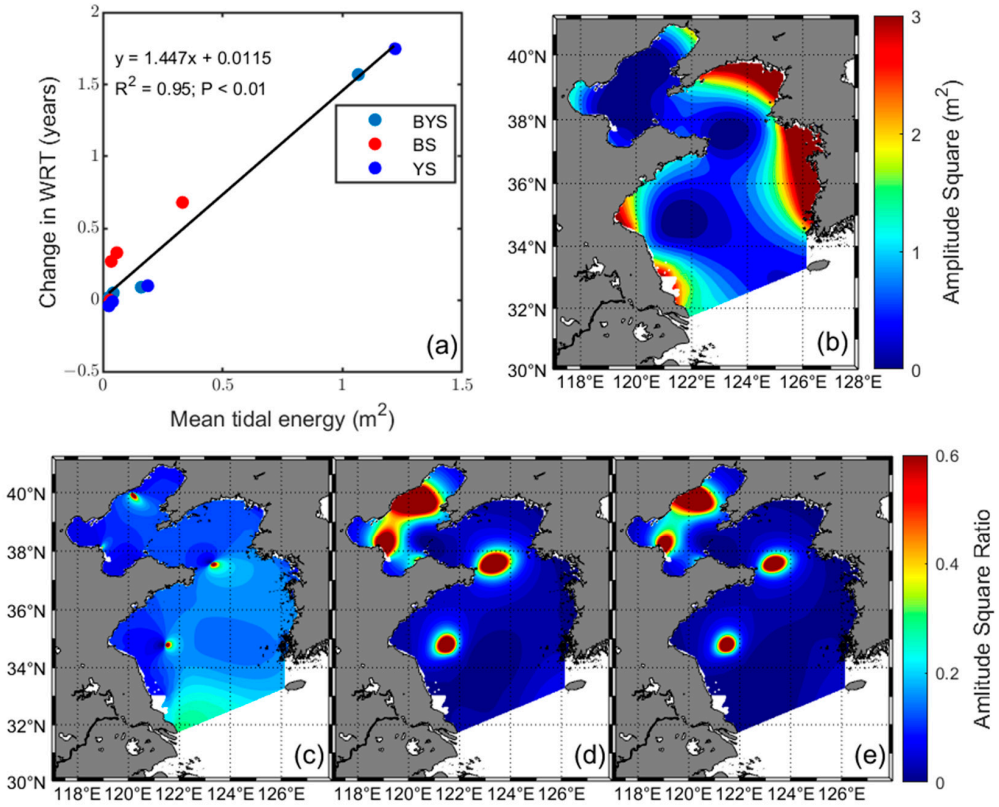


**Figure 11.** The change in WRT after the exclusion of tidal constituents vs. the excluded tidal energy averaged over the respective regions (**a**). The WRT in the four experiments that excluded solely individual tidal constituents (i.e., NoM2, NoS2, NoK1, and NoO1 cases) are used. Tidal energy is quantified by the square of the tidal amplitude. (**b**) Amplitude square of the $M_2$ tidal constituent, (**c**) the ratio of $S_2$ to $M_2$, (**d**) the ratio of $K_1$ to $M_2$, (**e**) the ratio of $O_1$ to $M_2$.

## 5. Conclusions

This study examines the tidal-driven WRT in the BYS, elucidating the influence of various tidal constituents, including semidiurnal and diurnal tides, on WRT. We determined that the tidal-driven WRT values for BYS, BS, and YS are 2.11 years, 2.40 years, and 2.05 years, respectively. The tidal-driven WRT exhibits a significant spatially heterogeneous pattern, which correlates with the distribution of the tidal-driven LRC. Our results indicate that semidiurnal tides exert a greater influence on WRT compared to diurnal tides. Specifically, semidiurnal tides substantially decrease WRT across the entire BYS, whereas diurnal tides primarily affect WRT in the BS. The various tidal constituents have distinct effects on the spatial distribution of WRT. The $M_2$ tidal constituent is the most influential in reducing WRT and facilitating water exchange due to its predominant energy contribution within the tidal system. In contrast, $K_1$ and $O_1$ have more localized effects on WRT, particularly in the central BS, where their energy ratios relative to $M_2$ are relatively high. Although the amplitude of the $S_2$ constituent is greater than those of $K_1$ and $O_1$, its contribution to LRC and, consequently, to WRT is limited due to the overlapping tidal wave effects with $M_2$. This research enhances the understanding of the impact of tidal dynamics on long-term water transport and its associated timescales, which are crucial for improving our understanding and predictions of material transport and ecosystem dynamics in tidal-dominated environments.

**Author Contributions:** Conceptualization, Q.F. and L.L.; data curation, H.J. and C.D.; formal analysis, C.D., K.J. and X.L.; methodology, Q.F. and L.L.; visualization, C.D. and K.J.; writing—original draft, Q.F. and H.J.; writing—review and editing, L.L. All authors have read and agreed to the published version of the manuscript.

**Funding:** This research was funded by the Observation and Research Station of Laizhou Bay Marine Ecosystem, MNR, and Shandong Key Laboratory of Marine Ecological Restoration (SAL202407), the Key Discipline Project of Hebei Academy of Sciences (23A15), the Qingdao Natural Science Foundation-Original Exploration Project (23-2-1-228-zyyd-jch), the Qingdao Shinan District Science and Technology Plan Project (2023-1-013-CL), and the Qingdao Science and Technology Demonstration Project (24-1-8-cspz-11-nsh).

**Data Availability Statement:** The data presented in this study are available on request from the corresponding author. The data on tidal constituents used in this study can be obtained from the global ocean tide model TPXO8-atlas TOPEX/Poseidon (https://www.tpxo.net/tpxo-products-and-registration, accessed on 13 March 2025), and from the website (https://www.chaoxibiao.net/, accessed on 13 March 2025).

**Conflicts of Interest:** The authors declare no conflicts of interest.

## Abbreviations

The following abbreviations are used in this manuscript:

| | |
|---|---|
| WRT | water residence time |
| BYS | Bohai and Yellow Seas |
| LRC | Lagrangian residual currents |
| BS | Bohai Sea |
| YS | Yellow Sea |

## References

1. Bolin, B.; Rodhe, H. A note on the concepts of age distribution and transit time in natural reservoirs. *Tellus* **1973**, *25*, 58–62. [CrossRef]
2. Delhez, É.J.; Heemink, A.W.; Deleersnijder, É. Residence time in a semi-enclosed domain from the solution of an adjoint problem. *Estuar. Coast. Shelf Sci.* **2004**, *61*, 691–702. [CrossRef]
3. Takeoka, H. Fundamental concepts of exchange and transport time scales in a coastal sea. *Cont. Shelf Res.* **1984**, *3*, 311–326. [CrossRef]
4. Messager, M.L.; Lehner, B.; Grill, G.; Nedeva, I.; Schmitt, O. Estimating the volume and age of water stored in global lakes using a geo-statistical approach. *Nat. Commun.* **2016**, *7*, 13603. [CrossRef]
5. Lucas, L.V.; Deleersnijder, E. Timescale methods for simplifying, understanding and modeling biophysical and water quality processes in coastal aquatic ecosystems: A review. *Water* **2020**, *12*, 2717. [CrossRef]
6. Gao, Y.; Jia, J.; Lu, Y.; Yang, T.; Lyu, S.; Shi, K.; Zhou, F.; Yu, G. Determining dominating control mechanisms of inland water carbon cycling processes and associated gross primary productivity on regional and global scales. *Earth-Sci. Rev.* **2021**, *213*, 103497. [CrossRef]
7. Shen, J.; Du, J.; Lucas, L.V. Simple relationships between residence time and annual nutrient retention, export, and loading for estuaries. *Limnol. Oceanogr.* **2022**, *67*, 918–933. [CrossRef]
8. John, S.; Muraleedharan, K.R.; Revichandran, C.; Azeez, S.A.; Seena, G.; Cazenave, P.W. What controls the flushing efficiency and particle transport pathways in a tropical estuary? Cochin Estuary, Southwest Coast of India. *Water* **2020**, *12*, 908. [CrossRef]
9. Lin, L.; Liu, D.; Fu, Q.; Guo, X.; Liu, G.; Liu, H.; Wang, S. Seasonal variability of water residence time in the Subei Coastal Water, Yellow Sea: The joint role of tide and wind. *Ocean Model.* **2022**, *180*, 102137. [CrossRef]
10. Jepsen, S.M.; Harmon, T.C.; Sadro, S.; Reid, B.; Chandra, S. Water residence time (age) and flow path exert synchronous effects on annual characteristics of dissolved organic carbon in terrestrial runoff. *Sci. Total Environ.* **2019**, *656*, 1223–1237. [CrossRef]
11. Lin, L.; Fu, Q.; Jin, K.; Sun, Z. Investigation of water exposure time as a foundation for improving programs for coastal pollutant emission reduction. *Ocean Coast. Manag.* **2023**, *245*, 106880. [CrossRef]
12. Du, J.; Shen, J. Water residence time in Chesapeake Bay for 1980–2012. *J. Mar. Syst.* **2016**, *164*, 101–111. [CrossRef]
13. Xiong, J.; Shen, J.; Qin, Q. Exchange flow and material transport along the salinity gradient of a long estuary. *J. Geophys. Res. Ocean.* **2021**, *126*, e2021JC017185. [CrossRef]

14. Xiong, J.; Shen, J.; Qin, Q.; Du, J. Water exchange and its relationships with external forcings and residence time in Chesapeake Bay. *J. Mar. Syst.* **2021**, *215*, 103497. [CrossRef]
15. Luo, C.; Lin, L.; Shi, J.; Liu, Z.; Cai, Z.; Guo, X.; Gao, H. Seasonal variations in the water residence time in the Bohai Sea using 3D hydrodynamic model study and the adjoint method. *Ocean Dyn.* **2021**, *71*, 157–173. [CrossRef]
16. Lin, L.; Liu, D.; Guo, X.; Luo, C.; Cheng, Y. Tidal effect on water export rate in the eastern shelf seas of China. *J. Geophys. Res. Ocean.* **2020**, *125*, e2019JC015863. [CrossRef]
17. Stanev, E.V.; Ricker, M. Interactions between barotropic tides and mesoscale processes in deep ocean and shelf regions. *Ocean Dyn.* **2020**, *70*, 713–728. [CrossRef]
18. Bao, R.; van der Voort, T.S.; Zhao, M.; Guo, X.; Montluçon, D.B.; McIntyre, C.; Eglinton, T.I. Influence of hydrodynamic processes on the fate of sedimentary organic matter on continental margins. *Glob. Biogeochem. Cycles* **2018**, *32*, 1420–1432. [CrossRef]
19. Pei, Q.; Sheng, J.; Ohashi, K. Numerical Study of Effects of Winds and Tides on Monthly-Mean Circulation and Hydrography over the Southwestern Scotian Shelf. *J. Mar. Sci. Eng.* **2022**, *10*, 1706. [CrossRef]
20. Safak, I.; Wiberg, P.L.; Richardson, D.L.; Kurum, M.O. Controls on residence time and exchange in a system of shallow coastal bays. *Cont. Shelf Res.* **2015**, *97*, 7–20. [CrossRef]
21. Lin, S.; Sheng, J. Interactions between Surface Waves, Tides, and Storm-Induced Currents over Shelf Waters of the Northwest Atlantic. *J. Mar. Sci. Eng.* **2023**, *11*, 555. [CrossRef]
22. Du, J.; Shen, J.; Zhang, Y.J.; Ye, F.; Liu, Z.; Wang, Z.; Wang, Y.; Yu, X.; Sisson, M.; Wang, H.V. Tidal response to sea-level rise in different types of estuaries: The Importance of Length, Bathymetry, and Geometry. *Geophys. Res. Lett.* **2018**, *45*, 227–235. [CrossRef]
23. Wu, Z.; Zhou, C.; Wang, P.; Fei, Z. Responses of tidal dynamic and water exchange capacity to coastline change in the Bohai Sea, China. *Front. Mar. Sci.* **2023**, *10*, 1118795. [CrossRef]
24. Guo, X.; Yanagi, T. Three-dimensional structure of tidal current in the East China Sea and the Yellow Sea. *J. Oceanogr.* **1998**, *54*, 651–668. [CrossRef]
25. Liu, Z.; Lin, L.; Xie, L.; Gao, H. Partially implicit finite difference scheme for calculating dynamic pressure in a terrain-following coordinate non-hydrostatic ocean model. *Ocean Model.* **2016**, *106*, 44–57. [CrossRef]
26. Mellor, G.L.; Yamada, T. Development of a turbulence closure model for geophysical fluid problems. *Rev. Geophys.* **1982**, *20*, 851–875. [CrossRef]
27. Deleersnijder, E.; Campin, J.M.; Delhez, E.J. The concept of age in marine modelling: I. Theory and preliminary model results. *J. Mar. Syst.* **2001**, *28*, 229–267. [CrossRef]
28. Delhez, É.J.; Deleersnijder, É. The concept of age in marine modelling: II. Concentration distribution function in the English Channel and the North Sea. *J. Mar. Syst.* **2002**, *31*, 279–297. [CrossRef]
29. Lin, L.; Liu, Z. Partial residence times: Determining residence time composition in different subregions. *Ocean Dyn.* **2019**, *69*, 1023–1036. [CrossRef]
30. Delhez, E.J.M. Transient residence and exposure times. *Ocean Sci.* **2006**, *2*, 1–9. [CrossRef]
31. Delhez, É.J.; Deleersnijder, É. The boundary layer of the residence time field. *Ocean Dyn.* **2006**, *56*, 139–150. [CrossRef]
32. Zimmerman, J.T.F. On the Euler-Lagrange transformation and the Stokes' drift in the presence of oscillatory and residual currents. *Deep. Sea Res. Part A Oceanogr. Res. Pap.* **1979**, *26*, 505–520. [CrossRef]
33. Shizuo, F.; Lian, J.; Wensheng, J. A Lagrangian mean theory on coastal sea circulation with inter-tidal transports I. Fundamentals. *Acta Oceanol. Sin.* **2008**, *6*, 1–16.
34. Liu, G.; Liu, Z.; Gao, H.; Gao, Z.; Feng, S. Simulation of the Lagrangian tide-induced residual velocity in a tide-dominated coastal system: A case study of Jiaozhou Bay, China. *Ocean Dyn.* **2012**, *62*, 1443–1456. [CrossRef]
35. Lin, L.; Liu, H.; Huang, X.; Fu, Q.; Guo, X. Effect of tides on river water behavior over the eastern shelf seas of China. *Hydrol. Earth Syst. Sci.* **2022**, *26*, 5207–5225. [CrossRef]
36. Chen, D.X. *Marine Atlas of Bohai Sea, Yellow Sea, East China Sea: Hydrology*; China Ocean Press: Beijing, China, 1992. (In Chinese)
37. Fang, G.; Wang, Y.; Wei, Z.; Choi, B.H.; Wang, X.; Wang, J. Empirical cotidal charts of the Bohai, Yellow, and East China Seas from 10 years of TOPEX/Poseidon altimetry. *J. Geophys. Res. Oceans.* **2004**, *109*, C11. [CrossRef]
38. Xu, P.; Mao, X.; Jiang, W. Mapping tidal residual circulations in the outer Xiangshan Bay using a numerical model. *J. Mar. Syst.* **2016**, *154*, 181–191. [CrossRef]
39. Wu, H.; Shen, J.; Zhu, J.; Zhang, J.; Li, L. Characteristics of the Changjiang plume and its extension along the Jiangsu Coast. *Cont. Shelf Res.* **2014**, *76*, 108–123. [CrossRef]

40. Yao, Z.; He, R.; Bao, X.; Wu, D.; Song, J. $M_2$ tidal dynamics in Bohai and Yellow Seas: A hybrid data assimilative modeling study. *Ocean Dyn.* **2012**, *62*, 753–769. [CrossRef]
41. Hammons, T.J. Tidal power. *Proc. IEEE* **1993**, *81*, 419–433. [CrossRef]